

1225-0767(ISSN Print)  
2287-6715(ISSN Online)  
한국연구재단 우수등재학술지

# Journal of Ocean Engineering and Technology

Vol. 35, No. 3 (Serial Number 160)

June 2021

한국해양공학회지



[www.joet.org](http://www.joet.org)



The Korean Society of Ocean Engineers

## Editorial Board

### ■ Editor-in-Chief

Joonmo Choung Inha University, Korea

### ■ Manuscript Editors

Hyeongsik Choi Korea Maritime and Ocean University, Korea

Joon-Young Kim Korea Maritime and Ocean University, Korea

Seokhwan Ahn Jungwon University, Korea

Sungwon Shin Hanyang University, Korea

Woo Dong Lee Gyeongsang National University, Korea

### ■ Editorial Board Members

Ahmet Ergin Istanbul Technical University, Turkey

Atila Incecik University of Strathclyde, UK

Beom-Seon Jang Seoul National University, Korea

Bo Woo Nam Seoul National University, Korea

Chang Yong Song Mokpo National University, Korea

Chong Hyun Lee Jeju National University, Korea

Do Kyun Kim Newcastle University, UK

Dongho Jung Korea Research Institute of Ships & Ocean Engineering, Korea

Erkan Oterkus University of Strathclyde, UK

Geoffrey Lyons BPP-TECH, UK

Gökhan Tansel Tayyar Istanbul Technical University, Turkey

Gyung Cho Tongmyong University, Korea

Hee Jin Kang Korea Research Institute of Ships & Ocean Engineering, Korea

Hooi-Siang Kang Universiti Teknologi Malaysia, Malaysia

Hyeon Kyu Yoon Changwon National University, Korea

Hyun-Sik Kim Tongmyong University, Korea

Jinwhan Kim Korea Advanced Institute of Science and Technology, Korea

Jong Chun Park Pusan National University, Korea

Junbong Jang Dong-A University, Korea

Kangsu Lee Korea Research Institute of Ships & Ocean Engineering, Korea

Kookhyun Kim Tongmyong University, Korea

Kwang-Jun Paik Inha University, Korea

Masashi Kashiwagi Osaka University, Japan

Moo Hyun Kim Texas A&M University, USA

Narakorn Srini Newcastle University, UK

Norimi Mizutani Nagoya University, Japan

Se-Min Jeong Chosun University, Korea

Seongim Choi Virginia Tech, USA

Seung Min Park Hyein Engineering & Construction, Co., Ltd., Korea

Soonchul Kwon Pusan National University, Korea

Sungnam Hong Gyeongsang National University, Korea

Sung-Woong Choi Gyeongsang National University, Korea

Taemin Ha Kangwon National University, Korea

TaeSeong Kim Loughborough University, UK

TaeSoon Kang GeoSystem Research Corp., Korea

Tak Kee Lee Gyeongsang National University, Korea

Weoncheol Koo Inha University, Korea

Yeon-Joong Kim Inje University, Korea

Yong Uk Ryu Chonnam National University, Korea

Younghun Kim Kyungnam University, Korea

Youngsub Lim Seoul National University, Korea

## Research Ethics Board

### ■ Chief

Sung-Bu Suh Dongeui University, Korea

### ■ Research Ethics Board Members

Han Koo Jeong Kunsan National University, Korea

Jinwhan Kim Korea Advanced Institute of Science and Technology, Korea

Yong Uk Ryu Chonnam National University, Korea

**Published on** June 30, 2021

**Published by** The Korean Society of Ocean Engineers (KSOE)

Room 1302, 13, Jungang-daero 180beon-gil, Dong-gu, Busan, 48821, Korea

TEL: +82-51-759-0656 FAX: +82-51-759-0657 E-mail: ksoehj@ksoe.or.kr URL: http://www.ksoe.or.kr

**Printed by** Hanrimwon Co., Ltd., Seoul, Korea E-mail: hanrim@hanrimwon.co.kr

**ISSN(print)** 1225-0767 **ISSN(online)** 2287-6715

This journal was supported by the Korean Federation of Science and Technology Societies (KOFST) grant funded by the Korean government.

© 2021 by The Korean Society of Ocean Engineers (KSOE)

This is an open access article distributed under the terms of the creative commons attribution non-commercial license (<http://creativecommons.org/licenses/by-nc/4.0>) which permits unrestricted non-commercial use, distribution, and reproduction in any medium, provided the original work is properly cited.

# Journal of Ocean Engineering and Technology

한국해양공학회지

## CONTENTS

Volume 35, Number 3

June, 2021

---

### <Original Research Articles>

- Numerical Study on Unified Seakeeping and Maneuvering of a Russian Trawler in Wind and Waves  
Van Minh Nguyen, Thi Thanh Diep Nguyen, Hyeon Kyu Yoon and Young Hun Kim ..... 173
- Development of a Camera Self-calibration Method for 10-parameter Mapping Function  
Sung-Min Park, Chang-je Lee, Dae-Kyeong Kong, Kwang-il Hwang, Deog-Hee Doh and Gyeong-Rae Cho .... 183
- Comparison of Numerical Analyses and Model Test for Evaluation on Hydroelastic and Higher-order  
Springing Responses of Fixed Cylindrical Structure  
Hyun-Sung Kim, Younguk Won, Young Jae Oh, Kangsu Lee and Byoung Wan Kim ..... 191
- Numerical Investigation of Residual Strength of Steel Stiffened Panel Exposed to Hydrocarbon Fire  
Jeong Hwan Kim, Dae Yu Baeg and Jung Kwan Seo ..... 203
- Effect of Internal Fluid Resonance on the Performance of a Floating OWC Device  
Il Hyoung Cho ..... 216
- Performance Analysis of Multiple Wave Energy Converters due to Rotor Spacing  
Sunny Kumar Poguluri, Dongeun Kim, Haeng Sik Ko and Yoon Hyeok Bae ..... 229
- ### <Technical Article>
- Engagement-Scenario-Based Decoy-Effect Simulation Against an Anti-ship Missile Considering Radar Cross Section  
and Evasive Maneuvers of Naval Ships  
Kookhyun Kim ..... 238

## GENERAL INFORMATION

“Journal of Ocean Engineering and Technology” is the official journal published by “The Korean Society of Ocean Engineers (KSOE)”. The ISO abbreviation is “J. Ocean Eng. Technol.” and acronym is “**JOET**”. It was launched in 1987. It is published bimonthly in February, April, June, August, October, and December each year. Supplement numbers are published at times.

Journal of Ocean Engineering and Technology (JOET) is a medium for the publication of original research and development work in the field of ocean engineering. JOET covers the entire range of issues and technologies related to the following topics:

**Ships and offshore platforms:** Design of marine structures; Resistance and propulsion; Seakeeping and maneuvering; Experimental and computational fluid dynamics; Ocean wave mechanics; Fatigue strength; Plasticity; Optimization and reliability; Arctic technology and extreme mechanics; Noise, vibration, and acoustics; Concrete engineering; Thermodynamics and heat transfer; Hydraulics and pneumatics;  
**Coastal civil engineering:** Coastal structures; Port and harbor structures; Soil mechanics; Drilling and exploration; Hydraulics of estuary; Seismic engineering; Coastal disaster prevention engineering;  
**Ocean renewable energy platforms:** Offshore wind turbines; Wave energy platforms; Tidal current energy platforms; Floating photovoltaic energy platforms;  
**Marine robots:** Robot sensor system; Autonomous navigation; Robot equipments; Spatial information and communications; Underwater network; Design of underwater vehicles;  
**Multidisciplinary areas:** Design for safety; IT-based design; IT-based production engineering; Welding mechanics; Control engineering; GPS and GIS; Inspection and sensor; Port and logistics; Leisure boat and deep sea water; Offshore process systems engineering; Marine metallic materials; Marine organic materials; Marine Composite materials; Materials properties; Corrosion and Anti-corrosion; Tribology;

It contains original research articles, case reports, brief communications and reviews on technical issues. Conference papers, research papers, diploma papers and academic articles can be submitted.

All of the manuscripts are peer-reviewed. **JOET** has a system where two or more peer reviewers must review each submitted paper and it is operated very strictly.

**JOET** is an open access journal distributed under the terms of the creative commons attribution non-commercial license (<http://creativecommons.org/licenses/by-nc/4.0>). Therefore, all ocean engineers and researchers around the world can easily access all journal articles via the journal homepage (<http://www.joet.org>) and download the PDF-based original texts or view the web-based XML texts for free.

**JOET** is being indexed in some prominent database such as Korean Citation Index (KCI), Google Scholar, Science Central, Korea Science and Directory of Open Access Journals (DOAJ).

For correspondences concerning business matters, author needs to contact KSOE Secretariat by email or phone (e-mail: [ksoehj@ksoe.or.kr](mailto:ksoehj@ksoe.or.kr) or Tel: +82 51 759 0656). Correspondences for publication matters can be asked via email to the Editor-in-Chief (email: [heroeswise2@gmail.com](mailto:heroeswise2@gmail.com)).

# Numerical Study on Unified Seakeeping and Maneuvering of a Russian Trawler in Wind and Waves

Van Minh Nguyen<sup>1</sup>, Thi Thanh Diep Nguyen<sup>2</sup>, Hyeon Kyu Yoon<sup>3</sup> and Young Hun Kim<sup>4</sup>

<sup>1</sup>Researcher, Department of Transportation Mechanical Engineering, University of Danang – University of Science and Technology, Vietnam

<sup>2</sup>Graduate student, Department of Eco-friendly Offshore Plant FEED Engineering, Changwon National University, Changwon, Korea

<sup>3</sup>Professor, Department of Naval Architecture and Marine Engineering, Changwon National University, Changwon, Korea

<sup>4</sup>Professor, Department of Naval Architecture, Ocean, and IT Engineering, Kyungnam University, Changwon, Korea

**KEY WORDS:** Ship maneuvering in waves, Russian trawler, Unified Seakeeping and Maneuvering

**ABSTRACT:** The maneuvering performance of a ship on the actual sea is very different from that in calm water due to wave-induced motion. Enhancement of a ship's maneuverability in waves at the design stage is an important way to ensure that the ship navigates safely. This paper focuses on the maneuvering prediction of a Russian trawler in wind and irregular waves. First, a unified seakeeping and maneuvering analysis of a Russian trawler is proposed. The hydrodynamic forces acting on the hull in calm water were estimated using empirical formulas based on a database containing information on several fishing vessels. A simulation of the standard maneuvering of the Russian trawler was conducted in calm water, which was checked using the International Maritime Organization (IMO) standards for ship maneuvering. Second, a unified model of seakeeping and maneuvering that considers the effect of wind and waves is proposed. The wave forces were estimated by a three-dimensional (3D) panel program (ANSYS-AQWA) and used as a database when simulating the ship maneuvering in wind and irregular waves. The wind forces and moments acting on the Russian trawler are estimated using empirical formulas based on a database of wind-tunnel test results. Third, standard maneuvering of a Russian trawler was conducted in various directions under wind and irregular wave conditions. Finally, the influence of wind and wave directions on the drifting distance and drifting angle of the ship as it turns in a circle was found. North wind has a dominant influence on the turning trajectory of the trawler.

## 1. Introduction

The maneuvering performance of a ship on the actual sea is very different from that in calm water due to wave-induced motion. It is crucial to account for the ship's maneuverability in waves at the design stage. Numerous prior studies have investigated the maneuverability of ships in waves. According to the International Towing Tank Conference (ITTC) (ITTC, 2011), there are four methods of predicting the movements of a ship maneuvering in waves: experiments, two-time scale, unified theory, and contract for difference (CFD) methods.

Yasukawa (2006) proposed a method of estimating the hydrodynamic force components, including added mass, wave damping, and wave excitation forces. In his study, the basic motion equations were divided into two groups, high-frequency induced

motion problems, and low-frequency maneuvering problems. Yasukawa (2006, 2008) performed a free-running model test in regular waves using the SR108 container ship. The experiment was conducted with various wavelengths in head sea and beam sea conditions. Skejic and Faltinsen (2007, 2008) presented a seakeeping and maneuvering analysis of two ships. They focused on overtaking and replenishment maneuvers between two ships.

Seo et al. (2011) applied linear and nonlinear ship motion analysis to analyze ship-maneuvering performance in high-amplitude waves. The maneuvering performance of the S-175 container ship was discussed with regard to wave slope. Also, the wave drift force was calculated using the direct pressure integration method. Skejic (2013) presented a maneuvering simulation of ships in a seaway and discussed the significant role of unified maneuvering and seakeeping. Zhang et al. (2017) proposed a method for predicting ship maneuvering in regular

Received 15 December 2020, revised 2 March 2021, accepted 2 May 2021

Corresponding author Hyeon Kyu Yoon: +82-55-213-3683, [hkyoon@changwon.ac.kr](mailto:hkyoon@changwon.ac.kr)

This paper was presented on the subject of "Numerical Study on Unified Seakeeping and Maneuvering of a Russian Trawler in Wind and Wave" in the proceedings of 2020 Korean Society of Ocean Engineers Fall Conference.

© 2021, The Korean Society of Ocean Engineers

This is an open access article distributed under the terms of the creative commons attribution non-commercial license (<http://creativecommons.org/licenses/by-nc/4.0>) which permits unrestricted non-commercial use, distribution, and reproduction in any medium, provided the original work is properly cited.

waves of the S-175 container ship. Wang and Wan (2018) used a CFD solver called naoe-FOAM-SJTU to analyze a ship's maneuverability in waves.

Previous studies only focused on the influence of regular waves on the ship's maneuverability. However, the ocean waves are actually irregular waves, so it is really necessary to study the effect of the irregular waves on the maneuvering performance of the ship, especially when designing a trawler. This paper proposes a unified model of seakeeping and maneuvering, which is used to predict the maneuverability of a Russian trawler in wind and waves. In this study, ANSYS-AQWA was utilized to estimate wave drift forces and moments. In addition, the wind forces and moments acting on the Russian trawler were estimated using empirical formulas, which are based on a database containing wind tunnel test data.

Standard maneuvers of the Russian trawler were conducted in calm water, wind, and irregular wave conditions, and the effect of the operation scenario on turning trajectories are discussed. Previous studies have not investigated the operation conditions of this vessel. In this study, the operation conditions of the trawler in the Sea of Okhotsk were investigated to determine the wave and wind conditions for operation conditions. The ship's maneuverability in different seasons was checked with changes in the wind and wave directions.

## 2. Mathematical Formulation

### 2.1 Coordinate System

In order to predict a ship's maneuvering performance in wind and waves, two right-handed coordinate systems were adopted, including a body-fixed coordinate system  $Oxy$  and an earth-fixed coordinate system  $Ox_0y_0$ , as shown in Fig. 1. The body-fixed coordinate system advances with the ship's forward speed  $U$  and rotates with rotation speed  $r$ . In addition,  $\delta$ ,  $\psi$ ,  $\mu$ ,  $\beta$ , and  $\psi_A$  are the rudder angle, heading angle, incident wave direction, drift angle, and incident wind direction, respectively. The ship's position is expressed with respect to the earth-fixed coordinate system.

### 2.2 Equation of Motion

Two types of hydrodynamic models are commonly used to predict the maneuverability of a ship: the Abkowitz model and Maneuvering Modeling Group (MMG) model. In this study, the MMG model for

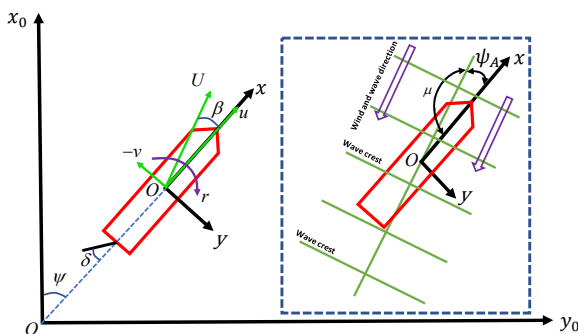


Fig. 1 Maneuvering coordinate system in wind and waves

maneuvering motion in 3DOF was applied, which is described by Eq. (1).  $u$  and  $v$  are the velocity components in the x-axis and y-axis direction, respectively.  $\dot{u}$  and  $\dot{v}$  are the surge acceleration and sway acceleration, respectively.  $\dot{r}$ ,  $I_{zz}$ ,  $m$ , and  $x_G$  are the angular acceleration, the moment of inertia about the z axis, the ship's mass, and the longitudinal position of the ship's center of gravity, respectively.  $X$  and  $Y$  are the hydrodynamic forces, and  $N$  is the moment around the z-axis. The subscripts  $H$ ,  $P$ , and  $R$  denote the hydrodynamic forces due to the hull, propeller, and rudder in calm water, respectively. The subscripts  $W$  and  $A$  denote the hydrodynamic forces induced by waves and wind, respectively.

$$m(\dot{u} - vr - x_G \dot{r}^2) = X_H + X_R + X_P + X_W + X_A \quad (1)$$

$$m(\dot{v} + ur + x_G \dot{r}) = Y_H + Y_R + Y_W + Y_A$$

$$I_{zz} \dot{r} + mx_G(\dot{v} + ur) = N_H + N_R + N_W + N_A$$

### 2.3 Hull Force

In this study, the mathematical model of hydrodynamic forces suggested by Yoshimura and Ma (2003) was used to predict the ship's maneuvering performance in calm water. They proposed empirical formulas to predict the hydrodynamic derivatives are based on a database of hydrodynamic derivatives containing information on several fishing vessels, including a recent European wide-beam vessel.  $X_H$ ,  $Y_H$  and  $N_H$  are modeled as functions of the non-dimensional sway velocity and non-dimensional yaw rate using Eq. (2).  $u'$  and  $v'$  are non-dimensional velocity components in the x-axis and y-axis directions, respectively.  $r'$  is the non-dimensional yaw rate, and  $X_0$  is the ship resistance.  $X'_{vv}$ ,  $X'_{rr}$ ,  $X'_{vr}$ ,  $X'_{vvvv}$ ,  $Y'_v$ ,  $Y'_r$ ,  $Y'_{vvv}$ ,  $Y'_{vvr}$ ,  $Y'_{vrr}$ ,  $Y'_{rrr}$ ,  $N'_v$ ,  $N'_r$ ,  $N'_{vvv}$ ,  $N'_{vvr}$ ,  $N'_{vrr}$ , and  $N'_{rrr}$  are the hydrodynamic derivatives of the polynomials and are estimated based on empirical formulas for fishing vessels suggested by Yoshimura and Ma (2003).

$$X_H = -X_0 + \frac{1}{2} \rho L_{pp}^2 dU^2 (X'_{vv} v'^2 + X'_{rr} r'^2 + X'_{vr} v'r' + X'_{vvvv} v'^4) \quad (2)$$

$$Y_H = \frac{1}{2} \rho L_{pp}^2 dU^2 (Y'_v v' + Y'_r r' + Y'_{vvv} v'^3 + Y'_{vvr} v'^2 r' + Y'_{vrr} v' r'^2 + Y'_{rrr} r'^3)$$

$$N_H = \frac{1}{2} \rho L_{pp}^2 dU^2 (N'_v v' + N'_r r' + N'_{vvv} v'^3 + N'_{vvr} v'^2 r' + N'_{vrr} v' r'^2 + N'_{rrr} r'^3)$$

### 2.4 Rudder Force

The rudder force and moment can be estimated through a combination of the interaction factor and the rudder normal force using Eq. (3).  $F_N$ ,  $a_H$ , and  $t_R$  are the rudder's normal force, the rudder's force increase factor, and the steering resistance deduction factor, respectively. The rudder's normal force is expressed in Eq. (4).  $x_R$  and  $x_H$  are the longitudinal position of the rudder and the additional lateral force component, respectively.

$$X_R = -(1 - t_R) F_N \sin \delta \quad (3)$$

$$Y_R = -(1 + a_H) F_N \cos \delta$$

$$N_R = -(x_R + a_H x_H) F_N \cos \delta$$

$$F_N = \frac{1}{2} \rho A_R U_R^2 f_\alpha \sin \alpha_R \quad (4)$$

$$\text{where } f_\alpha = \frac{6.13A}{\Lambda + 2.25}$$

$$U_R = \sqrt{u_R^2 + v_R^2}$$

$$\alpha_R = \delta - \tan^{-1} \left( \frac{v_R}{u_R} \right) \approx \delta - \frac{v_R}{u_R}$$

$$v_R = U \gamma_R \beta_R \quad \text{and} \quad \beta_R = \beta - l'_R$$

$$u_R = \epsilon u (1 - w_p) \sqrt{\eta \left\{ 1 + \kappa \left( \sqrt{1 + \frac{8K_T}{\pi J_P^2}} - 1 \right) \right\}^2 + (1 - \eta)}$$

where  $v_R$  and  $u_R$  are the lateral and longitudinal inflow velocities induced on the rudder by propeller rotation, respectively.  $\Lambda$  and  $A_R$  are the rudder aspect ratio and the rudder area.  $f_\alpha$  represents the rudder lift gradient coefficient, and  $U_R$  represents the resultant inflow velocity to the rudder.  $\eta$  denotes the ratio of the propeller diameter to the rudder span.  $\epsilon$  represents the ratio of the wake fraction at the rudder position to that of the propeller position.  $\kappa$  represents the interaction between the propeller and rudder.

$\alpha_R$  denotes the effective inflow angle to the rudder.  $\beta_R$  represents the effective inflow angle to the rudder, and  $\gamma_R$  represents the flow straightening coefficient.  $l'_R$  is an experimental constant that is used to express  $v_R$  accurately.  $w_p$  represents the wave coefficient at propeller position. The interaction force coefficients  $t_R$ ,  $a_H$ ,  $l'_R$ , and  $\epsilon$  can be obtained from Yoshimura and Ma's empirical formulas for fishing vessels.

## 2.5 Propeller Force

The longitudinal force of the propeller  $X_P$  can be estimated using Eq. (5).  $t_p$ ,  $\rho$ , and  $D_p$  are the thrust deduction factor, the water density, and the diameter of the propeller, respectively. For simplicity, the thrust deduction factor  $t_p$  is assumed to be constant at any given propeller load.  $K_T$  is the thrust coefficient, which can be expressed as the 3rd polynomial of the propeller advance ratio  $J_P$  using Eq. (6).  $k_0$ ,  $k_1$ ,  $k_2$ , and  $k_3$  are coefficients representing  $K_T$ .

$$X_P(u, n) = (1 - t_p) T \quad (5)$$

$$K_T(J_P) = k_0 + k_1 J_P + k_2 J_P^2 + k_3 J_P^3 \quad \text{and} \quad J_P = \frac{u(1 - w_p)}{n_p D_P} \quad (6)$$

$$\text{where } T = \rho n_p^2 D_P^4 K_T(J_P)$$

## 2.6 Wave Drift Force and Moment

The steady wave-induced forces in irregular waves can be estimated using Eq. (7).  $H_{1/3}$  and  $g$  denote the significant wave height and the gravity acceleration, respectively.  $\bar{C}_{XW}$ ,  $\bar{C}_{YW}$ , and  $\bar{C}_{NW}$  denote the average value of the steady wave-induced force and moment coefficients in irregular waves estimated using Eq. (8).  $\bar{C}_{XW}$ ,  $\bar{C}_{YW}$ , and  $\bar{C}_{NW}$  are estimated based on the short-term prediction technique by Yasukawa et al. (2017). These coefficients are stored in files in databases and used when simulating the ship's maneuverability in irregular waves.  $S_{\zeta\zeta}(\omega)$  and  $G(\theta)$  denote the wave spectrum and the wave direction distribution function, respectively. The ITTC spectrum is used as the wave spectrum  $S_{\zeta\zeta}(\omega)$ . The cosine-squared spreading function is used as the wave direction distribution function ( $\theta$ ).  $C_{XW}(\omega, \chi)$ ,  $C_{YW}(\omega, \chi)$ , and  $C_{NW}(\omega, \chi)$  denote the wave-induced steady force and moment coefficient in regular waves expressed as a function of the wave frequency  $\omega$  and the wave direction  $\chi$ .

$$X_W = \rho g H_{1/3}^2 L_{pp} \bar{C}_{XW}(T, \chi) \quad (7)$$

$$Y_W = \rho g H_{1/3}^2 L_{pp} \bar{C}_{YW}(T, \chi)$$

$$N_W = \rho g H_{1/3}^2 L_{pp}^2 \bar{C}_{NW}(T, \chi)$$

$$\bar{C}_{XW}(T, \chi) = 2 \int_{-\pi}^{\pi} G(\theta) d\theta \int_0^{\infty} C_{XW}(\omega, \chi) \frac{S_{\zeta\zeta}(\omega)}{H_{1/3}^2} d\omega \quad (8)$$

$$\bar{C}_{YW}(T, \chi) = 2 \int_{-\pi}^{\pi} G(\theta) d\theta \int_0^{\infty} C_{YW}(\omega, \chi) \frac{S_{\zeta\zeta}(\omega)}{H_{1/3}^2} d\omega$$

$$\bar{C}_{NW}(T, \chi) = 2 \int_{-\pi}^{\pi} G(\theta) d\theta \int_0^{\infty} C_{NW}(\omega, \chi) \frac{S_{\zeta\zeta}(\omega)}{H_{1/3}^2} d\omega$$

## 2.7 Wind Force and Moment

The hydrodynamic forces due to wind can be obtained using the empirical formula presented by Kitamura et al. (2017), which is based on a wind tunnel test and is shown in Eq. (9).  $L_{OA}$  is the overall length of the ship,  $A_F$  is the frontal projected area,  $A_L$  is the lateral projected area, and  $C$  is the distance from mid-ship to the centroid of  $A_L$ .  $H_C$  is the height of centroid of  $A_L$  from the calm water level.  $C_{XLI}$ ,  $C_{ALF}$ ,  $C_{CF}$ , and  $C_{YLI}$  are coefficients of the multiple regression formulae. The hydrodynamic coefficients due to wind can be estimated using Eq. (10).

$$X_A = \frac{1}{2} \rho_A A_F U_A^2 C_X(\psi_A) \quad (9)$$

$$Y_A = \frac{1}{2} \rho_A A_F U_A^2 C_Y(\psi_A)$$

$$N_A = \frac{1}{2} \rho_A A_L L_{OA} U_A^2 C_N(\psi_A)$$

$$C_X(\psi_A) = C_{XLF} \left( \sin\psi_A - \frac{1}{2} \sin\psi_A \cos^2\psi_A \right) \sin\psi_A \cos\psi_A \quad (10)$$

$$+ C_{LFF} \cos\psi_A + C_{ALF} \sin\psi_A \cos^3\psi_A$$

$$C_Y(\psi_A) = C_{YLF} \left( \cos\psi_A - \frac{1}{2} \sin^2\psi_A \cos\psi_A \right) \sin\psi_A \cos\psi_A + C_{CF} \sin^2\psi_A$$

$$C_N(\psi_A) = C_Y(\psi_A) \left[ 0.927 \frac{C}{L_{OA}} - 0.149 \left( \psi_A - \frac{\pi}{2} \right) \right]$$

### 3. Numerical Method

#### 3.1 Simulation Conditions

In order to investigate the ship maneuverability, a Russian trawler designed by Deahea Ship Design Corporation was selected. Fig. 2 shows the geometry of the Russian trawler. The principal dimensions are listed in Table 1.

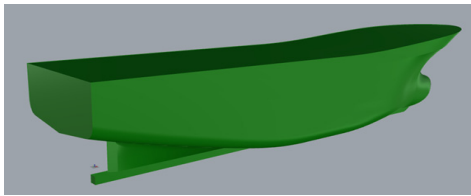


Fig. 2 Geometry of the Russian trawler

Table 1 Principal dimensions of the Russian trawler

Item	Unit	Symbol	Value
Length between perpendiculars	m	$L_{pp}$	32.45
Breath	m	$B$	9.00
Displacement	t	$\Delta$	587
Draft at bow	m	$d_f$	2.40
Draft at stern	m	$d_a$	3.34
Mean draft	m	$d$	3.00
Effective mean	m	$d_{em}$	3.49
Block coefficient (by $d_{em}$ )	-	$C_B$	0.559

The standard maneuvers of the trawler in calm water are conducted with constant propeller revolution. The propeller revolution is selected to produce a speed of 12 knots (6.17 m/s) when the trawler vessel moves forward in calm water. The propeller speed was 4.384 revolutions per second. Simulations of the ship turning in a circle were conducted in wind and irregular waves based on the operation conditions in the Sea of Okhotsk.

The maximum wind speed was selected for the simulation according to the wind direction in Table 2. East wind is defined using the period of April to May, South wind is defined using the period of May to September, and North wind is defined using the period of September to April of the following year. The maximum wind speed is the time

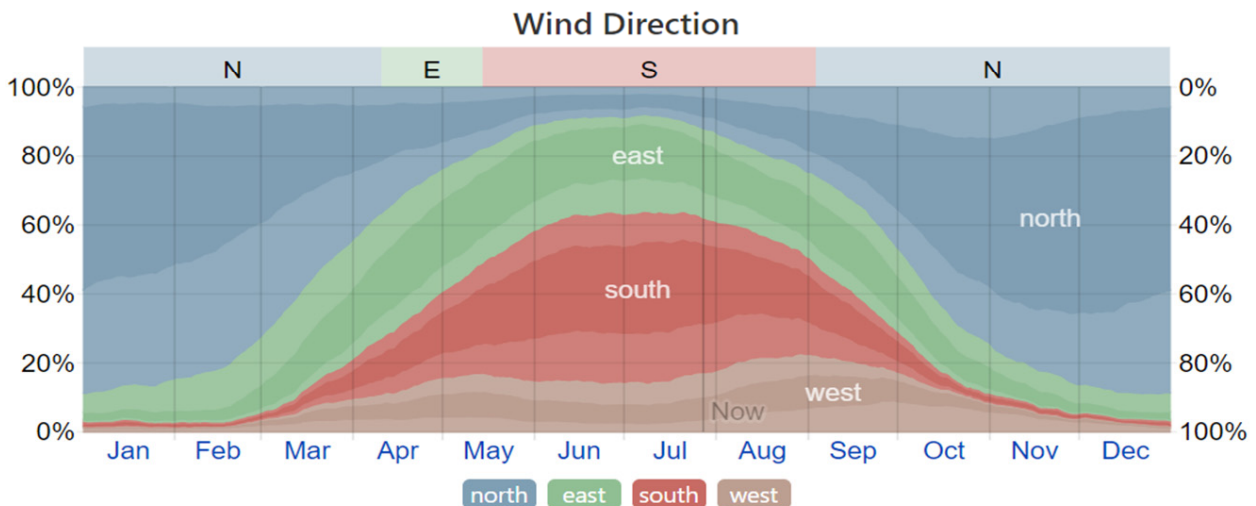
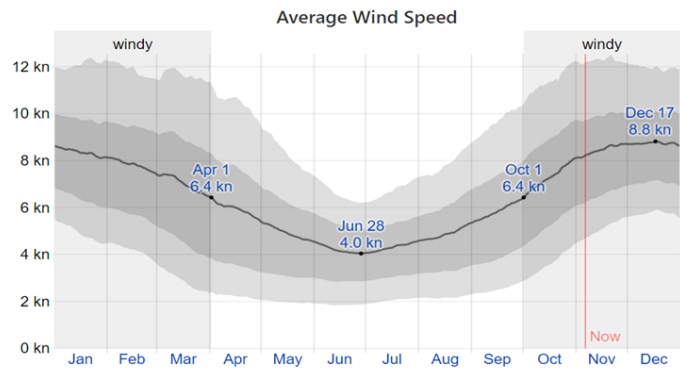


Fig. 3 Operation scenario in the Sea of Okhotsk (Weather Spark, 2020)

**Table 2** Operation scenario in the Sea of Okhotsk

Item	Apr. -May	May-Sep.	Sep. -Apr
Wind direction	East wind (38%)	South wind (50%)	North wind (89%)
Average wind speed (m/s)	2.1		3.3
Maximum wind speed (m/s)	5.1	5.1	6.2

**Table 3** Hydrodynamic coefficients

Hull coefficients	Value	Hull coefficients	Value
$X'_{vv}$	-4.06E-02	$Y'_{vvr}$	7.55E-02
$X'_{rr}$	-6.90E-03	$Y'_{vrr}$	-4.50E-01
$X'_{vr}$	-1.59E-01	$N'_v$	-1.35E-01
$X'_{vvv}$	3.87E-01	$N'_{vvv}$	-3.37E-01
$Y'_v$	-6.10E-01	$N'_r$	-6.99E-02
$Y'_{vvv}$	-1.36E+00	$N'_{rrr}$	-8.20E-03
$Y'_r$	5.45E-02	$N'_{vvr}$	-4.62E-01
$Y'_{rrr}$	-1.75E-02	$N'_{vrr}$	-1.81E-02

selection value that is equivalent to each wind direction. The wind direction and average wind speed at 10 m above the ground in the Sea of Okhotsk were obtained from the Weather Spark website. The wind speed and wind direction change dramatically depending on seasonal variation. Fig. 3 shows the wind direction and wind speed in the Sea of Okhotsk. A comparison of the wind speed and wind direction in various seasons is presented in Table 2.

3.2 Hydrodynamic Coefficients

The hydrodynamic coefficients of the trawler were estimated based on the empirical formulas presented by Yoshimura and Ma (2003). The hydrodynamic coefficients of the trawler are listed in Table 3. The interaction coefficients among the hull, propeller, and rudder were also estimated based on Yoshimura and Ma’s empirical formulas and are listed in Table 4.

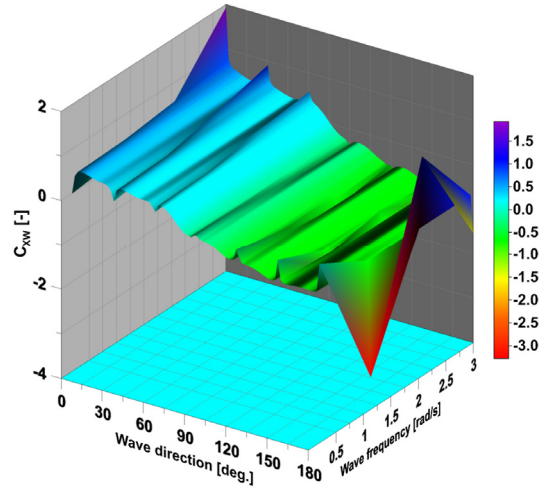
**Table 4** Interaction coefficients

Interaction coefficients	Value	Interaction coefficients	Value
$1-t_R$	0.853	$\gamma_R$	0.458
$a_H$	0.048	$\epsilon$	0.995
$x'_H$	-0.450	$\kappa$	0.428
$l'_R$	-0.936	-	-

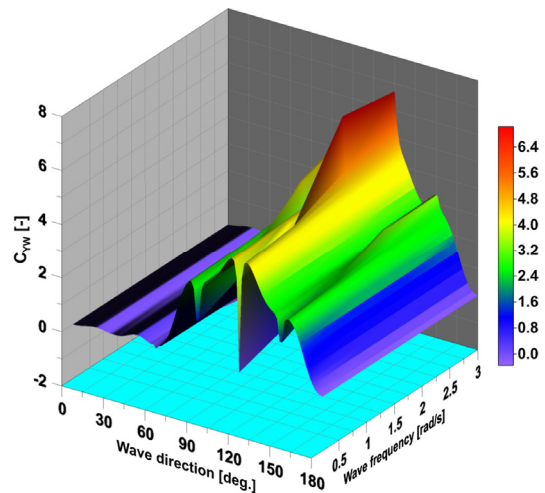
3.3 Hydrodynamic Force Due to Waves

Fig. 4 shows the wave drift forces and moment in various wave directions and wave frequencies. The surge drift force has a similar tendency to the overall trend of the surge drift force in the head sea. The maximum value of surge drift force occurs at low wave frequencies, where the wavelength is greater than the ship’s length.

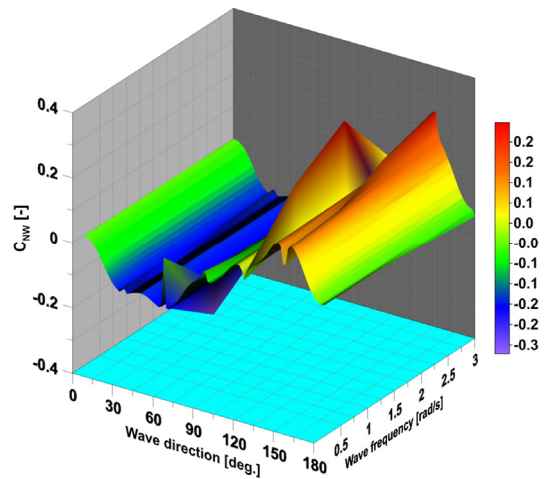
The wavelength is greater than the length of the vessel when the wave frequency is smaller than 1.35 rad/s. The surge drift force decreases gradually with an increase in the wave frequency and wave direction and almost disappears in following sea.



(a) Surge drift force



(b) Sway drift force



(c) Yaw drift moment

**Fig. 4** Wave drift forces and moment

The maximum value of the sway drift force occurs at high wave frequency and in oblique sea, especially at a wave direction of 120 degrees. The sway drift force decreases gradually as the wave frequency decreases and it almost disappears in the head sea and the following sea. At wave directions of 180 degrees and 0 degrees, a small value of the sway drift force is observed without a distinct peak. The maximum value of yaw drift moment occurs in oblique sea, especially at wave directions of 150 degrees and 60 degrees. The yaw drift moment increases significantly at high wave frequency, while it decreases gradually as the wave frequency decreases and almost disappears in the head sea and the following sea.

### 3.4 Drifting Distance and Drifting Angle

To analyze the turning trajectories in irregular wave and wind conditions, we applied the drifting distance and the drifting angle suggested by Kim et al. (2019). The drifting distance  $Dr_d$  is the distance between lines that are perpendicular to the tangent to the turning trajectory, as shown in Fig. 4. For example,  $Dr_{d_{90-450}}$  represents the magnitude of the vector between two points corresponding to heading angles of 90 degrees and 450 degrees.

The drifting angle  $Adr$  is the angle between the tangential line of the turning trajectory and the ship's approach direction in the  $x$  direction, as shown in Fig. 5. For instance,  $Adr_{90-450}$  represents the angle between the ship's approach direction in the  $x$  direction and the tangential line of two points corresponding to heading angles of 90 degrees and 450 degrees. The relative drift angle  $Rdr$  is the angle between the drifting angle and the wave propagation direction, which can be estimated using Eq. (11).  $\delta$  is the rudder angle,  $\chi$  is the wave propagation direction, and  $Adr$  is the drifting angle. The relative drifting distance  $Rdr$  is suggested by Kim et al. (2019) to describe the ship's turning trajectory in waves.

$$Rdr = \text{sign}(\delta)(\chi - Adr) \tag{11}$$

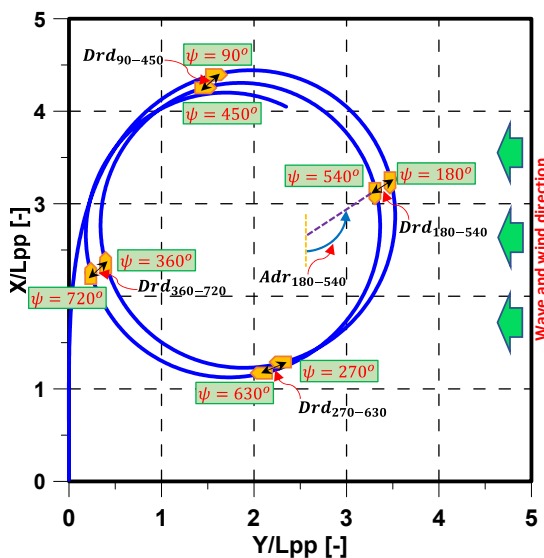


Fig. 5 Definition of drifting distance and drifting angle

## 4. Results and Discussion

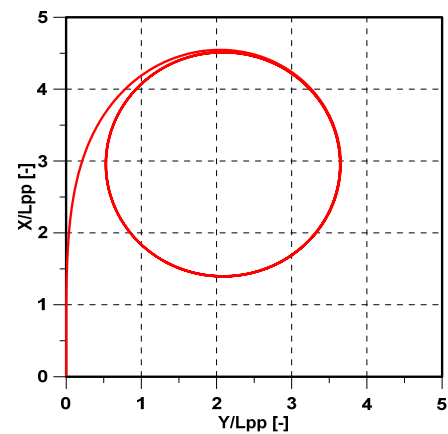
### 4.1 Turning Circle in Calm Water

The predicted turning trajectory of the trawler in calm water is shown in Fig. 6(a). The surge velocity, sway velocity, and yaw rate of

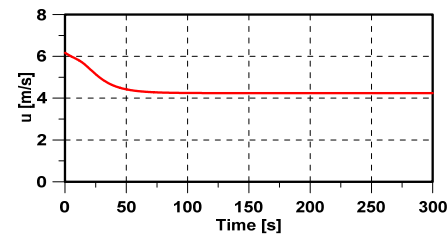
Table 5 Maneuver parameters in turning circle in calm water

Item	Trawler	IMO standard
Advance ( $L_{pp}$ ) <sup>(1)</sup>	4.496	4.5
Tactical diameter ( $L_{pp}$ )	3.600	5.0

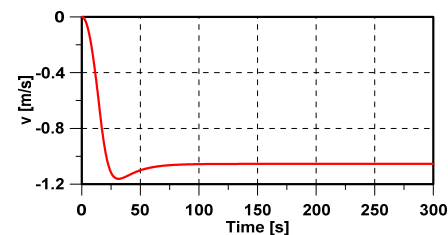
<sup>(1)</sup> Length between perpendiculars



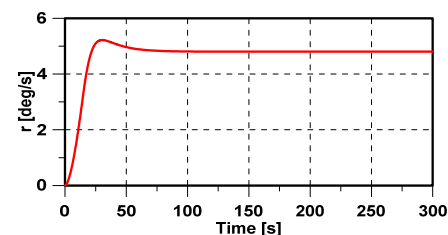
(a) Ship's trajectory



(b) Surge velocity



(c) Sway velocity



(d) Yaw rate

Fig. 6 Turning circle in calm water

the turning circle in calm water are shown in Figs. 6(b), 6(c), and 6(d), respectively. The results of the advance and the tactical diameter of the trawler are compared to the standards of the International Maritime Organization (IMO) for ship maneuverability, as shown in Table 5. Therefore, the turning ability of the trawler in calm water is confirmed and satisfied with the value proposed by the IMO's standards.

#### 4.2 Turning Circle in Wind and Waves

In order to investigate the effect of the operation scenario, we simulated the movements of the trawler as it turns in a circle in wind and irregular waves. The wave direction is similar to the wind direction. The maximum wind speed was selected in this simulation. Fig. 7 shows the turning trajectories of the trawler in the operation scenario for various wind directions. It can be seen that the wind direction and significant wave height have dominant effects on the turning trajectories of the trawler.

The direction of the wind and waves slightly influences the advance of the trawler, while it significantly affects the tactical diameter, as shown in Fig. 8. This happens because the ship turns at the initial stage until the heading angle is 90 degrees, and the ship's trajectory changes slightly. During the initial turning, the hydrodynamic forces induced by the rudder produce a surge acceleration, sway acceleration, and yaw acceleration. There is a gradual increase in the hydrodynamic forces and moment acting on the ship hull, which consist of an acceleration-dependent term and velocity-dependent term.

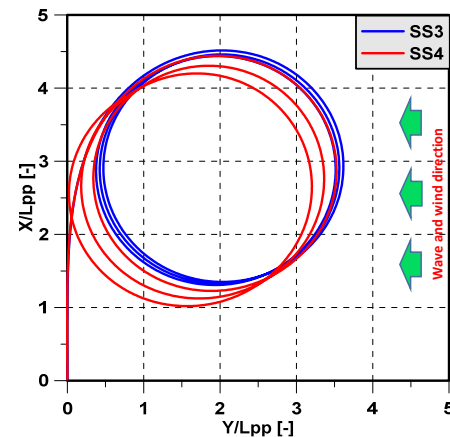
When the ship turns at times less than 50 s, the hydrodynamic forces and moment are changed by the motion induced by wind and waves, as shown in Fig. 9. However, these hydrodynamic forces are very small in comparison to the hydrodynamic forces caused by the acceleration in the initial turning. Therefore, the ship's trajectory changes very slightly at the early stages of turning. This is the reason why the advance is relatively similar when the ship turns in various wind and wave directions.

The changing of the hydrodynamic forces and moment changed by the motion induced by wind and waves for North wind (green line) can be divided into 4 phases: A, B, C, and D. Phase A is related to the occurrence of the maximum value of the sway and yaw moment changed by the motion induced by wind and waves. These hydrodynamic forces occur when the incident wave direction is 90 degrees, as shown in Fig. 9. Phase B involves the occurrence of the maximum surge force changed by the motion induced by wind and waves at the incident wave direction of 180 degrees or the incident wind direction of 0 degrees, as seen in Fig. 9. In this case, the sway force and yaw moment changed by the motion induced by wind and waves are approximately zero.

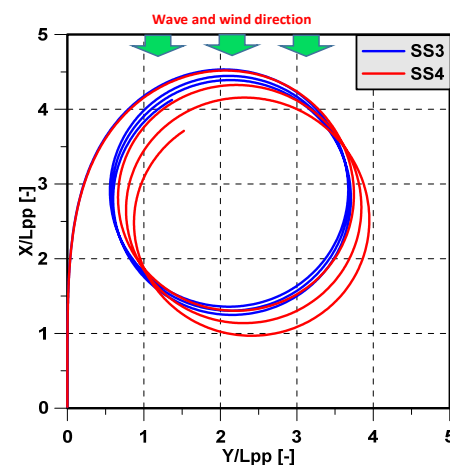
Phase C is similar to phase A and causes a large sway force and yaw moment changed by the motion induced by wind and waves when the incident wave direction reaches 90 degrees. At the time of phase C, the speed of the ship has reached steady turning, and the effects of the acceleration changes are small. Likewise, phase D is similar to phase B and causes the greatest reduction in surge force changed by the motion

induced by wind and waves, even though the sway and yaw moment changed by the motion induced by wind and waves are close to zero.

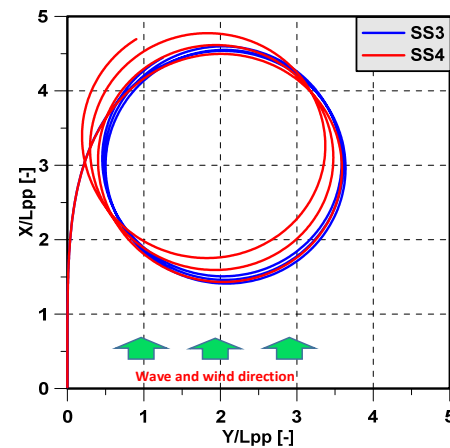
Fig. 10 shows the drifting distance and drifting direction for various wind directions. It is evident that the North wind has the dominant influence on the turning trajectory of the trawler. In particular, when the ship moves in the North wind, the value of the drifting distance is bigger than that of the East or South winds, as shown in Fig. 10. The



(a) East wind



(b) North wind



(c) South wind

Fig. 7 Turning circle in wind and irregular waves

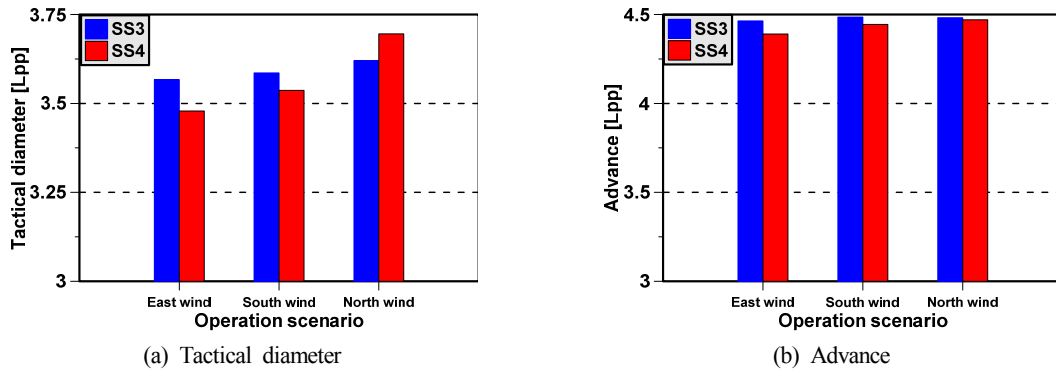


Fig. 8 Maneuver parameters in wind and waves

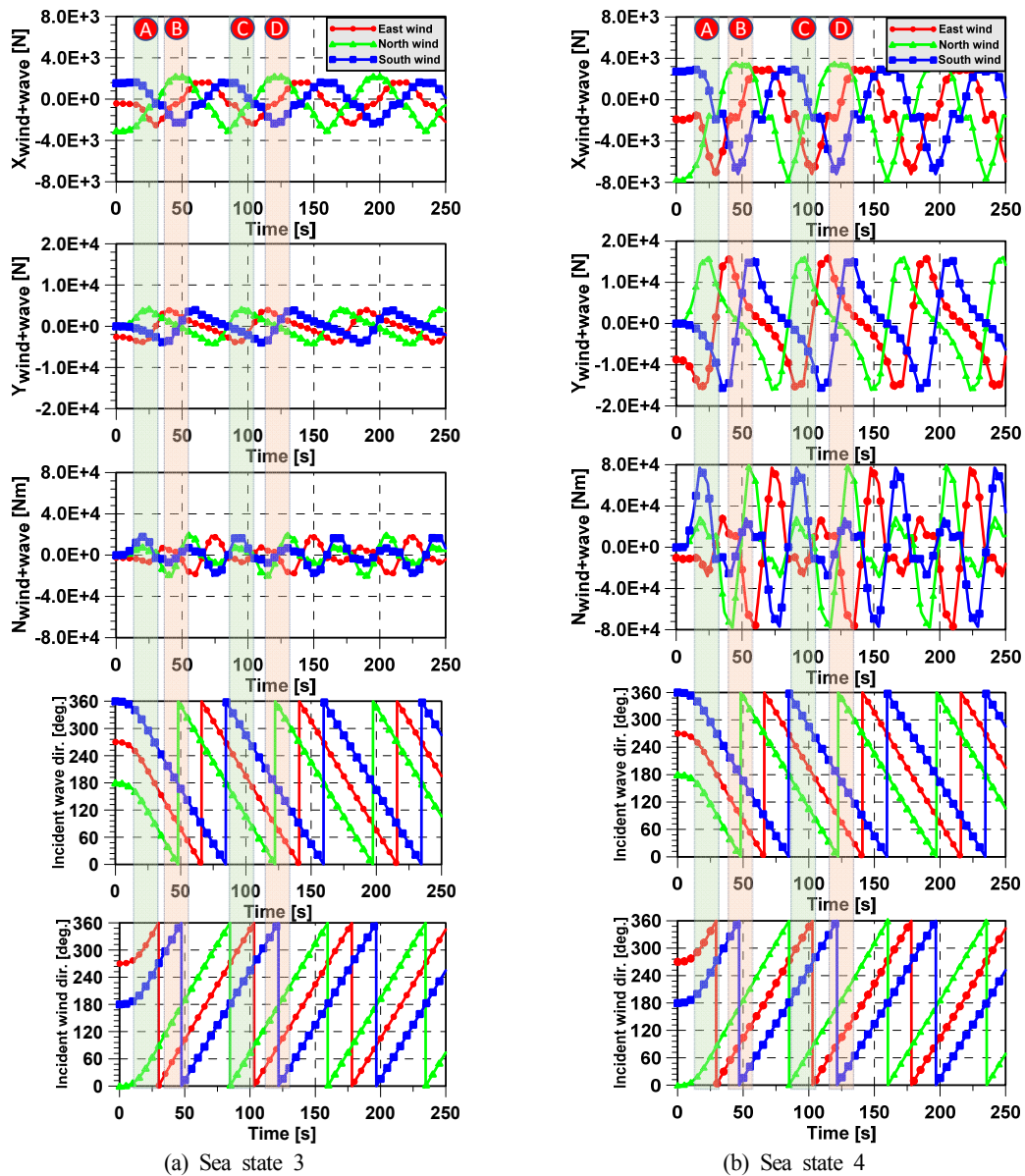


Fig. 9 Comparison of maneuvering motion in wind and waves

South wind has the smallest influence on the drifting distance. The drifting direction is approximately parallel to the wind and wave-propagation direction. This happens because the North wind causes a change of the wave direction relative to ships in the 90-degree

direction and 180 degrees earlier than East wind and South winds.

This is the reason why the ship turning in North wind causes the largest drifting distance. It is also why the ship's tactical diameter in the North wind is the largest, as shown in Fig. 8. The ship enters the

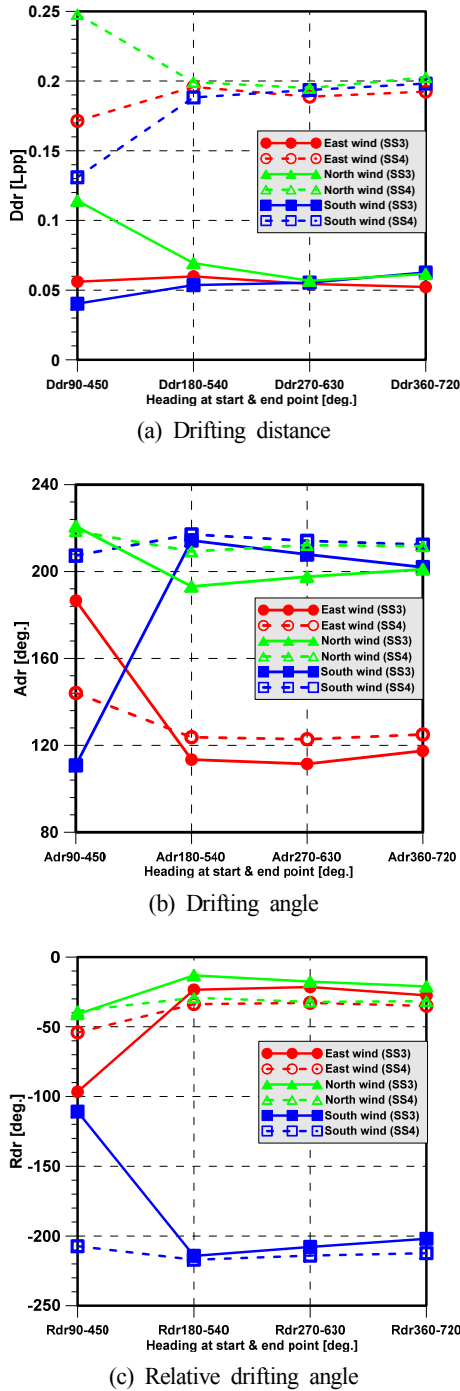


Fig. 10 Drifting parameters in turning circle in wind and waves

steady turning phases after 50 s due to the hydrodynamic force and moment acting on the hull and the control force and moment due to rudder and propeller reaching equilibrium. However, the surge velocity, sway velocity, and yaw rate oscillate in wind and irregular waves due to the hydrodynamic forces changed by the motion induced by wind and waves. This makes the ship's trajectory change dramatically after initial turning.

Fig. 11 shows the maneuvering motion including the surge velocity, sway velocity, and yaw rate with various wind directions and the significant wave heights. It can be seen that the approach surge

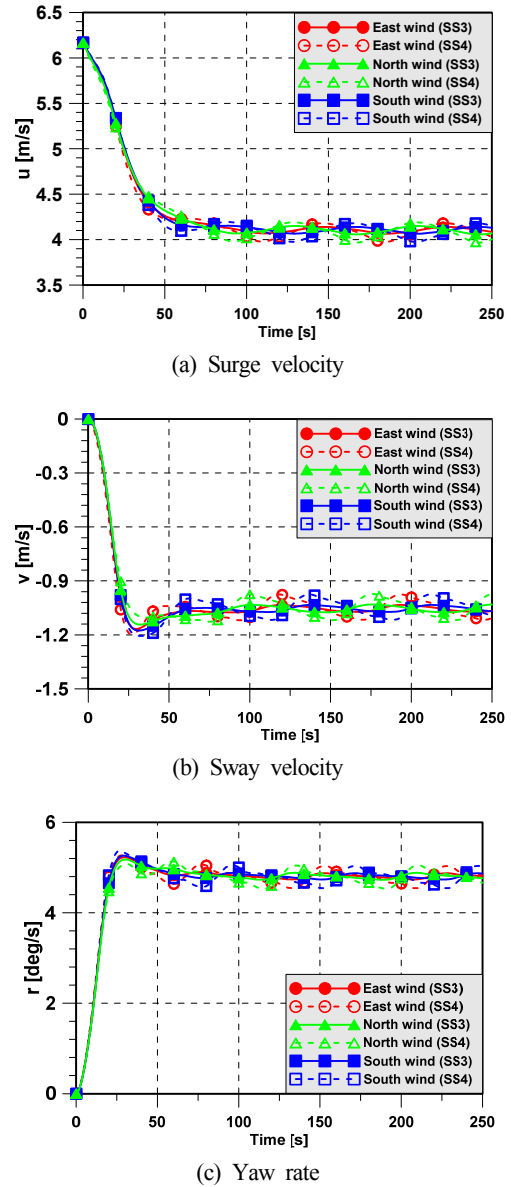


Fig. 11 Comparison of maneuvering motion in wind and waves

velocities with various wind directions are similar to the approach surge velocities in calm water, while the sway velocity and yaw rate oscillate in wind and irregular waves. Although the speed at the beginning of a turn differs greatly depending on the wind direction, the histories of speed variations in various wind directions become similar during steady turns, as shown in Fig. 11. For this reason, the drifting distance and drift angle are quite different during the initial circle, but these values become similar after the second and third circles. The results of the relative drifting angle reveal the difference between the propagation direction and the drifting angle, and the drifting direction is similar to the wind and wave propagation direction when the ship reaches the second and third circles.

## 5. Conclusions

In this paper, the movements of a trawler as it turned in circles in

calm water, wind, and irregular waves were simulated using a unified model of seakeeping and maneuvering. Our concluding remarks are as follows. First, the operation scenario of the trawler in the Sea of Okhotsk was analyzed. The hydrodynamic coefficients of the trawler were estimated using empirical formulas. The hydrodynamic forces due to wind and irregular waves were estimated, and the wave drift forces and moment in irregular waves are estimated by applying a short-term prediction technique.

Second, the standard maneuvering parameters in calm water satisfy the criteria of the IMO standards for a ship's maneuverability. The direction of the wind and waves slightly influences the advance of the trawler, while it significantly affects the tactical diameter because the ship's trajectory changes slightly at the initial stage. Finally, the North wind has a dominant effect on the tactical diameter and the turning trajectories of the trawler. The North wind causes the largest drifting distance. Moreover, the drifting distance and drifting angle become similar after the second and third circles, although these values are quite different at the beginning of the first turn.

### Funding

This research was supported by the programs, "Development of design and construction method of 36 m class trawlers for fishing in the Far East Waters for the support of Russia export." Which is funded by the Ministry of Trade, Industry and Energy (MOTIE, Korea), and "Development of Autonomous Ship Technology (2019-2020, Development of autonomous system having intelligent navigation decision making function)," which is funded by the Ministry of Oceans and Fisheries (MOF, Korea).

### References

- International Towing Tank Conference (ITTC). (2011). Final Report and Recommendation to the 26th ITTC. Proceedings of 26th International Towing Tank Conference, Rio de Janeiro, Brazil.
- Kim, D.J., Yun, K., Park, J.Y., Yeo, D.J., & Kim, Y.G. (2019). Experiment Investigation on Turning Characteristics of KVLCC2 Tanker in Regular Waves. *Ocean Engineering*, 175, 197-206. <https://doi.org/10.1016/j.oceaneng.2019.02.011>
- Kitamura, F., Ueno, M., Fujiwara, T., & Sogihara, N. (2017). Estimation of Above Water Structural Parameters and Wind load on Ships. *Ship and Offshore Structures*, 12(8), 1100-1108. <https://doi.org/10.1080/17445302.2017.1316556>
- Skejic, R., & Faltinsen, O.M. (2007). A Unified Seakeeping and Maneuvering Analysis of Two Interacting Ships. Proceedings of the 2nd International Conference on Marine Research and Transportation, 209-218.
- Skejic, R., & Faltinsen, O.M. (2008). A Unified Seakeeping and Maneuvering Analysis of Ships in Regular Waves. *Journal of Marine Science and Technology*, 13, 371-394. <https://doi.org/10.1007/s00773-008-0025-2>
- Seo, M.G., Kim, Y.H., & Kim, K.H. (2011). Effects on Nonlinear Ship Motion on Ship Maneuvering in Large Amplitude Waves. *Journal of the Society of Naval Architects of Korea*, 48(6), 516-527. <https://doi.org/10.3744/SNAK.2011.48.6.516>
- Skejic, R. (2013). Ships Maneuvering Simulations in a Seaway – How Close Are We to Reality? Proceedings of International Workshop on Next Generation Nautical Traffic Models 2013, 91-101.
- Wang, J.H., & Wan, D.C. (2018). CFD Investigations of Ship Maneuvering in Waves Using Naoe-FOAM-SJTU Solver. *Journal of Marine Science and Application*, 17, 443-458. <https://doi.org/10.1007/s11804-018-0042-4>
- Weather Spark. (2020). Average Weather in Okhotsk. Retrieved December 2020 from <https://weatherspark.com/y/144221/Average-Weather-in-Okhotsk-Russia-Year-Round>
- Yasukawa, H. (2008). Simulations of Ship Maneuvering in Waves (2nd Report: Zig-Zag and Stopping Maneuvers). *Journal of the Japan Society of Naval Architects and Ocean Engineers*, 7, 163-170. <https://doi.org/10.2534/jjasnaoe.7.163>
- Yasukawa, H. (2006). Simulations of Ship Maneuvering in Wave (1st Report: Turning Motion). *Journal of the Japan Society of Naval Architects and Ocean Engineers*, 4, 127-136. <https://doi.org/10.2534/jjasnaoe.4.127>
- Yasukawa, H., Zaky, M., Yonemasu, I., & Miyake, R. (2017). Effect of Engine Output on Maneuverability of a VLCC2 in Still Water and Adverse Weather Conditions. *Journal of Marine Science and Technology*, 22, 574-586. <https://doi.org/10.1007/s00773-017-0435-0>
- Yoshimura, Y., & Ma, N. (2003). Manoeuvring Prediction of Fishing Vessels. Proceeding of MARSIM'03 Conference, Kanazawa, Japan, 1-11.
- Zhang, W., Zou Z.J., & Deng D.H. (2017). A Study on Prediction of Ship Maneuvering in Regular Waves. *Ocean Engineering*, 137, 367-381. <https://doi.org/10.1016/j.oceaneng.2017.03.046>

### Author ORCIDs

Author name	ORCID
Nguyen, Van Minh	0000-0002-0404-7952
Nguyen, Thi Thanh Diep	0000-0003-3521-6680
Yoon, Hyeon Kyu	0000-0001-6639-0927
Kim, Young Hun	0000-0002-3072-6852

## Development of a Camera Self-calibration Method for 10-parameter Mapping Function

Sung-Min Park<sup>1</sup>, Chang-je Lee<sup>2</sup>, Dae-Kyeong Kong<sup>3</sup>,  
 Kwang-il Hwang<sup>4</sup>, Deog-Hee Doh<sup>4</sup> and Gyeong-Rae Cho<sup>2</sup>

<sup>1</sup>Graduate Student, Korea Maritime & Ocean University, Busan, Korea

<sup>2</sup>Researcher, Korea Maritime & Ocean University, Busan, Korea

<sup>3</sup>Researcher, Samsung Electronics Co. Ltd., Suwon, Korea

<sup>4</sup>Professor, Korea Maritime & Ocean University, Busan, Korea

**KEY WORDS:** Mapping function, Calibration, Self-calibration, Disparity map, TomoPIV, TomoPTV

**ABSTRACT:** Tomographic particle image velocimetry (PIV) is a widely used method that measures a three-dimensional (3D) flow field by reconstructing camera images into voxel images. In 3D measurements, the setting and calibration of the camera's mapping function significantly impact the obtained results. In this study, a camera self-calibration technique is applied to tomographic PIV to reduce the occurrence of errors arising from such functions. The measured 3D particles are superimposed on the image to create a disparity map. Camera self-calibration is performed by reflecting the error of the disparity map to the center value of the particles. Vortex ring synthetic images are generated and the developed algorithm is applied. The optimal result is obtained by applying self-calibration once when the center error is less than 1 pixel and by applying self-calibration 2–3 times when it was more than 1 pixel; the maximum recovery ratio is 96%. Further self-correlation did not improve the results. The algorithm is evaluated by performing an actual rotational flow experiment, and the optimal result was obtained when self-calibration was applied once, as shown in the virtual image result. Therefore, the developed algorithm is expected to be utilized for the performance improvement of 3D flow measurements.

### 1. Introduction

Particle image velocimetry (PIV) is a contactless and quantitative flow measurement method that is widely used for internal and external flow measurements in various fields, such as fluid machinery, ocean engineering, and environment-friendly energy generation. In particular, PIV is an effective visualization method for experimental approaches in complex marine areas such as the flow field measurement of submerged bodies in the ocean (Hong et al., 2019) and flow structure analysis of breaking waves (Jo et al., 2009). In this method, tracer particles are placed in the fluid flow and the behavior of the particles is examined using cameras by particle tracing, thereby finding a vector or vector field. This method has evolved from two-dimensional (2D) PIV and 2D particle tracking velocimetry (PTV) that involve finding a three-dimensional (3D) vector or vector field through the use of an observation equation in the images obtained from two or more cameras. Various methods have been studied and

developed, including stereoscopic PIV (SPIV), holographic PIV (HPIV), tomographic PIV (TomoPIV), and tomographic PTV (TomoPTV) (Arroyo and Greated, 1991; Doh et al., 2012a; Elsinga et al., 2006; Hinsch, 2002).

Among them, TomoPIV is a 3D flow-measurement method that reconstructs 2D pixel images that are obtained using several cameras as a 3D voxel image and utilizes the 3D cross-correlation in the reconstructed voxel image to measure the velocity field (Doh et al., 2012b; Elsinga et al., 2006). The novelty of TomoPIV is the reconstruction of a 3D image from multiple 2D images obtained from different perspectives. Among the many 3D reconstruction methods, algebraic reconstruction techniques (ART), multiple ART (MART), simultaneous ART (SART), and simultaneous multiplicative ART (SMART) are widely used (Andersen and Kak, 1984; Byrne, 1993; Herman and Lent, 1976). These methods have both advantages and disadvantages depending on the calculation time, accuracy, and flow field characteristics.

Received 12 January 2021, revised 20 April 2021, accepted 12 May 2021

Corresponding author Gyeong-Rae Cho: +82-51-410-4957, v\_pascal@daum.net

© 2021, The Korean Society of Ocean Engineers

This is an open access article distributed under the terms of the creative commons attribution non-commercial license (<http://creativecommons.org/licenses/by-nc/4.0>) which permits unrestricted non-commercial use, distribution, and reproduction in any medium, provided the original work is properly cited.

In 3D measurements using PIV, the observation equation setting of cameras and the camera calibration significantly impact the results. Thus, many studies have been conducted to improve the observation equations and calibration methods (Prasad, 2000; Soloff et al., 1997). However, there are camera calibration errors depending on the hardware and algorithm. To reduce the occurrence of such errors, a volume self-calibration (VSC) method has been developed (Wieneke, 2008). The VSC method first determines the 2D particle positions in the 2D camera images, followed by the positions of all particles that can exist in the 3D space. The difference between the positions of particles at the time when the particles in the 3D space were projected to each camera and the positions of the particles in the image is the calibration error of the camera. The error is minimized by a method that reflects the error in the position values of the particles and performs the calibration again. The VSC method has been continuously improved by many researchers (Wieneke, 2008; Lynch and Scarano, 2014).

Among them, Doh et al. (2012a) used an equation derived from pinhole model's observation by exploiting 10 intuitive parameters to develop TomoPIV and VolumePTV algorithms, and they compared the advantages and disadvantages of each algorithm. In this study, we perform self-calibration by using the VSC method through the observation equation with 10 parameters proposed by Doh et al. (2012a). We also develop a VSC algorithm that improves the performance of the TomoPIV and TomoPTV algorithms.

## 2. Camera Calibration

### 2.1 Principle of Calibration

The observation equation of cameras is an equation that shows the relationship between the camera coordinates and the spatial coordinate system; it is expressed as follows:

$$(x_i, y_i) = M_i(X, Y, Z) \quad (1)$$

In Eq. (1),  $M_i$  is an observation equation for the image coordinates  $(x_i, y_i)$  and the spatial coordinates  $(X, Y, Z)$  for the  $i$ -th camera. For every camera, the corresponding observation equation is used to convert the spatial coordinates to the image coordinates. Conversely, a point on the image is represented in a 3D space by using the inverse transform of Eq. (2):

$$(X, Y) = M_i^{-1}(x_i, y_i, Z) \quad (2)$$

In other words, a point on the image is represented by a line-of-sight (LOS) function, for which it is expressed in the form of a straight line according to the position of  $Z$  in the space. Therefore, a point on the image has a solution corresponding to a straight line in the space, and it is represented as a line in each camera. Finally, the position that minimizes the LOS error of the matching particles of each camera is

determined as a 3D position. Various methods of camera observation equations have shown the relation between the space and the camera image; however, in this study, we used an observation equation that had 10 elements [camera's external elements  $(d, \alpha, \beta, \kappa, m_x, m_y)$  and internal elements  $(c_x, c_y, k_1, k_2)$ ] used by Doh et al. (2012a), which were intuitively represented by using the camera distances and rotation angles. It is expressed as follows:

$$\begin{aligned} x &= c_x \frac{X_m - m_x}{d - Z_m} + \Delta x, \\ y &= c_y \frac{Y_m - m_y}{d - Z_m} + \Delta y, \quad \begin{bmatrix} X_m \\ Y_m \\ Z_m \end{bmatrix} = M_Z M_Y M_X \begin{bmatrix} X \\ Y \\ Z \end{bmatrix} \end{aligned} \quad (3)$$

$c_x$  and  $c_y$  denote the ratio between the image and space for the  $x$ - and  $y$ -axes, respectively, and  $d$  denotes the shortest distance between the center of the camera and the plane that passes through the zero-point of the space.  $X_m$ ,  $Y_m$ , and  $Z_m$  are the spatial coordinates rotated by  $\alpha$ ,  $\beta$ , and  $\kappa$  on the  $X$ -,  $Y$ -, and  $Z$ -axes, respectively, in the space.  $m_x$  and  $m_y$  denote the misalignment between the  $z$ -axis in the image space and the  $Z$ -axis in the 3D space, and  $\Delta x$  and  $\Delta y$  are the equations that represent the degree of refraction of the lens, which are expressed as follows:

$$\Delta x = (x/r) \times (k_1 r^2 + k_2 r^4) \quad (4)$$

$$\Delta y = (y/r) \times (k_1 r^2 + k_2 r^4), \quad r = \sqrt{x^2 + y^2} \quad (5)$$

### 2.2 Camera Self-calibration

The camera calibration uses a 3D position point  $P(X, Y, Z)$  in the space and a position point  $p(x, y)$  on the image to determine the element values of the observation equation that minimize the error of Eqs. (3)–(5). It uses special marks such as circles or cross marks on the calibration plate to provide the  $X$  and  $Y$  information; by providing the  $Z$  information while vertically moving at certain intervals on the calibration plate, the 3D position information  $P(X, Y, Z)$  is obtained. Here, the cameras are used to obtain the image of the calibration plate, and image processing is used to obtain the position of the marked points,  $p(x, y)$ . Using the position information that is obtained in this way, the element values of the observation equation are determined in such a way that the RMS (root-mean-square) error of the position points is minimized; based on this, the camera is calibrated. The obtained camera calibration values have many errors arising from the error of the mark points on the calibration plate, the error of  $Z$ -axis movement on the calibration plate, the error of image acquisition device, algorithm errors occurring during the process of finding the center and finding the optimal solution, and others. These errors have adverse effects on the reconstruction of voxel images. Moreover, the reliability of the 3D measurement result can be considerably improved by minimizing these errors.

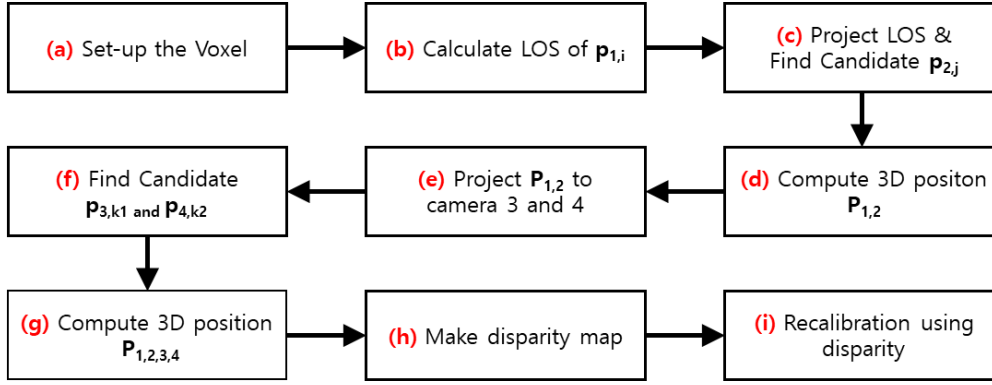


Fig. 1 Process for self-calibration

To this end, this study developed a self-calibration method that minimizes the errors of the cameras using the process shown in Fig. 1.

The centers of particles are obtained in every camera image. The process for self-calibration includes the following steps: (a) The region and shape of a virtual 3D voxel space are determined from the entire region to be measured. Here, for the size of the voxel image, the ratio of the pixel and the voxel is maximally set to 1 to reduce the errors in the calculation (Scarano, 2013). (b) The inverse transform of the observation equation for the  $i$ -th particle,  $p_{1,i}$  in the image of camera 1 is utilized to obtain the LOS. (c) The obtained LOS is projected to camera 2, and all particles,  $p_{2,j}$ , within a certain distance (1.5 voxels is used in this study) from the LOS are obtained. (d) Particles  $p_{1,i}$  and  $p_{2,j}$  that are selected in the two cameras are used to find the 3D position,  $P_{1,2}$ . In other words,  $P_{1,2}$  is the position in the 3D space where two straight lines meet, i.e., the LOS of  $p_{1,i}$  and the LOS of  $p_{2,j}$ . (e) When the LOS for a single particle is projected to the other camera, the projected LOS is a straight line across the image in the other camera. Therefore, multiple particles exist on the straight line, and from this, results are obtained, including not only the actual particles but also many virtual particles. To reduce the number of such virtual particles, the obtained 3D particle,  $P_{1,2}$ , is projected onto the images of the remaining cameras 3 and 4. (f) If a particle exists within a certain distance (1.5 voxels) from the position of the particle projected onto the camera ( $p_{3,k1}$  and  $p_{4,k2}$ ), then it is determined to be a real particle; otherwise, it is determined to be a virtual particle. (g) For only the particles that are determined to be real particles, the new 3D particle's position is calculated using the least square method from the selected 2D particle positions ( $p_{1,i}$ ,  $p_{2,j}$ ,  $p_{3,k1}$  and  $p_{4,k2}$ ) corresponding to each camera. (h) This process is used to find all possible 3D particles for every particle of camera 1, and the particles corresponding to the coincident regions that are set up based on the voxel position are classified and collected. (i) The 3D particles that are collected for each region are used to compose a disparity map.

The disparity map refers to an image that shows the difference between a particle position on the camera image and a particle position that is obtained by projecting onto the image of the camera the 3D particle that was calculated using that particle. To obtain the disparity map, all 3D particles of the corresponding region are first projected

onto each camera image in order to obtain the coordinates. The error between the projected coordinates and the particle's center on the image is obtained, and the particles of the Gaussian distribution with a sigma of 1 voxel are drawn at the position distanced by the error from the center and superimposed on the disparity map. In this study, the pixel size was magnified by a factor of 10 to improve the accuracy. For a high degree of accuracy, it is necessary to superimpose many particles deemed as real particles. Therefore, in this study, we calculated the 3D positions from thousands of test images until more than 10,000 particles are superimposed in each voxel region, and we superimposed them on the disparity map to draw the Gaussian particles, thereby composing the entire disparity map.

If the peak point is obtained in the disparity map for all regions, then the distance between the peak point and the center is the calibration error. As the last step, the obtained fixed error is reflected in the center value of the particle to perform the recalibration, and the parameters of the camera observation equation are then changed to perform the self-calibration.

### 2.3 Evaluation of Camera Self-calibration using Virtual Image

To evaluate the performance of the self-calibration method developed in this study, we set the measurement region to be  $-50$  mm to  $50$  mm,  $-50$  mm to  $50$  mm, and  $-15$  mm to  $15$  mm on the X, Y, and Z axes, respectively. The camera image size was set to  $512 \times 512$  pixels, and the cameras were placed in a row by setting the rotation angle of the X-axis to  $-20^\circ$ ,  $-5^\circ$ ,  $5^\circ$ , and  $20^\circ$ . The voxel size was  $500 \times 500 \times 150$  voxels, and 1 mm corresponds to 5 voxels. To produce a virtual image, we used a ring vortex flow field that is expressed by the following equation for the flow of particles:

$$d = \begin{bmatrix} u \\ v \\ w \end{bmatrix} = \frac{8r}{l} e^{-((r_1+r_2)/l)} \quad (6)$$

where  $d$  is the vector size,  $u$ ,  $v$ , and  $w$  are the vector components.  $l$  represents the thickness of the ring vortex,  $r_1$  and  $r_2$  denote the distance from the center of the ring vortex. Fig. 2 shows the virtual ring vortex flow field that is applied in this study, and its thickness and size are 16 mm and 40 mm, respectively.

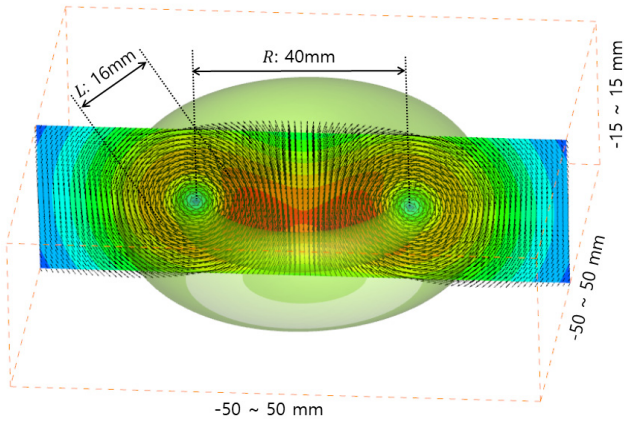


**Fig. 2** Ring vortex flow field

In this study, after performing the initial calibration using a virtual calibration plate, a particle with a diameter of 2.5 voxels was created in the voxel space, and then thousands of virtual particles [particle per pixel (PPP) = 0.01] were created. Based on the created voxel image, a virtual image was produced again using the following equation:

$$I_i = \sum_{j \in L_i} w_{ij} V_j \quad (7)$$

where superscript  $i$  denotes a pixel in the camera image,  $j$  denotes a voxel in the 3D space,  $I$  is the virtual image, and  $V$  is the voxel image.  $w_{ij}$  denotes the weight according to the distance between the camera pixel's LOS and voxel. In other words, the brightness of the virtual image is determined by the sum of values obtained by multiplying the weight by all voxels existing in a certain range of the LOS. In this study, the above method was used to produce voxel images and the virtual image for each camera.

As explained in Section 2.2, the voxel space was subdivided into  $5 \times 5$

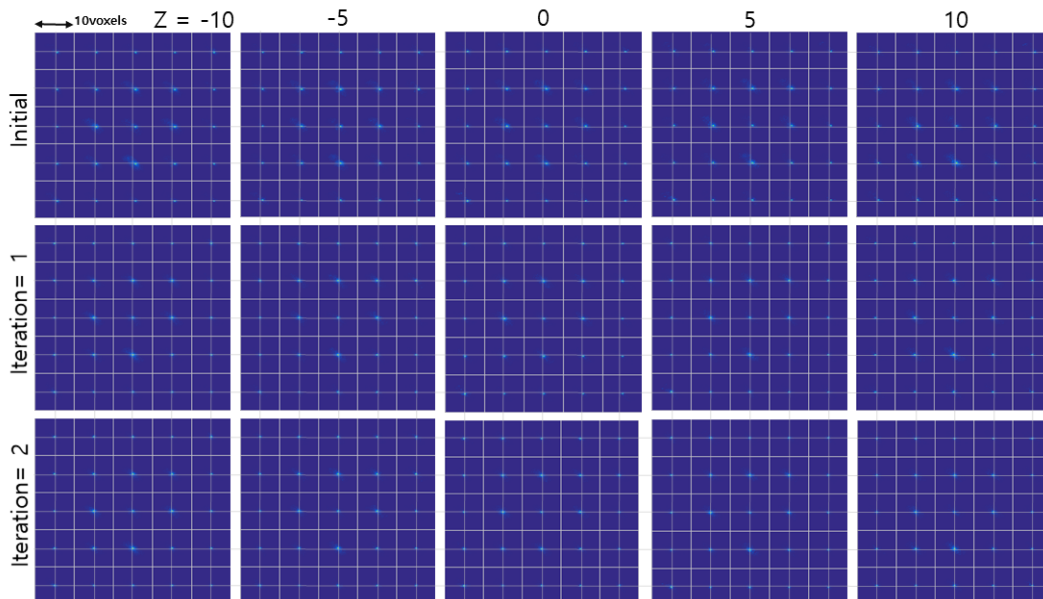
$5 \times 5$  regions for the self-calibration, and the process of Section 2.2 was performed repeatedly for each region, thereby producing a disparity map, as shown in Fig. 3.

Fig. 3 shows disparity maps of 125 points according to 25 points on the XY plane, and 5 points of z-axis for camera 1. First, in the disparity map that is based on the initial calibration values without self-calibration, the misaligned center has a large error, but the regions are widely distributed. As the self-calibration is performed, the shapes of particles in the disparity map converged at the center point and improved.

The error in the algorithm was evaluated by assigning a random error to the center of the particle in order to evaluate the degree of convergence of the self-calibration, and the results are shown in Fig. 4.

As shown in Fig. 4, the errors are high initially because of the given random errors, but as the first self-calibration is performed, most of the errors were improved. When the center error was 1 pixel or higher, the optimal result could be obtained by repeating the self-calibration two or three times, and even if the self-calibration was repeated, there was no further improvement above a certain level. This result shows that the developed self-calibration algorithm significantly improves the errors that can occur during the camera calibration process. Furthermore, it was found that it is not necessary to repeat the self-calibration more than two or three times depending on the error size.

Next, a multiplicative algebraic reconstruction technique (MART) algorithm was used to reconstruct the voxel image (Atkinson and Soria, 2009; Elsinga et al., 2006; Worth et al., 2010; Doh et al., 2012b). The MART algorithm is a reconstruction algorithm that is widely used in the field of tomography. This method combines the 3D image intensity along the LOS to obtain the projected 2D image and reconstructs a 3D image by making a comparison with the original image. This process is repeated to reconstruct the entire 3D voxel



**Fig. 3** Disparity map of camera 1 with iteration

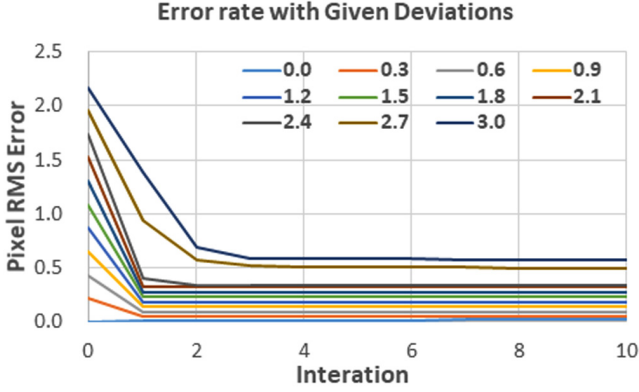


Fig. 4 Error rate with given random error of particle's center

image, and the algorithm is represented by the following equation:

$$V^{k+1} = V^k \left( \frac{I_i}{\sum_{j \in L_i} \omega_{ij} V_j^k} \right)^{\mu \omega_{ij} N} \quad (8)$$

where  $\mu$  is the coefficient of convergence, and  $\omega$  is the coefficient of weight according to the distance between the LOS for the  $i$  coordinate of the image selected as the weight and the voxel  $j$ . In other words, this algorithm reconstructs the voxel image in such a way that the ratio of the sum of all voxel images existing on the LOS to the brightness of the image at the pixel position on the image will converge to 1. The voxel image reconstructed by the MART method and the voxel image produced virtually were directly compared using the following equation to evaluate the accuracy of the proposed algorithm:

$$Q = \frac{\sum_{X,Y,Z} V_R(X,Y,Z) \cdot V_C(X,Y,Z)}{\sqrt{\sum_{X,Y,Z} V_R^2(X,Y,Z) \cdot \sum_{X,Y,Z} V_C^2(X,Y,Z)}} \quad (9)$$

In Eq. (9),  $Q$  denotes the recovery ratio, which indicates the reconstruction accuracy, and the superscripts  $R$  and  $C$  represent the reconstructed and created voxel images, respectively. Fig. 5 shows the

recovery ratio of the voxel image according to the PPP (number of particles per pixel). Here, the recovery ratio indicates the degree of recovery of the particles, which existed before the calculation, after performing the calculation based on the virtual image. The voxel images were created by setting PPP to 0.002–0.1. The performance of the constructed calculation algorithm was determined by evaluating the recovery ratio. Fig. 5 shows the reconstruction performance results that are expressed by Eq. (9) of the voxel image according to the result of the self-calibration for each PPP. When the recovery ratio is 1, it means that the reconstructed image and the created image match perfectly.

The “Make” indicator that is illustrated in each figure shows the result of reconstructing the voxel image by employing the variable values of the cameras used in the voxel image creation, and the “Init” indicator shows the result of reconstructing using the camera calibration values without the self-calibration. The “Iter. 1,” “Iter. 2,” “Iter. 3,” and “Iter. 5” indicators show the results of reconstructing the voxel image after performing the self-calibration process 1, 2, 3, and 5 times, respectively. Furthermore, the x-axis in the figure represents the number of iterations in the MART algorithm. The value 0 is the voxel value that is initialized using the MLOS (multiplied line-of-sight), and finally, the MART algorithm was repeated 10 times for the calculation.

As a result (Make) of performing the MART algorithm with the ground truth used in the virtual image creation, a recovery ratio close to 90% was obtained. However, it decreased as the PPP increased, showing the maximum recovery ratio of about 70% when the PPP was 0.1. The number of virtual particles increased significantly as the number of particles in the space increased, and the voxel ratio decreased significantly as the number of particles increased.

“Init.” indicates the recovery ratio when the calibration is performed using the calibration plate and the self-calibration is not performed. The best recovery ratio is shown when PPP is 0.004, but it decreases sharply as the number of particles increases. Based on the result of performing the self-calibration algorithm developed in this study, the recovery ratio was higher compared to the case when the

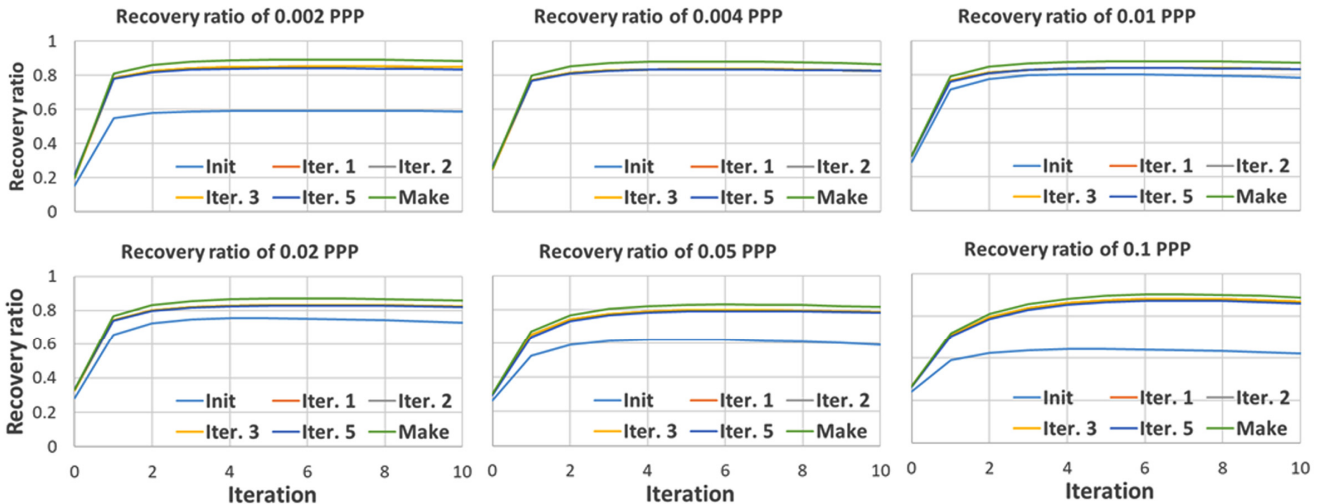


Fig. 5 Recovery ratio with MART iteration, according to change PPP from 0.002 to 0.1

self-calibration was not performed. A high improvement rate was observed in the first self-calibration, but even when the self-calibration was performed two, three, or five times, the result was similar to that of the first self-calibration. This implies that a good result can be obtained by performing self-calibration only once. Furthermore, when the MART algorithm was repeated five times with a PPP of 0.05, a recovery ratio of 74% was shown based on the recovery ratio of Make, but when the self-calibration was performed, a high recovery ratio of 96% was shown. Based on this result, it was determined that the developed self-calibration algorithm exhibits significant improvement.

### 3. Performance Evaluation Using Experimental Data

To evaluate the performance of the algorithm developed in this study, we created an experimental flow, as shown in Fig. 6. The size of the water tank was  $(440 \times 440 \times 220) \text{ mm}^3$ , and a pump having a flow rate of 540 L/h was installed to create a constantly rotating flow. Then, polyamide nylon particles with a diameter of 50 microns were inserted. An 8-W Laser System Europe Blits Pro Laser was used as the light source, and the laser light was projected with a thickness of about  $10 \times 10 \text{ mm}$ , as indicated by the green region in Fig. 6. Four high-speed cameras were installed by arranging them in a row in such a way that

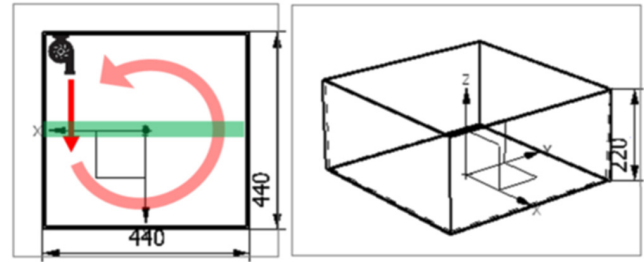


Fig. 6 Experimental circulation flow setup

the rotation angle will be approximately  $-15^\circ$ ,  $-5^\circ$ ,  $5^\circ$ , and  $15^\circ$  from the front side.

A flat calibration plate of a circular pattern was used to perform the calibration. Here, the total measurement area was  $(40 \times 10 \times 10) \text{ mm}^3$ . Fig. 7 shows an image of the first camera obtained in the experiment. To minimize the number of virtual particles, a small number of particles were entered to obtain a low-density particle image (1,000 particles, or about 0.001 PPP in an image of  $1,216 \times 1,200$  resolution); then, after performing the self-calibration, a high-density particle image (about 10,000 particles or 0.01 PPP) was obtained for the tomographic PIV measurement, and the velocity vector was measured.

Fig. 8 shows the disparity map obtained when performing the self-calibration. As shown in Fig. 8(a), when the self-calibration was

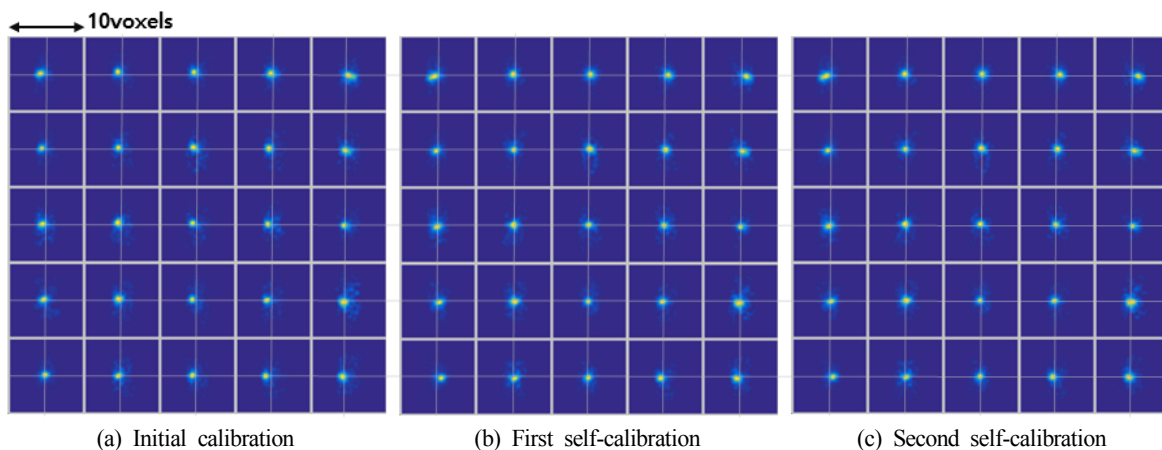


(a) for self-calibration



(b) for tomographic PIV

Fig. 7 Experimental images of camera 1. (a) for self-calibration, PPP  $\doteq$  0.001, (b) for tomographic PIV, ppp = 0.01



(a) Initial calibration

(b) First self-calibration

(c) Second self-calibration

Fig. 8 Disparity map of self-calibration

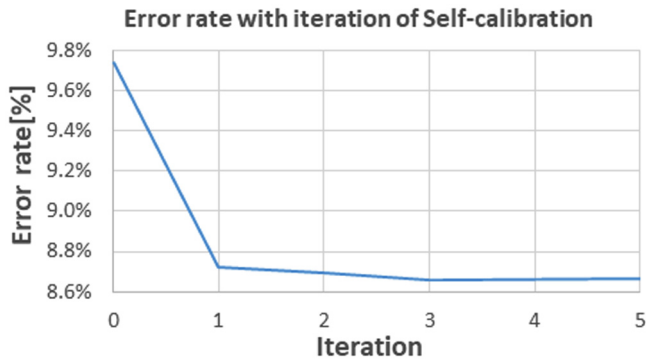


Fig. 9 Error rate with iteration of self-calibration

not performed, the center of the particle was misaligned sufficiently for it to be distinguished by the human eye. In the case of the center, most errors were less than 0.2 pixel, but in the case of the flank, some errors were larger than 0.5 pixel. When the self-calibration was performed, these errors decreased significantly, and after performing the first self-calibration, the pixel errors of all points had converged to less than 0.2 pixel. However, when the self-calibration was performed two or more times, the pixel errors did not change much. This implies that a sufficiently good improvement effect can be obtained by performing the self-calibration once or twice in the experiment.

To analyze the effect on the actual experimental results, we used a fast Fourier transform (FFT) cross-correlation in two recovered continuous voxel images to obtain the vector, and we evaluated the errors based on the method of using a median filter expressed by the following equation:

$$E_i = |v_i - v_m| / v_m > 1.0 \quad (10)$$

In the equation,  $v_m$  is the value located in the middle when a total of 27 vectors were arranged in  $3 \times 3 \times 3$  regions.  $v_i$  is the current vector. When the rate of change of the vector was larger than median  $v_m$ , it was determined to be an error. Fig. 9 shows the error rate of all vectors when the evaluation was performed with the median filter. When the camera's self-calibration was not performed, ~10% of all vectors were determined to be errors. After completing the self-calibration stage, the error rate decreased to 8.8%, and as the self-calibration was repeated, the result showed a slight improvement. However, after repeating it more than three times, there was no further improvement in the result. Instead, when the self-calibration was performed five times, the error rate increased by 0.002%, which was negligible. Based on these results, it is found that the optimal frequency of performing the self-calibration is three times in the case of the given experiment. Furthermore, the optimal frequency of self-calibration can be determined through the error rate analysis using the median filter.

#### 4. Conclusion

This study discusses the measurement performance improvement of the TomoPIV method, which is a 3D velocity field measurement

method of a flow field using an observation equation of a ten-parameter-based pinhole model of cameras. Furthermore, we developed a self-calibration algorithm that uses the initial calibration values of the cameras to calculate the 3D particle positions. After producing a disparity map in order to reconvert the 3D positions of these particles on a 2D image, it re-corrected the particle positions based on it to perform the re-calibration of the camera parameters.

The developed algorithm was used to evaluate virtual images using the vortex core flow. When the self-calibration was performed using the initial calibration values of the camera parameters, a relatively high recovery ratio was observed, and the result improved slightly when the calibration was performed repeatedly.

Furthermore, the actual 3D flow was measured using optical devices and cameras, and after performing an evaluation using a median filter-based method of removing the errors, it was found that the result obtained when the self-calibration was performed was much higher than that of the conventional calibration method. The optimum number of times that the self-calibration was performed could be determined through the error rate evaluation using the median filter.

Based on the above results, it was determined that the self-calibration method developed in this study can significantly improve the 3D PIV/PTV results using 10 parameters.

#### Funding

This research was supported by Basic Science Research Program through the National Research Foundation of Korea (NRF) funded by the Korea Government (No. 2018R1A2B6009387, 2021R111A1A01054535).

#### References

- Arroy, M.P., & Greated, C.A. (1991). Stereoscopic Particle Image Velocimetry. *Measurement Science and Technology*, 2(12), 1181–1186. <https://doi.org/10.1088/0957-0233/2/12/0122>
- Andersen, A.H., & Kak, A.C. (1984). Simultaneous Algebraic Reconstruction Technique (SART): A Superior Implementation of the ART Algorithm. *Ultrason Imaging*, 6, 81–94. [https://doi.org/10.1016/0161-7346\(84\)90008-7](https://doi.org/10.1016/0161-7346(84)90008-7)
- Atkinson, C., & Soria, J. (2009). An Efficient Simultaneous Reconstruction Technique for Tomographic Particle Image Velocimetry. *Experiments in Fluids*, 47, 553. <https://doi.org/10.1007/s00348-009-0728-0>
- Byrne, C.L. (1993). Iterative Image Reconstruction Algorithms Based on Cross-entropy Minimization. *IEEE Transactions on Image Processing*, 2(1), 96–103. <https://doi.org/10.1109/83.210869>
- Doh, D.H., Lee, C.J., Cho, G.R., & Moon, K.R. (2012a). Performances of Volume-PTV and Tomo-PIV. *Open Journal of Fluid Dynamics*, 2, 368–374. <https://doi.org/10.4236/OJFD.2012.24A047>
- Doh, D.H., Cho, G.R., & Kim, Y.H. (2012b). Development of a

- Tomographic PTV. *Journal of Mechanical Science and Technology*, 26, 3811–3819. <https://doi.org/10.1007/s12206-012-1007-1>
- Elsinga, G., Scarano, F., Wieneke, B., & van Oudheusden, B.W. (2006). Tomographic particle image velocimetry. *Experiments in Fluids*, 41, 933–947. <https://doi.org/10.1007/s00348-006-0212-z>
- Herman, G.T., & Lent, A. (1976). Iterative Reconstruction Algorithms. *Computers in Biology and Medicine*, 6(4), 273–294. [https://doi.org/10.1016/0010-4825\(76\)90066-4](https://doi.org/10.1016/0010-4825(76)90066-4)
- Hirsch, K.D. (2002). Holographic Particle Image Velocimetry. *Measurement Science and Technology*, 13(7), R61–R72. <https://doi.org/10.1088/0957-0233/13/7/201>
- Hong, J.W., Jeong, S.W., & Ahn B.K. (2019). PIV Measurements of Non-cavitating Flow in Wake of Two-dimensional Wedge-shaped Submerged Body. *Journal of Ocean Engineering and Technology*, 33(1), 26–32. <https://doi.org/10.26748/KSOE.2018.066>
- Jo, H.J., Lee, E.J., & Doh, D.H. (2009). A Study on Flow Structure of Breaking Wave through PIV Analysis. *Journal of Ocean Engineering and Technology*, 23(1), 43–47. <https://www.joet.org/journal/view.php?number=2089>
- Lynch, K.P., & Scarano, F. (2014). Experimental Determination of Tomographic PIV Accuracy by a 12-camera System. *Measurement Science and Technology*, 25(8), 1–10. <https://doi.org/10.1088/0957-0233/25/8/084003>
- Prasad, A. (2000). Stereoscopic Particle Image Velocimetry. *Experiments in Fluids*, 29, 103–116. <https://doi.org/10.1007/s003480000143>
- Scarano, F. (2013). Tomographic PIV: Principles and Practice. *Measurement Science and Technology*, 24(1), 012001. <https://doi.org/10.1088/0957-0233/24/1/012001>
- Soloff, S.M., Adrian, R.J., & Liu, Z.C. (1997). Distortion Compensation for Generalized Stereoscopic Particle Image Velocimetry. *Measurement Science and Technology*, 8(12), 1441–1454. <https://doi.org/10.1088/0957-0233/8/12/008>
- Wieneke, B. (2008). Volume Self-calibration for 3D Particle Image Velocimetry. *Experiments in Fluids*, 45, 549–556. <https://doi.org/10.1007/s00348-008-0521-5>
- Worth N.A., Nickels T.B., & Swaminathan N. (2010). A Tomographic PIV Resolution Study Based on Homogeneous Isotropic Turbulence DNS Data. *Experiments in Fluids*, 49, 637–656. <https://doi.org/10.1007/s00348-010-0840-1>

### Author ORCIDs

Author name	ORCID
Park, Sung-min	0000-0003-4281-0186
Lee, Chang-je	0000-0002-8106-1934
Kong, Dae-kyeong	0000-0001-6076-3972
Hwang, Kwang-il	0000-0003-4850-3558
Doh, Deog-hee	0000-0001-6093-2975
Cho, Gyeong-rae	0000-0003-1443-5286

# Comparison of Numerical Analyses and Model Test for Evaluation on Hydroelastic and Higher-order Springing Responses of Fixed Cylindrical Structure

Hyun-Sung Kim<sup>1,5</sup>, Younguk Won<sup>2</sup>, Young Jae Oh<sup>3</sup>, Kangsu Lee<sup>4,6</sup> and Byoung Wan Kim<sup>4,6</sup>

<sup>1</sup>Researcher, Offshore Platform Research Division, Korea Research Institute of Ships and Ocean Engineering, Daejeon, Korea

<sup>2</sup>Research Technician, Offshore Platform Research Division, Korea Research Institute of Ships and Ocean Engineering, Daejeon, Korea

<sup>3</sup>Junior Engineer, Offshore Platform Research Division, Korea Research Institute of Ships and Ocean Engineering, Daejeon, Korea

<sup>4</sup>Principal Researcher, Offshore Platform Research Division, Korea Research Institute of Ships and Ocean Engineering, Daejeon, Korea

<sup>5</sup>Graduate Student, Ship and Ocean Engineering, University of Science and Technology, Daejeon, Korea

<sup>6</sup>Professor, Ship and Ocean Engineering, University of Science and Technology, Daejeon, Korea

**KEY WORDS:** Hydroelastic response, Springing response, Fixed structure, Model test, HOBEM, Morison analysis method

**ABSTRACT:** Studies on very large offshore structures are increasing owing to the development of deep sea, large-scale energy generation using ocean resources, and so on. The enlargement of offshore structures makes the hydroelastic effect and low natural frequency related responses important. Numerical analyses and model tests for hydroelastic and higher-order springing responses of fixed cylindrical structures are conducted in this study. The panel methods with and without the hydroelastic effect with shell elements, and the Morison analysis method with beam elements are applied. To observe the hydroelastic effect for structural strength, two structures are considered: bottom-fixed cylindrical structures with high and low bending stiffnesses, respectively. The surge motions at the top of the structure and bending stresses on the structure are observed under regular and irregular wave conditions. The regular wave conditions are generated considering the ratios of the cylindrical outer diameter to the wave lengths, and keeping the wave steepness constant. The model tests are performed in the three-dimensional ocean engineering basin in the KRISO (Korea Research Institute of Ships and Ocean Engineering). From the numerical and experimental results, in which the hydroelastic responses are only observed in the case of the structure with a low bending stiffness, it is confirmed that the hydroelastic responses are highly dependent on the structural stiffness. Additionally, the higher-order phenomenon on the specified wave condition is analyzed by observing the higher-order springing responses when the incident wave frequency or its multiples with the high wave height coincides with the natural frequency of the structure.

## 1. Introduction

Because offshore oil production operations are entering distant waters with increase of water depths, oil production and storage structures are being enlarged to ensure those structural stabilities. Furthermore, as researches and developments on eco-friendly energies, such as offshore wind power generation, wave power generation, floating photovoltaic power generation and so on, are being actively undertaken, the related studies on large structures for large-scale power generation are also increasing. Additionally, the researches and developments for very large structures, including floating LNG (liquefied natural gas) bunkering, floating airports, and

so on, are in constant progress. The enlargement of offshore structures increases the relative deformations of the structures, and thus, the hydroelastic effect, which is the interaction between the waves and structural deformation, becomes important. To rigorously estimate the wave-induced and structural responses of large offshore structures, fluid-structure interaction analysis is required, and the hydroelastic effect must be considered. Various numerical analysis methods have been developed and studied based on the aeroelasticity concept in aeronautical engineering to address the need for analysis that considers the hydroelastic effect of offshore structures (Heller and Abramson, 1959). Studies on hydroelastic analysis were conducted by Bett et al. (1977) and Bishop & Price (1977) based on the strip theory, which is

Received 6 January 2021, revised 10 May 2021, accepted 28 May 2021

Corresponding author Byoung Wan Kim: +82-42-866-3932, [kimbw@kriso.re.kr](mailto:kimbw@kriso.re.kr)

It is noted that this paper is revised edition based on proceedings of KAOST 2020 in Busan.

© 2021, The Korean Society of Ocean Engineers

This is an open access article distributed under the terms of the creative commons attribution non-commercial license (<http://creativecommons.org/licenses/by-nc/4.0>) which permits unrestricted non-commercial use, distribution, and reproduction in any medium, provided the original work is properly cited.

the early fluid analysis method for ships, and beam theory. The second-order nonlinear strip theory was applied to the existing method to solve nonlinear problems with large ranges of motion and deformation (Jensen and Pedersen, 1981). Attempts were also made to solve three-dimensional hydroelastic analysis problems by applying the potential theory and the finite element method (Wu, 1984; Price and Wu, 1985; Bishop et al., 1986). Lakshminarayana et al. (2015) conducted the study on a fluid-structure interaction using the computational fluid dynamics (CFD) method. Additionally, several methods were developed to predict the hydroelastic response of large offshore structures; these hydroelastic analysis methods were applied in studies on hydroelastic problems of various offshore structures, ranging from ships to semi-submersible structures (Andrianov, 2005; Kim et al., 2014). Major studies on very large floating offshore structures include the Mega-Float project (Japan Technical Research Association) and the Mobile Offshore Base (MOB) project (US Navy) (Rognass et al., 2001; Shuku et al., 2001).

Also, as offshore structures become larger, the natural frequency of the structures decreases and becomes close to the wave frequency or its multiples. If the height of the incident wave is large and the multiples of the frequency approach the natural frequency of the structure, the higher-order component of the wave force generates resonance responses, resulting in the springing phenomenon with the occurrence of regular natural frequency responses. Numerical and experimental studies have been conducted on this phenomenon mainly for very large ships (Hong and Kim, 2014; Shin et al., 2015).

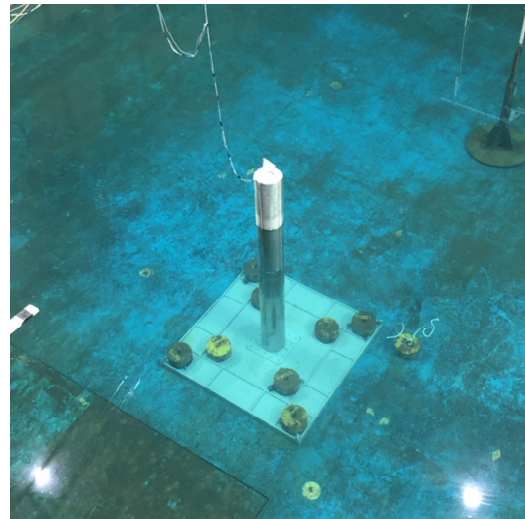
Most studies on the hydroelastic responses and higher-order springing phenomenon of offshore structures have focused on floating structures, including ships. In this study, numerical analyses and model tests were performed to consider the hydroelastic and higher-order springing responses of fixed cylindrical structures, and the result of each numerical analysis method was analyzed and compared to the result of the model tests. As numerical analysis methods to study the hydroelastic responses of fixed cylindrical structures, the panel method that considers only wave diffraction but not the hydroelastic effect, the panel method that considers the radiation effect for the bending modes of the structure and applies the hydroelastic effect, and the Morison analysis method with beam elements are applied (Kim et al., 2018). In the panel method, the higher-order boundary element method (HOBEM; Choi et al., 2000; Hong et al., 2005) and the shell elements of the finite element method (FEM) (Bathe, 1996; Kim et al., 2018) are applied. The surge motions at the top of the structure and stress responses acting on the main body are studied, and the response amplifier operator (RAO) characteristics under regular wave conditions and the responses under irregular wave conditions are evaluated. To compare the responses based on the structural strength of the structure, two cases are evaluated: the case where the hydroelastic effect was insignificant owing to high structural strength and the other case where the hydroelastic effect was large owing to low structural strength. The case where the springing phenomenon occurs under certain model test conditions with the case

of low structural strength is also considered. From the results of the numerical and experimental studies, it is confirmed that the structural strength has a significant effect on the hydroelastic responses of the structure, and that the higher-order springing responses occur when the wave height is large and the wave frequency or its multiples approaches the natural frequency.

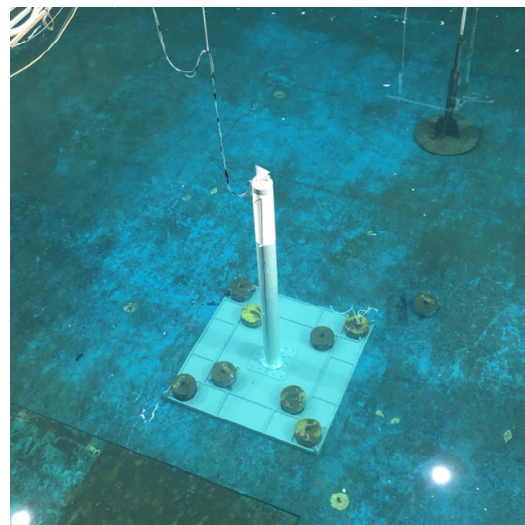
## 2. Model Tests

### 2.1 Structures for Model Tests

To compare the hydroelastic responses depending on the structural strength of the fixed cylindrical structures in the numerical analyses and model test, two cases are considered: the stiff-type structure with a small hydroelastic effect and the flexible-type structure with a large hydroelastic effect. The structures are 74 m in height and 6 m (stiff-type) or 4.32 m (flexible-type) in outer diameter on a real scale.



(a) Stiff type structure (Aluminum)



(b) Flexible type structure (PVC)

**Fig. 1** Test models installed at ocean engineering basin in KRISO (Kim et al., 2020)



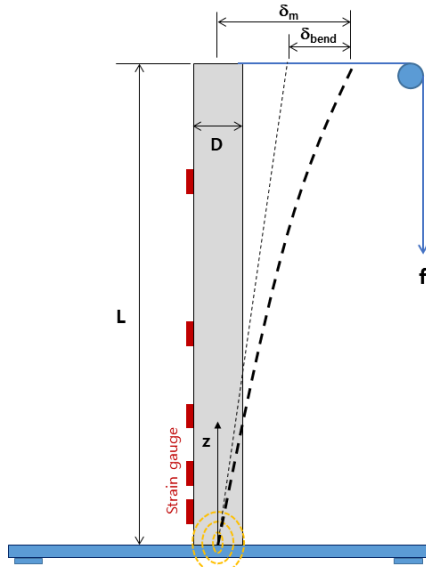
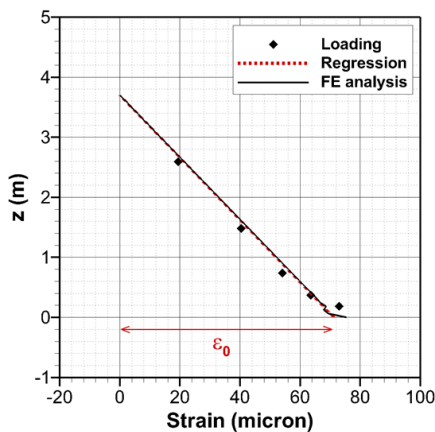
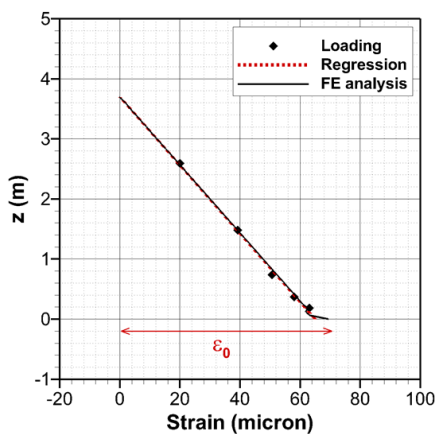


Fig. 3 Loading test to find  $E$  and  $K_\theta$



(a) Stiff type structure (Aluminum)



(b) Flexible type structure (PVC)

Fig. 4 Results of loading test to find  $E$  and  $K_\theta$

The results in Fig. 4 indicate that the regression lines and results of finite element analysis using shell elements are almost identical. The displacement at the top of the structure, denoted as  $\delta_m$ , can be

Table 2 Loading test results

Item	Notation	Structure type	
		Stiff type (Aluminum)	Flexible type (PVC)
Load	$f$	294.21 N	14.7105 N
Length	$L$	3.7 m	3.7 m
Diameter	$D$	0.3 m	0.216 m
Strain	$\epsilon_0$	$71.203 \times 10^{-6}$	$64.954 \times 10^{-6}$
Young's modulus	$E$	74.29 GPa	3.852 GPa
Bending stiffness in real scale	$EI_{real}$	$7.338 \times 10^{12}$ N·m <sup>2</sup>	$2.896 \times 10^{11}$ N·m <sup>2</sup>
Measured displacement	$\delta_m$	0.005 m	0.002892 m
Displacement by bending	$\delta_{bend}$	0.00217 m	0.00274 m
Rotational spring constant	$K_\theta$	$1.421 \times 10^6$ N·m/rad	$1.366 \times 10^6$ N·m/rad
Rotational spring constant in real scale	$K_{\theta,real}$	$2.274 \times 10^{11}$ N·m/rad	$2.186 \times 10^{11}$ N·m/rad

measured during the loading test, and this displacement can be expressed as the sum of the displacement by bending deformation ( $\delta_{bend}$ ) and the displacement by the rotational spring effect at the bottom connection part (Fig. 3). By applying this relation and the beam theory, the rotational spring constant,  $K_\theta$ , at the bottom connection part can be derived.

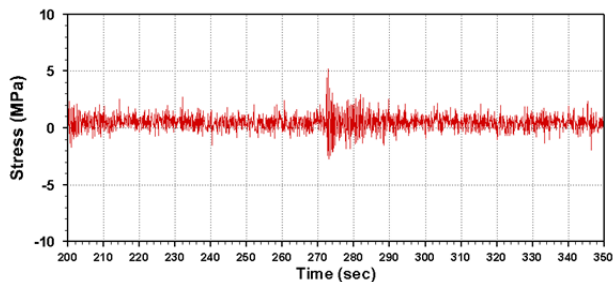
$$\delta_{bend} = \frac{fL^3}{3EI} \quad (2)$$

$$K_\theta = \frac{fL^2}{\delta_m - \delta_{bend}} \quad (3)$$

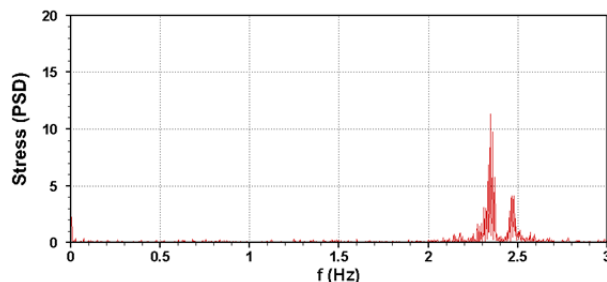
Table 2 shows the results obtained from the above process. The real-scale values for numerical analyses are determined by applying the similarity law to the model test results.

### 2.3 Hammering Test

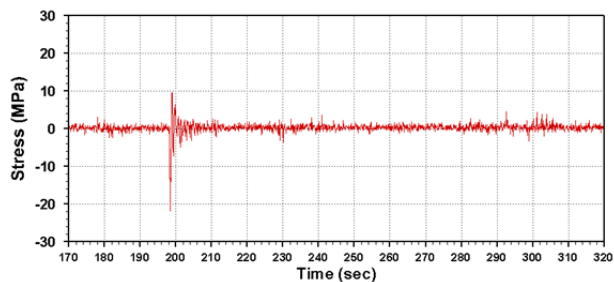
The natural frequency of a structure is one of the most important factors in evaluating hydroelastic responses. In this study, it is numerically evaluated through finite element analysis using shell elements. And the actual natural frequencies of the test models are measured by performing hammering tests. These are performed by applying an impact to the top of the structures under dry and wet conditions. Figs. 5–6 show the time series and power spectral density (PSD) results on hammering tests, and the overall results are summarized in Table 3. The natural period of the stiff-type structure is 0.838 s in a wet condition, which is slightly different from that in the dry condition. The hydroelastic effect is predicted to be small in both conditions because the results are outside the range of wave period. The natural period of the flexible-type structure is 2.571 s in the wet



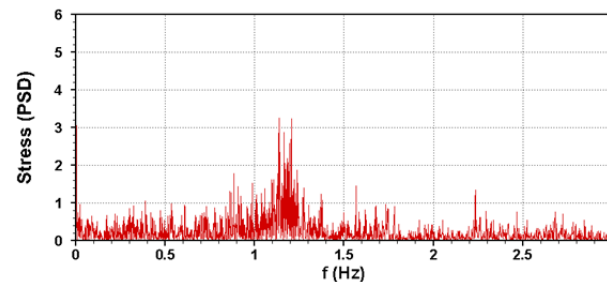
(a) Time series of hammering test in dry condition



(b) PSD of hammering test in dry condition

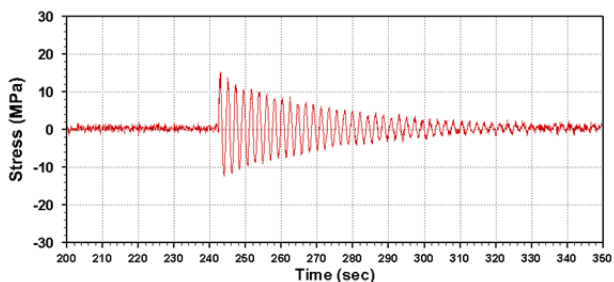


(c) Time series of hammering test in wet condition

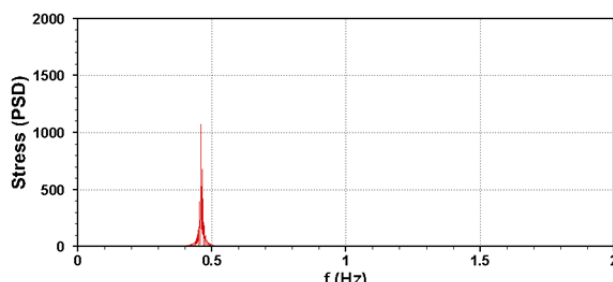


(d) PSD of hammering test in wet condition

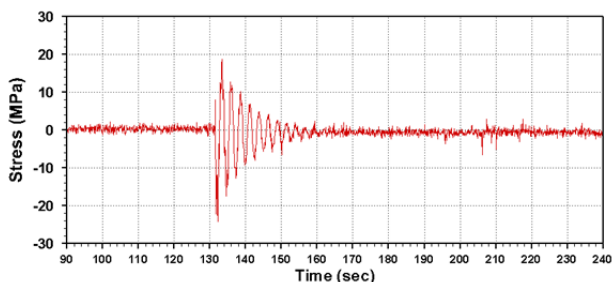
**Fig. 5** Hammering test results of stiff type structure



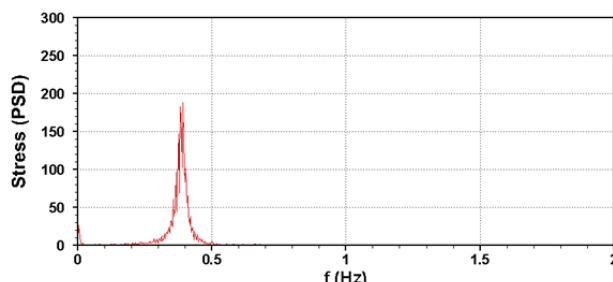
(a) Time series of hammering test in dry condition



(b) PSD of hammering test in dry condition



(c) Time series of hammering test in wet condition



(d) PSD of hammering test in wet condition

**Fig. 6** Hammering test results of flexible structure

**Table 3** Hammering test results

Item	Natural frequency		Natural period	
	Stiff type	Flexible type	Stiff type	Flexible type
Shell eigenvalue analysis (dry)	2.567 Hz	0.489 Hz	0.390 s	2.044 s
Hammering test (dry)	2.329 Hz	0.456 Hz	0.429 s	2.194 s
Hammering test (wet)	1.193 Hz	0.387 Hz	0.838 s	2.571 s

condition, which is within the range of the wave period under the test condition, and the hydroelastic effect would be confirmed.

**2.4 Environmental Conditions**

The model tests are conducted by applying a wave load as the only

**Table 4** Regular wave conditions

Case	Wave period ( $T$ ) (s)		Wave height ( $H$ ) (m)	
	Real	Model	Real	Model
01	2.235	0.500	0.390	0.020
02	2.401	0.537	0.450	0.023
03	2.773	0.620	0.600	0.030
04	3.396	0.759	0.900	0.045
05	4.384	0.980	1.500	0.075
06	6.200	1.386	3.000	0.150
07	7.595	1.698	4.500	0.225
08	8.779	1.963	6.000	0.300
09	11.656	2.606	10.200	0.510

acting environmental load, and varying the ratio of the wavelength ( $\lambda$ ) to the outer diameter ( $D$ ) of the structure from 1.3 to 34 in the regular wave condition. The wave height ( $H$ ) is set such that its ratio to the wavelength ( $H/\lambda$ ) is 1/20 (Table 4). For the irregular wave condition, the JONSWAP spectrum is used, and the significant wave height ( $H_s$ ) of 5 m and the modal period ( $T_p$ ) of 12.4 s are considered. Fig 7 shows the calibration and theoretical results for the irregular wave condition for the model test.

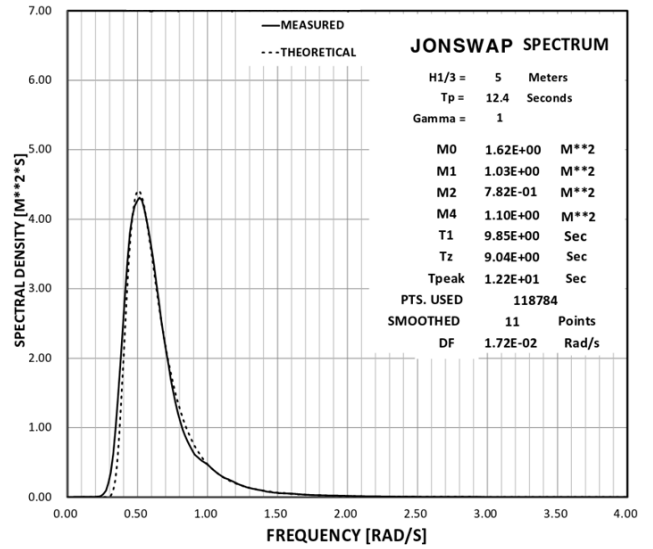


**Fig. 7** Spectrum and calibration results on irregular wave condition

### 3. Numerical Analysis

#### 3.1 Numerical Analysis Model

For the numerical analysis to study the hydroelastic effect of the fixed cylindrical structures, the panel method using the higher-order

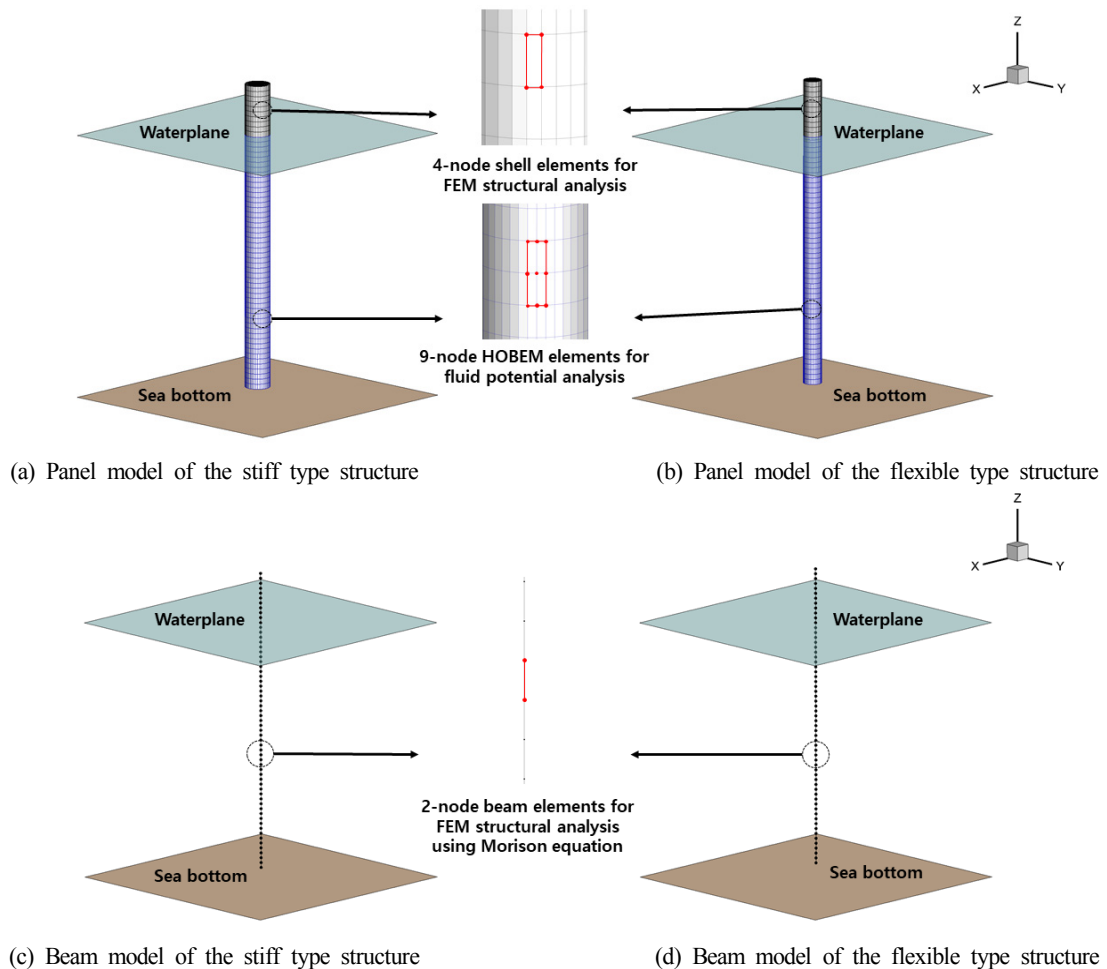


**Fig. 8** Numerical models for potential flow and structural analyses

boundary element method (HOBEM) and shell elements, and the Morison analysis method using the beam elements are applied. The panel analyses are performed separately for when only diffraction is considered without a hydroelastic effect and when the radiation effect for the bending modes is considered, and the results are compared. Fig. 8 shows the numerical models consisting of the panel and beam elements.

### 3.2 Numerical Analysis Methods

The higher-order boundary element method (HOBEM) is applied as a fluid analysis method to calculate the hydrodynamic load acting on the fixed cylindrical structures. The higher-order boundary element method is a type of numerical analysis method for calculating the flow field of waves around a structure, which only divides the boundary of the floating structure using the Green function rather than dividing the fluid domain.

This method improves convergence and accuracy by applying 9-node higher-order elements instead of 4-node elements of the existing boundary element method (Choi et al., 2000; Hong et al., 2005). The velocity potential satisfying the governing equation and the boundary conditions is calculated, based on which the hydrodynamic coefficients of the motion equation in the frequency domain can be determined.

$$\nabla^2 \phi = 0 \quad (4)$$

$$\frac{\partial \phi}{\partial z} = \frac{\omega^2}{g} \phi \quad \text{at } z = 0 \quad (5)$$

$$\frac{\partial \phi}{\partial z} = 0 \quad \text{on } z = -h \quad (6)$$

$$\lim_{r \rightarrow \infty} \sqrt{r} \left( \frac{\partial \phi}{\partial r} - ik\phi \right) = 0 \quad (7)$$

$$\frac{\partial \phi}{\partial n} = -i\omega n \cdot \vec{u} \quad (8)$$

Eq. (4) is the governing equation in a fluid domain, and Eqs. (5)–(8) represent the free surface boundary condition, sea bed boundary condition, radiation condition, and body surface boundary condition, respectively. In the above equations,  $\phi$  is the wave-induced velocity potential that consists of three components: incident, scattered, and radiation potentials. For the panel method that does not consider the hydroelastic effect, only the incident potential and scattered potential are considered. In case that the hydroelastic effect is considered, the analysis is performed not only by considering the incident and scattered potentials but also the radiation potential for the bending modes of the structures.  $\omega$  is the wave frequency,  $h$  is the water depth, and  $r$  is the radiation boundary.  $\vec{n}$  and  $\vec{u}$  denote the normal and displacement vectors of the structures, respectively. Based on the Bernoulli equation, and the velocity potential that satisfies the governing equation and boundary conditions, the hydrodynamic

pressure in a frequency domain can be obtained as follows.

$$p(\omega) = i\omega\rho\phi \quad (9)$$

The pressure RAO (Response Amplitude Operator) of the frequency domain in Eq. (9) can be transformed into the time domain through the inverse Fourier transform and random time series methods, as follows.

$$p(t) = \begin{cases} \frac{H}{2} \text{Re}[p(\omega)e^{-i\omega t}] & \text{in regular wave} \\ \sum_{j=1}^{n_w} \sqrt{2S(\omega_j)\Delta\omega} \text{Re}[p(\omega_j)e^{-i(\omega_j t + \psi_j)}] & \text{in irregular wave} \end{cases} \quad (10)$$

$S(\omega)$  in Eq. (10) represents the irregular wave spectrum, and the JONSWAP spectrum is applied in the numerical analyses of this study.  $n_w$  denotes the number of spectrum partitions and  $\psi_j$  is the random phase angle. By applying the time-domain pressure load obtained through Eq. (10) to the motion equation for the structural analysis, the displacements and stresses in the time domain can be determined for structures to which wave load is applied (Eq. (11)).

$$[M]\{\ddot{u}\} + [C]\{\dot{u}\} + [K + K_B]\{u\} = \{f\} \quad (11)$$

In the above Eq. (11),  $[M]$ ,  $[C]$ , and  $[K]$  represent the mass, damping, and stiffness matrices, respectively.  $\{u\}$  is the displacement vector, and  $\{f\}$  is the external force vector including the pressure load caused by the wave.  $[K_B]$  denotes the buoyancy spring matrix of the structure.

In the Morison analysis method using beam elements, the load acting on the structure is assumed to be the sum of the drag and inertial force, and the velocity of the water particles could be determined using the velocity potential. The Morison equation can be expressed as shown in Eq. (12).

$$\begin{aligned} \vec{f}_M = & \frac{1}{2} C_D \rho \left| \vec{v}_r \right| \vec{v}_r D \Delta s + C_M \rho a_{pn} \vec{A}_M \Delta s \\ & - C_A \rho a_{sn} \vec{A}_M \Delta s + \frac{1}{2} C_F \rho \left| \vec{v}_F \right| \vec{v}_F S_F \Delta s \end{aligned} \quad (12)$$

In Eq. (12),  $D$ ,  $A_M$ , and  $S_F$  are the width, projected area, and perimeter length for the beam elements, respectively,  $\Delta s$  is the length of the beam elements, and  $\rho$  is the fluid density.  $C_D$ ,  $C_M$ ,  $C_A$ , and  $C_F$  denote the drag, mass, added mass, and friction coefficients, respectively, and corresponding values of 1.2, 2.0, 1.0, and 0.05 are applied in this study.  $\vec{v}_r$  and  $\vec{v}_F$  denote the relative velocity in the normal and tangential directions between the water particles and beam elements.  $\vec{a}_{pn}$  and  $\vec{a}_{sn}$  denote the relative acceleration in the normal direction and the tangential direction, respectively.

$$\vec{v}_r = (\vec{v}_p - \vec{v}_s) - ((\vec{v}_p - \vec{v}_s) \cdot \vec{t}) \vec{t} \quad (13)$$

$$\vec{v}_r = ((\vec{v}_p - \vec{v}_s) \cdot \vec{t}) \vec{t} \quad (14)$$

$$\vec{a}_{pm} = \vec{a}_p - (\vec{a}_p \cdot \vec{t})\vec{t} \quad (15)$$

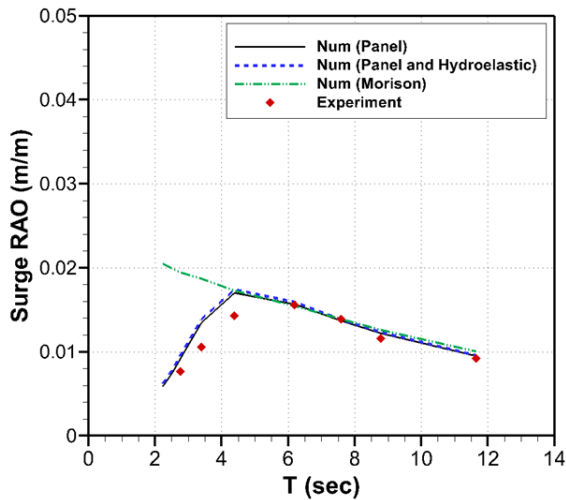
$$\vec{a}_{sn} = \vec{a}_s - (\vec{a}_s \cdot \vec{t})\vec{t} \quad (16)$$

In Eqs. (13)–(16),  $\vec{v}_p$  and  $\vec{a}_p$  are the velocity and acceleration of the water particles, respectively.  $\vec{v}_s$  and  $\vec{a}_s$  are the velocity and acceleration of beam elements, and  $\vec{t}$  is the unit tangential vector of the beam elements. By substituting the Morison load obtained through the equations into the motion equation (Eq. (11)), the structural analysis can be performed to determine the displacements and stresses of the structure composed of beam elements.

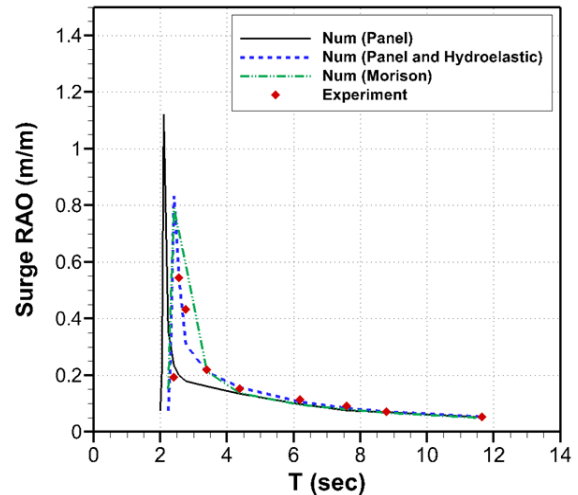
### 3.3 Comparison of Numerical Analysis and Test Results

Figs. 9–10 show the results under regular wave conditions. Fig. 9 shows the surge motion results at the top of the structures, and Fig. 10 shows the stress results at the bottom part of the structures. The results

on the surge motions at the top and the stresses at the bottom of the stiff type structure confirm that there is no significant difference between considering and not considering the hydroelastic effect, and that the numerical analysis and test results are similar. Based on this, the hydroelastic effect is found to be small when the structural strength is large. However, for the flexible-type structure, the hydroelastic responses occur by the low stiffness of the structure in the model test. Thus, the result of the numerical analysis, which does not consider the hydroelastic effect of the structure, varies from the results of model test for the flexible type structure. This implies that the hydroelastic effect needs to be considered if a structure is flexible. Comparing the Morison analysis and test results, the analysis and test results are similar when the wavelength is long relative to the outer diameter of the structure, but they are different when the wavelength is short relative to the outer diameter of the structure. If the wavelength is relatively short compared to the outer diameter of the structure, the diffraction effect should be considered through the boundary element

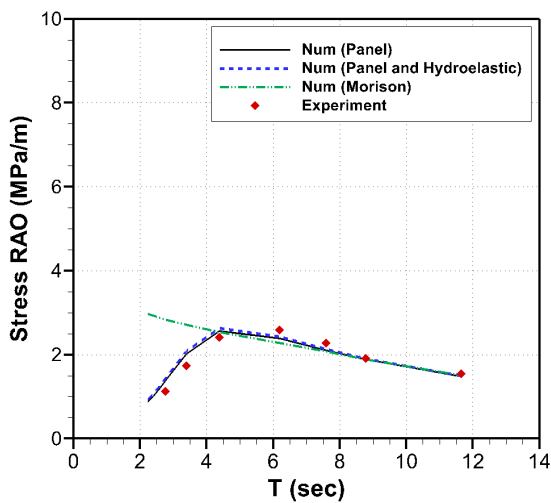


(a) Stiff type structure

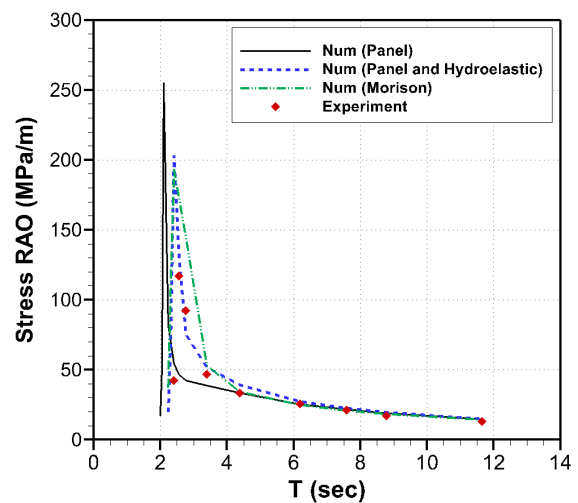


(b) Flexible type structure

Fig. 9 Comparison results on surge RAO



(a) Stiff type structure



(b) Flexible type structure

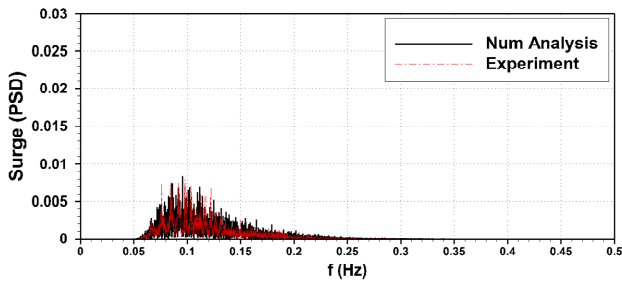
Fig. 10 Comparison results on stress RAO

method, and so on.

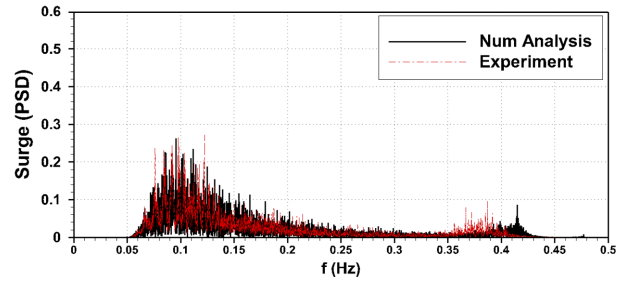
Figs. 11–12 show the power spectral density (PSD) results on the surge motions at the top and the stresses at the bottom part of the structures under irregular wave conditions. The results of numerical analyses correspond to the ones of the panel analysis, which consider the hydroelastic effect, and are similar to the model test results in all cases. For the flexible type structure, it is confirmed that the wave frequency responses occur near 0.1 Hz, and the natural frequency responses of the structure occur near 0.4 Hz. For the stiff type structure, the natural frequency is rarely measured, and only responses

near the wave frequency are observed.

Under regular wave conditions, if the wave height is high, and the multiples of the wave frequency coincide with the natural frequency of the structure, the higher-order components of the wave force may cause a resonance, resulting in the springing phenomenon where the natural frequency responses of the structure occur regularly. This phenomenon is observed under the conditions of the model tests in which the actual phenomenon is embodied. Among the test conditions, the phenomenon is found to occur at the case having a wave height of 4.5 m and a period of 7.595 s (0.13 Hz) as shown in Fig. 13. Under this

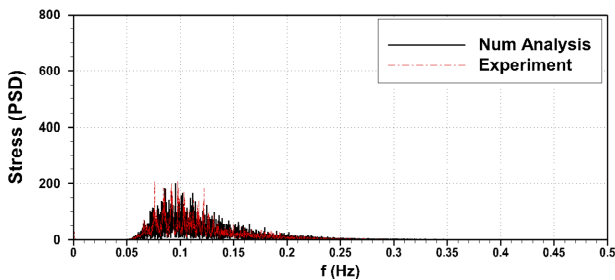


(a) Stiff type structure

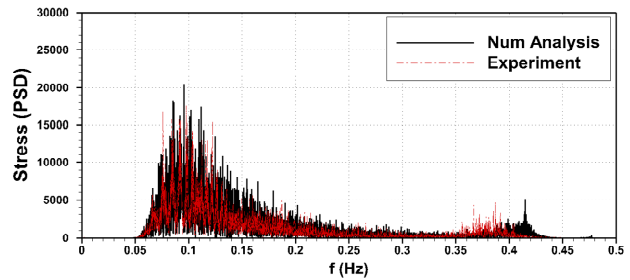


(b) Flexible type structure

Fig. 11 Surge PSD results in irregular wave condition

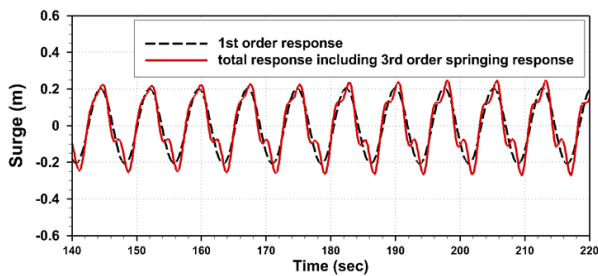


(a) Stiff type structure

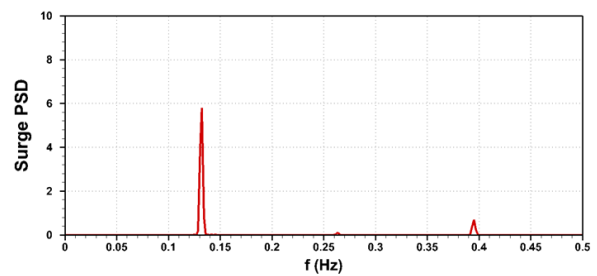


(b) Flexible type structure

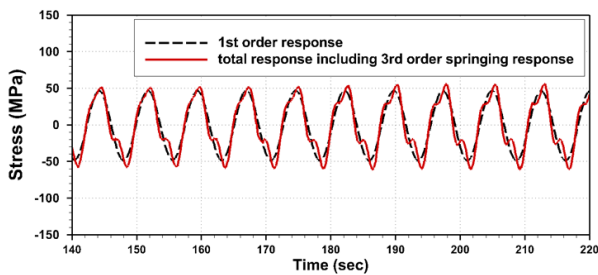
Fig. 12 Stress PSD results in irregular wave condition



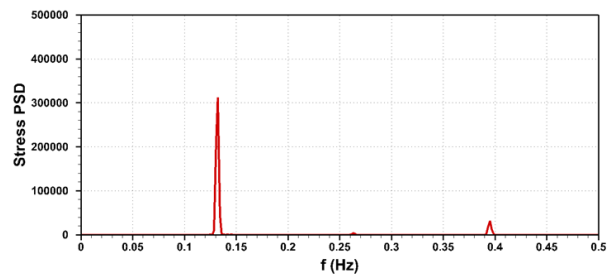
(a) Surge time series



(b) Surge PSD



(c) Stress time series



(d) Stress PSD

Fig. 13 Regular wave test results for considering springing phenomenon at  $H = 4.5$  m and  $T = 7.595$  s

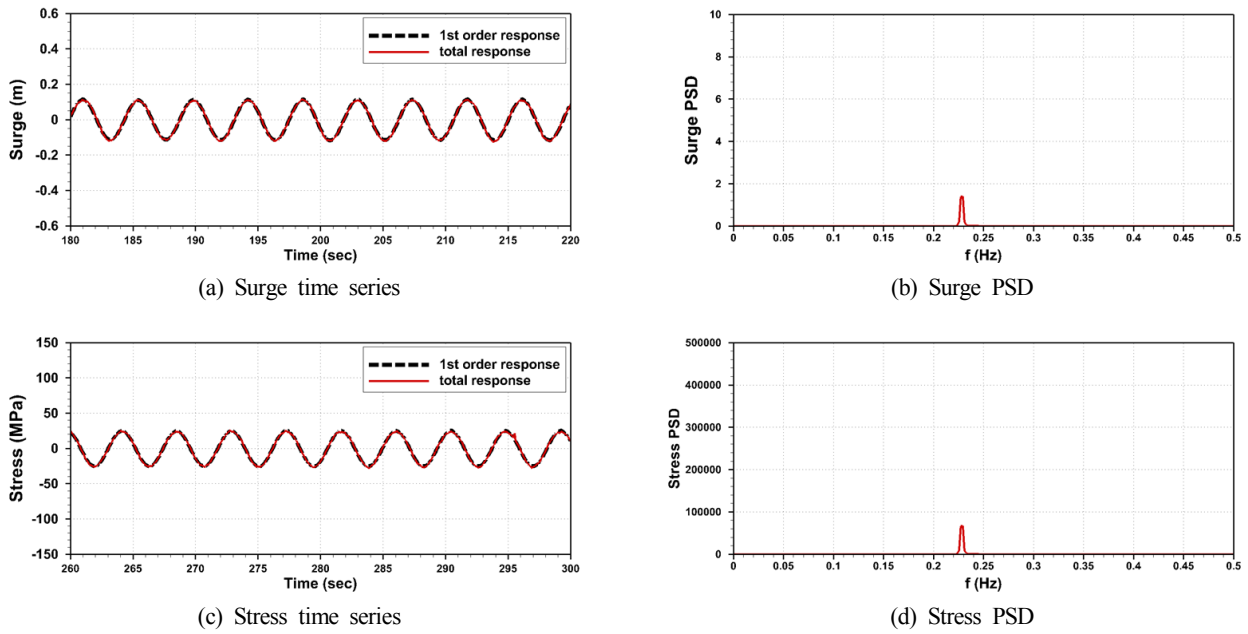


Fig. 14 Regular wave test results at  $H = 1.5$  m and  $T = 4.384$  s

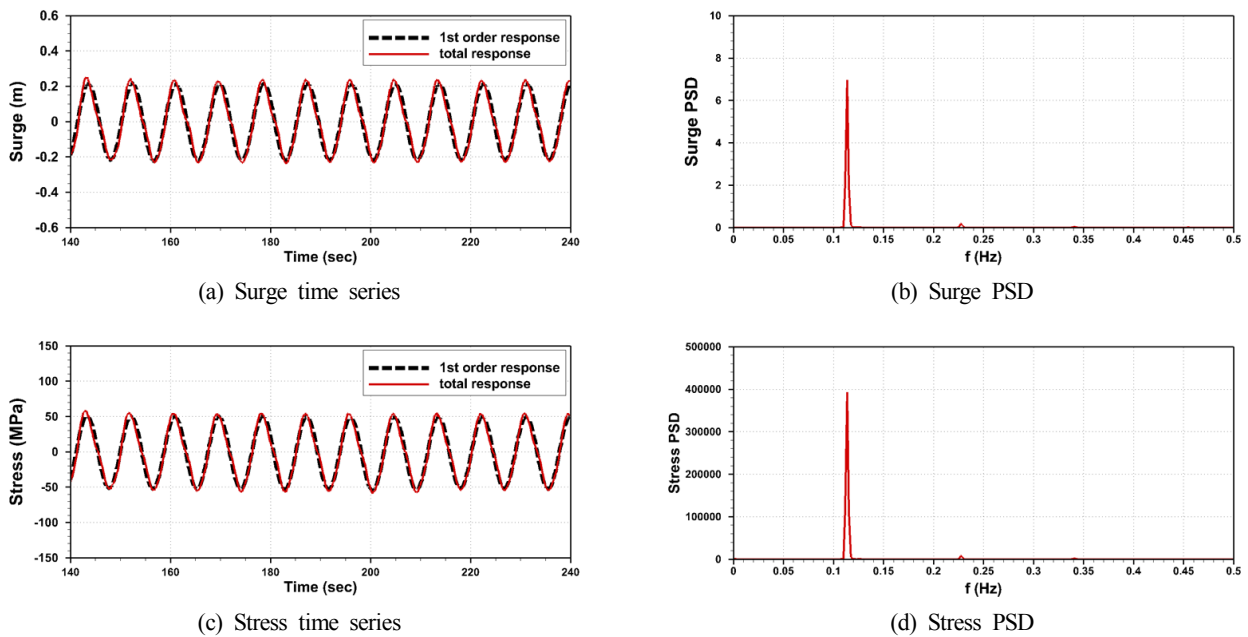


Fig. 15 Regular wave test results at  $H = 6.0$  m and  $T = 8.779$  s

condition, it is confirmed that the natural frequency response (third-order springing response) also occurs regularly in addition to the wave frequency response (first-order response), because the triple of the wave frequency of 0.13 Hz, 0.39 Hz, almost coincides with the natural frequency of 0.387 Hz. The time-series results in Fig. 13 (a) and (c) show the difference between the first-order response results and the third-order springing response results.

Among the wave conditions, the double of the wave frequency is close to the natural frequency of the structure when the wave period is 4.384 s (0.23 Hz), but there is no springing phenomenon because the wave height is small (Fig. 14). Even when the wave height is large (6 m), no springing phenomenon is observed if the multiples of the wave

frequency differ from the natural frequency of the structure (Fig. 15). In these cases, it could be confirmed that there is no difference between the first-order responses and the overall responses in the time series results (Figs. 14–15 (a) and (c)).

#### 4. Conclusion

In this study, the hydroelastic response and higher-order springing one that is a nonlinear response of the waves for fixed cylindrical structures are evaluated numerically and experimentally. Furthermore, the cases where each structural stiffness is high and low are studied to confirm the hydroelastic responses based on the structural stiffness of

the structure. For the numerical analysis methods, the panel method with no hydroelastic effect considered but only the scattering effect, the panel method with the hydroelastic effect considered by applying the radiation effect for the bending modes of the structure, and the Morison analysis method using beam elements are reviewed; the corresponding results are compared and analyzed.

Among the waves, the surge motions at the top and stresses at the bottom part of the fixed cylindrical structures are compared and reviewed. When the stiffness of the structures is high, the difference between the panel method with and without hydroelastic effect considered is small, and the results are also found to be similar to the model test results. In case that the structure is flexible, there are differences on the analysis results with and without hydroelastic effect considered, and the results on analysis with hydroelastic effect considered is similar to the ones of model test. Through these results, it is confirmed that the analysis considering the hydroelastic effect is necessary when a structure is flexible. The Morison analysis method using beam elements is found to give different results from the model test when the wavelengths are relatively short compared to the outer diameter of the structure. This indicates that the scattering effect of the wave caused by the structure should be considered if the wave is shorter than the size of the structure, which can be achieved through the boundary element method and so on.

Furthermore, under regular wave conditions in the model tests, when the wave height is large and the multiples of the wave frequency coincide with the natural frequency of the structure, the higher-order components of the wave force result in a higher-order springing phenomenon where the natural frequency response occurs regularly. This phenomenon can be observed in the model tests that realize the actual phenomenon. It is found that the phenomenon does not occur when either of the two conditions of a high wave height and the coincidence of the multiples of the wave frequency with the natural frequency is not satisfied. In the future, nonlinear phenomena such as a higher-order springing phenomenon will be studied through the improvement of numerical fluid analysis methods.

### Acknowledgements

We acknowledge that this study is part of the research conducted with support from the Korea Institute of Ships and Ocean Engineering under the project, "Core Technology Development of Hydro-elasticity based Structural Damage Assessment for Offshore Structures considering Uncertainties (Grant No. PES3930)". We appreciate the support for research funding.

### References

- Andrianov, A.I. (2005). Hydroelastic Analysis of Very Large Floating Structures (Doctoral Thesis). Delft University of Technology, Delft, Netherlands.
- Bathe, K.J. (1996). *Finite Element Procedure*. Prentice Hall.
- Betts, C.V., Bishop, R.E.D., & Price, W.G. (1977). The Symmetric Generalized Fluid Forces Applied to a Ship in a Seaway. *Transactions of the Royal Institution of Naval Architecture*, 119, 265–278.
- Bishop, R.E.D., & Price, W.G. (1977). The Generalized Antisymmetric Fluid Forces Applied to a Ship in a Seaway. *International Shipbuilding Progress*, 24(269), 3–14. <https://www.doi.org/10.3233/ISP-1977-2426901>
- Bishop, R.E.D., Price, W.G., & Wu, Y. (1986). A General Linear Hydroelasticity Theory of Floating Structures Moving in a Seaway. *Philosophical Transactions of Royal Society, London*, A316. <https://doi.org/10.1098/rsta.1986.0016>
- Choi, Y.R., Hong, S.Y., & Choi, H.S. (2000). An Analysis of Second-order Wave Forces on Floating Bodies by Using a Higher-Order Boundary Element Method. *Ocean Engineering*, 28(1), 117–138. [https://doi.org/10.1016/S0029-8018\(99\)00064-5](https://doi.org/10.1016/S0029-8018(99)00064-5)
- Heller, S.R., & Abramson, H.N. (1959). Hydroelasticity: A New Naval Science. *Journal of America Society of Naval Engineers*, 71(2), 205–209. <https://doi.org/10.1111/j.1559-3584.1959.tb02326.x>
- Hong, S.Y., & Kim, B.W. (2014). Experimental Investigations of Higher-order Springing and Whipping-WILS Project. *International Journal of Naval Architecture and Ocean Engineering*, 6(4), 1160–1181. <https://doi.org/10.2478/IJNAOE-2013-0237>
- Hong, S.Y., Kim, J.H., Cho, S.K., Choi, Y.R., & Kim, Y.S. (2005). Numerical and Experimental Study on Hydrodynamic Interaction of Side-by-Side Moored Multiple Vessels. *Ocean Engineering*, 32(7), 783–801. <https://doi.org/10.1016/j.oceaneng.2004.10.003>
- Jensen, J.J., & Pedersen, P.T. (1981). Bending Moments and Shear Forces in Ships Sailing in Irregular Waves. *Journal of Ship Research*, 25(4), 243–251.
- Kim, B.W., Cho, S.K., & Sung, H.G. (2018). Time Domain Full Ship Finite Element Analysis with or Without Scattering or Radiation Potential. *Proceedings of 2018 Joint Conference of the Korean Association of Ocean Science and Technology Societies*, 97–100.
- Kim, H.S., Kim, B.W., Won, Y., Oh, Y.J., & Lee, K. (2020). Numerical and Experimental Evaluation on Wave-Induced Responses of Cylindrical Structure with or without Hydroelastic Effect. *Proceedings of 2020 Joint Conference of the Korean Association of Ocean Science and Technology Societies*, 869–872
- Kim, J.G., Cho, S.P., Kim, K.T., & Lee, P.S. (2014). Hydroelastic Design Contour for the Preliminary Design of Very Large Floating Structures. *Ocean Engineering*, 78, 112–123. <https://doi.org/10.1016/j.oceaneng.2013.11.006>
- Lakshminarayanan, P.A., Temarel, P., & Chen, Z. (2015). Coupled Fluid-Structure Interaction to Model Three-Dimensional Dynamic Behaviour of Ship in Waves. *Proceedings of 7th International Conference on Hydroelasticity in Marine*

- Technology, Split, Croatia, 623-636.
- Price, W.G., & Wu, Y. (1985). Structural Responses of a SWATH of Multi-Hulled Vessel Traveling in Waves. Proceedings of International Conference on SWATH Ships and Advanced Multi-hulled Vessels. Royal Institution of Naval Architects, London.
- Rognaas, G., Xu, J., Lindseth, S., & Rosendahl, F. (2001). Mobile Offshore Base Concepts: Concrete Hull and Steel Topsides. *Marine Structure*, 14(1-2), 5-23. [https://doi.org/10.1016/S0951-8339\(00\)00019-8](https://doi.org/10.1016/S0951-8339(00)00019-8)
- Shin, K.H., Jo, J.W., Hirdaris, S.E., Jeong, S.G., Park, J.B., Lin, F., Wang, Z., & White, N. (2015). Two- and Three- Dimensional Springing Analysis of a 16,000 TEU Container Ship in Regular Waves. *Ships and Offshore Structures*, 10(5), 498-509. <https://doi.org/10.1080/17445302.2015.1014255>
- Shuku, M., Shin, H., Inoue, S., Kobayashi, E., & Simamune, S. (2001). Overview of Mega-Float and Its Utilization. Mitsubishi Heavy Industries, Ltd. *Technical Review*, 38(2), 39-46.
- Wu, Y. (1984). Hydroelasticity of Floating Bodies (Ph D. Thesis). Brunel University, UK.

### Author ORCIDs

Author name	ORCID
Kim, Hyun-Sung	0000-0002-2627-6625
Won, Younguk	0000-0002-7065-2763
Oh, Young Jae	0000-0002-0568-0151
Lee, Kangsu	0000-0002-9505-6802
Kim, Byoung Wan	0000-0001-7325-1546

# Numerical Investigation of Residual Strength of Steel Stiffened Panel Exposed to Hydrocarbon Fire

Jeong Hwan Kim<sup>1</sup>, Dae Yu Baeg<sup>2</sup> and Jung Kwan Seo<sup>3,4</sup>

<sup>1</sup>Research Professor, The Korea Ship and Offshore Research Institute, Busan, Korea

<sup>2</sup>Graduate Student, Department of Naval Architecture and Ocean Engineering, Pusan National University, Busan, Korea

<sup>3</sup>Professor, Department of Naval Architecture and Ocean Engineering, Pusan National University, Busan, Korea

<sup>4</sup>Professor, The Korea Ship and Offshore Research Institute, Busan, Korea

**KEY WORDS:** Residual strength, Hydrocarbon jet fire, Thermal response analysis, Stiffened plate panel, Design formulae

**ABSTRACT:** Current industrial practices and approaches are simplified and do not describe the actual behavior of plated elements of offshore topside structures for safety design due to fires. Therefore, it is better to make up for the defective methods with integrated fire safety design methods based on fire resistance characteristics such as residual strength capacity. This study numerically investigates the residual strength of steel stiffened panels exposed to hydrocarbon jet fire. A series of nonlinear finite element analyses (FEAs) were carried out with varying probabilistic selected exposures in terms of the jet fire location, side, area, and duration. These were used to assess the effects of exposed fire on the residual strength of a steel stiffened panel on a ship-shaped offshore structure. A probabilistic approach with a feasible fire location was used to determine credible fire scenarios in association with thermal structural responses. Heat transfer analysis was performed to obtain the steel temperature, and then the residual strength was obtained for the credible fire scenarios under compressive axial loading using nonlinear FEA code. The results were used to derive closed-form expressions to predict the residual strength of steel stiffened panels with various exposure to jet fire characteristics. The results could be used to assess the sustainability of structures at risk of exposure to fire accidents in offshore installations.

## 1. Introduction

Ships and ship-shaped offshore installations can be exposed to hydrocarbon fires and explosions. These dangers have serious consequences for human health, structural safety, and the surrounding environment (Czujko, 2001; HSE, 2000). Current industrial practices develop an initial design prediction to prevent and mitigate the escalation of accidental events, which requires appropriate understanding of related design methods and effectiveness. The safety concerns are reflected in current regulations and guidelines for qualitative or quantitative fire and explosion risk analysis (QRA) and risk management (Vinnem, 2007; NORSOK, 2010; Nolan, 1996; Paik and Czujko, 2011; Seo et al., 2017).

In current fire safety design (Franssen and Real, 2010; Purkiss, 2006), the fire scenario of steel structures is generally considered as fire heat exposed to the surface of structural members with the same intensity. For the thermal structural response, heat intensities are

assumed to remain the same throughout the exposed fire duration. However, this method tends to be simplified and does not describe the actual behavior, which accompanies time, space characteristics, radiation, and convection. The outcome of these assumptions results in time-release changes of flammable materials in fire accidents. Current industrial practices in fire safety design methods consist of various applicable of international/national regulations, standards, and guidance. Therefore, it is better to make up for the defective methods with integrated fire safety design methods based on fire resistance characteristics such as the residual strength capacity. An essential integrated fire safety design method requires fire computational fluid dynamics (CFD) simulations and thermal finite element analysis (FEA) simulation (Paik et al., 2010; Shetty et al., 1998).

For these reasons, previous researchers have suggested procedures or guidance for fire risk analysis that consist of probabilistic-based fire accidental design loads, fire CFD analyses, and nonlinear FE analyses. Applications for ships and offshore installations have also been

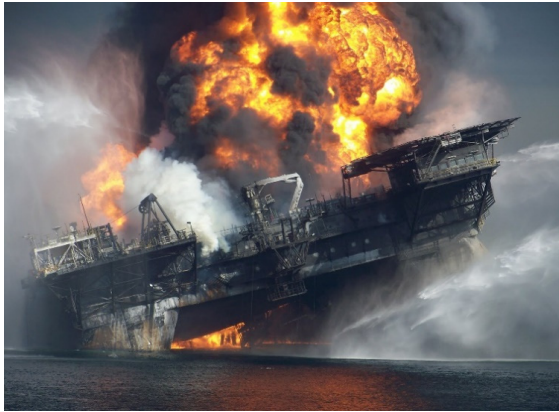
Received 19 January 2021, revised 15 May 2021, accepted 31 May 2021

Corresponding author Jung Kwan Seo: +82-51-510-2415, [seojk@pusan.ac.kr](mailto:seojk@pusan.ac.kr)

It is noted that this paper is revised edition based on proceedings of the Annual Autumn Conference of KSOE 2018 in Incheon.

© 2021, The Korean Society of Ocean Engineers

This is an open access article distributed under the terms of the creative commons attribution non-commercial license (<http://creativecommons.org/licenses/by-nc/4.0>) which permits unrestricted non-commercial use, distribution, and reproduction in any medium, provided the original work is properly cited.



(a) Major fire accident (Deepwater Horizon, 2010)



(b) Minor fire accident (Hercules Jack-up, 2013)

**Fig. 1** Fire accidents at offshore platforms

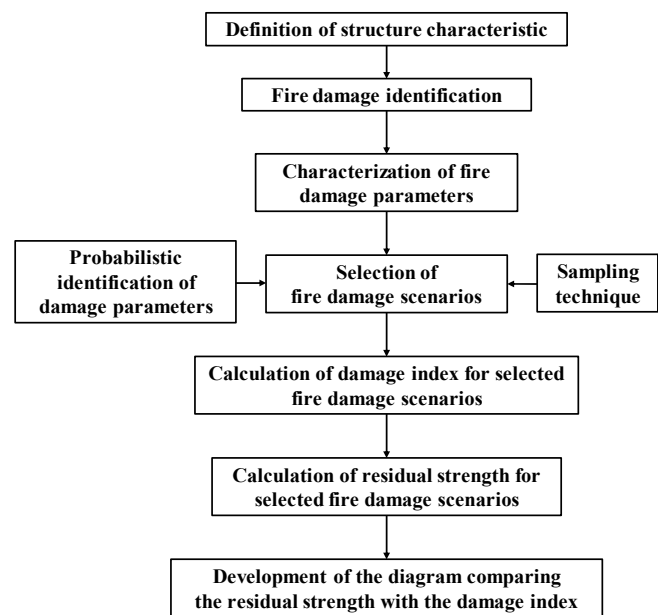
suggested and examined (Soares et al., 1998, Paik et al., 2013; Kim et al., 2013; Salem et al., 2016). Most of the methodologies assumed only one-dimensional steel structures because the structures consist of primary structural strength members (beams, columns, etc.). However, ship-shaped offshore structures and the topsides of an offshore installation include living quarters, process modules, drilling modules, etc., which are mostly assembled or welded steel plates with primary structural strength members. Therefore, their structural layout and arrangement have to be considered regarding functional, performance, and safety requirements for the design philosophy.

The most common fire accident case in offshore platforms is when a pressurized leak gas causes a jet fire. The main constituent is hydrocarbon gas materials in offshore installations, which can lead to various fire characteristics. Therefore, it is necessary to study the jet fire load characteristics with flammable hydrocarbon material in topside process modules of platforms (Sun et al., 2017). However, current approaches and studies of fire exposure areas and fire duration only consider major fire accidents (Fig. 1(a)) in safety design and management, but minor fire accidents (Fig. 1(b)) should also be considered for structural sustainability in operating conditions.

Current industrial practices and approaches provide only limited information on plated elements of offshore topside structures for safety design and assessment of sustainability due to fires. Therefore, the effect of residual strength capacity and the thermal response behavior of plated structures during a fire should be identified. This study looks at the residual strength of plated panels under fire load by numerical analysis using a nonlinear finite element method (FEM). The results were used to derive closed-form expressions to predict the residual strength of steel stiffened panels with various exposures to jet fire areas and times.

## 2. Residual Strength versus Damage Index Diagram

Fig. 2 shows the proposed approach for determining residual strength and fire damage index in this study. Credible scenarios for all possible exposed fire scenarios for a target structure were selected using probabilistically characterized variables that affect the structural

**Fig. 2** Proposed method for the development of residual strength versus damage index diagram (R-D diagram)

damage. A fire damage index in a credible scenario is identified as a phenomenological fire exposure characteristic, such as location and time. The residual strength (ultimate strength) capacity of stiffened panel structures in a fire scenario can be analyzed by appropriate numerical tools. The proposed procedure was conducted for each of the selected credible scenarios in realistic fire accidents, and a diagram can show the reduction or sustainable structural strength (residual strength) and the fire's effect on the damage index. This diagram serves as a first-cut design evaluation and is used to identify the acceptance criteria for ships and offshore installations' safety design against fire accidental damage.

### 2.1 Fire Load Identification

Once an object's structural topology has been defined with geometrical and material properties, the type of fire load should be identified. Fire is a complex chain reaction where fuel is combined with oxygen, generating heat, smoke, and light. Most hydrocarbon

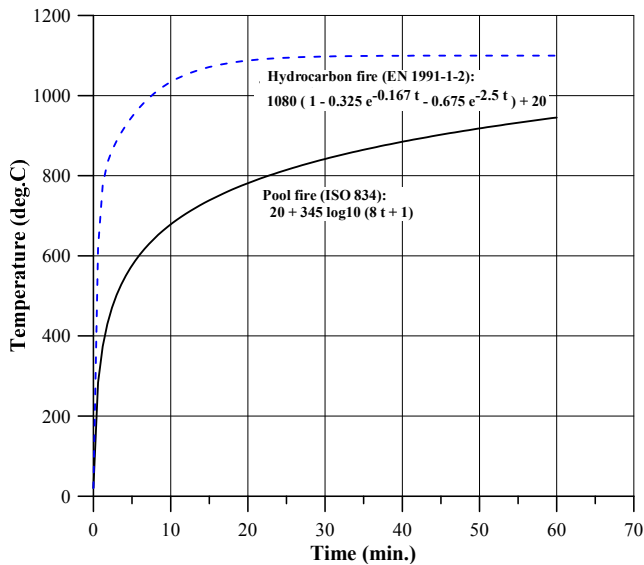


**Fig. 3** The time versus gas temperature profile for hydrocarbon (EN 1991-1-2, 2002) and pool (ISO, 1999) fires

fires can be divided into jet fires and pool fires for health, structural safety, and environmental safety requirements for a design philosophy. A jet fire occurs when a flammable liquid or gas is ignited after its release from a pressurized, punctured vessel or pipe and is a turbulent diffusion flame resulting from the combustion of a hydrocarbon fuel continuously released with some significant momentum in a particular direction. A pool fire occurs when a flammable liquid leaks from a vessel or pipeline to form a fluid reservoir, which then ignites. Common characteristics of a hydrocarbon jet fire are a turbulent flame, a high heat flux, and the capability of eroding a material that it impacts. Pool fires are turbulent diffusions, burning above an upward-facing, vaporizing liquid fuel. The vaporizing fuel has almost zero or low initial momentum. The fire load can be obtained by performing a CFD analysis or using a profile specified in the regulations, such as hydrocarbon fire and pool fire regulations (ISO, 1999). Fig. 3 shows the general profiles for hydrocarbon and pool fires.

## 2.2 Characterization of Fire Damage Variables

After determining the type of fire load, the damage parameters that affect the residual ultimate strength should be characterized. The location and exposed areas of fire damage were the basic parameters used in this study. The other parameters depend on the type of damage. For example, gas temperature is a critical parameter of fire damage when calculating the residual ultimate strength of structures. CFD may be performed to calculate a more accurate damage index. CFD simulation results, such as temperature, time, and heat flux etc., may give damage parameters to calculate the residual ultimate strength of structures.

## 2.3 Credible Fire Damage Scenarios

The fire damage scenarios were established via sampling techniques based on characterized damaged parameters, which were calculated using the probability density function. A small number of fire damage

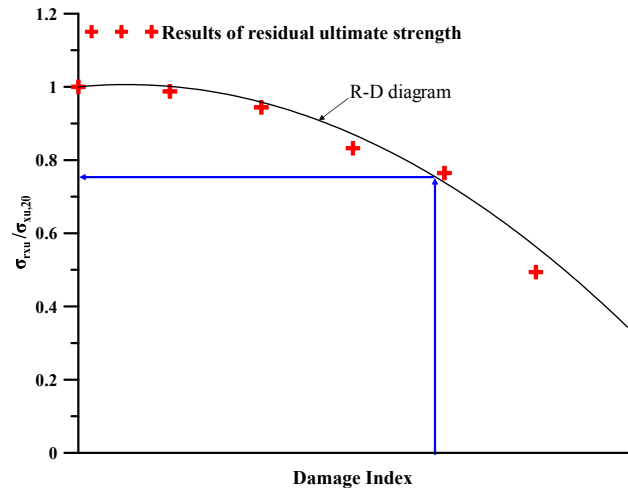


**Fig. 4** R-D diagram

scenarios were selected based on scenario sampling methods, such as the Latin hypercube sampling method (LHS), etc. It was necessary to consider as many damage scenarios as possible to develop an R-D diagram that could reflect a smaller interval of random variables in a wider range of damage extent.

## 2.4 Calculation of Damage and Residual Strength for the Scenarios

After selecting the fire damage scenarios, the fire damage index can be defined in the form of an R-D diagram. A residual strength analysis was performed for each selected fire damage scenario. The fire damage index ( $r/b$ ) was determined by the ratio of the flame radius ( $r$ ) and the breadth of the plate ( $b$ ). Candidate methods (numerical, analytical, and experimental methods) are able to calculate the residual strength. In this study, numerical methods were most commonly applied to structural analysis as they have been found to be the most efficient (Kim et al., 2014). Once the fire damage index and the ultimate strength were simulated for the selected fire damage scenarios, the diagram was expressed in form of Fig. 4. R-D diagrams can be used to predict the residual strength with fire exposure damage.

## 3. Applied Examples

### 3.1 Definition of Structure Characteristics

Fig. 5 shows a floating, production, storage and offloading (FPSO) structure, which is one type of ship-shaped offshore installation. Steel stiffened panels were used to construct part of the deck of the FPSO. It was supported by girders and frames along the longitudinal and transverse edges. The spacing of the stiffeners was  $a = 4000$  mm between the transverse stiffeners and  $b = 800$  mm between the longitudinal stiffeners. This study considered T-bars as both longitudinal and transverse stiffeners. Fig. 6 and Table 1 show the cross sections of the longitudinal and transverse stiffeners (Paik and Thayaballi, 2003).

The stiffened plate panel was modeled using shell elements to perform the heat transfer analysis and nonlinear structural response

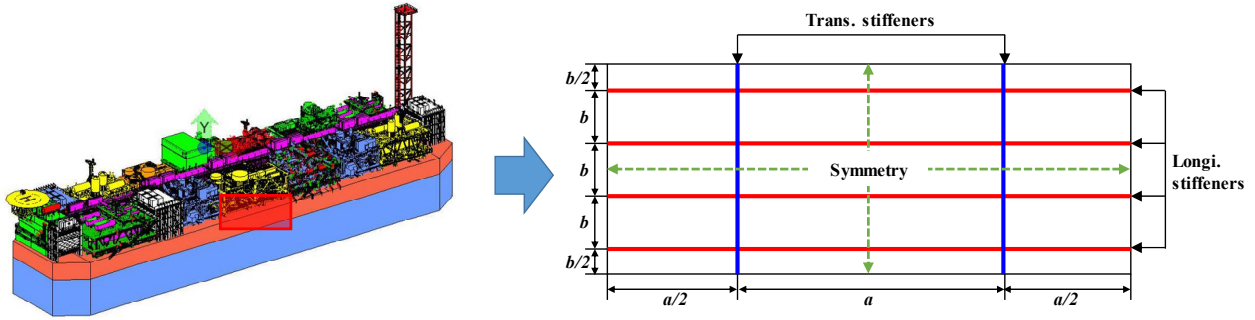


Fig. 5 The steel stiffened panel part of the FPSO deck

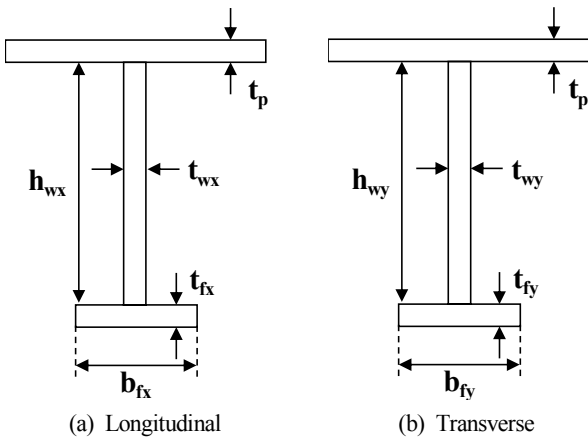


Fig. 6 Longitudinal (a) and transverse (b) stiffeners

Table 1 Principal dimensions of plate girders and stiffeners.

Longitudinal (x-direction)		Transverse (y-direction)	
$t_p$ (mm)	6	$t_p$ (mm)	6
$h_{wx}$ (mm)	125	$h_{wy}$ (mm)	430
$t_{wx}$ (mm)	7	$t_{wy}$ (mm)	12
$b_{fx}$ (mm)	75	$b_{fy}$ (mm)	150
$t_{fx}$ (mm)	7	$t_{fy}$ (mm)	15

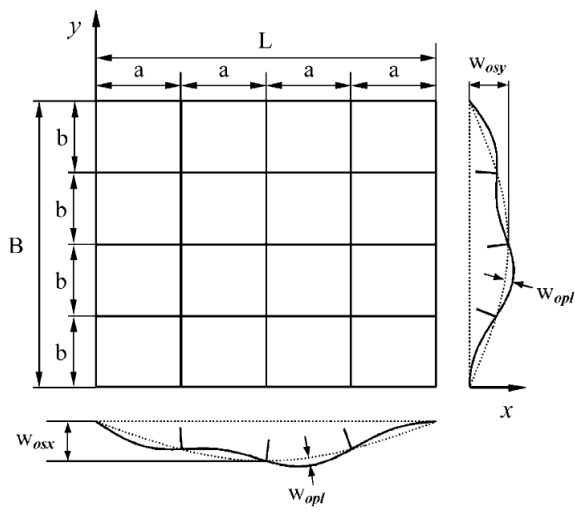
analysis. The mesh size was 45 mm, and the number of four-noded shell elements was 17 in between the longitudinal stiffeners (Hughes and Paik, 2010). The stiffened plate panels are considered to have welding-induced initial deflections (in Fig. 7(a)). The initial deflections are denoted by  $w_{opl}$  for plating between stiffeners and  $w_{osx}$  and  $w_{osy}$  for x- and y-stiffeners, respectively. The stiffened plate panel may also have welding-induced residual stresses. Fig. 7(b) shows the typical idealization of residual stresses in plating between stiffeners. The simplified residual stresses are considered uniform compressive residual stresses, which are denoted by  $\sigma_{rsx}$  and  $\sigma_{rsy}$  for x- and y-stiffeners, respectively. In this study, both initial deflection and residual stress were considered.

### 3.2 Characterization of Fire Damage Parameters

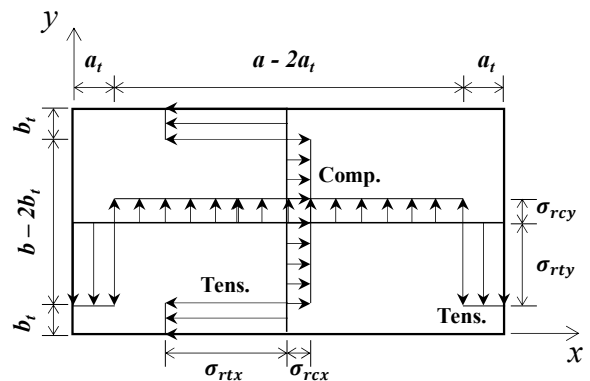
The fire damage parameters for the calculation of the fire damage index can be defined as follows:

- $X_1$  - Fire duration (min): the time exposed to fire
- $X_2$  - Exposed side: the side exposed to fire
- $X_3$  - Fire position: location of flame center
- $X_4$  - Fire area: extent of flame

In general, fire profiles can be obtained through numerical, analytical, and experimental methods. The jet and pool fire curves



(a) Pattern of initial deflection



(b) Distribution of welding induced residual stress

Fig. 7 Initial deflection and residual stress of stiffened plate panel

shown in Fig. 3 were obtained by analytical methods. With the numerical method, the temperature-time profile was calculated using CFD programs. The temperature-time profile could also be obtained by measuring the gas temperature in experiments. In this study, jet fire was calculated by the analytical method and used as the fire type. The fire duration, position, and radius of the flame were primary parameters to calculate the extent of fire damage.

### 3.3 Selection of Fire Damage Scenarios

A total of 120 scenarios were selected to calculate the fire damage index, and the range of each parameter was probabilistically defined. The fire duration was classified into six groups with 10 min. per group, and the probability density of each group was equal. Table 2 shows the probability of fire duration. The direction of the side exposed to fires affects the temperature and strength of structures. In this study, it was assumed that the plate was only exposed to fire as shown in Fig. 8.

Fig. 9 shows the position of the flame center, and Table 3 represents the probability of fire position. The fire position was classified into four groups as follows:

- A - Center of plate
- B - Intersection of plate and transverse stiffener
- C - Intersection of plate and longitudinal stiffener
- D - Intersection of transverse and longitudinal stiffener

As the shape of flames resembles circles, the shape of the fire was

**Table 2** Probability of fire duration

Duration time (min)	Probability (%)
10	16.667
20	16.667
30	16.667
40	16.667
50	16.667
60	16.667
Total	100

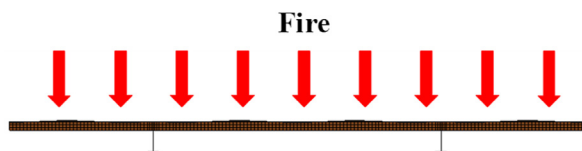


**Fig. 8** The direction of the side exposed to fires

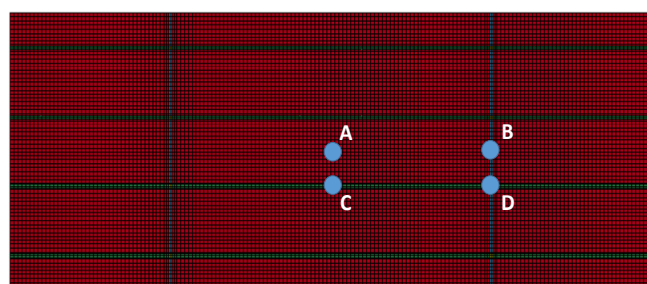


**Fig. 9** Position of flame center

**Table 3** Probability of fire position

Fire position	Probability (%)
A	25
B	25
C	25
D	25
Total	100

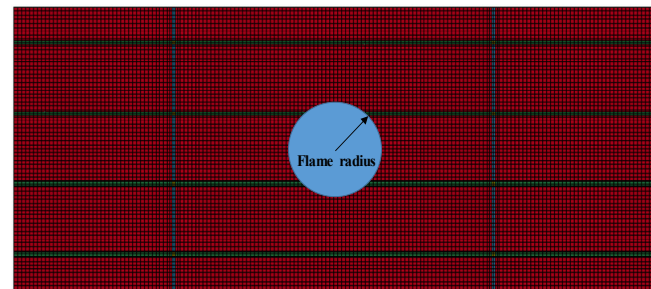


**Fig. 10** Concepts of fire area based on flame radius

**Table 4** Probability of fire area

Fire radius $r$	Radius-breadth ratio ( $r/b$ )
200	0.25
400	0.50
600	0.75
800	1.00
1000	1.25
Total	-

assumed to be circular. The probabilistic characteristics of the fire area were identified based on the radius of the flame. Fig. 10 and Table 4 show the shape and probability of the fire area. Table A1 lists 120 representative fire damage scenarios using the four major parameters that were considered. The selected scenarios included all of the variables for each parameter.

### 3.5 Calculation of Damage Index for Selected Fire Damage Scenarios

The fire damage index for selected scenarios was calculated using LS-DYNA code, which uses shell elements to model the structures (ANSYS, 2018). The gas temperature did not determine the temperature of the exposed steel because of the effects of radiation and convection. Thus, a heat transfer analysis needed to be carried out to identify the steel temperature while considering the effects of radiation and convection (Kim et al., 2013).

Fig. 11 shows the heat transfer analysis method conceptually. The applied method conducts the heat flux and temperature between the gas ( $T_g$ ) and surface ( $T_{s1}$ ) of the steel structural element with an exposed side. Radiation, convection, and heat loss should be considered for the unexposed side. In the case of shell elements in LS-DYNA, the temperature was uniform ( $T_{s1} = T_{s2}$ ) in the steel

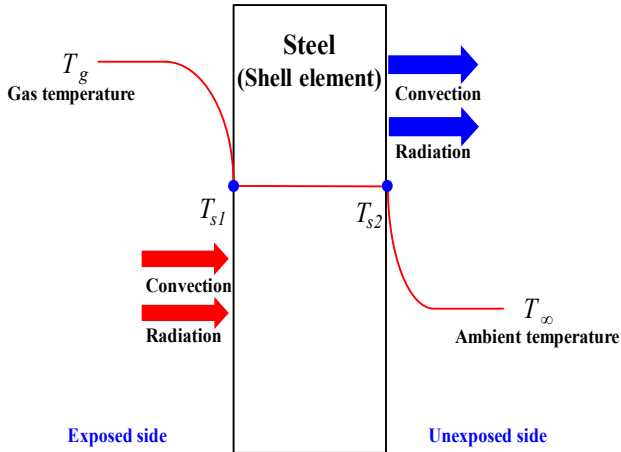


Fig. 11 Concepts of method for heat transfer analysis in LS-DYNA

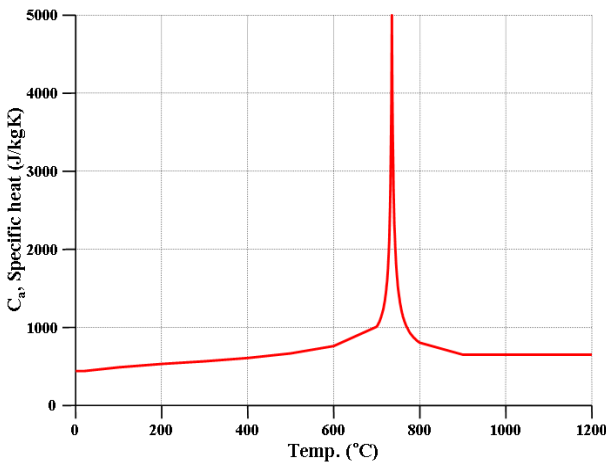
thickness direction. In this study, the coefficient of convection was  $h_c = 25 \text{ W/m}^2\text{K}$ , and the emissivity of carbon steel was  $\epsilon_s = 0.7$  (Franssen and Real, 2010). The temperature-dependent specific heat

and thermal conductivity of carbon steel shown in Fig. 12 were considered to result in an accurate heat transfer analysis. Fig. 13 shows a typical temperature distribution of fire position A after 10 minutes.

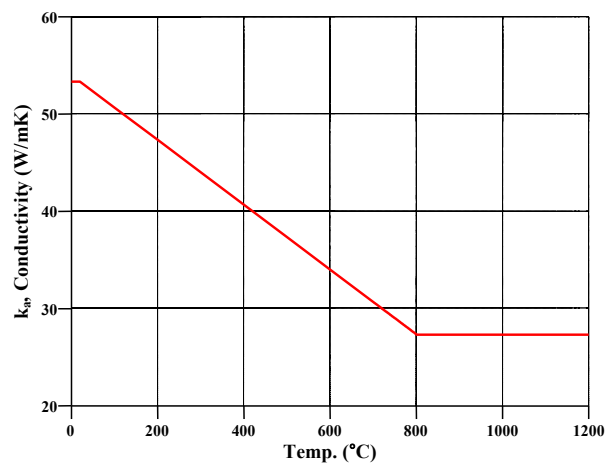
### 3.6 Calculation of Residual Strength

The residual strength analysis was performed using LS-DYNA with the shell element models that were used for the heat transfer analysis to calculate the residual ultimate strength. To perform the residual ultimate strength analysis under fire conditions, the mechanical properties related to temperature changes needed to be applied properly. This study used the elastic perfectly plastic material model according to the steel temperature. The strength of steel should be taken as 0.2% of the proof strength, and the section modulus and the cross-sectional effective area can be determined with EN 1993-1-5 (2006) and the mechanical properties at 20°C.

Fig. 14 shows the relation between the characteristics of the yield stress and elastic modulus of carbon steel and temperature increments. The yield stress and elastic modulus of the steel stiffened panel at 20°C



(a) Specific heat



(b) Thermal conductivity

Fig. 12 Thermal properties of carbon steel: (a) specific heat and (b) thermal conductivity

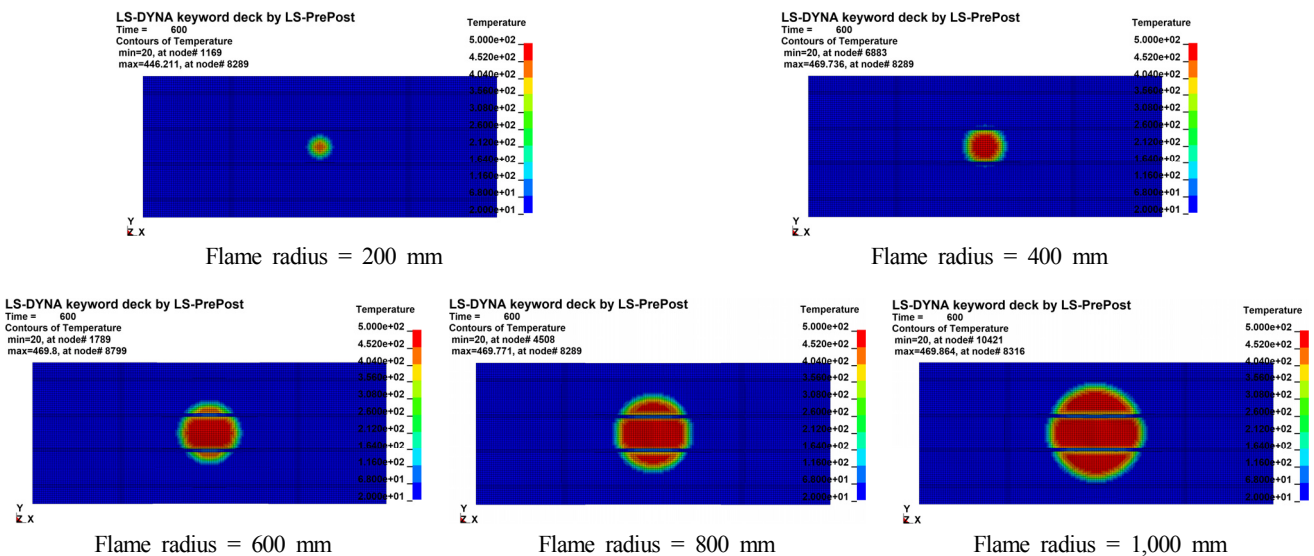


Fig. 13 Temperature distribution of steel stiffened panel at 10 min (Fire position A)

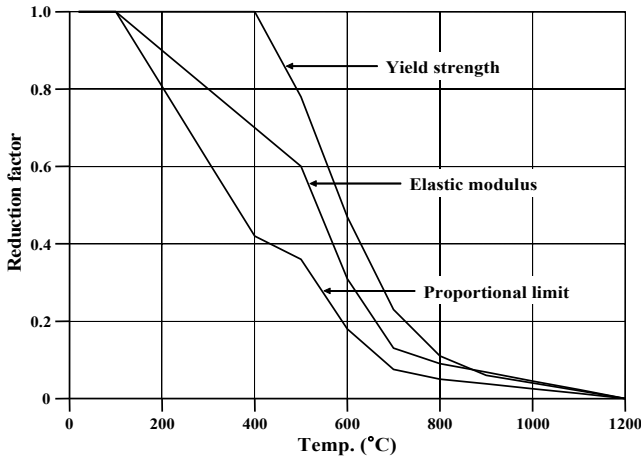


Fig. 14 Mechanical properties of steel versus temperature increments

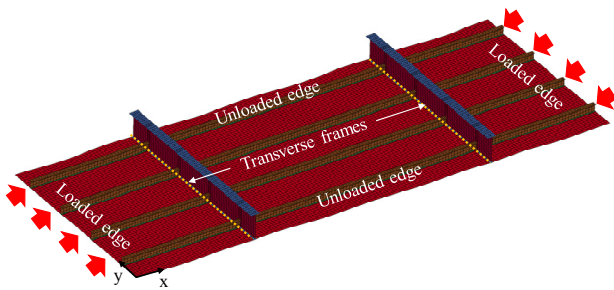


Fig. 15 The boundary and loading conditions

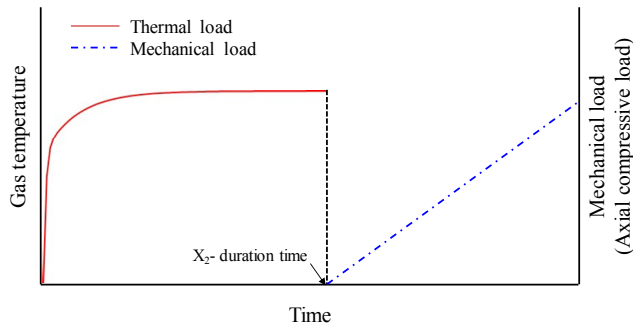


Fig. 16 Loading condition

were 240 MPa and 200 GPa, respectively, and the Poisson ratio was 0.3. The residual strength analysis considered a reduction factor for the stress-strain relationship of carbon steel at elevated steel temperatures. Fig. 15 and Table 5 show the boundary conditions and loading conditions. A uniaxial compressive load in the longitudinal direction was applied, and the mechanical load was applied after the thermal load, as shown in Fig. 16.

Table 5 Boundary conditions ( $U$  = translational degree of freedom,  $R$ = rotational degree of freedom)

Part	Description <sup>1)</sup>
Loaded edge	$U_x = 0, U_y = 0, U_z = 0, R_x = 1, R_y = 0, R_z = 1$
Unloaded edge	$U_x = 0, U_y = 0, U_z = 0, R_x = 0, R_y = 1, R_z = 1$
Transverse frames (dotted line)	$U_x = 0, U_y = 0, U_z = 1, R_x = 0, R_y = 0, R_z = 0$

<sup>1)</sup> 1 is translational constraint, 0 is no translational constraint

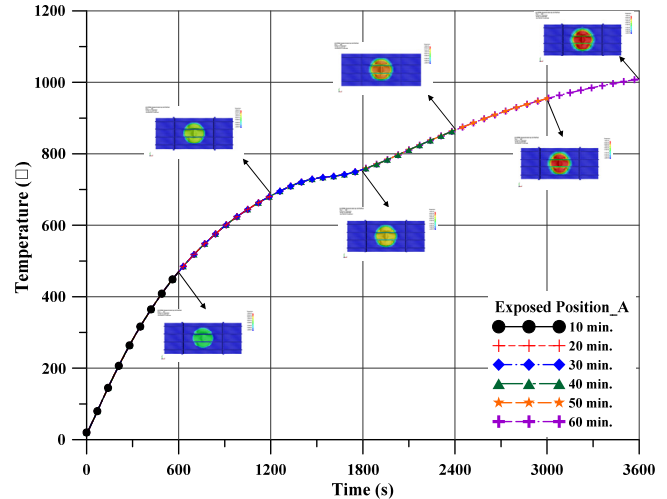


Fig. 17 Steel temperature versus exposure time of position A

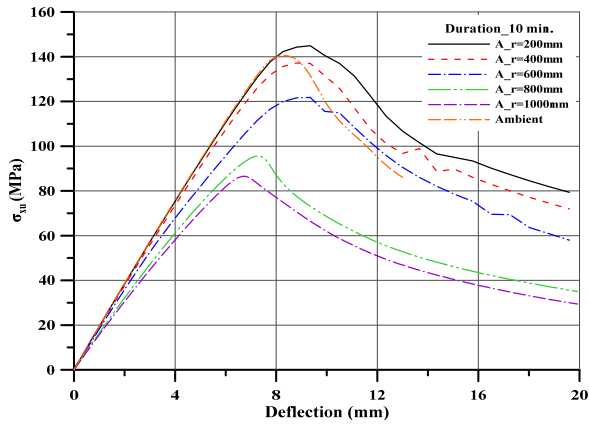
Fig. 17 shows the steel temperature versus exposure time of position A at various time durations. As shown in the figure, when the fire duration is more than 40 minutes, the steel temperature distribution of the stiffened panel does not reach steady state, but it can be confirmed that the temperature rises slowly. Fig. 18 shows the typical ultimate strength behavior of the steel stiffened panel under axial compression at various time durations among 120 selected fire damage scenarios. As expected, the ultimate strength was lower when the radius of the flame was widened. The overall lateral deflection shape of the plate along the longitudinal direction tended to be similar to the initial applied imperfection mode shape. This finding could help to identify the effect of fire damage on the compressive ultimate strength of the steel stiffened panel.

#### 4. Development of R-D Diagram

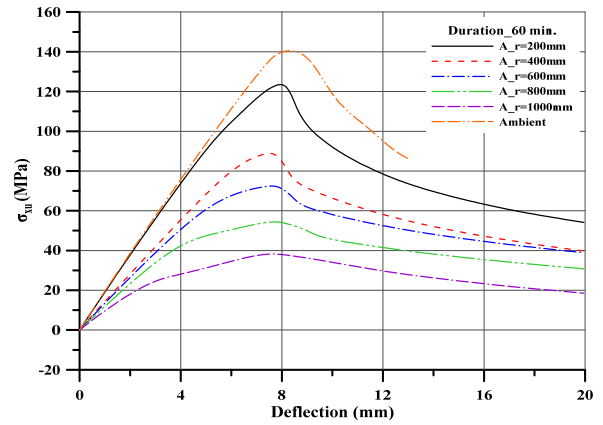
Fig. 19 shows the variation of the residual ultimate strength reduction factor of the steel stiffened panel under longitudinal axial compression with different sizes and locations of the area exposed to fire, which was obtained by FEA. The R-D diagram was developed using the residual ultimate strength reduction factor. In this study, R-D diagrams were developed based on the yield stress and ultimate strength at ambient temperature.

##### 4.1 R-D Diagram Based on Residual Strength

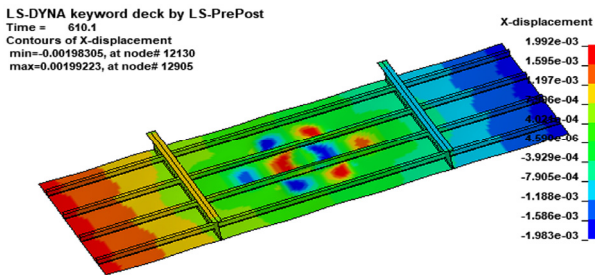
R-D formulae are proposed to estimate the ultimate strength of a stiffened panel under a compressive axial load at each fire position. In



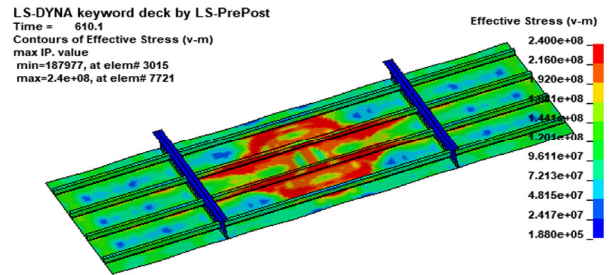
(a) 10 minutes



(b) 60 minutes

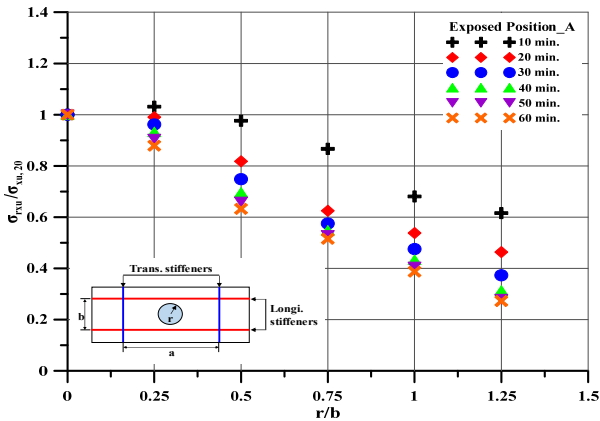


(c) Deformation of Flame radius = 1,000 mm

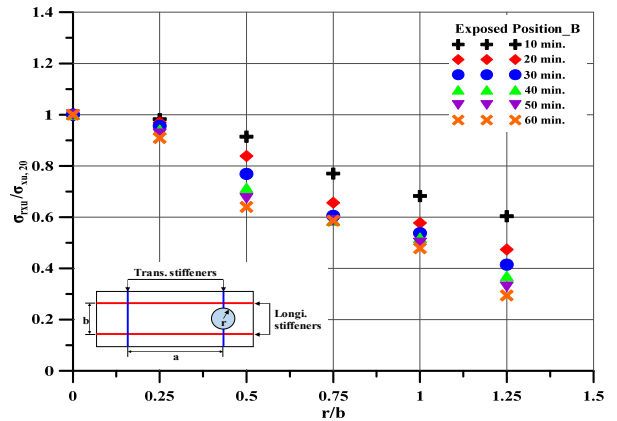


(d) von Misses Stress of Flame radius = 1,000 mm

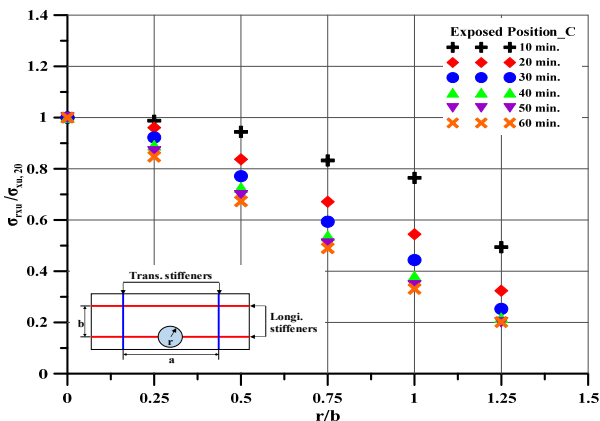
Fig. 18 Typical ultimate strength behavior of steel stiffened panel after 10 and 60 minutes of fire exposure (Position A)



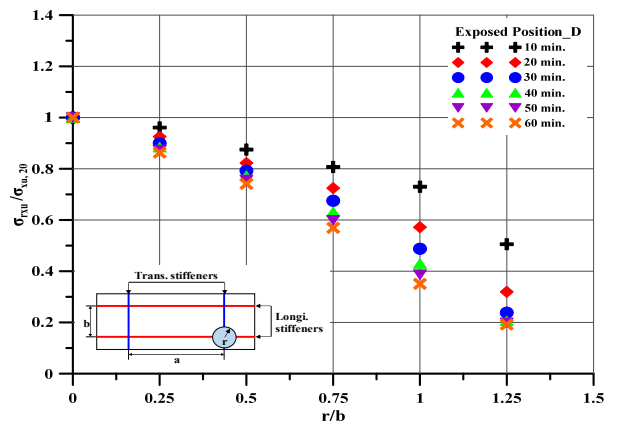
(a) Fire position A



(b) Fire position B



(c) Fire position C



(d) Fire position D

Fig. 19 Variation of the ultimate strength reduction factor of the steel stiffened panel under longitudinal axial compression with different sizes and locations of the area exposed to fire: (a) Fire position A, (b) Fire position B, (c) Fire position C, and (d) Fire position D

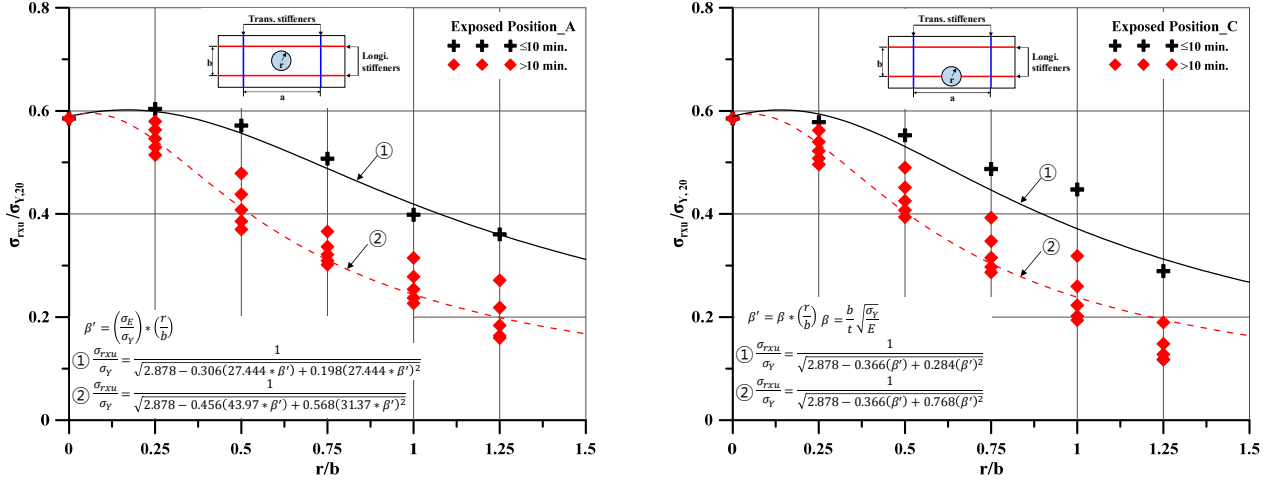


**Fig. 20** The empirical formulae for fire position A and fire position C

design practice, it is considered that Positions A to D can be determined as critical fire positions. Positions B and D are both on webs of a large transverse frame. These fire positions tend to have conservative residual strength compared to Positions A and C. Therefore, the formulae were derived from a numerical database of 120 cases, the elastic buckling strength, and the plate slenderness ratio.

The design formulae were derived using the least squares method based on the FEA results. The fire duration was divided at 10 min. for formulations. The residual ultimate strength ( $\sigma_{rxu}$ ) under a compressive axial load at fire position A was formulated as follows:

$$\frac{\sigma_{rxu}}{\sigma_Y} = \frac{1}{\sqrt{2.87 - 0.30(27.4 \times \beta') + 0.198(27.4 \times \beta')^2}} \quad \text{for } 4 \times 8.30 \quad (1)$$

$$\frac{\sigma_{rxu}}{\sigma_Y} = \frac{1}{\sqrt{2.87 - 0.45(43.9 \times \beta') + 0.568(31.3 \times \beta')^2}} \quad \text{for } > 10 \text{ min} \quad (2)$$

For fire position C, the design formulae of residual ultimate strength were derived as follows:

$$\frac{\sigma_{rxu}}{\sigma_Y} = \frac{1}{\sqrt{2.878 - 0.366(\beta') + 0.284(\beta')^2}} \quad \text{for } 2840.3 \quad (3)$$

$$\frac{\sigma_{rxu}}{\sigma_Y} = \frac{1}{\sqrt{2.878 - 0.366(\beta') + 0.768(\beta')^2}} \quad \text{for } > 10 \text{ min} \quad (4)$$

where,

$$\beta' = \left(\frac{\sigma_E}{\sigma_Y}\right) \times \left(\frac{r}{b}\right), \sigma_E = k \frac{\pi^2 E}{12(1-\nu^2)} \left(\frac{t}{b}\right)^2 \quad \text{for Eqs. (1)-(2)}$$

$$\beta' = \beta \times \left(\frac{r}{b}\right), \beta = \frac{b}{t} \sqrt{\frac{\sigma_Y}{E}} \quad \text{for Eqs. (3)-(4)}$$

$k$  = Buckling coefficient (It can be approximated to  $k = 4$ )

The accuracy of the present formulae calculated against the ratio of the flame radius and the breadth of the plate was checked by comparison with the FEA results at fire position A, as shown in Fig. 20. The mean, standard deviation, and coefficient of variation values for the design formulae in Eqs. (1)–(2) were 0.985 and 0.977, 0.028 and 0.120, and 0.029 and 0.123, respectively. Likewise, the values for the design formulae in Eqs. (3)–(4) were 1.038 and 0.972, 0.091 and 0.180, and 0.088 and 0.185, respectively.

#### 4.2 Development of Design Formulae Based on Residual Ultimate Strength

A residual ultimate strength reduction factor ( $R_{xu}$ ) is proposed to estimate the ultimate strength of a steel stiffened plate panel under longitudinal axial compression with varying area and duration of fire exposure. The residual ultimate strength reduction factor can be defined by a polynomial equation in terms of flame radius and plate aspect ratio as follows:

$$R_{xu} = \alpha_{u1} \left(\frac{r}{b}\right)^3 + \alpha_{u2} \left(\frac{r}{b}\right)^2 + \alpha_{u3} \left(\frac{r}{b}\right) + 1 \quad (5)$$

where

$$\alpha_{u1} = \begin{cases} -0.052 \left(\frac{a}{b}\right)^2 + 0.526 \left(\frac{a}{b}\right) - 1.328 & \text{for } \leq 10 \text{ min} \\ -1.542 \left(\frac{a}{b}\right)^2 + 7.232 \left(\frac{a}{b}\right) + 2.932 & \text{for } > 10 \text{ min} \end{cases}$$

$$\alpha_{u2} = \begin{cases} 0.071 \left(\frac{a}{b}\right)^2 - 0.732 \left(\frac{a}{b}\right) + 1.527 & \text{for } \leq 10 \text{ min} \\ 1.767 \left(\frac{a}{b}\right)^2 - 7.937 \left(\frac{a}{b}\right) - 5.683 & \text{for } > 10 \text{ min} \end{cases}$$

$$\alpha_{u3} = \begin{cases} -0.020 \left(\frac{a}{b}\right)^2 + 0.199 \left(\frac{a}{b}\right) + 0.095 & \text{for } \leq 10 \text{ min} \\ -0.248 \left(\frac{a}{b}\right)^2 + 0.796 \left(\frac{a}{b}\right) + 2.295 & \text{for } > 10 \text{ min} \end{cases}$$

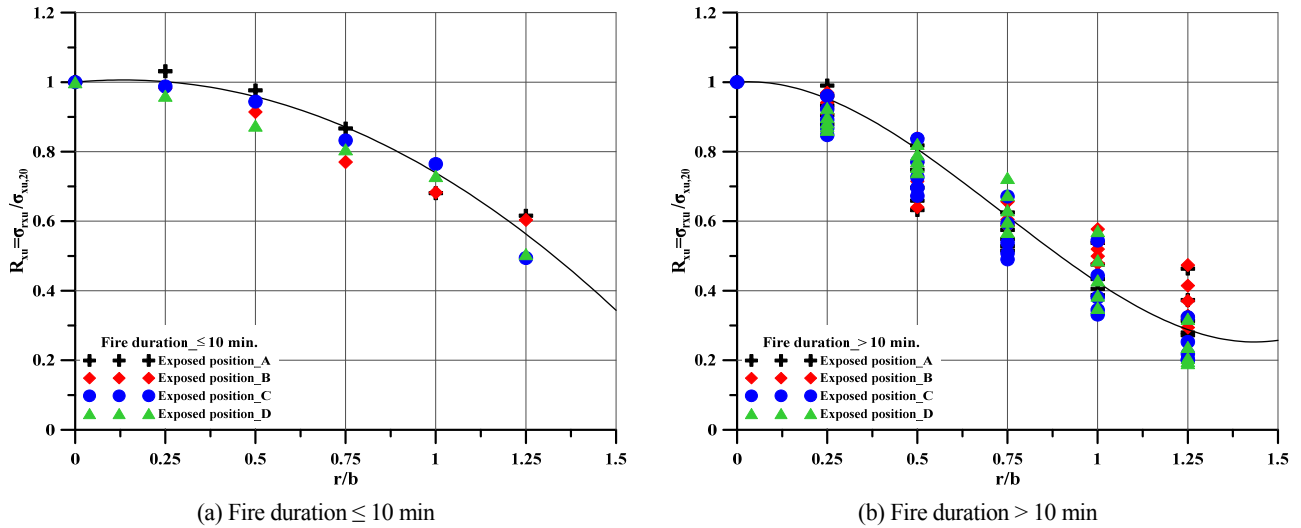


**Fig. 21** Accuracy of the residual ultimate strength reduction factor: (a) fire duration  $\leq 10$  min and (b) fire duration  $> 10$  min

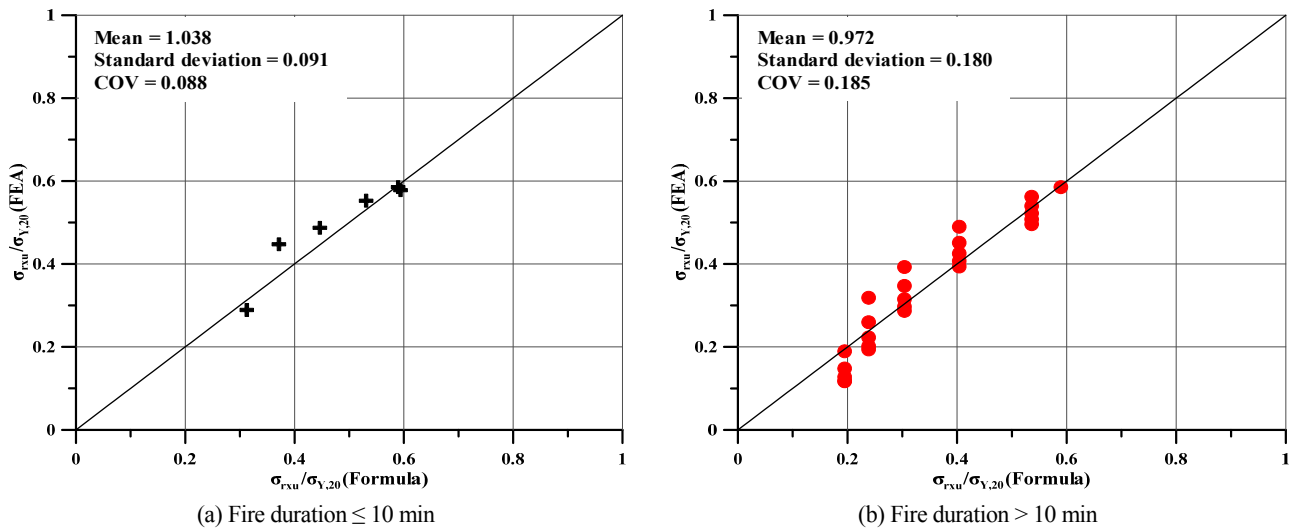


**Fig. 22** The mean, standard deviation, and COV for residual ultimate strength reduction factor

A polynomial equation is among the most frequently used empirical equations for fitting functions (Kim et al., 2019). The polynomial equation has well-known and understood properties. Also, a polynomial equation is computationally easy to use and has moderate flexibility of shapes. However, polynomial models have poor extrapolatory properties. Polynomials may provide good fits within the range of data, but they will frequently deteriorate rapidly outside the range of the data. Fig. 21 shows the accuracy of Eq. (5) by comparison to the FEA results, and Fig. 22 indicates the mean, standard deviation, and COV.

## 5. Conclusions

This study presented methods for the development and application of an R-D diagram. As a first step, fire damage parameters were characterized. The selected parameters were the fire duration, fire position, and fire area. Heat transfer analysis was carried out to identify the fire damage index for selected fire damage scenarios. Subsequently, an ultimate strength analysis was performed for a steel

stiffened panel under longitudinal axial compression. The R-D diagram was developed using the residual ultimate strength reduction factor based on the yield stress and ultimate strength at ambient temperature. However, the empirical formula in this study has the following limitations:

- (1) The empirical formula only considers the configuration of the plate, not the shape of the stiffener.
- (2) The empirical formula cannot be applied to other types of loads and stiffened panels.

The final goal of this study is to develop an empirical equation that can calculate the residual ultimate strength that can be applied to all types of stiffened panels and load types. To develop the equation, the following plan will be carried out:

- (1) Numerical analysis for the development of empirical formulae considering the configuration of stiffener
- (2) Development of empirical formulae for the combined load, lateral load, shear load, and bending load.
- (3) Accuracy analysis of empirical formulae developed in this study

From the obtained R-D diagram, the residual strength of the structure under fire conditions in offshore installations could be easily predicted.

### Funding

This research was a part of the project titled, “Development of guidance for prevent of leak and mitigation of consequence in hydrogen ships”, which is funded by the Ministry of Oceans and Fisheries and was supported by the Global Advanced Engineer Education Program for Future Ocean Structures (P0012646), which is funded by the Ministry of Trade, Industry and Energy.

### References

- ANSYS Inc. (2018). User’s Manual for ANSYS/LS-DYNA 18.1. ANSYS Inc.
- Czujko, J. (2001). Design of Offshore Facilities to Resist Gas Explosion Hazard. Oslo, Norway: CorrOcean ASA.
- EN 1991-1-2. (2002). Eurocode 1: Actions on Structures. Part 1-2: General Actions-Actions on Structures Exposed to Fire. Brussels, Belgium: CEN.
- EN 1993-1-5. (2006). Eurocode 3: Design of Steel Structures. Part 1.5: Plated Structural Element. Brussels, Belgium: CEN.
- Franssen, J.M., & Real, P.V. (2010). Fire Design of Steel Structures, ECCS Eurocode Design Manuals. Berlin: Ernst & Sohn.
- HSE, 2000. Offshore Hydrocarbon Releases Statistics and Analysis, Offshore Technology Report OTO 2000 112. London: Health & Safety Executive.
- Hughes, O., & Paik, J.K. (2010). Ship Structural Analysis and Design. New Jersey, USA: The Society of Naval Architects and Marine Engineers.
- ISO. (1999). Fire-Resistance Tests-Elements of Building Construction - Part 1: General Requirements (ISO 834-1).
- Kim, D.K., Kim, B.J., Seo, J.K., Kim, H.B., Zhang, X., & Paik, J.K. (2014). Time-dependent Residual Ultimate Longitudinal Strength – Grounding Damage Index (R-D) Diagram. Ocean Engineering, 76, 163–171. <https://doi.org/10.1016/j.oceaneng.2013.06.023>
- Kim, D.K., Lim, H.L., & Yu, S.Y. (2019). Ultimate Strength Prediction of T-bar Stiffened Panel Under Longitudinal Compression by Data Processing: A Refined Empirical Formulation. Ocean Engineering, 192, 106522. <https://doi.org/10.1016/j.oceaneng.2019.106522>
- Kim, J.H., Kim, D.C., Kim, C.K., Islam, S., Park, S.I., & Paik, J.K. (2013). A Study on Methods for Fire Load Application with Passive Fire Protection Effects. Ocean Engineering, 70, 177–187. <https://doi.org/10.1016/j.oceaneng.2013.05.017>
- Nolan, D.P. (1996). Handbook of Fire and Explosion Protection Engineering Principles for Oil, Gas, Chemical, and Related Facilities. New Jersey, USA: Noyes Publications.
- NORSOK. (2010). Norwegian Standards – Risk and Emergency Preparedness Assessment (Z-013), NORSOK.
- Paik, J.K., & Czujko, J. (2011). Assessment of Hydrocarbon Explosion and Fire Risks in Offshore Installations: Recent Advances and Future Trends. The IES Journal Part A: Civil & Structural Engineering, 4(3), 167–179. <https://doi.org/10.1080/19373260.2011.593345>
- Paik, J.K., & Thayaballi, A.K. (2003). Ultimate Limit State Design of Steel-plated Structures. Chichester: John Wiley & Sons.
- Paik, J.K., Czujko, J., Kim, J.H., Park, S.I., Islam, M.D.S., & Lee, D.H. (2013). A New Procedure for the Nonlinear Structural Response Analysis of Offshore Installations in Fires. Transaction of Society of Naval Architects and Marine Engineers, 121, 224–250.
- Paik, J.K., Kim, B.J., Jeong, J.S., Kim, S.H., Jang, Y.S., Kim, G.S., ... Czujko, J. (2010). CFD Simulations of Gas Explosion and Fire Actions. Ships and Offshore Structures, 5, 3–12. <https://doi.org/10.1080/17445300902872028>
- Purkiss, J.A. (2007). Fire Safety Engineering Design of Structures, Second Edition. New York, USA: Elsevier.
- Salem, A.M., Dabess, E.M., Banawan, A.A., & Leheta, H.W. (2016). Fire Safety Design of Nilefloating Hotels. Ships and Offshore Structures, 11, 482–500. <https://doi.org/10.1080/17445302.2015.1027564>
- Seo, J.K., Lee, S.E., & Park, J.S. (2017). A Method for Determining Fire Accidental Loads and Its Application to Thermal Response Analysis for Optimal Design of Offshore Thin-walled Structures. Fire Safety Journal, 92, 107–121. <https://doi.org/10.1016/j.firesaf.2017.05.022>
- Shetty, N.K., Soares, C.G., Thoft-Christensen, P., & Jensen, F.M. (1998). Fire Safety Assessment and Optimal Design of Passive Fire Protection for Offshore Structures. Reliability Engineering & System Safety, 61(1–2), 139–149. [https://doi.org/10.1016/S0951-8320\(97\)00124-5](https://doi.org/10.1016/S0951-8320(97)00124-5)
- Soares, C.G., Gordo, J.M., & Teixeira, A.P. (1998). Elasto-plastic Behaviour of Plates Subjected to Heat Loads. Journal of Constructional Steel Research, 45(2), 179–198. [https://doi.org/10.1016/S0143-974X\(97\)00062-X](https://doi.org/10.1016/S0143-974X(97)00062-X)
- Sun, L., Yan, H., Liu, S., & Bai, Y. (2017). Load Characteristics in Process Modules of Offshore Platforms Under Jet Fire: The Numerical Study. Journal of Loss Prevention in the Process Industries, 47, 29–40. <https://doi.org/10.1016/j.jlp.2017.02.018>
- Vinnem, J.E. (2007). Offshore Risk Assessment: Principles, Modelling and Applications of QRA Studies. London: Springer.

### Author ORCIDs

Author name	ORCID
Kim, Jeong Hwan	0000-0002-2578-2569
Baeg, Dae Yu	0000-0002-3354-3736
Seo, Jung Kwan	0000-0002-3721-2432

## Appendix

Table A1 Results and fire damage scenarios (Continued)

No	time (min)	Fire Position	Flame radius (mm)	Maxi. temp (°C)	$\sigma_{rsu}$ (MPa)	$\sigma_{rsu} / \sigma_{rsu,20}$	No.	time (min)	Fire Position	Flame radius (mm)	Maxi. temp (°C)	$\sigma_{rsu}$ (MPa)	$\sigma_{rsu} / \sigma_{rsu,20}$
1	10	A	200	459.38	144.9	1.03	41	30	A	200	720.16	135.1	0.96
2	10	A	400	486.55	137.1	0.98	42	30	A	400	760.11	105.2	0.75
3	10	A	600	485.05	121.7	0.87	43	30	A	600	760.96	80.8	0.58
4	10	A	800	485.22	95.6	0.68	44	30	A	800	760.86	66.8	0.48
5	10	A	1000	485.22	86.5	0.62	45	30	A	1000	760.89	52.4	0.37
6	10	B	200	369.79	138.0	0.98	46	30	B	200	548.59	134.3	0.96
7	10	B	400	476.61	128.4	0.91	47	30	B	400	744.00	108.0	0.77
8	10	B	600	484.55	108.2	0.77	48	30	B	600	757.24	85.0	0.61
9	10	B	800	485.06	95.9	0.68	49	30	B	800	760.68	75.5	0.54
10	10	B	1000	485.05	84.8	0.60	50	30	B	1000	760.83	58.2	0.41
11	10	C	200	387.56	138.7	0.99	51	30	C	200	587.49	129.5	0.92
12	10	C	400	487.24	132.6	0.94	52	30	C	400	746.77	108.3	0.77
13	10	C	600	484.97	116.9	0.83	53	30	C	600	759.67	83.3	0.59
14	10	C	800	485.10	107.4	0.76	54	30	C	800	760.80	62.3	0.44
15	10	C	1000	485.39	69.4	0.49	55	30	C	1000	760.95	35.5	0.25
16	10	D	200	299.40	135.0	0.96	56	30	D	200	439.63	126.3	0.90
17	10	D	400	467.20	122.9	0.87	57	30	D	400	735.39	111.3	0.79
18	10	D	600	483.04	113.3	0.81	58	30	D	600	754.28	94.8	0.68
19	10	D	800	484.78	102.6	0.73	59	30	D	800	759.51	68.5	0.49
20	10	D	1000	485.08	71.0	0.51	60	30	D	1000	760.76	33.4	0.24
21	20	A	200	634.36	139.1	0.99	61	40	A	200	755.88	131.08	0.93
22	20	A	400	688.69	114.9	0.82	62	40	A	400	867.76	97.89	0.70
23	20	A	600	689.22	87.8	0.63	63	40	A	600	871.27	77.09	0.55
24	20	A	800	688.97	75.5	0.54	64	40	A	800	871.31	60.93	0.43
25	20	A	1000	688.99	65.1	0.46	65	40	A	1000	871.32	44.07	0.31
26	20	B	200	486.41	136.2	0.97	66	40	B	200	588.59	132.27	0.94
27	20	B	400	670.82	117.8	0.84	67	40	B	400	821.00	100.44	0.71
28	20	B	600	687.31	92.2	0.66	68	40	B	600	863.91	82.44	0.59
29	20	B	800	688.87	81.1	0.58	69	40	B	800	870.37	73.02	0.52
30	20	B	1000	688.95	66.5	0.47	70	40	B	1000	871.17	52.07	0.37
31	20	C	200	517.64	134.9	0.96	71	40	C	200	633.34	125.33	0.89
32	20	C	400	674.49	117.6	0.84	72	40	C	400	830.91	102.10	0.73
33	20	C	600	688.11	94.2	0.67	73	40	C	600	867.07	75.63	0.54
34	20	C	800	688.98	76.4	0.54	74	40	C	800	870.81	53.49	0.38
35	20	C	1000	689.07	45.5	0.32	75	40	C	1000	871.36	30.65	0.22
36	20	D	200	388.19	130.0	0.93	76	40	D	200	475.52	124.24	0.88
37	20	D	400	651.16	115.5	0.82	77	40	D	400	783.16	108.61	0.77
38	20	D	600	683.34	101.8	0.72	78	40	D	600	850.99	88.73	0.63
39	20	D	800	687.96	80.3	0.57	79	40	D	800	866.58	60.39	0.43
40	20	D	1000	688.92	44.9	0.32	80	40	D	1000	870.77	29.03	0.21

**Table A1** Results and fire damage scenarios

No	time (min)	Fire Position	Flame radius (mm)	Maxi. temp (°C)	$\sigma_{rsu}$ (MPa)	$\sigma_{rsu} / \sigma_{rsu,20}$	No.	time (min)	Fire Position	Flame radius (mm)	Maxi. temp (°C)	$\sigma_{rsu}$ (MPa)	$\sigma_{rsu} / \sigma_{rsu,20}$
81	50	A	200	800.16	127.15	0.91	101	60	A	200	836.13	123.48	0.88
82	50	A	400	950.95	92.63	0.66	102	60	A	400	1001.57	88.82	0.63
83	50	A	600	957.78	74.26	0.53	103	60	A	600	1011.24	72.43	0.52
84	50	A	800	957.98	56.95	0.41	104	60	A	800	1011.56	54.40	0.39
85	50	A	1000	960.25	39.33	0.28	105	60	A	1000	1011.57	38.26	0.27
86	50	B	200	617.03	130.05	0.93	106	60	B	200	638.37	127.73	0.91
87	50	B	400	889.25	94.53	0.67	107	60	B	400	935.54	89.91	0.64
88	50	B	600	945.62	82.43	0.59	108	60	B	600	995.88	82.33	0.59
89	50	B	800	955.96	70.14	0.50	109	60	B	800	1008.50	67.27	0.48
90	50	B	1000	957.74	46.07	0.33	110	60	B	1000	1011.14	41.34	0.29
91	50	C	200	666.28	121.89	0.87	111	60	C	200	691.74	119.07	0.85
92	50	C	400	902.64	97.78	0.70	112	60	C	400	950.90	94.55	0.67
93	50	C	600	950.81	71.28	0.51	113	60	C	600	1002.42	68.87	0.49
94	50	C	800	956.97	48.43	0.34	114	60	C	800	1010.08	46.56	0.33
95	50	C	1000	958.02	28.14	0.20	115	60	C	1000	1011.57	28.33	0.20
96	50	D	200	502.84	122.65	0.87	116	60	D	200	524.69	121.25	0.86
97	50	D	400	840.74	106.23	0.76	117	60	D	400	883.43	104.13	0.74
98	50	D	600	927.35	84.16	0.60	118	60	D	600	975.60	79.97	0.57
99	50	D	800	949.82	54.27	0.39	119	60	D	800	1000.97	49.30	0.35
100	50	D	1000	956.74	27.81	0.20	120	60	D	1000	1009.59	26.96	0.19

# Effect of Internal Fluid Resonance on the Performance of a Floating OWC Device

Il Hyoung Cho<sup>1</sup>

<sup>1</sup>Professor, Department of Ocean System Engineering, Jeju National University, Jeju, Korea

**KEY WORDS:** Wave energy converter, Oscillating water column, Matched eigenfunction expansion method, Internal fluid resonance, Capture width

**ABSTRACT:** In the present study, the performance of a floating oscillating water column (OWC) device has been studied in regular waves. The OWC model has the shape of a hollow cylinder. The linear potential theory is assumed, and a matched eigenfunction expansion method (MEEM) is applied for solving the diffraction and radiation problems. The radiation problem involves the radiation of waves by the heaving motion of a floating OWC device and the oscillating pressure in the air chamber. The characteristics of the exciting forces, hydrodynamic forces, flow rate, air pressure in the chamber, and heave motion response are investigated with various system parameters, such as the inner radius, draft of an OWC, and turbine constant. The efficiency of a floating OWC device is estimated in connection with the extracted wave power and capture width. Specifically, the piston-mode resonance in an internal fluid region plays an important role in the performance of a floating OWC device, along with the heave motion resonance. The developed prediction tool will help determine the various design parameters affecting the performance of a floating OWC device in waves.

## 1. Introduction

The utilization of ocean energy has become an important and urgent issue owing to its abundance and value as clean energy. In particular, the development of new energy sources is inevitably necessary to respond to the carbon emission trading system. However, the commercialization of ocean energy, that has economic feasibility, has not yet been realized because of expensive installation and power transmission costs along with irregularity of the ocean environment. Several efforts have been being taken to resolve these inherent demerits; these efforts include combined power generation, where at least two power sources among wind, wave, and current power are used for a single support structure, direct consumption of generated power at the site, and storing the generated power into the battery without transmission to land.

The technologies related to wave power generation have been developed since the 1980s mainly in Europe and Japan, where wave energy sources are abundant. Several devices have been suggested for wave energy generation, which are near the commercialization stage. Existing wave energy converters (WECs) are categorized as attenuator, point-absorber, and terminator types, based on the position

of the WEC with respect to the direction of incident wave propagation. The attenuator type composes of multiple WECs connected parallel to the direction of incident wave propagation; thus electrical energy is generated from the relative motion of converters at the joints by the action of the waves. The Pelamis is a well-known attenuator WEC. The point-absorber type can generate electricity regardless of the direction of incident wave propagation. Particularly, it enhances energy extraction efficiency by amplifying the heave motion of the WEC through resonance with the incident wave with a low energy density. Power buoy and Wavebob are typical point-absorber WEC. Lastly, the terminator type has a WEC positioned in the direction perpendicular to the propagation direction of the incident wave to extract wave energy. Examples of this type include Salter's duck WEC and dual-functional WEC that has a function of a breakwater.

For converting wave energy into electrical energy, the wave energy is modified through two-step transformations. The first step transformation converts the wave energy into the mechanical energy such as the kinetic and potential energy. These transformation devices are called the movable body, oscillating water column (OWC), and overtopping type (Falcão, 2010). In particular, an OWC device is presently installed and operated in several regions, as the technology

Received 3 February 2021, revised 15 March 2021, accepted 14 April 2021

Corresponding author Il Hyoung Cho: +82-64-754-3482, cho0904@jejunu.ac.kr

© 2021, The Korean Society of Ocean Engineers

This is an open access article distributed under the terms of the creative commons attribution non-commercial license (<http://creativecommons.org/licenses/by-nc/4.0>) which permits unrestricted non-commercial use, distribution, and reproduction in any medium, provided the original work is properly cited.

has been stabilized. Moreover, the maintenance cost is also fairly low due to a small number of moving machinery parts. The OWC has an enclosed air chamber positioned on top of a supporting structure (fixed, floating) having an open bottom. The free-surface inside the air chamber oscillates up and down due to incident waves, thus inducing airflow due to pressure difference between inside and outside of the chamber; the airflow rotates a turbine located on a passage outside the air chamber; in the final stage, electricity is produced from the generator. The Wells turbine and impulse turbine are used as a second step transformation device that converts the flow energy of air into electrical energy, changing bidirectional airflow into unidirectional turbine's rotation. The OWC device was first proposed by Masuda (1979); since then, it has been extensively studied by numerous researchers through analytical, numerical, and experimental approaches. The OWC devices are installed in many regions throughout the world, and the Land Installed Marine Powered Energy Transformer (LIMPET) installed in Scotland in 2000 is known as the world's first wave power generation system that is operated through connection with an existing power grid (Heath et al., 2000). The Korea Research Institute of Ships and Ocean Engineering (KRISO) has recently constructed a real-sea pilot plant that houses fixed type OWC ( $31.2 \times 37.0$  m) at water depth 15 m near Chagwido Island, Jeju, and is currently conducting tests to evaluate its performance and efficiency.

To analyze the performance of the fixed and floating OWC device, Evans and Porter (1995, 1997) calculated the wave-energy absorption efficiency by solving the radiation problem due to oscillating pressure in the air chamber and the diffraction problem of a fixed OWC in waves. Mavrakos (1985, 1988) analyzed the diffraction and radiation problems of a hollow cylinder using a matched eigenfunction expansion method (MEEM). Sioris and Memos (1999) performed numerical analysis using the Green's function method and obtained results that were different from those of Mavrakos (1985, 1988). Cho (2002) used a MEEM to analyze the performance of a fixed cylindrical OWC device. Hong et al. (2004) and Suzuki et al. (2004) numerically analyzed the performance of a floating OWC device using a higher-order boundary element method. Mavrakos and Konispoliatis (2012) used a MEEM to theoretically calculate the extracted power and efficiency of a floating OWC device. Bull (2015) investigated the motion responses and oscillating pressure in the air chambers of a Backward Bent Duct Buoy (BBDB), which belongs to the floating OWC, and an axisymmetric OWC considering the resonance of the internal fluid of an air chamber; they further examined the coupling effect between a floating OWC device and air pressure using a commercially available code WAMIT. Gomes et al. (2012, 2016) carried out systematic researches on the energy extraction performance of an axisymmetric floating OWC device. They replaced the surface of the internal fluid with a thin disk having no weight under the assumption that the size of an air chamber is smaller compared to the wavelength of incident waves and evaluated the extraction power of an OWC device from the relative heave motion between the floating OWC and disk. Regular waves were extended to irregular waves, and

the optimization of design parameters was performed using an objective function. Park et al. (2018) evaluated the performance of an axisymmetric floating OWC device using a finite element method (FEM) under a linear potential theory. For considering the damping effects of power take-off, the nonlinear modified kinematic and dynamic free surface boundary conditions proposed by Koo et al. (2010) were linearized to be applied. Furthermore, Luo et al. (2014) applied computational fluid dynamics (CFD) codes for considering viscosity effects. They analyzed the coupling effect of the heave motion of a floating OWC device and oscillating air pressure using a commercially available code FLUENT, which is based on the Navier-Stokes equations.

In this study, the extracted wave power and absorption efficiency of a floating OWC device of a hollow cylinder shape has been extensively investigated in the frequency domain by extending the analytical tool developed by Bae and Cho (2013). Boundary value problems for the diffraction and radiation (heave motion of a floating OWC device, oscillating pressure in the air chamber) were formulated and analytically solved using a MEEM to obtain the hydrodynamic force as well as the flow rate of the internal fluid of the air chamber. Subsequently, the equation of the heave motion of a floating OWC coupled with oscillating pressure in the air chamber was formulated and solved; finally, the extracted wave power and capture width of the OWC device was calculated. Particularly, the piston-mode resonance of the internal fluid in the air chamber was intensively examined. Using the developed predictive tool, the effects of the shape (radius, draft, thickness, etc.) of a floating OWC device and turbine characteristics on the hydrodynamic loads, flow rate, oscillating air pressure, heave motion response, and extraction efficiency were clarified.

## 2. Mathematical Formulation

A floating OWC device consisting of a hollow cylindrical body

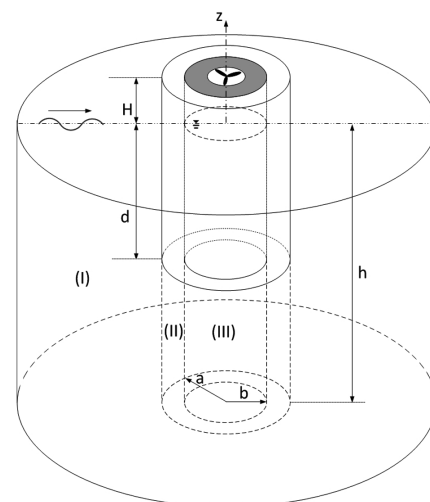


**Fig. 1** Schematic of a floating axisymmetric OWC wave energy converter

with an inner radius  $b$ , outer radius  $a$ , draft  $d$ , and an air chamber with a height  $H$  is selected as a calculation model as shown in Fig. 1. The cylindrical coordinate system is introduced, in which the origin is set on the free surface, and the direction of the  $z$ -axis is set vertically upward. Air pressure inside the air chamber is expressed as the sum of atmospheric pressure  $P_{atm}$  and oscillating pressure  $P_c(t)$  due to waves. The oscillating pressure is assumed to be constant inside the air chamber in space. When the incident wave exhibits a harmonic motion with a frequency  $\omega$ , the velocity potential can be written by  $\Phi(r, \theta, z, t) = \text{Re}\{\phi(r, \theta, z)e^{-i\omega t}\}$  under the assumption of a linear potential theory. The velocity potential  $\phi(r, \theta, z)$ , which is a complex function, can be expressed as the sum of the scattering potential ( $\phi_1$ ), i.e., the sum of incident potential ( $\phi_0$ ) and diffracted potential ( $\phi_D$ ), and the radiated potential ( $\phi_2$ ) due to the heave motion of a floating OWC, and the radiated potential ( $\phi_3$ ) due to oscillating air pressure in the chamber, as shown in Eq. (1). All motion modes are constrained, and only the heave motion is taken into consideration. Since the calculation model is axisymmetrical, the radiated potential is not associated with the  $\theta$ -axis, unlike the scattered potential that is a function of  $(r, \theta, z)$ .

$$\phi(r, \theta, z) = -\frac{ig}{\omega} A\phi_1(r, \theta, z) + u\phi_2(r, z) + p_c\phi_3(r, z), \quad (1)$$

where  $A$  is the amplitude of incident wave,  $u$  is the heave motion velocity ( $U(t) = \text{Re}\{ue^{-i\omega t}\}$ ) of a floating OWC, and  $p_c$  is the oscillating pressure ( $P_c(t) = \text{Re}\{p_c e^{-i\omega t}\}$ ) in the chamber. The velocity potential  $\phi_j$  ( $j=1,2,3$ ) in Eq. (1) satisfies the boundary value problem shown below (Eq. (2)).

$$\begin{cases} \frac{\partial^2 \phi_1}{\partial r^2} + \frac{1}{r} \frac{\partial \phi_1}{\partial r} + \frac{1}{r^2} \frac{\partial^2 \phi_1}{\partial \theta^2} + \frac{\partial^2 \phi_1}{\partial z^2} = 0, \\ \frac{\partial^2 \phi_j}{\partial r^2} + \frac{1}{r} \frac{\partial \phi_j}{\partial r} + \frac{\partial^2 \phi_j}{\partial z^2} = 0, \quad j=2,3 \\ \frac{\partial \phi_j}{\partial z} = 0 \quad z = -h, \quad j=1,2,3 \\ \frac{\partial \phi_j}{\partial z} - \frac{\omega^2}{g} \phi_j = \begin{cases} \frac{i\omega}{\rho g} & \text{for } j=3 \\ 0 & \text{for } j=1,2 \end{cases} \\ \frac{\partial \phi_j}{\partial n} = 0, \quad j=1,3, \quad \frac{\partial \phi_j}{\partial z} = n, \quad j=2, \quad \text{on the body} \\ (k_1 r)^{1/2} \left( \frac{\partial}{\partial r} - ik_1 \right) (\phi_1 - \phi_0) \rightarrow 0 \quad \text{as } r \rightarrow \infty, \\ (k_1 r)^{1/2} \left( \frac{\partial \phi_j}{\partial r} - ik_1 \phi_j \right) \rightarrow 0 \quad \text{as } r \rightarrow \infty, \quad j=2,3 \end{cases} \quad (2)$$

where,  $k_1$  is the wave number, and  $n$  is a unit normal vector.

The velocity potential is determined by solving the boundary value problem of the scattering ( $j=1$ ) and radiation ( $j=2,3$ ) given above. The hydrodynamic force  $F_j(t) = \text{Re}\{f_j e^{-i\omega t}\}$  in the vertical direction on a floating OWC and the flow rate ( $Q_j(t) = \text{Re}\{q_j e^{-i\omega t}\}$ ) due to surface oscillation of interior fluid are expressed as follows.

$$f = i\omega\rho \iint_{S_B} \phi n dS = Af_1 + uf_2 + p_c f_3 \quad (3)$$

$$q = \iint_{S_c} \frac{\partial \phi}{\partial z} dS = Aq_1 + uq_2 + p_c q_3$$

where,  $S_B$  is the bottom surface of a floating OWC, and  $S_c (= \pi b^2)$  is the free-surface area inside the air chamber. Substituting Eq. (1) in Eq. (3),  $f_1$ ,  $f_2$  and  $f_3$  can be obtained as follows.

$$\begin{aligned} f_1 &= \rho g \iint_{S_B} \phi_1 n dS \\ f_2 &= i\omega\rho \iint_{S_B} \phi_2 n dS \\ f_3 &= i\omega\rho \iint_{S_B} \phi_3 n dS \end{aligned} \quad (4)$$

where,  $f_1$  is the wave exciting force, while  $f_2$  and  $f_3$  are the hydrodynamic vertical forces on an OWC device by heaving motion of a floating OWC and oscillating pressure in the air chamber, respectively.

If Eq. (1) is substituted in Eq. (3) in the same manner, the flow rate inside the air chamber can be calculated as follows.

$$\begin{aligned} q_1 &= -\frac{ig}{\omega} \iint_{S_c} \frac{\partial \phi_1}{\partial z} dS \\ q_2 &= \iint_{S_c} \left( \frac{\partial \phi_2}{\partial z} - 1 \right) dS \\ q_3 &= \iint_{S_c} \frac{\partial \phi_3}{\partial z} dS \end{aligned} \quad (5)$$

where  $q_1$  is the flow rate inside the air chamber due to an incident wave with a unit amplitude, while  $q_2$  and  $q_3$  are the flow rates due to the relative heave motion of a floating OWC and oscillating pressure with a unit pressure inside the chamber, respectively. The flow rate in Eq. (5) causes oscillating pressure inside the air chamber; thus, the turbine operates with the pressure difference from outside.

## 2.1 Diffraction Problem

For applying a MEEM, the whole fluid region is divided into regions (I), (II), and (III) as shown in Fig. 1. Region (I) is defined as  $r \geq a, -h \leq z \leq 0$ ; region (II) is defined as  $b \leq r \leq a, -h \leq z \leq -d$ , and region (III) is defined as  $0 \leq r \leq b, -h \leq z \leq 0$ . If the method of separation of variables is applied to the scattered potential ( $\phi_1$ ) using the eigenfunction ( $\cos l\theta$ ) in the  $\theta$ -axis direction, the following equation is obtained.

$$\phi_1(r, \theta, z) = \sum_{l=0}^{\infty} \phi_{1l}(r, z) \cos l\theta \quad (6)$$

The scattered potential  $\phi_{1l}^{(1)}$  that satisfies the boundary conditions belonging to region (I) in Eq. (2) is written as follows.

$$\phi_{1l}^{(1)}(r, z) = \beta_l J_l(k_1 r) \frac{f_0(z)}{f_0(0)} + \sum_{n=0}^{\infty} A_{1ln} \frac{K_l(k_{1n} r)}{K_l(k_{1n} a)} f_n(z) \quad (7)$$

When  $l=0$  in Eq. (7),  $\beta_l=1$ , and when  $l \geq 1$ ,  $\beta_l=2(i)^l$ .  $n=0$  represents the component of propagating waves, while  $n \geq 1$  means the component of evanescent waves that are only present around objects.  $J_l$  and  $K_l$  are the Bessel function of the first kind and the modified Bessel function of the second kind, respectively.

Eigenvalues ( $k_{10} = -ik_1$ ,  $k_{1n}, n=1,2,\dots$ ) satisfy the linear dispersion relation ( $k_{1n} \tan k_{1n} h = -\omega^2/g$ ) where the eigenfunction  $f_n(z)$  is given by

$$f_n(z) = N_n^{-1} \cos k_{1n}(z+h), \quad n=0,1,2,\dots \quad (8)$$

$$(N_n)^2 = \frac{1}{2} \left( 1 + \frac{\sin 2k_{1n} h}{2k_{1n} h} \right)$$

Eigenfunction  $f_n(z)$  defined in Eq. (8) satisfies the orthogonality.

$$\frac{1}{h} \int_{-h}^0 f_m(z) f_n(z) dz = \delta_{mn} \quad (9)$$

where,  $\delta_{mn}$  is the Kronecker-Delta function having a value of 1 when  $n=m$  and a value 0 when  $n \neq m$ .

The scattered potential satisfying the boundary conditions of region (II) is given by

$$\phi_{1l}^{(2)}(r, z) = \sum_{n=0}^{\infty} \varepsilon_n [R_{ln}(r) B_{1ln} + \tilde{R}_{ln}(r) \tilde{B}_{1ln}] \cos \lambda_n(z+h) \quad (10)$$

where,  $\varepsilon_n$  is the Neumann symbol having a value of 1 when  $n=0$  and a value 2 when  $n \geq 1$ . The eigenvalue in region (II) is  $\lambda_n = n\pi/(h-d)$ , ( $n=0,1,2,\dots$ ), and  $R_{ln}(r), \tilde{R}_{ln}(r)$  has the following form.

$$R_{ln}(r) = \frac{K_l(\lambda_n b) I_l(\lambda_n r) - K_l(\lambda_n r) I_l(\lambda_n b)}{K_l(\lambda_n b) I_l(\lambda_n a) - K_l(\lambda_n a) I_l(\lambda_n b)} \quad (11)$$

$$\tilde{R}_{ln}(r) = \frac{K_l(\lambda_n r) I_l(\lambda_n a) - K_l(\lambda_n a) I_l(\lambda_n r)}{K_l(\lambda_n b) I_l(\lambda_n a) - K_l(\lambda_n a) I_l(\lambda_n b)}$$

where,  $I_l$  is the modified Bessel function of the first kind.

The scattered potential in region (III) is given by

$$\phi_{1l}^{(3)}(r, z) = \sum_{n=0}^{\infty} C_{1ln} \frac{I_l(k_{1n} r)}{I_l(k_{1n} b)} f_n(z) \quad (12)$$

Unknowns  $A_{1ln}, B_{1ln}, \tilde{B}_{1ln}, C_{1ln}$  in Eqs. (7), (10), and (12) are calculated by imposing the continuity of the velocity potential and radial velocity at the interface ( $r=a, b$ ). The following equation (Eq.

(13)) can be obtained by applying the continuity of the velocity potential at  $r=a$ . In the process of derivation, the orthogonality of eigenfunction ( $\cos \lambda_n(z+h)$ ,  $n=0,1,\dots$ ) in region (II) is applied.

$$B_{1lm} = \frac{\beta_l J_l(k_1 a)}{f_0(0)} G_{m0} + \sum_{n=0}^{\infty} G_{mn} A_{1ln}, \quad m=0,1,2,\dots \quad (13)$$

$$\text{where } G_{mn} = \frac{1}{(h-d)} \int_{-h}^{-d} f_n(z) \cos \lambda_m(z+h) dz$$

In similar way, the following equation can be derived from the matching condition where the velocity potentials of regions (II) and (III) at  $r=b$  are the same.

$$\tilde{B}_{1lm} = \sum_{n=0}^{\infty} G_{mn} C_{1ln}, \quad m=0,1,2,\dots \quad (14)$$

The matching condition that  $\partial \phi_{1l}^{(1)}(r, z)/\partial r = \partial \phi_{1l}^{(2)}(r, z)/\partial r$  at  $r=a$  yields

$$\beta_l k_1 J_l'(k_1 a) \frac{f_0(z)}{f_0(0)} + \sum_{n=0}^{\infty} A_{1ln} q_{ln} \frac{f_n(z)}{h} \quad (15)$$

$$= \begin{cases} 0, & -d \leq z \leq 0 \\ \sum_{n=0}^{\infty} \varepsilon_n [W_{ln}(a) B_{1ln} + \tilde{W}_{ln}(a) \tilde{B}_{1ln}] \frac{\cos \lambda_n(z+h)}{(h-d)}, & -h \leq z \leq -d \end{cases}$$

where

$$W_{ln}(r) = \lambda_n (h-d) \frac{dR_{ln}(r)}{dr}$$

$$\tilde{W}_{ln}(r) = \lambda_n (h-d) \frac{d\tilde{R}_{ln}(r)}{dr}$$

$$q_{ln} = \frac{k_{1n} h K_l'(k_{1n} a)}{K_l(k_{1n} a)}$$

The following equation can be obtained by multiplying both sides of Eq. (15) with  $f_m(z)$ , ( $m=0,1,2,\dots$ ), integrating  $z$  from  $-h$  to 0 and applying the orthogonality of eigenfunction  $f_n(z)$  given in Eq. (9).

$$q_{lm} A_{1lm} = - \frac{\beta_l k_1 h J_l'(k_1 a)}{f_0(0)} \delta_{m0} \quad (16)$$

$$+ \sum_{n=0}^{\infty} \varepsilon_n G_{nm} [W_{ln}(a) B_{1ln} + \tilde{W}_{ln}(a) \tilde{B}_{1ln}], \quad m=0,1,2,\dots$$

Similarly, the following equation can be obtained from the matching condition where the radial velocities at  $r=b$  are the same.

$$p_{lm} C_{1lm} = \sum_{n=0}^{\infty} \varepsilon_n G_{nm} [W_{ln}(b) B_{1ln} + \tilde{W}_{ln}(b) \tilde{B}_{1ln}] \quad (17)$$

$$\text{where } p_{lm} = \frac{k_{1m} h I_l'(k_{1m} b)}{I_l(k_{1m} b)}$$

By eliminating  $A_{1ln}$ ,  $C_{1ln}$  from Eqs. (13), (14), (16), and (17), the algebraic equations of unknowns  $B_{1ln}$ ,  $\tilde{B}_{1ln}$  can be obtained. The number of eigenfunctions in the  $(z, \theta)$  direction is set to be finite  $(N, L)$ .

$$B_{1lm} + \sum_{k=0}^N F_{lmk}^{(11)} B_{1lk} + \sum_{k=0}^N F_{lmk}^{(12)} \tilde{B}_{1lk} = X_{1lm}^{(1)} \quad (18)$$

$$\sum_{k=0}^N F_{lmk}^{(21)} B_{1lk} + \tilde{B}_{1lm} + \sum_{k=0}^N F_{lmk}^{(22)} \tilde{B}_{1lk} = 0, \quad l=0,1,2,\dots,L$$

where,

$$F_{lmk}^{(11)} = -\varepsilon_k W_{lk}(a) \sum_{n=0}^N \frac{G_{kn} G_{mn}}{q_n}$$

$$F_{lmk}^{(12)} = -\varepsilon_k \tilde{W}_{lk}(a) \sum_{n=0}^N \frac{G_{kn} G_{mn}}{q_n}$$

$$F_{lmk}^{(21)} = -\varepsilon_k W_{lk}(b) \sum_{n=0}^N \frac{G_{kn} G_{mn}}{p_n}$$

$$F_{lmk}^{(22)} = -\varepsilon_k \tilde{W}_{lk}(b) \sum_{n=0}^N \frac{G_{kn} G_{mn}}{p_n}$$

$$X_{1lm}^{(1)} = \frac{\beta_l G_{m0}}{f_0(0)} \left( J_l(k_1 a) - \frac{k_1 h J_l'(k_1 a)}{q_0} \right)$$

Unknowns  $B_{1ln}$ ,  $\tilde{B}_{1ln}$ ,  $(n=0,1,2,\dots,N, l=0,1,2,\dots,L)$  are determined by solving the algebraic equations given in Eq. (18), and the remaining unknowns  $A_{1ln}$ ,  $C_{1ln}$  are determined by substituting them in Eqs. (16) and (17).

The wave exciting force ( $f_1$ ) in Eq. (4) can be calculating by integrating the scattered potential with respect to the bottom surface of a floating OWC.

$$f_1 = \rho g \iint_{S_b} \phi_1 n dS = 2\pi \rho g \int_b^a \phi_{10}^{(2)}(r, -d) r dr \quad (19)$$

The flow rate inside the air chamber due to incident wave defined in Eq. (5) is as follows.

$$q_1 = -\frac{ig}{\omega} \iint_{S_a} \frac{\partial \phi_1}{\partial z} dS = \left( -\frac{ig}{\omega} \right) 2\pi \int_0^b \frac{\partial \phi_{10}^{(3)}}{\partial z}(r, 0) r dr \quad (20)$$

## 2.2 Radiation Problem

For solving the radiation problems ( $j=2,3$ ) due to the heaving motion of a floating OWC and oscillating pressure in the air chamber, the fluid region is divided into regions (I), (II), and (III), and the radiated potential in each region is expressed by the series of eigenfunctions, as shown below.

$$\phi_j^{(1)} = \sum_{n=0}^{\infty} A_{jn} \frac{K_0(k_{1n} r)}{K_0(k_{1n} a)} f_n(z) \quad (21)$$

$$\phi_j^{(2)} = \psi_j(r, z) \delta_{j2} + \sum_{n=0}^{\infty} \varepsilon_n [R_{0n}(r) B_{jn} + \tilde{R}_{0n}(r) \tilde{B}_{jn}] \cos \lambda_n(z+h)$$

$$\phi_j^{(3)} = \psi_j(r, z) \delta_{j3} + \sum_{n=0}^{\infty} C_{jn} \frac{I_0(k_{1n} r)}{I_0(k_{1n} b)} f_n(z)$$

The particular solutions  $\psi_j(r, z)$ ,  $j=2,3$  satisfying the body boundary condition  $\partial \phi_j^{(2)}(r, -d) / \partial z = 1$  of a floating OWC and the free-surface boundary condition inside the air chamber are given by

$$\psi_2(r, z) = \frac{1}{2(h-d)} \left( (z+h)^2 - \frac{r^2}{2} \right) \quad (22)$$

$$\psi_3(r, z) = -\frac{i}{\rho \omega}$$

Similar to the diffraction problem in section (2.1), the algebraic equations of unknowns  $B_{jm}$ ,  $\tilde{B}_{jm}$ ,  $j=2,3$  can be derived from the matching condition where velocity potential and radial velocity are the same at  $r=a, b$ .

$$B_{jm} + \sum_{k=0}^N F_{0mk}^{(11)} B_{jk} + \sum_{k=0}^N F_{0mk}^{(12)} \tilde{B}_{jk} = X_{jm}^{(1)} \quad (23)$$

$$\sum_{k=0}^N F_{0mk}^{(21)} B_{jk} + \tilde{B}_{jm} + \sum_{k=0}^N F_{0mk}^{(22)} \tilde{B}_{jk} = X_{jm}^{(2)}$$

where

$$X_{2m}^{(1)} = -\frac{1}{(h-d)} \int_{-h}^{-d} \psi_2(a, z) \cos \lambda_m(z+h) dz + \sum_{n=0}^N \frac{G_{nm}}{q_{0n}} \int_{-h}^{-d} \frac{\partial \psi_2(a, z)}{\partial r} f_n(z) dz$$

$$X_{2m}^{(2)} = -\frac{1}{(h-d)} \int_{-h}^{-d} \psi_2(b, z) \cos \lambda_m(z+h) dz + \sum_{n=0}^N \frac{G_{nm}}{p_{0n}} \int_{-h}^{-d} \frac{\partial \psi_2(b, z)}{\partial r} f_n(z) dz$$

$$X_{3m}^{(1)} = 0, \quad X_{3m}^{(2)} = -\frac{i\omega}{\rho g K(h-d)} \int_{-h}^{-d} \cos \lambda_m(z+h) dz$$

Using  $B_{jm}$ ,  $\tilde{B}_{jm}$ ,  $j=2,3$  determined by solving the algebraic equation (23), unknowns  $A_{jm}$ ,  $C_{jm}$ ,  $j=2,3$  can be calculated as follows.

$$A_{2m} = \frac{1}{q_{0m}} \left\{ \int_{-h}^0 \frac{\partial \psi_2(a, z)}{\partial r} f_m(z) dz + \sum_{n=0}^{\infty} \varepsilon_n G_{nm} [W_{0n}(a) B_{2n} + \tilde{W}_{0n}(a) \tilde{B}_{2n}] \right\}$$

$$A_{3m} = \sum_{n=0}^{\infty} \varepsilon_n [W_{0n}(a) B_{3n} + \tilde{W}_{0n}(a) \tilde{B}_{3n}] \frac{G_{nm}}{q_{0m}} \quad (24)$$

$$C_{2m} = \frac{1}{p_{0m}} \left\{ \int_{-h}^0 \frac{\partial \psi_2(b, z)}{\partial r} f_m(z) dz + \sum_{n=0}^{\infty} \varepsilon_n G_{nm} [W_{0n}(b) B_{2n} + \tilde{W}_{0n}(b) \tilde{B}_{2n}] \right\}$$

$$C_{3m} = \sum_{n=0}^{\infty} \varepsilon_n [W_{0n}(b) B_{3n} + \tilde{W}_{0n}(b) \tilde{B}_{3n}] \frac{G_{nm}}{p_{0m}} \quad (25)$$

The hydrodynamic forces acting on a floating OWC due to the heaving motion and oscillating pressure inside the air chamber are expressed as follows.

$$f_2 = i\omega\rho \iint_{S_B} \phi_2 n dS = 2i\omega\rho\pi \int_b^a \phi_2^{(2)}(r, -d) r dr = i\omega a_{33} - b_{33} \quad (26)$$

$$f_3 = i\omega\rho \iint_{S_B} \phi_3 n dS = 2i\omega\rho\pi \int_b^a \phi_3^{(2)}(r, -d) r dr = -(R + i\omega I)$$

where  $a_{33}$ ,  $b_{33}$  are called the added mass and radiation damping coefficient.

The flow rate of internal fluid in the chamber due to the relative heaving motion of a floating OWC and oscillating pressure inside the chamber is expressed as follows.

$$q_2 = 2\pi \int_0^b \left[ \frac{\partial \phi_2^{(3)}(r, 0)}{\partial z} - 1 \right] r dr = (R + i\omega I - S_o) \quad (27)$$

$$q_3 = 2\pi \int_0^b \frac{\partial \phi_3^{(3)}(r, 0)}{\partial z} r dr = -(B - iC)$$

where  $B$  is radiation conductance, and  $C$  is radiation admittance.

### 2.3 Oscillating Air Pressure in the Chamber

To determine the oscillating pressure in the air chamber, a continuity equation is used, for which the rate of change of mass inside the air chamber is equal to the mass flow rate exiting a turbine. It is assumed that the air in the chamber is a compressible fluid, and the compression and expansion follows an adiabatic process.

$$\rho_a \frac{dV}{dt} + \frac{\rho_a V_o}{\gamma P_{atm}} \frac{dP_c}{dt} = -\rho_a Q_t \quad (28)$$

where  $\rho_a$  is the density of air,  $\gamma (= 1.4)$  is the specific heat for adiabatic situation,  $P_{atm}$  is atmospheric pressure, and  $V_o (= \pi b^2 H)$  is the volume of the air chamber. The flow rate  $Q_t (= C_t P_c)$  exiting a turbine is assumed to be linearly proportional to the oscillating pressure in the air chamber.  $C_t (= \hat{K}D/\hat{N}\rho_a)$  is the function of the damping coefficient ( $\hat{K}$ ) that is dependent on the shape of a turbine, turbine diameter ( $D$ ), and rotational velocity ( $\hat{N}$ ) of a turbine.

The rate of change ( $\frac{dV}{dt}$ ) of the volume of the air chamber in Eq. (28) is equal to the flow rate of the internal fluid inside the air chamber, which is determined previously. The oscillating pressure and flow rate inside the air chamber are assumed to be in a harmonic motion.

$$\frac{dV}{dt} = -\text{Re} \{ (Aq_1 + uq_2 + p_c q_3) e^{-i\omega t} \} \quad (29)$$

The following equation can be derived by substituting Eq. (29) in Eq. (28).

$$\left\{ C_t + B - i \left( \frac{\omega V_o}{\gamma P_{atm}} + C \right) \right\} p_c - \{ R + i\omega I - S_o \} u = Aq_1 \quad (30)$$

The equation of motion for the heave motion of a floating OWC is as follows.

$$-i\omega m u = f + f_v + f_c + f_s \quad (31)$$

where  $m (= \rho\pi(a^2 - b^2)d)$  is the mass of a floating OWC device.

In Eq. (31),  $f_c (= S_o p_c)$  is the force acting on the ceiling of the air chamber by oscillating air pressure, while  $f_s (= -i\rho g S_1 \frac{u}{\omega})$  is the vertical hydrostatic force of a floating OWC, where  $S_1 (= \pi(a^2 - b^2))$  is the waterplane area of a floating OWC device.

$f_v$  is the damping force due to viscosity; the viscous drag used in the present study is given by the following equation.

$$f_v = -\frac{1}{2} \rho S_1 C_d |u_r| u_r \quad (32)$$

In Eq. (32),  $C_d$  and  $u_r (= u - Av_z)$  are the drag coefficient and the relative heave velocity of a floating OWC device with respect to an incident wave, respectively.  $v_z$  is the vertical water particle velocity of an incident wave having a unit amplitude. The vertical particle velocity at the bottom surface of a floating OWC, where viscous drag acts predominantly, is used.

$$v_z = -\frac{igk_1}{\omega} \frac{\sinh k_1(h-d)}{\cosh k_1 h} \quad (33)$$

Due to the nonlinear viscous drag, which is proportional to the square of velocity in Eq. (32), the higher harmonic components ( $\omega, 2\omega, 3\omega, \dots$ ) are generated for input frequency  $\omega$ . Therefore, the velocity potential is expressed as a Fourier series represented in multiples of  $\omega$ ; only the first term is taken while the other terms are assumed to be small enough to be disregarded. The Fourier coefficient of the first term is  $8/3\pi$ . Eq. (32) can be rewritten as follows through an equivalent linearization.

$$f_v = -b_v u_r \quad (34)$$

where,  $b_v = \frac{4}{3\pi} \rho S_1 C_d |u_r|$

If  $f_v, f_c, f_s$  and hydrodynamic forces  $f = Af_1 + uf_2 + p_c f_3$  are substituted in Eq. (31), the equation for the heave motion of a floating OWC device in the frequency domain is as follows:

$$\left\{ -i\omega(m + a_{33}) + (b_{33} + b_v) + \frac{i\rho g S_1}{\omega} \right\} u + \{ R + i\omega I - S_o \} p_c = A(f_1 + b_v v_z) \quad (35)$$

The coupled Eqs. (30) and (35) can be expressed as a matrix form as

shown below.

$$\begin{bmatrix} \alpha_{11} & \alpha_{12} \\ -\alpha_{21} & \alpha_{22} + C_t \end{bmatrix} \begin{bmatrix} u \\ p_c \end{bmatrix} = A \begin{bmatrix} f_1 + b_v v_z \\ q_1 \end{bmatrix} \quad (36)$$

$$\begin{aligned} \text{where, } \alpha_{11} &= -i\omega(m + a_{33}) + (b_{33} + b_v) + i\frac{\rho g S_1}{\omega} \\ \alpha_{12} &= R + i\omega I - S_o \\ \alpha_{21} &= \alpha_{12}^* \\ \alpha_{22} &= B - i\left(\frac{\omega V_o}{\gamma P_{atm}} + C\right) \end{aligned}$$

The nonlinear equation (36) is solved with an iteration method to determine the heave motion velocity ( $u$ ) and oscillating air pressure ( $p_c$ ).

#### 2.4 Extraction Power

The time-averaged extracted power per unit width of a regular wave with an amplitude  $A$  is as follows.

$$\bar{P}_w = \frac{1}{2} \rho g A^2 C_g \quad (37)$$

where  $C_g$  is the group velocity.

The time-averaged power absorbed by an OWC device is the product of the oscillating pressure at a turbine and flow rate passing through a turbine. It is expressed as follows.

$$\bar{P} = \frac{1}{2} C_t |p_c|^2 \quad (38)$$

The oscillating pressure ( $p_c$ ) determined by solving the coupled equation (36) is substituted into Eq. (38) to obtain the time-averaged extracted power.

As a measure for evaluating the performance of an OWC device, the capture width representing the WEC's efficiency is used generally. The capture width has a length dimension and is expressed as the ratio of the time-averaged extracted power by an OWC device to the time-averaged power per unit width of the incident wave.

$$l_w = \frac{\bar{P}}{\bar{P}_w} = \frac{C_t}{\rho g C_g} \left| \frac{p_c}{A} \right|^2 \quad (39)$$

To determine the optimal turbine coefficient ( $C_t$ )<sub>opt</sub>, which gives the maximum time-averaged extraction power of Eq. (38), the equation  $d\bar{P}/dC_t = 0$  is used. The optimal turbine constant ( $C_t$ )<sub>opt</sub> calculated thereby is as follows.

$$(C_t)_{opt} = \left| \alpha_{22} + \alpha_{12} \alpha_{11}^{-1} \alpha_{21} \right| \quad (40)$$

If the coupling effect between the heave motion velocity ( $u$ ) of a floating OWC device and oscillating pressure ( $p_c$ ) in the air chamber is

ignored in Eq. (36), the heave motion velocity and oscillating pressure in the chamber are as follows.

$$u = \frac{A(f_1 + b_v v_z)}{-i\omega(m + a_{33}) + (b_{33} + b_v) + \frac{i\rho g S_1}{\omega}}, \quad p_c = \frac{Aq_1}{(C_t + B) - i\left(\frac{\omega V_o}{\gamma P_{atm}} + C\right)} \quad (41)$$

In that case, the optimal turbine constant ( $C_t$ )<sub>opt</sub> is as follows.

$$(C_t)_{opt} = \sqrt{B^2 + \left(\frac{\omega V_o}{\gamma P_{atm}} + C\right)^2} \quad (42)$$

### 3. Results and Discussions

For verifying the validity of the present solutions obtained using a MEEM, the calculation results are compared with those of Chau and

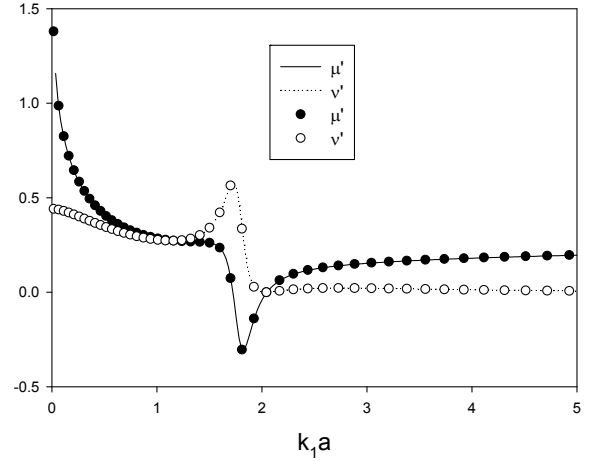


**Fig. 2** Comparison of non-dimensional added mass and radiation damping coefficients with Chau and Yeung's results (●, ○) ( $h/a = 1.0$ ,  $d/a = 0.25$ ,  $b/a = 0.5$ )

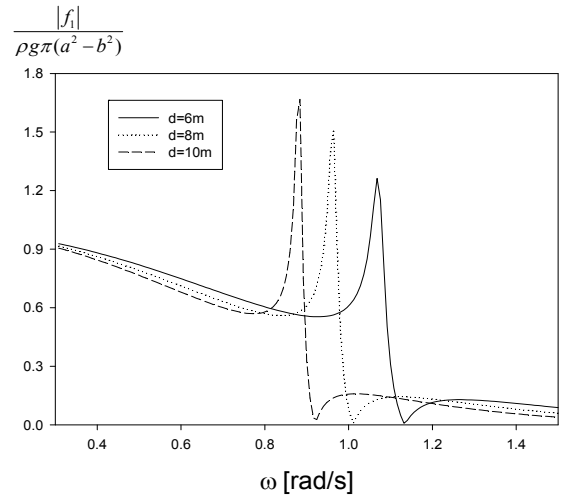


**Fig. 3** Non-dimensional wave exciting forces as a function of draft  $d$  with  $a = 6$  m,  $b = 4$  m,  $h = 30$  m

Yeung (2010) as shown in Fig. 2. A hollow cylindrical OWC device has the dimensions of  $h/a = 1.0$ ,  $d/a = 0.25$ ,  $b/a = 0.5$ . The solid line represents the present solutions using a MEEM, while the circle line represents the results obtained by Chau and Yeung (2010). The non-dimensional added mass ( $\mu' = a_{33}/\rho\pi a^3$ ) and radiation damping coefficient ( $\nu' = b_{33}/\rho\pi\omega a^3$ ) of a floating OWC device agree well with each other. Here, the number of eigenfunctions ( $N, L$ ) in  $z$  and  $\theta$  directions is 50 and 10, respectively. The same number of eigenfunctions is used in subsequent calculations.

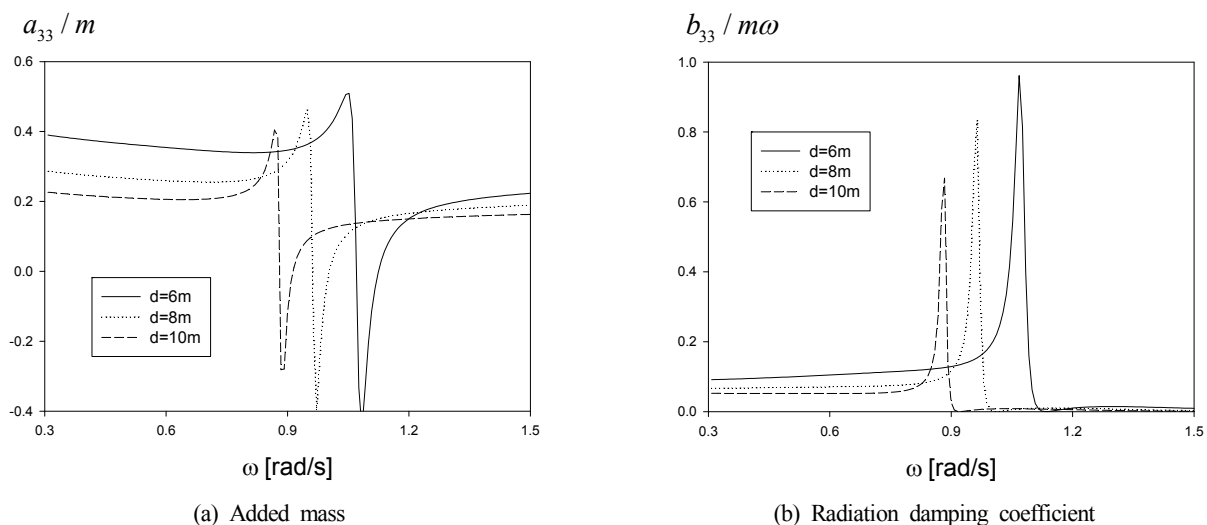
Fig. 3 shows the non-dimensional wave exciting forces with respect to the changes in the draft ( $d = 6, 8, \text{ and } 10 \text{ m}$ ). Here, the  $x$ -axis represents the frequency ( $\omega$ ) of the incident wave. The outer radius ( $a$ ) and inner radius ( $b$ ) of a floating OWC are 6 m and 4 m, respectively, and the water depth is 30 m. The drag coefficient ( $C_d$ ) due to viscosity is 0.7. A peak value is observed at a specific frequency within the calculation region, and the peak frequency moves towards the low-frequency region as the OWC's draft becomes deeper. The presence of these peak values can be explained based on the resonance. Two different types of natural frequency are present in a hollow cylindrical OWC. The first type is the natural frequency of a floating body's heave motion. The natural frequency of heave motion varies according to the draft ( $d$ ) of a floating OWC, where the natural frequency  $\omega_1 (= \sqrt{g/(d+a_{33}/m)})$  corresponding to three different drafts of 6, 8, and 10 m is 1.19 rad/s, 1.05 rad/s, and 0.95 rad/s, respectively. Specifically, the natural frequency of heave motion decreases as the draft increases. Another type is a piston-mode natural frequency that exists within the enclosed fluid region inside an air chamber. The surface motion at the piston mode oscillates vertically in unison without changes in the form. Fukuda (1977) proposed a simplified equation  $\omega_2 = \sqrt{g/(d+0.41\sqrt{S_o})}$  for natural frequency at the piston mode. When the simplified equation of Fukuda (1977) is applied to the present calculation model, the natural frequency of the piston mode is 1.05 rad/s, 0.95 rad/s, and 0.87 rad/s, corresponding to

drafts. Thus, the resonance frequency, where peak values are observed in Fig. 3, is closely related to the piston mode resonance.

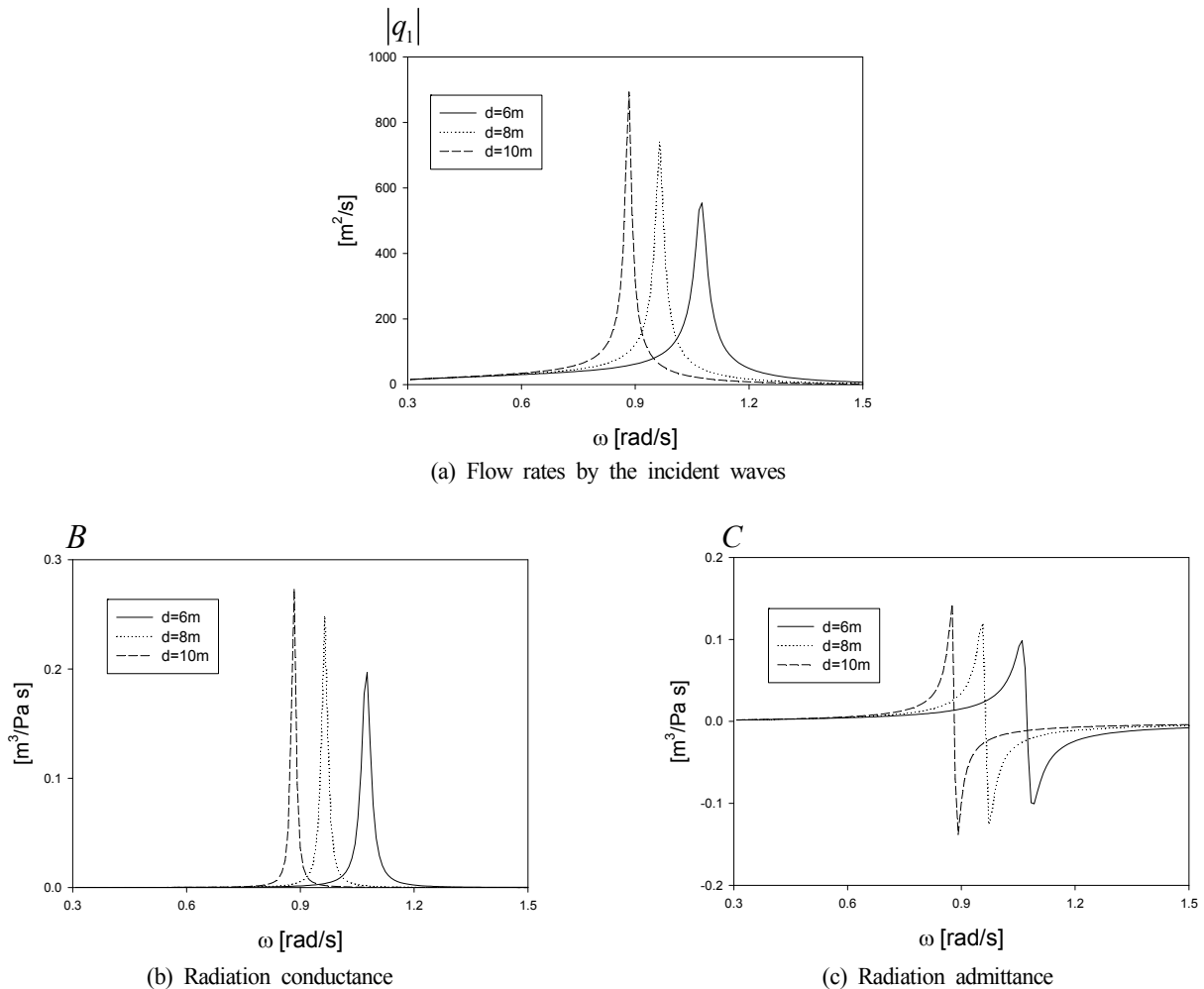
Fig. 4 shows the non-dimensional added mass ( $a_{33}/m$ ) and radiation damping coefficient ( $b_{33}/m\omega$ ) due to the heaving motion of a floating OWC under the same calculation conditions as those used for Fig. 3. The radiation damping coefficient has a peak value when the added mass changes significantly, from a positive to a negative value, at the resonance frequency at the piston mode. This unique phenomenon occurs when a fluid region inducing resonance is present inside an object in motion. This phenomenon is observed in the present model since the fluid region inducing resonance exists within the hollow OWC in heave motion. The added mass and radiation damping coefficient having unique characteristics influence the motion response of a floating OWC device. Only the resonance at the piston mode is displayed since the internal fluid region is smaller than the wavelength of incident wave; however, not only piston mode, but also sloshing mode resonance needs to be considered if the internal fluid region is not smaller than the wavelength of incident wave (Molin, 2001).

Fig. 5 shows the flow rate inside the air chamber due to the incident wave and oscillating pressure in the chamber. First, the flow rate ( $q_1$ ) due to an incident wave when an OWC is fixed has a peak value at the natural frequency of piston mode, similar to a wave exciting force. Meanwhile, the flow rate ( $q_3$ ) by oscillating pressure in the air chamber has real part ( $B$ ) and imaginary ( $C$ ) parts. The curve shapes are similar to those of the added mass and radiation damping coefficient shown in Fig. 4. As the draft decreases, the peak values of  $B$  and  $C$  also decrease, while the resonance width increases.

Fig. 6 shows the optimal turbine constant that results in maximum power as a function of frequency using Eq. (40). The optimal turbine constant has peak values at specific frequencies. Notably, the peak values of a turbine constant occur at the natural frequency of heave motion. Fig. 6(b) shows the response amplitude operator (RAO) of heave motion of a floating OWC when the optimal turbine constant is



**Fig. 4** Non-dimensional hydrodynamic coefficients (a) added mass (b) radiation damping coefficient as a function of draft  $d$  with  $a = 6 \text{ m}$ ,  $b = 4 \text{ m}$ ,  $h = 30 \text{ m}$



**Fig. 5** Induced flow rates due to the incident waves (a) and oscillating pressure (b), (c) as a function of draft  $d$  with  $a = 6$  m,  $b = 4$  m,  $h = 30$  m

applied. The RAO curve of heave motion has two peaks, at the natural frequency of heave motion and at the piston mode natural frequency of the internal fluid. A relatively larger heave motion occurs at the natural frequency of the internal fluid. Fig. 6(c) shows the oscillating pressure inside the air chamber with respect to the frequency of an incident wave when the optimal turbine constant is applied. As predicted, the oscillating pressure has a peak value at the internal fluid resonance frequency, and no significant variation is observed at the natural frequency of heave motion. The extracted power shown in Fig. 6(d) is determined by the turbine constant and the oscillating pressure in the air chamber, as shown in Eq. (38). The frequencies that produce the maximum values of oscillating pressure and turbine constant are different; therefore, two peak values are also observed in the extracted power curve, similar to the heave RAO curve. Fig. 6(e) shows the capture width, determined by dividing the extracted power by the power of incident wave per unit width. As expected, two peaks are present, where the peak value is relatively larger at the internal fluid resonance frequency, similar to the heave RAO and extracted power curves. Moreover, with the increase in the draft of a floating OWC, the peak value at the internal fluid resonance frequency increases while

the resonance width decreases; this is because the energy inside the internal fluid region cannot be escaped to the outside. Therefore, the draft of a floating OWC should be designed appropriately for maximizing energy absorption by identifying the wave characteristics of the installation site in advance.

Fig. 7 shows the heave RAO and capture width of a floating OWC with respect to the inner radius ( $b$ ) of 3 m, 4 m, and 5 m, which is another important design parameter. The draft ( $d$ ) and outer radius ( $a$ ) of a floating OWC are fixed at 8 m and 6 m, respectively. The drag coefficient of a floating OWC is 0.7, and the optimal turbine coefficient is used. The heave natural frequency of a floating OWC within the calculated frequency region is 1.03 rad/s, 1.05 rad/s, and 1.07 rad/s as the inner radius increases; meanwhile, the resonance frequency of internal fluid in the piston mode is 0.98 rad/s, 0.95 rad/s, and 0.92 rad/s, thus being unaffected greatly by the inner radius of a floating OWC. However, the peak value of heave motion amplitude at the internal fluid resonance increases as the inner radius increases. In the maximum capture width curve obtained by applying optimal turbine constant, the capture width has one peak at the internal fluid resonance frequency when the inner radius is the largest at 5 m; the

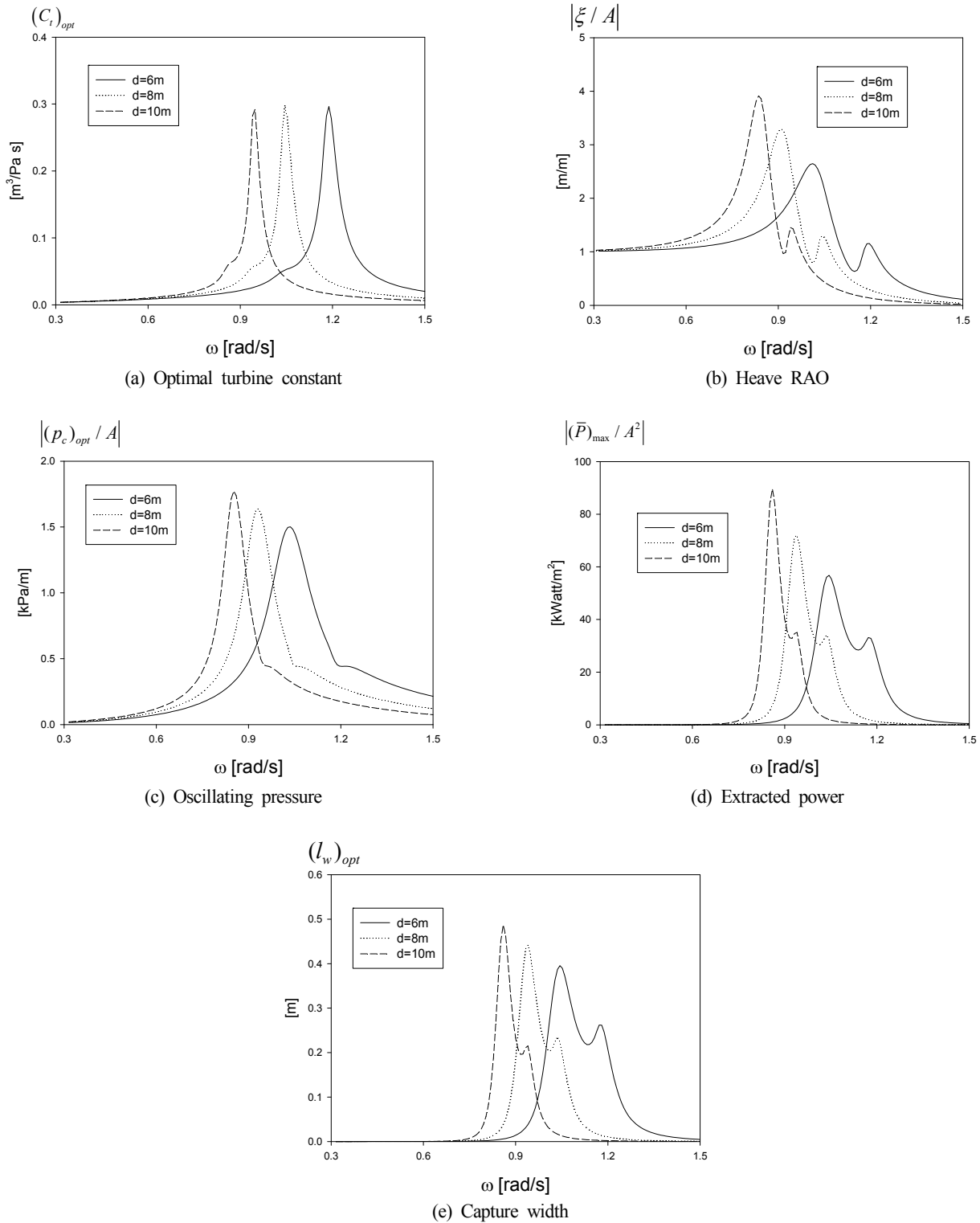


**Fig. 6** Optimal turbine constant and corresponding heave RAO, oscillating pressure, extracted power, and capture width as a function of draft  $d$  with  $a = 6$  m,  $b = 4$  m,  $h = 30$  m,  $H = 5$  m

peak value decreases when the inner radius is the smallest at 3 m, and it increases again at the heave natural frequency, thus yielding two peak values. Consequently, the peak value decreases with the decrease of inner radius, but the frequency range for wave energy extraction increases. Similar to the draft, the inner radius of a floating OWC also needs to be designed appropriately for the wave characteristics of the

installation site.

Fig. 8 shows a comparison of the coupled results between the oscillating pressure and the heave motion of a floating OWC with the uncoupled results obtained using Eq. (41). The heave RAO illustrated in Fig. 8(a) shows that the coupled heave RAO has a decreased peak value at the heave resonance frequency due to the influence of

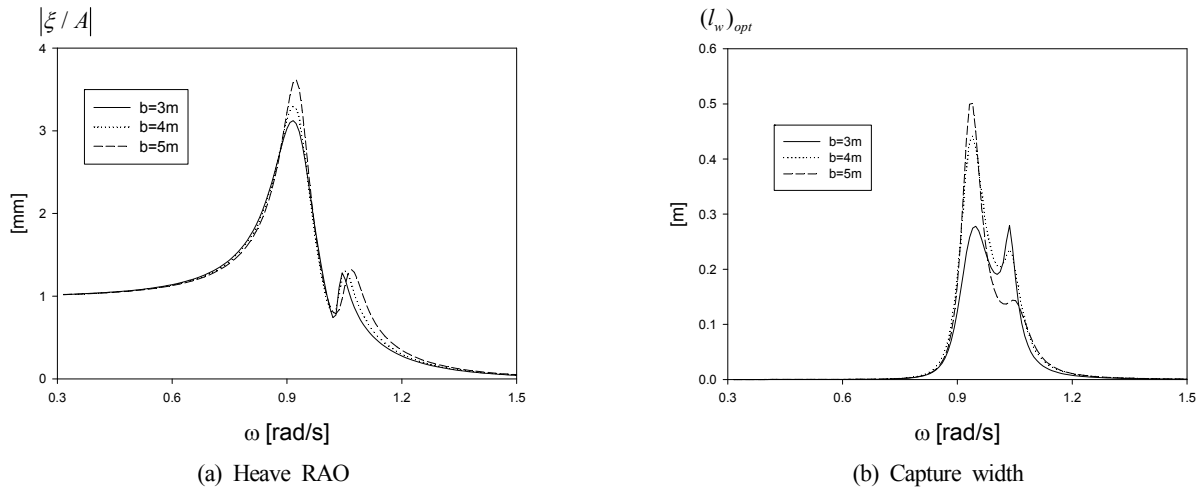


**Fig. 7** Heave RAO and capture width at optimal turbine condition as a function of radius  $b$  of inner fluid region with  $a = 6$  m,  $b = 8$  m,  $h = 30$  m,  $H = 5$  m

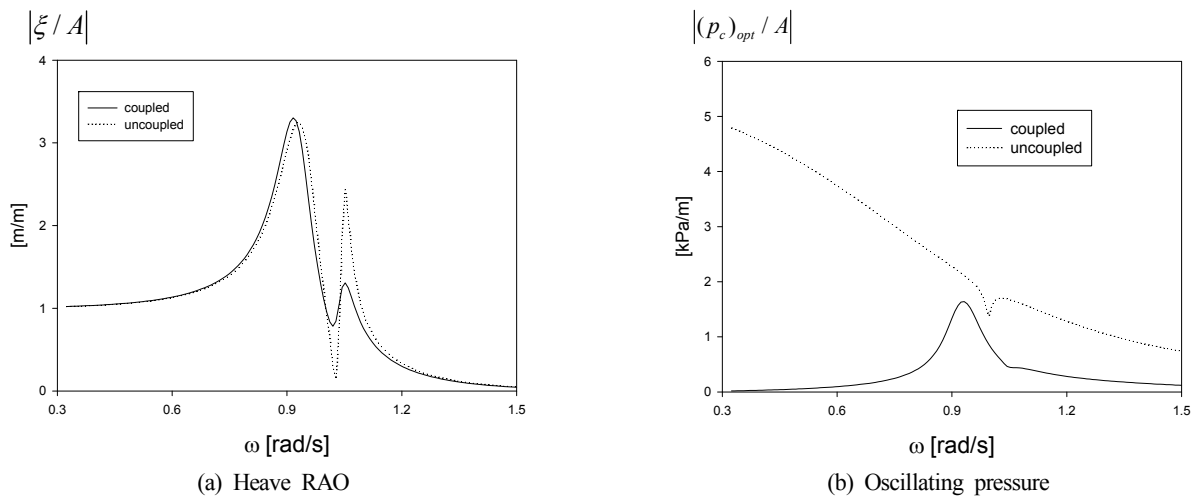


**Fig. 8** Comparison of heave RAO and oscillating air pressure between coupled and uncoupled condition at optimal turbine condition with  $a = 6$  m,  $b = 4$  m,  $d = 8$  m,  $h = 30$  m,  $H = 5$  m

oscillating pressure inside the air chamber. The oscillating pressure inside the air chamber illustrated in Fig. 8(b) shows that the results of oscillating pressure uncoupled with a floating OWC are identical to the results of the fixed type of an OWC. Thus, when the oscillating chamber pressure and heave motion of a floating OWC are coupled, the oscillating pressure is closer to zero due to a small relative heave motion as a floating OWC moves along with the incident long waves; subsequently, a peak value is observed at the internal fluid resonance frequency due to the large displacement of the internal fluid. As predicted from Fig. 8, the power generation of a floating OWC is less efficient than that of a fixed OWC in long waves. Therefore, it is recommended to design the system such that the heave motion of the OWC is minimized. To this end, a damping plate can be installed at the bottom of a floating OWC, or a tension-leg mooring system can be introduced to minimize the heave motion of the OWC. Furthermore, a latching control technique, which is often adopted in a movable-type WEC, can be introduced to a floating OWC to maximize the extraction efficiency.

## 4. Conclusions

The following conclusions have been drawn from investigation of the heave RAO, oscillating air pressure, extracted power, and capture width of a floating hollow cylindrical OWC device with respect to changes in draft and radius of an OWC.

(1) The oscillating chamber pressure, which significantly affects the extracted power of a floating OWC device, is considerably influenced by the heave motion of an OWC. Therefore, an equation of motion in which the heave motion of an OWC and oscillating air pressure in the chamber are coupled needs to be solved to accurately evaluate the performance of a floating OWC device. In the present study, a nonlinear viscous drag is considered through an equivalent linearization technique.

(2) When an enclosed fluid region is present inside an OWC, the resonance of internal fluid is generated, and a corresponding double peaks are observed, unlike the motion characteristics of a general floating body exhibiting a single resonance. The heave motion

response at the internal fluid resonance frequency is relatively larger than that at the heave natural frequency. The added mass at the internal fluid resonance frequency has a negative value, the corresponding radiation damping coefficient has a peak value. Furthermore, the flow rate of internal fluid due to oscillating pressure in the chamber, called radiation admittance and radiation conductance, shows a similar tendency as added mass and radiation damping coefficient.

(3) The changes in draft and diameter of a floating OWC affect the two different resonance frequencies existing in the hollow cylindrical OWC model. The corresponding peak values and resonance width are changed too with the draft and radius. Therefore, the wave characteristics of the installation site need to be examined in advance to appropriately design the draft and radius for yielding the maximum extraction power.

(4) For a floating OWC device that is identical in shape to a fixed OWC, the power generation efficiency in the long waves is less than that of the fixed OWC. Therefore, the damping plate can be installed at the bottom of a floating OWC, or a tension-leg mooring system can be introduced to minimize the heave motion of an OWC. Moreover, a latching control technique can be introduced to a floating OWC to maximize extraction efficiency.

### Funding

This research was funded by the Korea Institute of Energy Technology Evaluation and Planning (KETEP) and the Ministry of Trade, Industry & Energy (MOTIE) of the Republic of Korea (Grant No. 20163010071690).

### References

- Bae, Y.H., & Cho, I.H. (2013). Characteristics of Heaving Motion of Hollow Circular Cylinder. *Journal of Ocean Engineering and Technology*, 27(5), 43–50. <https://doi.org/10.5574/KSOE.2013.27.5.043>
- Bull, D. (2015). An Improved Understanding of the Natural Resonances of Moonpools Contained within Floating Rigid-Bodies: Theory and Application to Oscillating Water Column Devices. *Ocean Engineering*, 108, 799–812. <https://doi.org/10.1016/j.oceaneng.2015.07.007>
- Chau, F.P., & Yeung, R.W. (2010). Inertia and Damping of Heaving Compound Cylinders. *Proceedings of 25th International Workshop on Water Waves and Floating Bodies*, Harbin, China.
- Cho, I.H. (2002). Wave Energy Absorption by a Circular Cylinder Oscillating Water Column Device. *Journal of Korean Society of Coastal and Ocean Engineers*, 14(1), 8–18.
- Evans, D.V., & Porter, R. (1995). Hydrodynamic Characteristics of an Oscillating Water Column Device. *Applied Ocean Research*, 17(3), 155–164. [https://doi.org/10.1016/0141-1187\(95\)00008-9](https://doi.org/10.1016/0141-1187(95)00008-9)
- Evans, D.V., & Porter, R. (1997). Efficient Calculation of Hydrodynamic Properties of OWC Type Devices. *Journal of Offshore Mechanics and Arctic Engineering*, 119(4), 210–218. <https://doi.org/10.1115/1.2829098>
- Falcão, A.F.O. (2010). Wave Energy Utilization: A review of the Technologies. *Renewable and Sustainable Energy Reviews*, 14(3), 899–918. <https://doi.org/10.1016/j.rser.2009.11.003>
- Fukuta, K. (1977). Behavior of Water in Vertical Well with Bottom Opening of Ship, and Its Effects on Ship-Motion. *Journal of the Society of Naval Architects of Japan*, 141, 107–122. <https://doi.org/10.2534/jjasnaoe1968.1977.107>
- Gomes, R.P.F., Henriques, J.C.C., Gato, L.M.C., & Falcão, A.F.O. (2012). Hydrodynamic Optimization of an Axisymmetric Floating Oscillating Water Column for Wave Energy Conversion. *Renewable Energy*, 44, 328–339. <https://doi.org/10.1016/j.renene.2012.01.105>
- Gomes, R.P.F., Henriques, J.C.C., Gato, L.M.C., & Falcão, A.F.O. (2016). Wave Power Extraction of a Heaving Floating Oscillating Water Column in a Wave Channel. *Renewable Energy*, 99, 1262–1275. <https://doi.org/10.1016/j.renene.2016.08.012>
- Heath, T., Whittaker, T.J.T., & Boake, C.B. (2000). The Design, Construction and Operation of the LIMPET Wave Energy Converter (Islay, Scotland)[Land Installed Marine Powered Energy Transformer]. *Proceedings of 4th European Wave Energy Conference*, Aalborg, Denmark.
- Hong, D.C., Hong, S.Y., & Hong, S.W. (2004). Numerical Study on the Reverse Drift Force of Floating BBDB Wave Energy Absorbers. *Ocean Engineering*, 31(10), 1257–1294. <https://doi.org/10.1016/j.oceaneng.2003.12.007>
- Koo, W.C., Kim, M.H., & Choi, Y.R. (2010). Numerical Analysis of Chamber Flow and Wave Energy Conversion Efficiency of a Bottom-mounted Oscillating Water Column Wave Power Device. *Journal of the Society of Naval Architects of Korea*, 47(3), 388–397. <https://doi.org/10.3744/SNAK.2010.47.3.388>
- Masuda, Y. (1979). Experimental Full-scale Results of Wave Power Machine Kaimei in 1978. *Proceeding of First Symp Wave Energy Utilization*, Gothenburg, Sweden, 349–363.
- Mavrakos, S.A. (1985). Wave Loads on a Stationary Floating Bottomless Cylindrical Body with Finite Wall Thickness. *Applied Ocean Research*, 7(4), 213–224. [https://doi.org/10.1016/0141-1187\(85\)90028-8](https://doi.org/10.1016/0141-1187(85)90028-8)
- Mavrakos, S.A. (1988). Hydrodynamic Coefficients for a Thick-walled Bottomless Cylindrical Body Floating in Water of Finite Depth. *Ocean Engineering*, 15(3), 213–219. [https://doi.org/10.1016/0029-8018\(88\)90040-6](https://doi.org/10.1016/0029-8018(88)90040-6)
- Mavrakos, S.A., & Konispoliatis, D.N. (2012). Hydrodynamics of a Free Floating Vertical Axisymmetric Oscillating Water Column Device. *Journal of Applied Mathematics*, 1–12. <https://doi.org/10.1155/2012/142850>
- Molin, B. (2001). On the Piston and Sloshing Modes in Moonpools. *Journal of Fluid Mechanics*, 430, 27–50.
- Luo, Y., Nader, J.R., Cooper, P., & Zhu, S.P. (2014). Nonlinear 2D

- Analysis of the Efficiency of Fixed Oscillating Water Column Wave Energy Converters. *Renewable Energy*, 64, 55–265. <https://doi.org/10.1016/j.renene.2013.11.007>
- Park, W.S., Jeong, S.T., Choi, H., & Lee, U.J. (2018). Performance Evaluation of an Axisymmetric Floating Wave Power Device with an Oscillating Water Column in the Vertical Cylinder. *Journal of Korean Society of Coastal and Ocean Engineers*, 30(1), 29–38. <https://doi.org/10.9765/KSCOE.2018.30.1.29>
- Sioris, J.A., & Memos, C.D. (1999). Response of a Floating Annulus to Water Waves. *Marine Structures*, 12(1), 41–66. [https://doi.org/10.1016/S0951-8339\(99\)00006-4](https://doi.org/10.1016/S0951-8339(99)00006-4)
- Suzuki, M., Arakawa, C.S., & Takahashi, S. (2004). Performance of Wave Power Generating System Installed in Breakwater at Sakata Port in Japan. *Proceedings of 14th International Offshore and Polar Engineering Conference*, Toulon, France, ISOPE-I-04-137.

### Author ORCID

Author name	ORCID
Cho, Il Hyoung	0000-0002-4005-2724

# Performance Analysis of Multiple Wave Energy Converters due to Rotor Spacing

Sunny Kumar Poguluri<sup>1</sup>, Dongeun Kim<sup>2</sup>, Haeng Sik Ko<sup>3</sup> and Yoon Hyeok Bae<sup>4</sup>

<sup>1</sup>Post Doctor, Department of Ocean System Engineering, Jeju National University, Jeju, Korea

<sup>2</sup>Graduate Student, Multidisciplinary Graduate School Program for Wind Energy, Jeju National University, Jeju, Korea

<sup>3</sup>Researcher, Coastal Development and Ocean Energy Research Center, Korea Institute of Ocean Science and Technology, Busan, Korea

<sup>4</sup>Professor, Department of Ocean System Engineering, Jeju National University, Jeju, Korea

**KEY WORDS:** Salter's duck, Wave energy converter, Multibody, Rotor spacing, Numerical analysis

**ABSTRACT:** A numerical hydrodynamic performance analysis of the pitch-type multibody wave energy converter (WEC) is carried out based on both linear potential flow theory and computational fluid dynamics (CFD) in the unidirectional wave condition. In the present study, Salter's duck (rotor) is chosen for the analysis. The basic concept of the WEC rotor, which nods when the pressure-induced motions are in phase, is that it converts the kinetic and potential energies of the wave into rotational mechanical energy with the proper power-take-off system. This energy is converted to useful electric energy. The analysis is carried out using three WEC rotors. A multibody analysis using linear potential flow theory is performed using WAMIT (three-dimensional diffraction/radiation potential analysis program), and a CFD analysis is performed by placing three WEC rotors in a numerical wave tank. In particular, the spacing between the three rotors is set to 0.8, 1, and 1.2 times the rotor width, and the hydrodynamic interaction between adjacent rotors is checked. Finally, it is confirmed that the dynamic performance of the rotors slightly changes, but the difference due to the spacing is not noticeable. In addition, the CFD analysis shows a lateral flow phenomenon that cannot be confirmed by linear potential theory, and it is confirmed that the CFD analysis is necessary for the motion analysis of the rotor.

## 1. Introduction

A wave energy converter (WEC) that generates electrical energy from wave energy is a subject of high research interest in academia. Salter's duck, which is a pitch-type WEC positioned on the water surface to primarily convert wave energy into rotational kinetic energy of a floating body (rotor), is one of the oldest WECs and has been researched since the 1970s (Salter et al., 1975). Salter's duck maximizes wave energy absorption by designing the front and rear shapes differently and thus is theoretically known to have nearly 90% energy absorption efficiency (Swift-Hook et al., 1975). Several recent studies in South Korea have designed Salter's duck-type WECs suitable for the western waters of Jeju Island. The design parameters and performance of a rotor have been verified through a parametric study of optimal motion performance using the wave data of the western waters of Jeju Island (Poguluri and Bae, 2018), a study on estimating viscous coefficients of a rotor using computational fluid dynamics (CFD) (Poguluri et al., 2019a), and a numerical and experimental study on the linear behavior of a rotor (Kim et al.,

2019a). These previous studies, however, focused on only one WEC rotor, so the effects of hydrodynamic interactions between adjacent modules must be analyzed considering how multiple WECs are simultaneously installed in the seas in general (Kim et al., 2020). Previous studies on analyzing dynamic behavior by arranging multiple WECs include an analysis of multiple cylindrical WECs in a heaving motion in the frequency domain (Lee et al., 2018) and in the time domain (Bae and Lee, 2017) as well as a study on optimal arrangement for improving the overall performance of multiple cylindrical WECs (Kim and Bae, 2019b). In these studies, a multibody analysis was performed for cylindrical WECs in the frequency domain to which a linear potential theory was applied, based on which the motion performance of individual WECs was evaluated by solving the coupled equations of motion in the time domain. An approach for computing performance changes and interactions may be effective for multiple cylindrical WECs with a fairly weak nonlinearity of motions; however, there are limitations in examining performance changes and interactions of arrayed WEC rotors based only on linear potential theory, because asymmetrical WEC rotors applied in this study have a

Received 19 January 2021, revised 6 May 2021, accepted 7 May 2021

Corresponding author Yoon Hyeok Bae: +82-64-754-3485, [yh.bae@jejunu.ac.kr](mailto:yh.bae@jejunu.ac.kr)

© 2021, The Korean Society of Ocean Engineers

This is an open access article distributed under the terms of the creative commons attribution non-commercial license (<http://creativecommons.org/licenses/by-nc/4.0>) which permits unrestricted non-commercial use, distribution, and reproduction in any medium, provided the original work is properly cited.

greater nonlinearity of motions than cylindrical WECs. Therefore, this study conducted a frequency domain analysis based on linear potential theory in addition to a CFD analysis for simulating nonlinearity of motion in order to examine the performance of multiple WEC rotors with an asymmetrical shape.

First, WAMIT, a three-dimensional diffraction/radiation potential analysis program based on linear potential theory, was used to calculate motion characteristics of three arrayed rotors in the frequency domain, and the response characteristics were analyzed by adjusting the spacing between arrayed rotors. Motion response characteristics were analyzed when three rotors were arranged using a commercial CFD code that adequately reflects nonlinear characteristics of rotor motions. The spacing between three rotors was adjusted during a CFD analysis to observe the changes in motion characteristics, and the effects of hydrodynamic interactions of adjacent WEC rotors were quantitatively computed.

## 2. Numerical Analysis Conditions

To conduct a numerical analysis in the frequency domain based on linear potential theory, the coupled equations of motion of three arrayed WEC rotors were established first, and then the hydrodynamic coefficients of the coupled equations of motion were computed using WAMIT. A response amplitude operator (RAO) of three rotors in the frequency domain was calculated, and the results were compared. For a CFD analysis, wave generation and wave absorption were performed using a three-dimensional numerical wave tank in which three rotors were arranged in the center to perform a regular wave simulation for 60 s. The performance was compared using the average amplitude of motions after obtaining the motion response of each rotor through this process.

### 2.1 Linear Motion Equation of Multiple Arrayed Rotors

When three WEC rotors are arranged on a still water surface, each rotor is not mechanically coupled with another rotor but still moves in the same fluid domain; thus, the equation of motion must be established considering the effects of hydrodynamic interactions. The coupled equations of motion of three rotors with three degrees of freedom (DOF) can be expressed as shown in Eq. (1), where the subscripts 1, 2, and 3 indicate rotors no. 1, 2, and 3, respectively.

$$\begin{bmatrix} I_{11} + a_{11} & a_{12} & a_{13} \\ a_{21} & I_{22} + a_{22} & a_{23} \\ a_{31} & a_{32} & I_{33} + a_{33} \end{bmatrix} \begin{Bmatrix} \ddot{\xi}_1 \\ \ddot{\xi}_2 \\ \ddot{\xi}_3 \end{Bmatrix} + \begin{bmatrix} b_{11} + b_{vis} & b_{12} & b_{13} \\ b_{21} & b_{22} + b_{vis} & b_{23} \\ b_{31} & b_{32} & b_{33} + b_{vis} \end{bmatrix} \begin{Bmatrix} \dot{\xi}_1 \\ \dot{\xi}_2 \\ \dot{\xi}_3 \end{Bmatrix} + \begin{bmatrix} k_{11} & 0 & 0 \\ 0 & k_{22} & 0 \\ 0 & 0 & k_{33} \end{bmatrix} \begin{Bmatrix} \xi_1 \\ \xi_2 \\ \xi_3 \end{Bmatrix} = \begin{Bmatrix} f_1(t) \\ f_2(t) \\ f_3(t) \end{Bmatrix} \quad (1)$$

As shown in Fig. 1, the analysis was conducted by designating two rotors on each side as rotor 1 and rotor 3 and the rotor in the center as rotor 2.

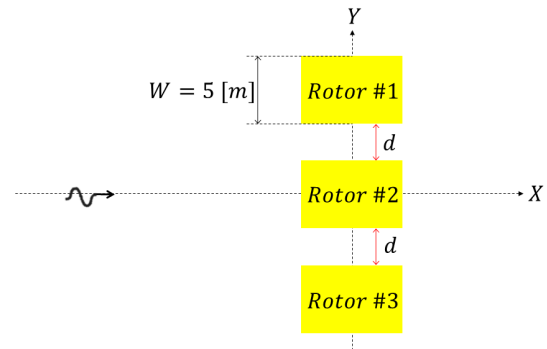


Fig. 1 Schematic representation of arrayed rotors (top view)

In Eq. (1),  $\ddot{\xi}_n$ ,  $\dot{\xi}_n$ , and  $\xi_n$ , represent the rotational acceleration, velocity, and displacement, respectively, of rotor  $n$  ( $n=1, 2, 3$ ). Moreover,  $I_{nn}$ ,  $a_{nn}$ ,  $b_{nn}$ , and  $k_{nn}$  represent the mass moment of inertia, added mass moment of inertia, radiation damping coefficient, and restoring moment coefficient, respectively, of rotor  $n$ .  $b_{vis}$  represents the viscous damping coefficient, which was experimentally computed by performing a free decay test in a two-dimensional wave tank.  $f_n(t)$  represents the wave exciting moment in the direction of rotational motion of rotor  $n$ . From Eq. (1), the added mass moment of inertia  $a$  and radiation damping coefficient  $b$  have coupled terms among three rotors, which are expressed as  $a_{nm}$  and  $b_{nm}$  ( $n \neq m$ ) using different subscripts. These refer to the added mass moment of inertia and radiation damping coefficient of rotor  $n$  due to rotational motions of rotor  $m$ . The added mass moment of inertia, radiation damping coefficient, and wave exciting moment including coupled terms were computed using a multibody analysis of WAMIT. The wave exciting moment was computed using diffraction potential while having the behavior of three rotors confined; hydrodynamic forces acting on the structure being moved and hydrodynamic forces (coupled added mass moment of inertia and coupled radiation damping coefficient) acting on adjacent rotor without being moved were computed by having three rotors move sequentially one at a time using radiation potential.

To construct the same environment as the 3D CFD analysis when performing a multibody analysis using WAMIT, walls were built 5 m from both ends of the arrayed rotors. The motion performance of the arrayed rotors may partially change owing to the wall effects of both sides, but this is an inevitable arrangement for comparison in the same simulation environment as the 3D CFD analysis. Fig. 2 illustrates three rotors and a mesh model of the wall for a WAMIT multibody analysis where the number of meshes used for one rotor is 2,800.

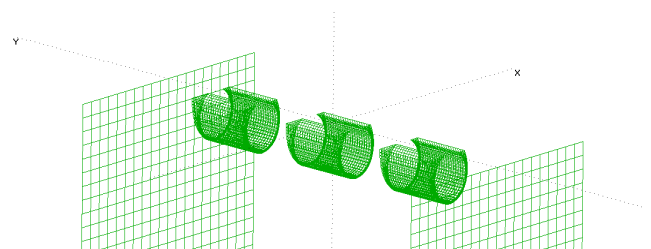


Fig. 2 Mesh model for multibody analysis

## 2.2 Experimental Calculation of Viscous Damping Coefficient

Viscous damping coefficient  $b_{vis}$  was calculated by performing a free decay test in a 2D wave tank. When a rotor in still water is forced to rotate at a certain angle upward or downward from equilibrium position and confinement is removed, the rotor moves in two-way rotational motions where rotational displacement gradually decreases during which a pitch displacement with respect to time is obtained using an image tracking technique as shown in Fig. 3. Subsequently, the damping ratio  $\zeta = 0.0928$  was calculated using the logarithmic decrement ratio relation expressed in Eq. (2). Here,  $\xi_i$  is a positive or a negative  $i$ -th peak value; as shown in Table 1, the damping ratio was calculated using only  $\xi_2$ - $\xi_5$  values in this study, excluding the initial transient response part of the free decay test (Kim et al., 2019a). The overall damping coefficient including the radiation damping coefficient and viscous damping coefficient was computed using the damping ratio obtained previously; an approximate viscous damping coefficient was computed by subtracting the numerical radiation damping coefficient obtained through WAMIT from the overall damping coefficient.

However, the effects of the reflected wave from the sides are present when conducting a free decay test in a 2D wave tank, in contrast to a 3D environment; thus, it is inappropriate to directly apply the calculated viscous damping coefficient in WAMIT analysis, which is based on 3D potential theory. Most radiated waves of the WEC rotors used in this study spread toward a beak during free decay motions owing to the characteristics of a shape, and radiated waves due to rotational motions were not generated on the sides of the rotors, which were vertical planes. Therefore, the radiated waves due to the internal walls of a 2D wave tank were considered not to have a significant effect on the damping motions of the rotors. The approximate viscous damping coefficient computed through the experiment conducted in a 2D wave tank was applied in a 3D CFD analysis in this study.

$$\zeta = \frac{1}{2\pi} \ln \left( \frac{\xi_2 - \xi_3}{\xi_4 - \xi_5} \right) \quad (2)$$

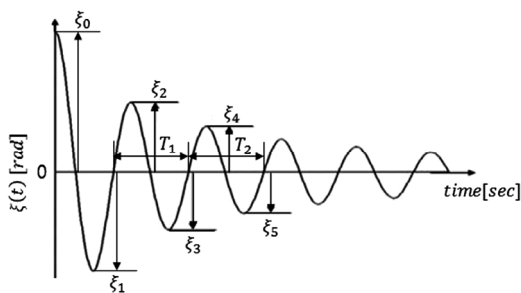


Fig. 3 Time-history data obtained through free decay test

Table 1 Specification of experimental model

Peak points	Peak displacement
$\xi_2$	-8.047
$\xi_3$	6.297
$\xi_4$	-4.421
$\xi_5$	3.587

## 2.3 CFD Analysis Conditions

A CFD analysis was conducted using commercial software STAR-CCM+, where a continuity equation (a governing equation of a turbulent flow) and the Reynolds-averaged Navier Stokes (RANS) equations (including momentum equations) were applied to single or multiple rotors. The computation domain is shown in Fig. 4, where three rotors are arranged in the center. Waves are advanced from the  $-x$  to the  $+x$  direction where the free surface is set to  $z = 0$ . Velocity inlet is located at the upstream side of the model, while the pressure outlet boundary is found in the downstream side. Top as pressure outlet and all other boundaries as wall boundaries except  $y = 0$  as symmetry. Wave forcing was applied at inlet and outlet boundaries with  $0.5 \times \lambda$ , where  $\lambda$  is the wave length. The forcing is performed using fifth-order Stokes wave theory. The middle portion in the vicinity of the WEC rotor of the computational domain was chosen as  $2 \times \lambda$ . Fifth-order Stokes waves were generated to represent realistic regular waves. Water depth is fixed at 40 m. The distance between the rotors on the sides and walls was set to 5 m. Considering the large rotational displacement of a rotor, overset meshes were used as shown in Fig. 5, where a variable grid method was applied in which small meshes were arranged around the rotors and larger meshes were arranged in the outer region for computational efficiency.

CFD analysis can simulate the nonlinearity of a rotor's motion because it can accommodate the effects of viscosity according to the application of a turbulence model. However, the motion response of an

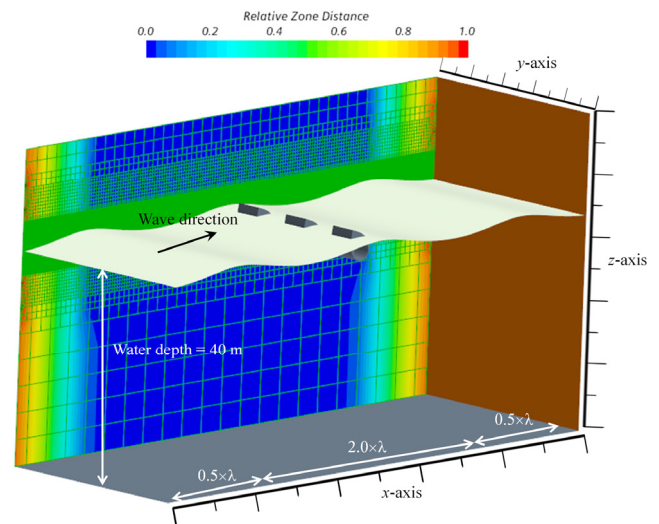


Fig. 4 Computation domain of the numerical wave tank

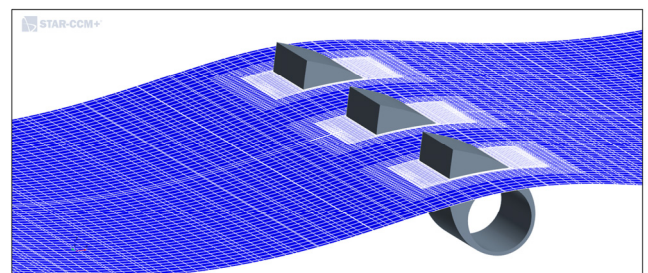


Fig. 5 Overset mesh around the rotors

RAO form for which the motion amplitude is normalized to the incident wave height, such as a potential flow, cannot be computed, and motion responses vary depending on the wave height used for the analysis. Therefore, rotor behavior was simulated for the wave height of 1.5 m, which corresponds to the wave height used in the downscaled experiment, and the wave height of 2 m, which was set as the operation conditions of the rotors. The changes in the normalized motion amplitude of a rotor with respect to the changes in the height of regular waves during a CFD analysis can be confirmed in the results of a previous study (Ko et al., 2020).

### 3. Results and Discussion

#### 3.1 Numerical Analysis Based on Linear Potential Theory

First, the RAO of the arrayed rotors computed by performing a WAMIT multibody analysis was verified. The spacing between the rotors was varied by 0.8, 1, and 1.2 times the rotor width ( $W=5$  m), and motion response was computed for each case for comparison. The analysis in this study was performed only for head waves whose incident wave angle was  $0^\circ$ , so the response of rotors 1 and 3 was the same because they were symmetrically positioned with respect to the  $x$ -axis of incident waves. Therefore, the RAO was illustrated by distinguishing between side and center rotors. The RAO of a single rotor is also illustrated with a solid line to compare the performance when only one rotor is arranged.

The RAO of multiple rotors was compared with respect to the changes in spacing, as shown in Fig. 6. The motion response near the

resonance frequency of rotor 2 (center), marked with a red dotted line, decreased far more than the motion response of rotors 1 and 3 (side) regardless of rotor spacing. Rotors 1 and 3, located on the sides, were mostly affected by hydrodynamic interactions through only one surface facing rotor 2 in the center, whereas the surfaces facing outward were less affected by the interactions with a neighboring rotor. Contrarily, rotor 2, located in the center, had neighboring rotors on both sides and thus was greatly affected by interactions; these hydrodynamic interactions had negative effects around the resonance frequency, which resulted in a decrease in motion response. The motion response of all three rotors outside the resonance frequency domain was almost identical under long period incident wave conditions of 0.8 rad/s or below, whereas the response of rotor 2 in the center was almost identical to or slightly smaller than that of the rotors on the sides.

Moreover, as rotor spacing increased from 0.8  $W$  to 1.0  $W$  to 1.2  $W$ , the motion amplitude of the rotors on the sides gradually increased near the resonance frequency, whereas the motion amplitude of the rotor in the center barely improved near the resonance frequency. Fig. 7 shows the radiation damping coefficients according to the changes in rotor spacing. The radiation damping coefficient of the rotors on the sides decreased near the resonance frequency as spacing increases (Fig. 7(a)), whereas the changes in the radiation damping coefficient of the rotor in the center were minimal near the resonance frequency (Fig. 7(b)). Based on the trend of changes in radiation damping coefficients, it can be inferred that the maximum motion amplitude gradually increased as rotor spacing increased only for the rotors on the sides.

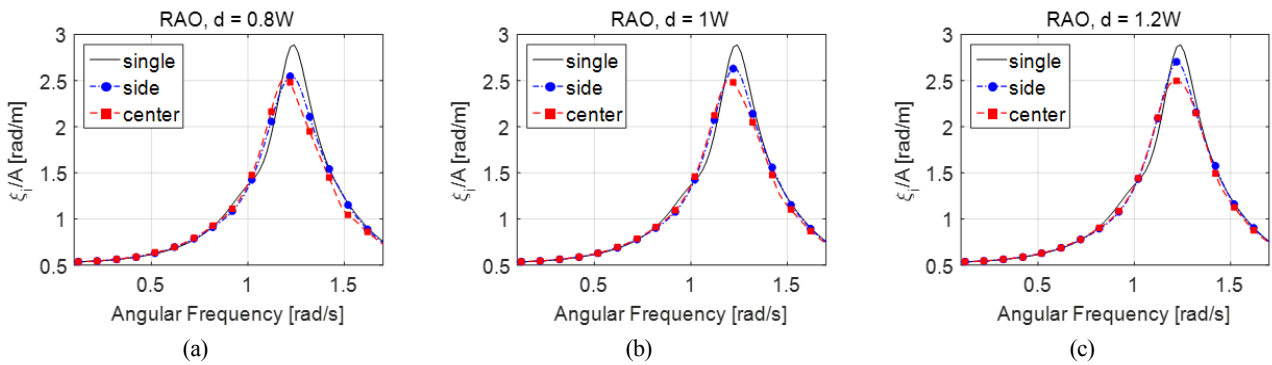


Fig. 6 Rotor RAO with respect to spacing

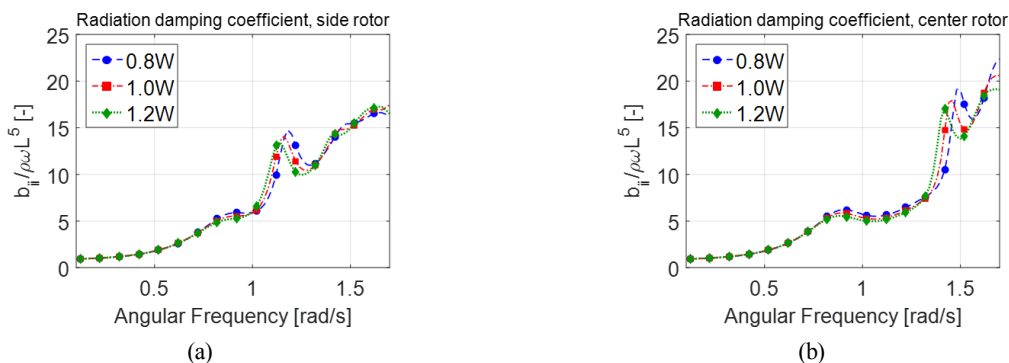


Fig. 7 Radiation damping coefficients of the rotors

**Table 2** RAO values of single and multiple rotors by potential analysis ( $T_z = 4.75$  s)

		Side		Center		q-factor
		RAO	Ratio (%)	RAO	Ratio (%)	
Multiple Rotors	0.8 $W$	2.107	92.82	1.948	85.81	0.905
	1.0 $W$	2.142	94.36	2.046	90.13	0.930
	1.2 $W$	2.161	95.20	2.151	94.76	0.951
Single rotor		2.270	100.00	2.270	100.00	-

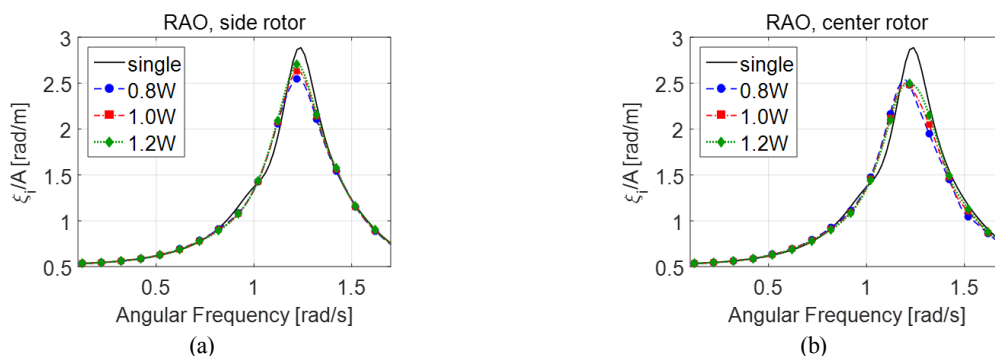
The RAO of a single rotor as illustrated by a solid line also was compared, as shown in Fig. 6. The RAO of the rotors on the sides approached the RAO of a single rotor near the resonance frequency as the spacing between arrayed rotors increased, whereas no significant changes in the RAO of a single rotor were observed. In this study, the RAO of WEC rotors was compared at zero crossing period  $T_z = 4.75$  s, which is the most frequent wave period occurring in the installation sea area, based on the design strategy of WEC rotors for maximizing the annual power generation time. Hence, the time average of the significant power generation amount, using seasonal wave distributions and the wave spectrum of the installation area, and annual power generation prediction have been separately examined in different studies (Lee et al., 2019). Table 2 presents the RAO values at  $T_z = 4.75$  s of single and multiple arrayed rotors.

As the rotor spacing increased, the RAO values also increased for both center and side rotors. For quantitative comparisons, the ratio (%) of RAO values of multiple rotors according to rotor spacing with respect to the RAO value of a single rotor (100%) is shown in Table 2. The performance of multiple rotors was approximately 85%–95% of the performance of a single rotor in terms of RAO, in which a single rotor outperformed multiple arrayed rotors at  $T_z = 4.75$  s. As shown in Fig. 6, however, the performance of multiple rotors may have been more outstanding than the performance of a single rotor at approximately 1.2 rad/s ( $T = 5.34$  s); the difference in the overall performance in the irregular wave environment must be compared by computing the motion spectrum of a rotor within the wave period range of the relevant waters (Kim et al., 2020). The RAO value of the center rotor was less than that of side rotors, but the rate of increase in RAO with respect to the increase in rotor spacing was greater in the center rotor. The effects of interactions were significantly reduced for the center rotor when the rotor spacing increased because it was

influenced by the hydrodynamic interactions of the side rotors. Only one side of the side rotors was affected by hydrodynamic interactions with the center rotor, so the increase in motion of the side rotors was less than that of the center rotor, even when the rotor spacing increased.

The RAO of the center and side rotors with respect to the changes in rotor spacing is shown in Fig. 8. The side rotors in Fig. 8(a) show that the motion response evidently increased near the resonance frequency as the rotor spacing increased, whereas no significant changes in motion response with respect to rotor spacing were observed in the regions other than the resonance frequency. Rotor 2, or the center rotor, in Fig. 8(b) shows that the motion response in the angular frequency range of 1.2–1.4 rad/s increased with increasing rotor spacing, similar to the response trend shown by the side rotors.

The interaction effects of arrayed rotors can be quantitatively represented as the ratio of the RAO value of a single rotor multiplied by 3 to the sum of each RAO value of three arrayed rotors, which is referred to as the q-factor. A q-factor greater than 1 indicates that the interactions of arrayed rotors have a positive effect on the rotor motion, whereas a q-factor less than 1 indicates that the motion of arrayed rotors becomes smaller than that of a single rotor owing to hydrodynamic interactions. The q-factor is expressed as a function of the frequency of incident waves, but here it was calculated based on the RAO value at  $T_z = 4.75$  s, as shown in Table 2. All calculated q-factors were less than 1 for three-rotor spacing conditions, which indicates that the three arrayed rotors had slightly reduced motion performance on average compared to a single rotor under the given incident wave conditions. Furthermore, the q-factor approached 1 as the spacing of rotors increased, and the performance of arrayed rotors became similar to that of a single rotor as the spacing sufficiently increased.

**Fig. 8** Rotor RAO with respect to location

3.2 Numerical Analysis Results Based on CFD

According to previous studies on the behavior of WEC rotors, the motion of a rotor has a highly nonlinear nature (Ko et al., 2019; Poguluri et al., 2019a; Poguluri et al., 2019b), which is attributed to the asymmetrical shape of a underwater rotor shape, the nonlinearity of a rotor’s restoring moment, and the effects of nonlinear viscous damping moment. Motion response based on linear potential theory is very similar to the actual motion response of a rotor when the rotational displacement of a rotor is very small (Kim et al., 2019a); however, different motion responses from a linear response nature are exhibited when the rotational displacement increases owing to the increased height of the incident wave. When multiple rotors are arrayed, the rotor behavior pattern becomes more difficult to predict owing to the nonlinear nature and the hydrodynamic interactions with neighboring rotors. Therefore, the behavior of one rotor was simulated using a commercial CFD code to analyze the characteristics of motion in previous studies (Ko et al., 2019; Poguluri et al., 2019a; Poguluri et al., 2019b); a 3D CFD analysis was performed for three arrayed rotors in this study.

Fig. 9(a) and (b) show the changes in the height of 1.5-m regular waves in the simulation of a single rotor and three rotors arranged in a numerical wave tank.

Fig. 9(a) shows the pattern at 57 s of a simulation, and Fig. 9(b) shows the pattern at 57.5 s of a simulation. Irregular flows around the

rotors can be observed from the pattern of wave height; in particular, the effects of radiated waves caused by the rotor motion are present at the front of the rotors, and the effects of both radiated waves and diffracted waves are present in the back of the rotors.

Fig. 10 shows the rotational displacement and angular velocity of a rotor at a wave height of 1.5 m in time series. Only the spacing of 1.0  $W$  is indicated when the three rotors are arranged. When the incident waves are regular waves, the rotational displacement and angular velocity of a single rotor and multiple rotors do not vary considerably. To quantitatively compare the rotors’ motion, RAO values at  $T_z = 4.75$  s were compared as shown in Tables 3 and 4 to correspond to the analysis based on linear potential theory. Table 3 shows the results of calculating the RAO at a wave height of 1.5 m, and Table 4 shows the simulation results at a wave height of 2 m.

The RAO values of side rotors tended to increase with increasing rotor spacing, which corresponds to the linear potential analysis result in Table 2. In the case of the center rotor, however, the RAO value increased when rotor spacing increased from 0.8  $W$  to 1.0  $W$  but slightly decreased when rotor spacing further increased to 1.2  $W$ . Compared to the simulation of a single rotor at a wave height of 1.5 m, the response of the side rotors becomes similar to that of a single rotor as the rotor spacing increases, in which the RAO slightly increases farther than a single rotor at a rotor spacing of 1.2  $W$ . The RAO of the center rotor was 96%-97% of that of a single rotor. The q-factor

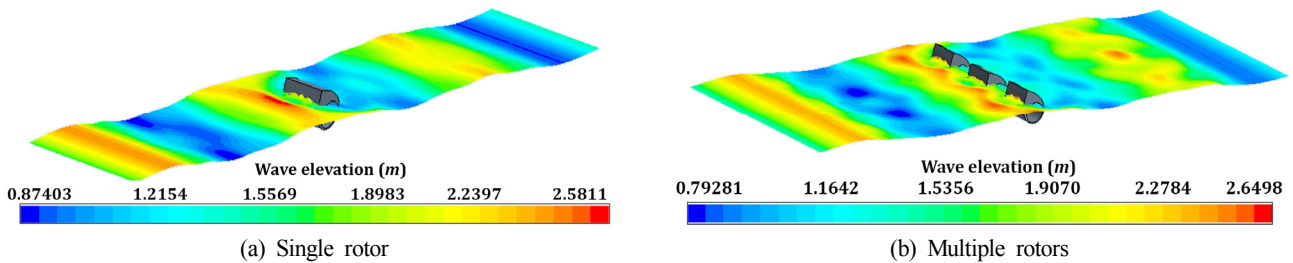


Fig. 9 Wave elevation along the numerical wave tank

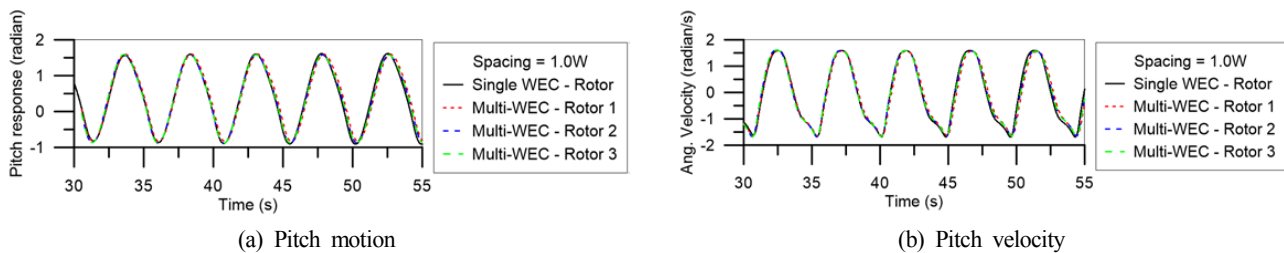


Fig. 10 Time series of the pitch response with 1.5-m wave height

Table 3 RAO values of single and multiple rotors by CFD analysis ( $H= 1.5$  m)

		Side		Center		q-factor
		RAO	Ratio (%)	RAO	Ratio (%)	
Multiple Rotors ( $H= 1.5$ m)	0.8 $W$	1.613	97.46	1.619	97.24	0.976
	1.0 $W$	1.635	98.79	1.622	97.42	0.985
	1.2 $W$	1.665	100.60	1.602	96.22	0.993
Single rotor		1.655	100.00	1.665	100.00	-

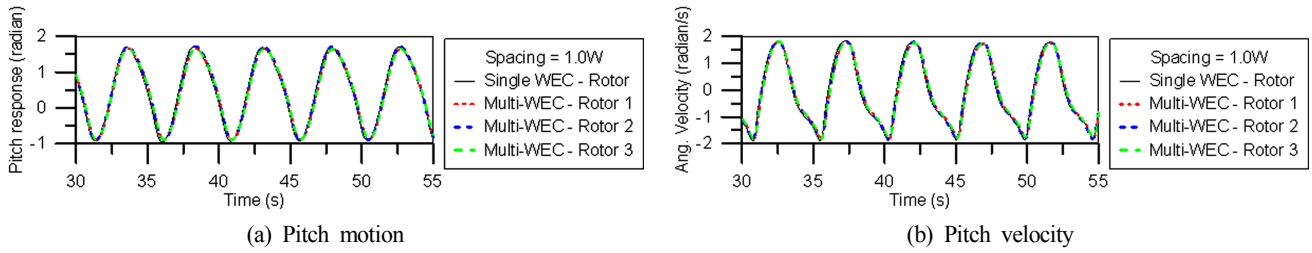


Fig. 11 Time series of the pitch response with 2.0-m wave height

Table 4 RAO values of single and multiple rotors by CFD analysis ( $H= 2.0$  m)

		Side		Center		q-factor
		RAO	Ratio (%)	RAO	Ratio (%)	
Multiple Rotors ( $H= 2.0$ m)	$0.8 W$	1.252	95.72	1.294	98.93	0.968
	$1.0 W$	1.277	97.63	1.311	100.23	0.985
	$1.2 W$	1.286	98.32	1.303	99.62	0.988
Single rotor		1.308	100.00	1.308	100.00	-

ranged from 0.976 to 0.993 as the rotor spacing increased; the interactions of the arrayed rotors had a fairly negative effect, with q-factor values less than 1, similar to the linear potential analysis results in Table 2. However, the q-factor values were closer to 1 overall compared to those of linear potential analysis, which signifies that the difference in the performance between a single rotor and arrayed rotors based on the CFD analysis is not greater than that of the linear potential analysis.

Fig. 11 shows the rotational displacement and angular velocity of a rotor at a wave height of 2.0 m in time series. The nonlinearity of the rotors' motion increased substantially as the height of incident waves increased to 2 m. The motion response of the rotors gradually showed the incident wave frequency component and additional harmonic frequency terms. Consequently, the response of the incident wave frequency component, which was most dominant, decreased as shown in Table 4.

The motion amplitude decreased as the wave height increased, but the increase in RAO with respect to the increase in rotor spacing was identical to the pattern shown for the wave height of 1.5 m. In addition, the RAO slightly decreased as the rotor spacing increased from  $1.0 W$  to  $1.2 W$  for the center rotor. In terms of the motion response pattern, the side rotors have approximately 95%–98% and the center rotor has 98%–100% of the motion amplitude of a single rotor. According to the results of the potential analysis and CFD analysis at the wave height of 1.5 m, the motion amplitude of a single rotor was closer to that of the side rotor than the center rotor. In the CFD analysis results at the wave height of 2 m, on the other hand, the motion amplitude of a single rotor was closer to the center rotor because of an increase in the nonlinearity of a rotor's motion from the increased amplitude of incident waves. The q-factor ranged from 0.968 to 0.988. Excluding the spacing of  $1.0 W$ , similar results to that of the CFD analysis at the wave height of 1.5 m were produced, in which the interaction effects of arrayed rotors had a negative influence on the motion performance of the rotor.

The RAO of the center rotor decreased slightly when the rotor spacing increased from  $1.0 W$  to  $1.2 W$  at wave heights of both 1.5 m and 2 m owing to slamming and large impact pressure forces on rotor 2 caused by a rigorous mixing of the flow resulting from violent liquid motions along the cylindrical passage of the rotor. The violent liquid motions were barely observed when the rotor spacing was  $0.8 W$  or  $1.0 W$ , but they became observable at the rotor spacing of  $1.2 W$  because the flow was more active in the lateral direction. In order to examine this phenomenon, the velocity of the fluid particle on the free surface at the rotor spacing of  $1.2 W$  is shown in Fig. 12.

As shown Fig. 12, a great number of flow velocity vectors were generated around the cylindrical passage of the center rotor, whereas no flow was observed around the side rotors. Violent fluid flow occurring in the cylindrical hole of the center rotor is a physical phenomenon that is difficult to obtain in a potential analysis and can be observed only in a CFD analysis or a scaled model test. A lateral flow interferes with a rotor's motion but also accelerates motion depending on the period of incident waves. The motion performance of arrayed rotors according to the effects of a flow passing through a cylindrical passage will be examined further in a separate study.

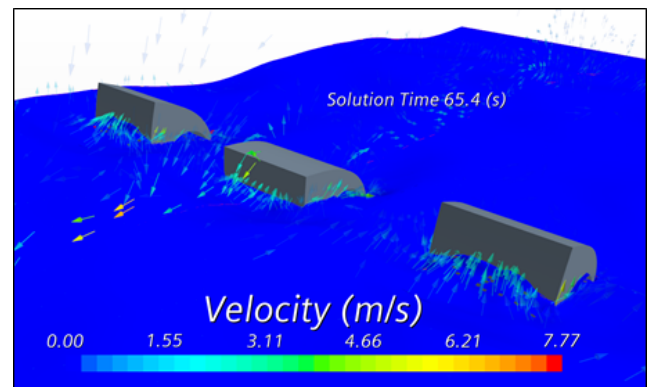


Fig. 12 Velocity magnitude of the multiple rotors with  $1.2 W$  spacing at  $T_z = 4.75s$

#### 4. Conclusion

This study aimed to examine the linear potential theory and a CFD analysis to comparatively analyze the motion performance of individual rotors and thus identify the characteristics of motion performance of multiple arrayed WEC rotors. The changes in motion response of multiple arrayed rotors were observed with respect to the position by adjusting the rotor spacing to 0.8, 1, and 1.2 times the width of the rotor. The rotational motion response of the rotor positioned in the center decreased farther than that of the rotor positioned on the sides in a frequency domain analysis based on linear potential theory. Furthermore, the responses of all three rotors increased as the rotor spacing increased. However, the ratio of an increase in the motion response of a rotor with respect to an increase in rotor spacing was greater in the center rotor than in the side rotors because the center rotor was influenced more significantly by the interactions with adjacent rotors. When multiple rotors were arranged, the motion performance of individual rotor could be adjusted through the optimal arrangement of rotors, and the overall performance of the arranged rotors could be determined by considering the arrangement spacing and incident wave period.

The asymmetrical WEC rotors used in this study had large rotational displacement and nonlinearity in motion; thus, analyzing their motion response based only on linear potential theory was subject to limitations. A CFD analysis was thus conducted to examine the difference in performance based on a nonlinear nature of motions, and the analysis results showed that the trend of motion response was similar to that of linear potential theory. When the rotor spacing was increased to 1.2 times the rotor width, however, the motion of the center rotor decreased slightly, which was judged to be due to the generation of lateral flow from the increased rotor spacing, thus resulting in intense fluid flow inside a cylindrical passage of a rotor. This lateral flow phenomenon cannot be observed in linear potential analysis, which necessitates a CFD analysis. At the incident wave period of  $T_z = 4.75$  s applied in this study, the motion of the center rotor decreased owing to a lateral flow but also may increase if the period of the incident wave changes; therefore, a further study is needed to conduct a multibody CFD analysis of the entire rotors in addition to motion analysis of various incident wave periods. The q-factor was calculated to examine the effects of hydrodynamic interactions based on rotor arrangements; at the incident wave period of  $T_z = 4.75$  s used in this study, the q-factors deduced from the linear potential and CFD analyses were less than 1, which indicated that the interactions had a negative influence on the motion performance of the rotors. The q-factor can vary depending on the period of incident waves, so a comprehensive review in multiple frequency ranges must be conducted based on the wave spectrum of the installation site. In conclusion, the motion performance of individual rotors varied slightly depending on the spacing between rotors, but the changes were insignificant, and no major difference in the motion performance

between a single rotor and arrayed rotors has been reported. Therefore, wave energy can be efficiently absorbed without a considerable loss of motion performance of rotors when a WEC system is operated in which multiple rotors are arranged or when a previously installed WEC is expanded by arranging additional rotors.

#### Acknowledgment

This work was performed during the author's research year at Jeju National University in 2018.

#### References

- Bae, Y.H., & Lee, H. (2017). Multi-DOF Time-domain Analysis of Wind-wave Hybrid Power Generation Platform. *Journal of Korean Society for Marine Environment and Energy*, 20(3), 127–135. <https://doi.org/10.7846/JKOSMEE.2017.20.3.127>
- Kim, D., Poguluri, S.K., Ko, H.S., Lee, H., & Bae, Y.H. (2019a). Numerical and Experimental Study on Linear Behavior of Salter's Duck Wave Energy Converter. *Journal of Ocean Engineering and Technology*, 33(2), 116–122. <https://doi.org/10.26748/KSOE.2019.023>
- Kim, D., & Bae, Y.H. (2019b). Time Domain Analysis of Optimal Arrangement of Wave Energy Converters placed on a Floating Platform. *Journal of Korean Society for Marine Environment and Energy*, 22(3), 125–132. <https://doi.org/10.7846/JKOSMEE.2019.22.3.125>
- Kim, D., Poguluri, S.K., & Bae, Y.H. (2020). Numerical Study on Linear Behavior of Arrayed Pitch Motion Wave Energy Converters. *Journal of Korean Society for Marine Environment and Energy*, 23(4), 269–276. <https://doi.org/10.7846/JKOSMEE.2020.23.4.269>
- Ko, H.S., Kim, D., Cho, I.H., & Bae, Y.H. (2019). Numerical and Experimental Study for Nonlinear Dynamic Behavior of an Asymmetric Wave Energy Converter. *Proceedings of The 29th International Ocean and Polar Engineering Conference, Honolulu, USA*, 182–186.
- Lee, H., Poguluri, S.K., & Bae, Y.H. (2018). Performance Analysis of Multiple Wave Energy Converters Placed on a Floating Platform in the Frequency Domain. *Energies*, 11(2), 406. <https://doi.org/10.3390/en11020406>
- Lee H., Cho, I.H., Ko, H.S., & Bae, Y.H. (2019). Estimation of Annual Energy Production of a Horizontal Cylinder Wave Energy Converter by Time-domain Analysis. *Journal of Korean Society for Marine Environment and Energy*, 22(3), 151–158. <https://doi.org/10.7846/JKOSMEE.2019.22.3.151>
- Poguluri, S.K., & Bae, Y.H. (2018). A Study on Performance Assessment of WEC Rotor in the Jeju Western Waters. *Ocean Systems Engineering*, 8(4), 361–380. <https://doi.org/10.12989/ose.2018.8.4.361>

- Poguluri, S.K., Cho, I.H., & Bae, Y.H. (2019a). A Study of the Hydrodynamic Performance of a Pitch-type Wave Energy Converter-Rotor. *Energies*, 12(5), 842. <https://doi.org/10.3390/en12050842>
- Poguluri, S.K., Ko, H.S., & Bae, Y.H. (2019b). CFD Investigation of Pitch-type Wave Energy Converter-rotor Based on RANS Simulations. *Ships and Offshore Structures*, 15(10), 1107-1119. <https://doi.org/10.1080/17445302.2019.1705632>
- Salter, S.H., Jeffrey, D.C., & Taylor, J. (1975). First year Interim Report on Edinburgh Wave Power Project: Study of Mechanism to Extract Power from Sea Waves. Edinburgh, United Kingdom: University of Edinburgh.
- Swift-Hook, D.T., Count, B.M., Glendenning, I., & Salter, S. (1975). Characteristics of a Rocking Wave Power Device. *Nature*, 254(5500), 504-506.

### Author ORCIDs

Author name	ORCID
Poguluri, Sunny Kumar	0000-0003-2081-9673
Kim, Dongeun	0000-0002-7698-7273
Ko, Haeng Sik	0000-0002-1744-8878
Bae, Yoon Hyeok	0000-0002-5198-4519

# Engagement-Scenario-Based Decoy-Effect Simulation Against an Anti-ship Missile Considering Radar Cross Section and Evasive Maneuvers of Naval Ships

Kookhyun Kim<sup>1</sup>

<sup>1</sup>Professor, School of Naval Architecture & Ocean Engineering, Tongmyong University, Busan, Korea

**KEY WORDS:** Decoy effect, Radar cross section, Evasive maneuver, State-space model, Sea-skimming active radar homing missile

**ABSTRACT:** The survivability of a naval ship is the ability of the ship and its onboard systems to remain functional and continue a designated mission in man-made hostile environments. A passive decoy system is primarily used as a weapon system for improving the survivability of a naval ship. In this study, an engagement scenario-based simulation program was developed for decoy effectiveness assessments against an anti-ship missile (ASM), which tracks a target with sea-skimming and active radar homing. The program can explain the characteristics of a target ship, such as the radar cross section and evasive maneuvers, as well as the operational performance of the onboard decoy system, the guidance method of the ASM, and the engagement environment's wind speed and direction. This paper describes the theory and formulations, configuration, and user interface of the developed program. Numerical examples of a decoy effect assessment of a virtual naval ship against an ASM are presented.

## 1. Introduction

The survivability of a naval ship is the ability of the ship and its onboard systems to remain functional and continue a designated mission in man-made hostile environments. The survivability can be categorized using three sub-parameters: susceptibility, vulnerability, and recoverability. The total survivability can be assessed combining the probability measures of the sub-parameters (Kim and Lee, 2014). Susceptibility is the probability of not avoiding being hit by threats like anti-ship missiles (ASMs) and depends on the performance of threats and anti-air warfare (AAW) systems against them, as well as their signature characteristics.

The signatures of naval ships, such as the radar cross section (RCS), infrared (IR) signature, and visual signature, directly influence the susceptibility to threats. Particularly, RCS of a target ship is a factor for determining the performance of passive or active decoy systems for onboard soft-kill warfare against ASMs that use active radar homing for targeting and tracking. The decoy effectiveness is used as an index for the performance of passive decoy systems. A cumulative Gaussian distribution model has been used as a simple tool for decoy effectiveness assessment (An and Seo, 2015) but cannot explain the

variation in RCS and performance of a decoy system for various engagement scenarios.

There have been studies on engagement scenario-based simulations (TTI, 2002; Kumar, 1990; Manji et al., 2002). Chapman and Benke (2000) described a ship-to-air defense model (SADM) for susceptibility assessment in engagement environments, which includes soft-kill ability modeling with active decoys, chaff, and jammers; hard-kill ability modeling with missiles, guns, and fire-control systems; and a command-and-control system to track targets and coordinate soft-kill and hard-kill responses. Dan et al. (2016) presented a modeling and simulation (M&S) technique for a decoy system and its countermeasure capability against ASMs. Lukenbill (1990) and Swee (2000) simulated a target aircraft in an anti-air missile engagement scenario based on a state-space model and various guidance methods. Poulos (1994) studied anti-air warfare for a small navy group in defensive scenarios. Regarding the decoy effect, Seo et al. (2012) estimated the dynamic behavior and the corresponding RCS of decoy clouds in an engagement environment with wind conditions. Kim (2020) introduced a framework on a decoy effect simulation against an ASM to consider the RCS and tactical diameter of warships.

In this research, an engagement scenario-based simulation program

Received 17 May 2021, revised 8 June 2021, accepted 14 June 2021

Corresponding author Kookhyun Kim: +82-51-629-1658, [kimk@tu.ac.kr](mailto:kimk@tu.ac.kr)

© 2021, The Korean Society of Ocean Engineers

This is an open access article distributed under the terms of the creative commons attribution non-commercial license (<http://creativecommons.org/licenses/by-nc/4.0>) which permits unrestricted non-commercial use, distribution, and reproduction in any medium, provided the original work is properly cited.

named ASMD/RCS (ASM Defense/RCS) was developed for decoy effectiveness assessments. This program was implemented in MATLAB/Simulink with the assumption that ASMs are the sea-skimming type and use an active radar homing for targeting and tracking (Kim, 2020). The theory and formulations were obtained from Swee (2000). ASMD/RCS can explain the RCS and evasive maneuvers of a target ship, the operational performance of an onboard passive-type decoy system, the tracking scheme of ASMs, and engagement environments, including the wind speed and direction. This paper describes details of the developed program, the theory and formulations, configuration, the scenario designation, and the user interface. A decoy effectiveness assessment of a virtual naval ship is presented as a numerical example.

## 2. Theory and Formulations

Countermeasures with a decoy system are a general means of avoiding being hit by ASMs. Traditionally, a passive-type decoy system has been used, which is a soft-kill method of guiding ASMs to a fake target that is generated with a decoy cloud instead of the real target ship (Fig. 1). The decoy effectiveness depends on the RCS characteristics of the target ship and the decoy system. Generally, the higher the difference in RCS level is between the target ship and the decoy, the lower the hit probability is. However, the characteristics of the ship, decoy, and engagement environments collectively influence the probability. Examples are the evasive maneuver and RCS pattern of the target ship, the deploying scheme (range and direction) and RCS of the decoy, the dynamic performance of the ASM, and environmental conditions, such as the wind speed, direction, etc. In this study, these characteristic parameters were considered for the decoy effect simulation in a more realistic engagement scenario.

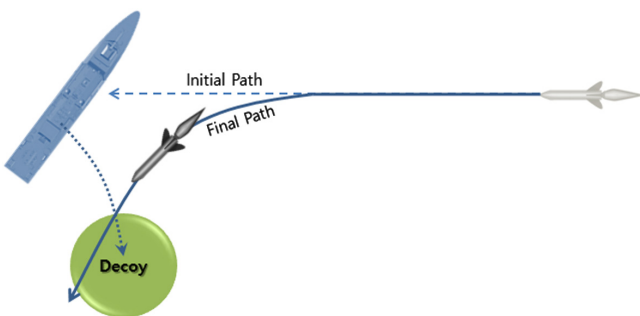


**Fig. 1** Concept of soft-kill against ASMs using passive-type decoy system

### 2.1 Target Ship Dynamics

The decoy effectiveness against ASMs depends on the evasive maneuvers of the target ship, which are based on the turning radius of the ship, as shown in Fig. 2. In general, the turning radius of the ship depends on the rudder angle and the instantaneous moving speed. In this study, however, the turning radius was calculated in meters with Eq. (1).

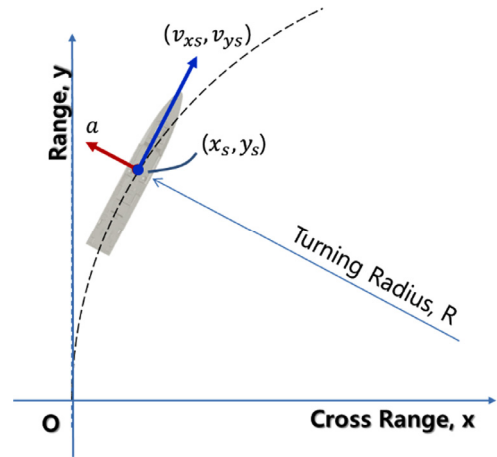


**Fig. 2** Turning radius of the target ship for evasive maneuver against ASMs

$$R = \frac{v_s^2}{a} = \frac{v_s^2}{g \cdot G_s^*} \quad (1)$$

where  $v_s = \sqrt{v_{x_s}^2 + v_{y_s}^2}$  is the instantaneous tangential speed of the target ship in m/s,  $a = g \cdot G_s^*$  is the instantaneous centripetal acceleration in  $\text{m/s}^2$ ,  $g$  is gravitational acceleration ( $9.81 \text{ m/s}^2$ ), and  $G_s^* = a/g$  is the g-value.

The target ship dynamics is implemented with the state-space equation below (Swee, 2000) based on the coordinate system in Fig. 2:

$$\begin{Bmatrix} \dot{x}_s \\ \dot{v}_{x_s} \\ \dot{y}_s \\ \dot{v}_{y_s} \end{Bmatrix} = \begin{bmatrix} 0 & 1 & 0 & 0 \\ 0 & 0 & 0 & -\omega_s \\ 0 & 0 & 0 & 1 \\ 0 & \omega_s & 0 & 0 \end{bmatrix} \begin{Bmatrix} x_s \\ v_{x_s} \\ y_s \\ v_{y_s} \end{Bmatrix} \quad (2)$$

where  $x_s$  and  $y_s$  are the coordinates of the cross range and the range in m, respectively,  $v_{x_s}$  and  $v_{y_s}$  are the instantaneous speed of the target ship in m/s,  $\omega_s = g \cdot G_s^*/v_s$  is the commanded evasive turning rate in  $1/\text{s}$  of the target ship and is constant during the simulation, and  $\dot{\quad}$  means the time derivative of these variables. For reference, a constant g-value  $G_s^*$  was used for the evasive maneuverability of the target ship instead of the centripetal acceleration. Negative and positive values mean starboard-side (right turn) and port-side evasive maneuvers (left turn) of the target ship, respectively.

### 2.2 Target Ship RCS

The inherent RCS pattern of the target ship influences the decoy effect on ASMs. The RCS pattern of the target ship varies with the azimuth angle, as shown in Fig. 3, which means that the RCS level also changes with the approach angle of the ASM, and the decoy effect varies with it as well. The predefined RCS pattern of the target ship was used to calculate the decoy RCS value of the azimuth angle corresponding to the ASM approach.

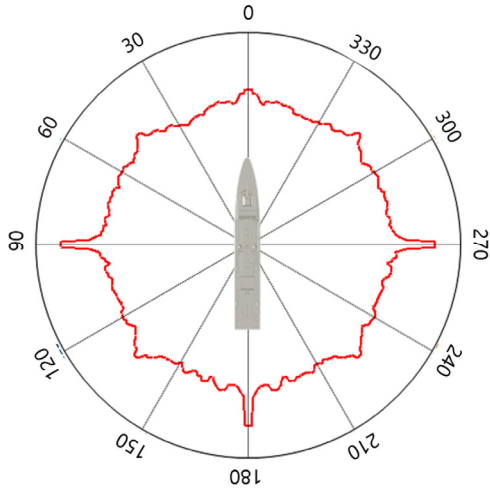


Fig. 3 RCS pattern of the target ship with azimuth angle

### 2.3 ASM Dynamics

The ability of an ASM to intercept a target ship mainly depends on the guidance method. Two main types of guidance methods can be employed: proportional navigation (PN) and command to line of sight (CLOS). PN is the most widely used homing guidance law and seeks to null the line-of-sight (LOS) angle rate by making the missile turn rate directly proportional to the LOS rate. CLOS uses only the angular coordinates between the ASM and the target ship, and the ASM is made to be in the LOS between the launcher and target. Any deviation of the missile from this line is corrected.

CLOS has inherent range limitations due to its sensitivity to angular tracking errors between the launching station and the ship target. PN is self-homing and relies on an on-board seeker to provide the target's LOS information directly, so it does not suffer from the range limitations encountered by CLOS (Swee, 2000). 2-dimensional missile dynamics was simulated by assuming an engagement scenario where the target ship does evasive maneuvers against sea-skimming ASMs that employ a PN homing law when tracking the ship target (Fig. 4).

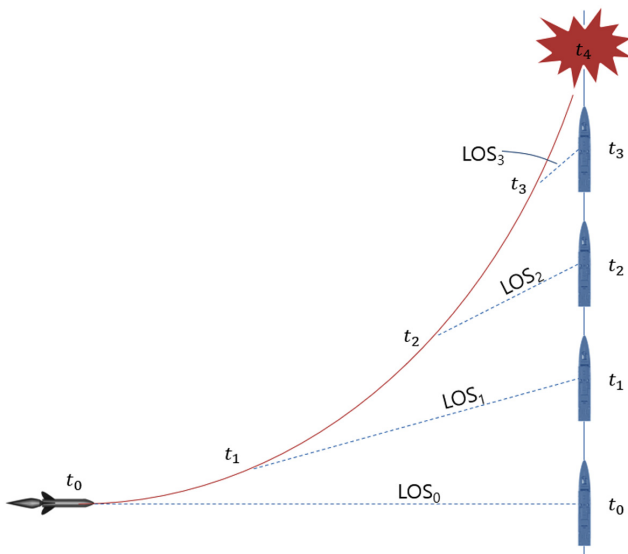


Fig. 4 Proportional navigation to intercept the ship target

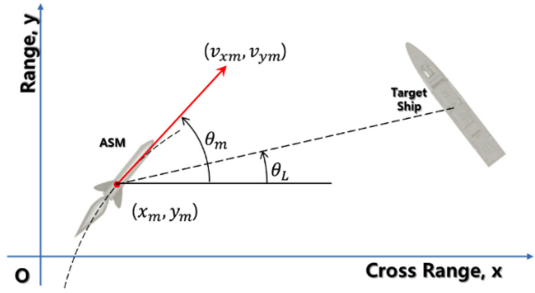


Fig. 5 ASM guidance to the target ship

Similarly to the target ship, the ASM dynamics can be implemented with the state-space equation below with the coordinate system in Fig. 5:

$$\begin{cases} \dot{x}_m \\ \dot{v}_{xm} \\ \dot{y}_m \\ \dot{v}_{ym} \end{cases} = \begin{bmatrix} 0 & 1 & 0 & 0 \\ 0 & 0 & 0 & -\omega_m \\ 0 & 0 & 0 & 1 \\ 0 & \omega_m & 0 & 0 \end{bmatrix} \begin{cases} x_m \\ v_{xm} \\ y_m \\ v_{ym} \end{cases} \quad (3)$$

where  $x_m$  and  $y_m$  are the coordinates of the cross range and the range in m,  $v_{xm}$  and  $v_{ym}$  are the instantaneous speeds of the ASM in m/s, respectively, and  $\omega_m$  is the commanded turning rate of the ASM in 1/s, which varies depending on the applied guidance method and state. Two types of PN can be applied: true- and pure-proportional navigation (TPN & PPN). This study employs TPN, and the commanded turn-rate of the ASM is calculated by Eq. (4):

$$\omega_m = \frac{N \cdot v_c \cdot \dot{\theta}_L}{\cos(\theta_m - \theta_L) \sqrt{v_{xm}^2 + v_{ym}^2}} \quad (4)$$

where  $N$  is a proportional constant that typically varies from 3 to 5 (3 was used in this study).  $v_c$  is the instantaneous closing velocity of the ASM to the target ship in m/s.  $\dot{\theta}_L$  is the LOS rate between the ASM and the target ship in rad/s.  $\theta_m$  and  $\theta_L$  are the moving directions of the ASM and the LOS angle with respect to the cross-range axis in rad, respectively.

### 2.4 Decoy Dynamics

The decoy dynamics is a complex problem that is influenced by the engagement environment, including the wind speed and direction.

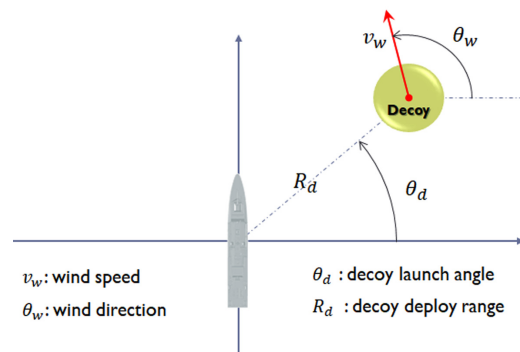
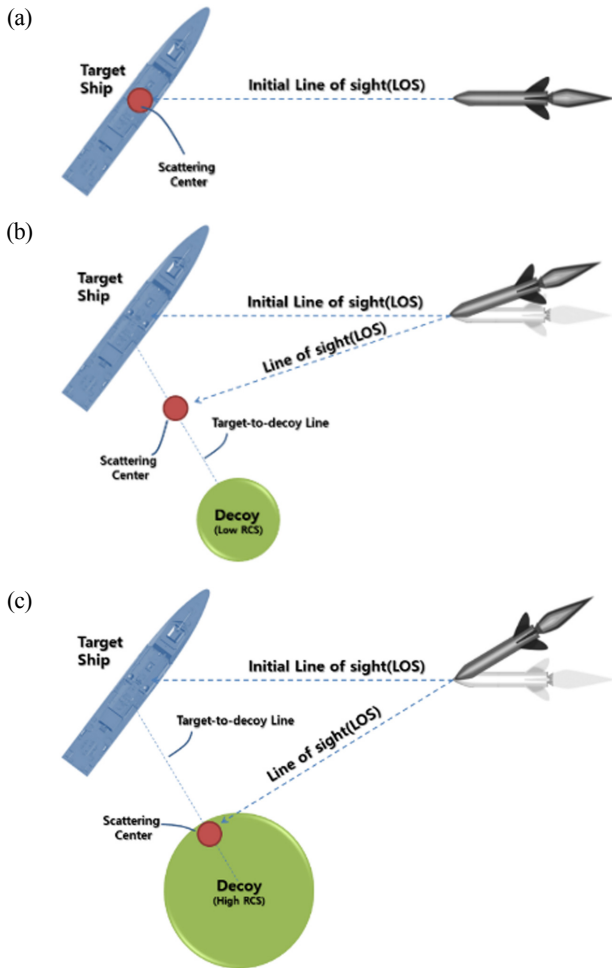


Fig. 6 Geometry of decoy dynamics

Therefore, the problem should be simplified for convenience in the simulation. This study assumes that the decoy operates as follows: (1) launching to the direction  $\theta_d$  in rad and deploying at the range  $R_d$  in m, (2) forming a decoy cloud and retaining its size, and (3) moving at the wind speed  $v_w$  in m/s along the wind direction  $\theta_w$  in rad, where the decoy has an omni-directional scatter, and the RCS level is kept constant during the simulation (Fig. 6).

### 2.5 Equivalent Scattering Center Targeting

The RCS of the target ship can be represented with a scattering source point called a “scattering center” in the far field, which is when the target ship is electromagnetically far enough from the ASMs. Interestingly, in an engagement environment, an ASM intercepts the virtual scattering center, not the real target ship (Fig. 7(a)). Therefore, when the target ship deploys a decoy with the intended RCS level to the offboard range and direction, the scattering center moves along the target-to-decoy line (Fig. 7(b) and Fig. 7(c)). As a result, the LOS moves, and the susceptibility changes. The larger the decoy RCS is, the further the scattering center is from the target ship, and the lower the susceptibility is to the ASM.



**Fig. 7** Scattering center position change by decoy RCS level: (a) no decoy, (b) small decoy (w/ low RCS), and (c) large decoy (w/ high RCS)

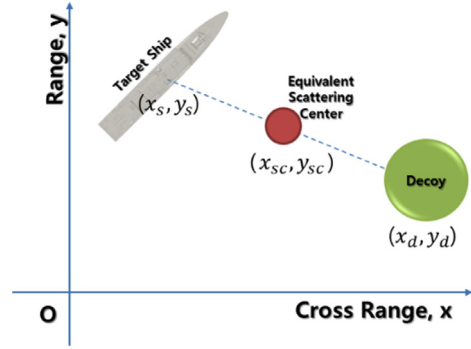


**Fig. 8** Equivalent scattering center position

Referring to the coordinate system in Fig. 8, this study estimates the RCS level  $\sigma_{sc}$  in dBsm and position  $(x_{sc}, y_{sc})$  in m of the equivalent scattering center, which is distinguished from that of the target ship using Eq. (5) and Eq. (6), respectively:

$$\sigma_{sc} = 10 \log_{10} (10^{\sigma_s/10} + 10^{\sigma_d/10}) \quad (5)$$

$$\begin{cases} x_{sc} = \frac{10^{\sigma_s/10} x_s + 10^{\sigma_d/10} x_d}{10^{\sigma_{sc}/10}} \\ y_{sc} = \frac{10^{\sigma_s/10} y_s + 10^{\sigma_d/10} y_d}{10^{\sigma_{sc}/10}} \end{cases} \quad (6)$$

where  $\sigma_s$  and  $\sigma_d$  are the RCS level in dBsm of the target ship and the decoy cloud, respectively.  $(x_d, y_d)$  is the instantaneous position of the decoy cloud in m and is determined by assuming that the deployed cloud moves along the wind direction with the same speed as the wind.

### 3. ASMD/RCS

ASMD/RCS was implemented using the theory and formulations presented in the previous section. ASMD/RCS can consider the performance of the target ship and the ASM, the engagement environments, and the way to simulate the decoy effectiveness (Fig.9).

The program consists of four blocks, as shown in Fig. 10: a decoy block, guide block, target ship block, and missile block. The decoy block includes the decoy performance and dynamics (RCS, deployment range and direction, and movement wind and its direction). The guide block implements the ASCM’s targeting and tracking with the missile-to-target guidance algorithm. The target ship block includes the target ship performance and status (the initial

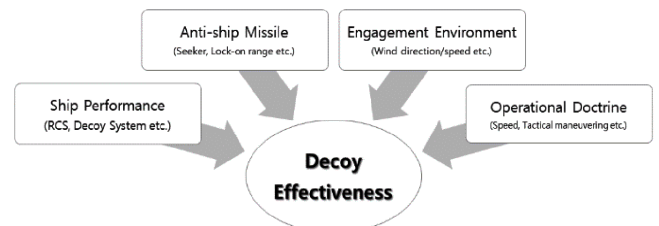


**Fig. 9** Considerations of ASMD/RCS for decoy effectiveness assessment

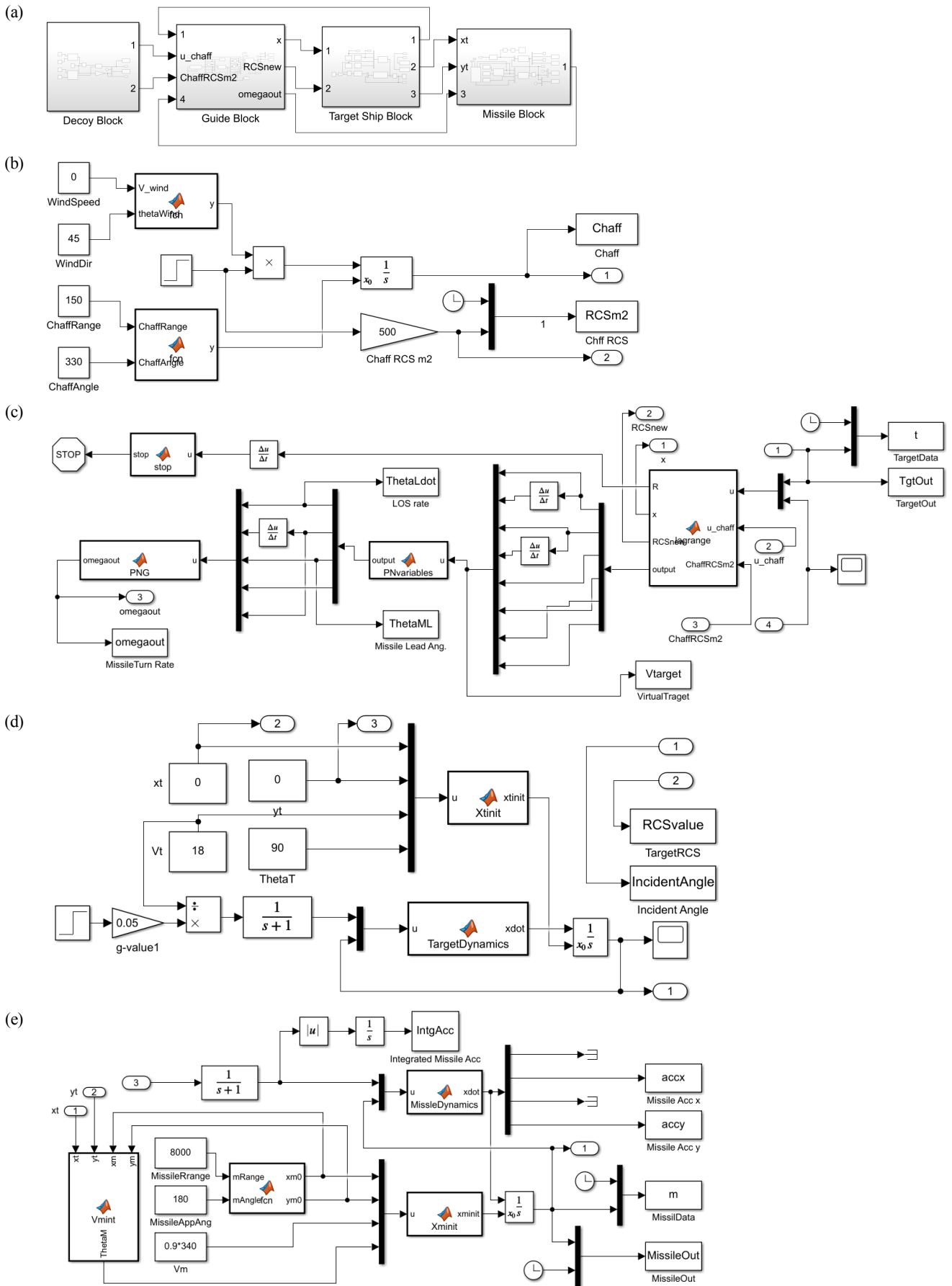


Fig. 10 ASMD/RCS block configuration: (a) ASMD/RCS, (b) decoy block, (c) guide block, (d) target ship block, and (e) missile block

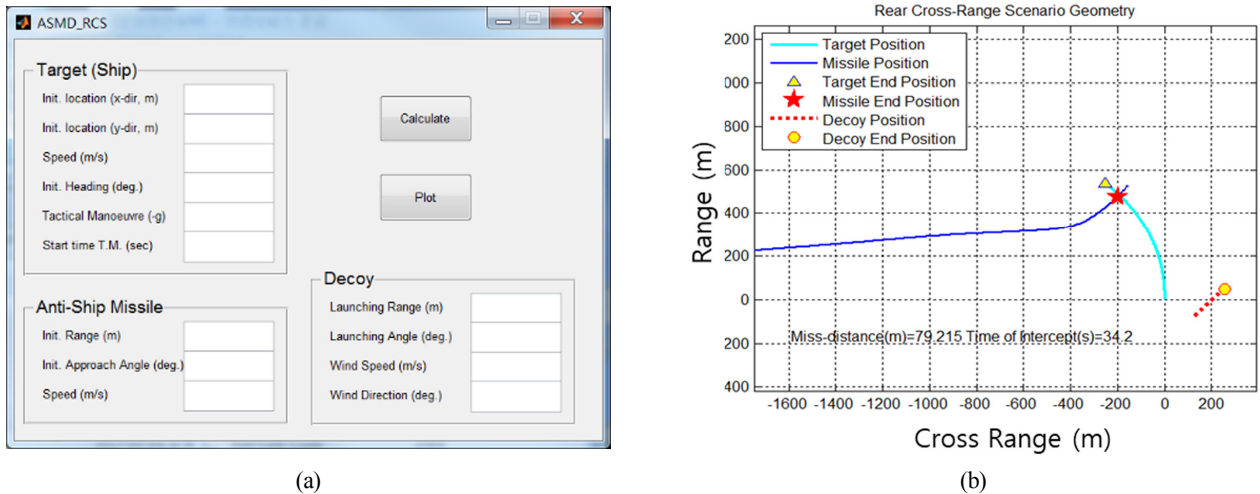


Fig. 11 ASMD/RCS (a) user interface and (b) engagement trajectory viewer

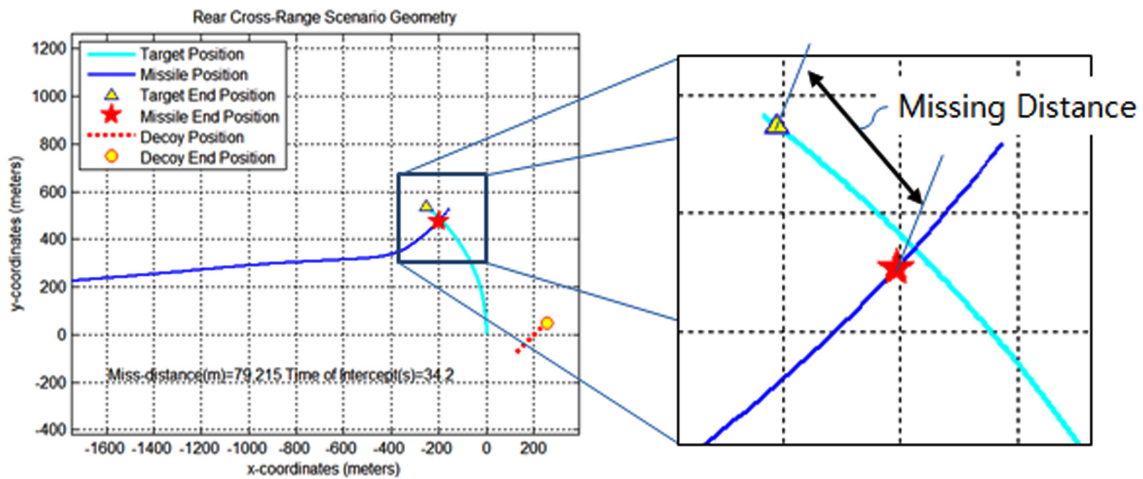


Fig 12 Definition of missing distance

position, RCS, speed, direction, and evasive maneuver of the target ship). Finally, the missile block simulates the ASM dynamics.

Fig. 11 shows the program’s user interface and a plot of the simulation results. The interface is composed of 13 input boxes for simulation parameters and two buttons for program execution and a result plot. The plot displays trajectories of the ASM, the target ship, and the decoy, as well as text-based results, such as the missing distance and time to intercept. The term “missing distance” means the closest point of approach (CPA) synchronized from the center of the target ship to the ASM trajectory at the moment “time of intercept” (Fig. 12). This judges whether the target ship will be intercepted by the ASM or not by assessing whether the resultant missing distance in  $m$  exceeds the pre-defined threshold. This study uses two times the length of the target ship as a threshold.

### 4. Numerical Examples

#### 4.1 Engagement Scenarios

Decoy effect simulations were conducted using ASMD/RCS in some engagement scenarios. Following the input parameter symbols in

Fig. 13, the engaging speed  $v_m$ , lock-on range  $R_m$ , and approach angle  $\theta_m$  of the ASM were set to Mach 0.9 (~306 m/s), 8 km, and 180 degrees, respectively. The centripetal acceleration was limited to 20-g. The length of the target ship was 45 m, and the corresponding missing distance threshold was two times the target ship length. The ship speed  $v_s$  was 35 knots (~18 m/s), and the RCS pattern  $\sigma_s$  is shown in Fig. 14. The decoy is launched toward any direction  $\theta_d$  and deployed at a range  $R_d$  of 150 m.

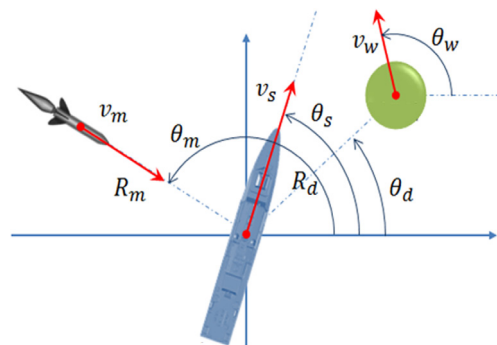
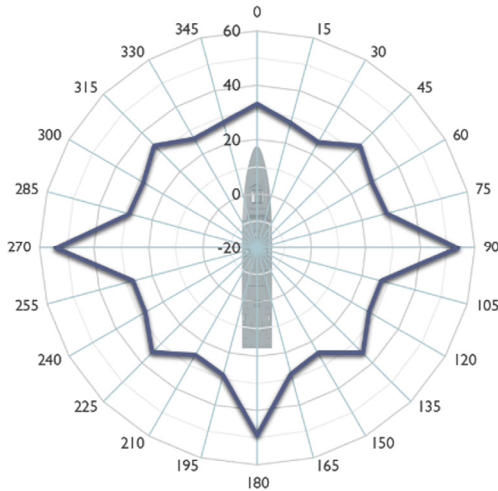


Fig. 13 Input parameter for engagement simulation



**Fig. 14** RCS pattern of the target ship for engagement simulation

The RCS level  $\sigma_d$  of the decoy varies (27, 30, 33, 37, and 40 dBsm, which correspond to 500, 1000, 2000, 5000, and 10000 m<sup>2</sup>, respectively). There is only one chance of launching a decoy, and an evasive maneuver is done during the engagement at the same time as the ASM lock-on. The simulation designated three engagement scenarios with varying g-value  $G_s^*$  of the target ship to 0-g, 0.05-g, and -0.05-g when the wind speed  $v_w$  and direction  $\theta_w$  were 10 knots (~5.14 m/s) and 45 degrees, respectively.

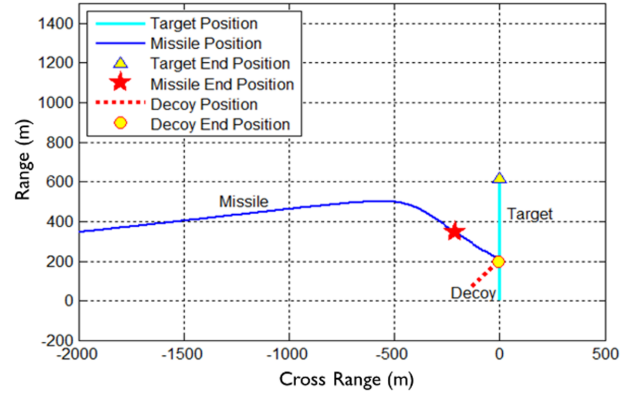
**4.2 Simulation Results**

Fig. 15 shows simulation results for the scenarios for when the decoy launching direction  $\theta_d$  is 135 degrees and the RCS of the target ship is 40 dBsm (10,000 m<sup>2</sup>). The target ship survives when doing no evasive maneuver (0-g), but it is intercepted when doing the port-side (0.05-g) and starboard-side (-0.05-g) evasive maneuvers. In starboard-side evasive maneuvers, the primary deception succeeds, but the ship is eventually intercepted. This means that ASMD/RCS can simulate complicated engagement scenarios more realistically.

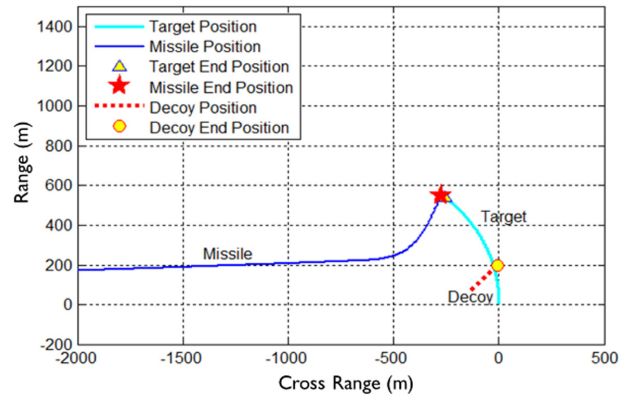
Fig. 16 shows polar plots of the simulated missing distance versus the decoy launching direction  $\theta_d$  for the scenarios. The curves present the simulated missing distance with respect to the RCS level  $\sigma_d$  of the decoy (27 dBsm (500 m<sup>2</sup>), 30 dBsm (1,000 m<sup>2</sup>), 33 dBsm (2,000 m<sup>2</sup>), 37 dBsm (5,000 m<sup>2</sup>), and 40dBsm (10,000 m<sup>2</sup>)). The dotted red reference line shows the pre-defined threshold (two times the target ship length: 90 m).

With no evasive maneuver (0-g), the missing distance increased as the decoy RCS increased. When the decoy RCS levels were above 37 dBsm (5,000 m<sup>2</sup>), the target ship was hit less overall. When the decoy of 33 dBsm (2,000 m<sup>2</sup>) was launched between 150 degrees and 300 degrees, the target ship was hit less. When the decoy RCS level was 40 dBsm (10,000 m<sup>2</sup>), wind reduced the susceptibility of the 300-degree and 330-degree decoy deployments.

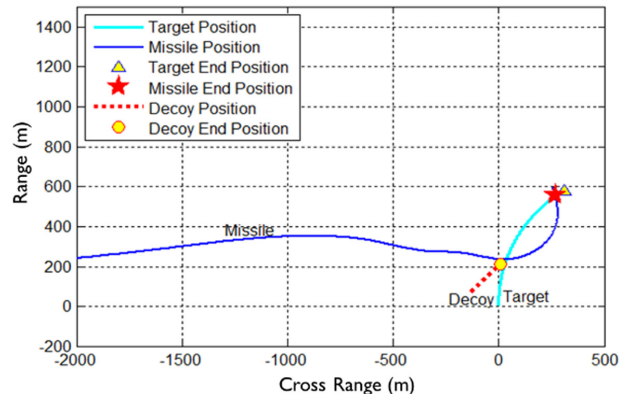
For the port-side evasive maneuver (0.05-g), the decoy effect was minimal in general. An evasive maneuver works unfavorably in terms of susceptibility to ASMs. The decoy was moved by the wind along



(a)



(b)



(c)

**Fig. 15** Engagement simulation results when the decoy launching direction  $\theta_d$  is 135 degrees: (a) no evasive maneuver (0-g), (b) port-side evasive maneuver (0.05-g), and (c) starboard-side (-0.05-g) evasive maneuver

the 45-degree direction, which slightly increased the susceptibility of the decoy deployments at 0 degrees, 300 degrees, and 330 degrees. For the starboard-side evasive maneuver (-0.05-g), the missing distance increased as the decoy RCS increased. Simultaneously, the susceptibility was reduced when the decoy was deployed toward 120 to 240 degrees. It was confirmed that the ASMD/RCS program was successfully implemented and could be applied to decoy effect simulations of various engagement scenarios.

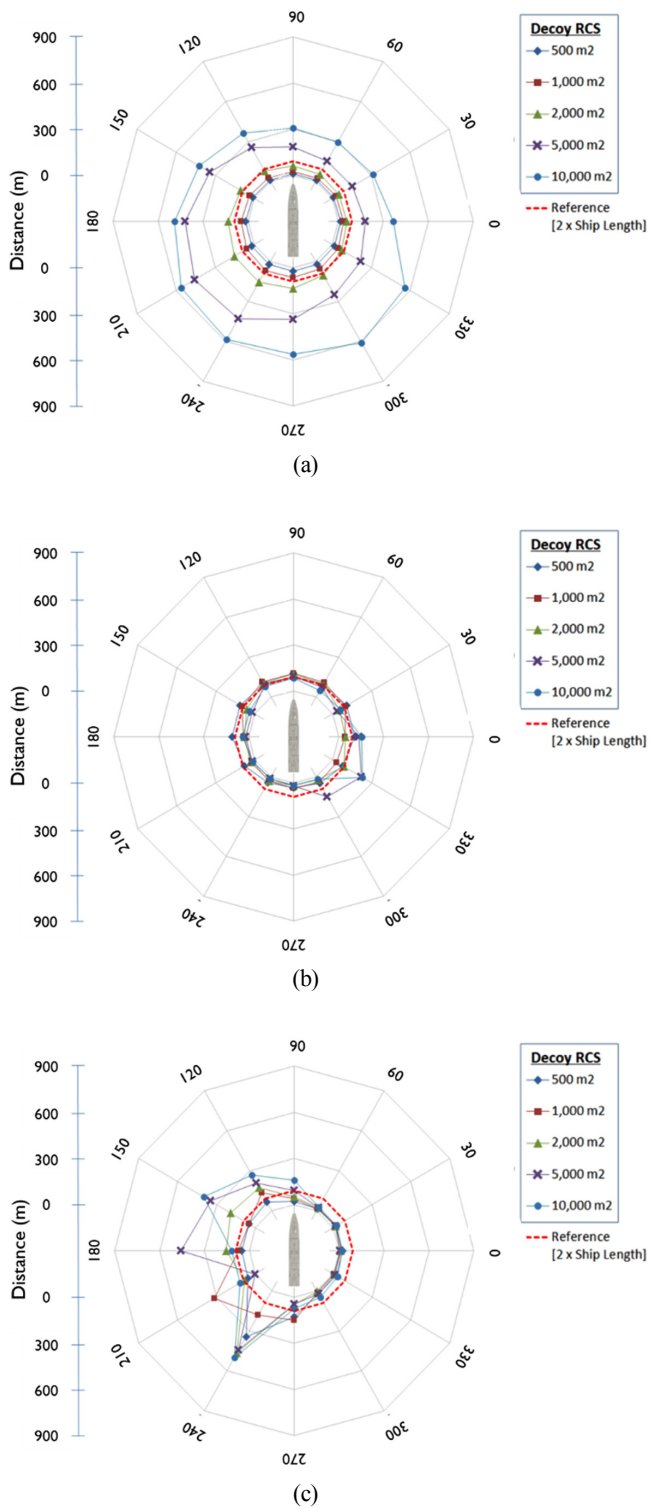


**Fig. 16** Simulated missing distance versus the decoy launching direction  $\theta_d$  in engagement scenarios: (a) no evasive maneuver (0-g), (b) port-side evasive maneuver (0.05-g), and (c) starboard-side evasive maneuver (-0.05-g).

### 5. Conclusions

An engagement scenario-based simulation program named ASMD/RCS was developed based on a state-space model to assess the

decoy effect on a sea-skimming ASM using an active radar homing for targeting and tracking. The programs can consider the RCS and tactical maneuvers of the target ship, the onboard decoy system performance, the ASM guidance algorithm, and the engagement environment’s wind speed and direction. The program provides a user interface for input parameters, executing the program, and plotting results. Numerical simulations of virtual engagement scenarios were conducted for various RCSs and launching directions of the decoy. The results showed that the input parameter variations in engagement environments influence the decoy effect. It is expected that the program could be practically used for assessing a decoy system’s performance for naval ships.

### Acknowledgments

This research was supported by Tongmyong University Research Grants 2019 (2019A020-1).

### References

An, B., & Seo, S. (2015). A Study on the Setting Procedure of Standard Value and Design Target Value for the RCS Reduced Design for Naval Ships. *Journal of Korean Institute of Electromagnetic Engineering and Science*, 26(6), 581–588. <https://doi.org/10.5515/KJKIEES.2015.26.6.581>

Chapman, S.J., & Benke, K. (2000). Assessment of Ship Air Defence Performance by Modelling and Simulation. *Proceedings of the Simulation Technology and Training Conference*, Perth WA, Australia, 235–241.

Dan, J., Hao, C., & Lei, Z. (2016). A Simulation Study of Chaff Echo Signal Based on LFM. *International Journal of Signal Processing, Image Processing and Pattern Recognition*, 9(4), 131–140. <https://doi.org/10.14257/ijsp.2016.9.4.12>

Kim, K., & Lee, J. (2014). Integrated Survivability Assessment Given Multiple Penetration Hits. *Journal of Ocean Engineering and Technology*, 28(1), 69–76. <https://doi.org/10.5574/KSOE.2014.28.1.069>

Kim, K. (2020). Decoy Effectiveness Simulation Against Anti-Ship Missile Considering RCS and Tactical Diameter of Warship. *Proceeding of Korean Society of Ocean Engineers Fall Conference, On-line*, 198–200.

Kumar, R. (1990). Defense of Surface Ships Against Anti-Ship Missiles (Master’s thesis). Naval Postgraduate School, Monterey CA, USA.

Lukenbill, F.C. (1990). A Target Missile Engagement Scenario Using Classical Proportional Navigation (Master’s thesis). Naval Postgraduate School, Monterey CA, USA.

Manji, N., Kocakanat, M., & Kitsikis, A. (2002). Quantifying the Effects of Chaff Screening on Hardkill and Softkill Coordination (Report No. RTO-MP-097(I)). Ottawa Canada: Defense R&D Canada.

- Poulos, A.M. (1994). An Anti-air Warfare Study for a Small Size Navy (Master's thesis). Naval Postgraduate School, Monterey CA, USA.
- TTI. (2002). User's Guide: ASCMA Anti-Ship Cruise Missile ECM Effectiveness Simulator. 3.2, Ottawa, Ontario, Canada: Tactical Technologies Inc.
- Seo, D.W., Nam, H., Kwon O., & Myung, N.H. (2012). Dynamic RCS Estimation of Chaff Clouds. *IEEE Transactions on Aerospace and Electronic Systems*, 48(3), 2114-2127. <https://doi.org/10.1109/TAES.2012.6237582>
- Swee, J. CS. (2000). Missile Terminal Guidance and Control Against Evasive Target (Master's thesis). Naval Postgraduate School, Monterey CA, USA.

### Author ORCID

Author name	ORCID
Kim, Kookhyun	0000-0002-4214-4673

# Instructions for Authors

## General information

To submit a manuscript to the Journal of Ocean Engineering and Technology (JOET), it is advised to first carefully read the aims and the scope section of this journal, as it provides information on the editorial policy and the category of papers it accepts. Unlike many regular journals, JOET usually has no lag in acceptance of a manuscript and its publication. Authors that find a match with the aims and the scope of JOET are encouraged to submit as we publish works from all over the world. JOET adheres completely to guidelines and best practices published by professional organizations, including Principles of Transparency and Best Practice in Scholarly Publishing (joint statement by COPE, DOAJ, WAME, and OASPA (<http://doaj.org/bestpractice>) if otherwise not described below. As such, JOET would like to keep the principles and policies of those professional organizations during editing and the publication process.

## Research and publication ethics

Details on publication ethics are found in <http://joet.org/authors/ethics.php>. For the policies on research and publication ethics not stated in the Instructions, Guidelines on Good Publication (<http://publicationethics.org/>) can be applied.

## Requirement for membership

One of the authors who submits a paper or papers should be member of the Korean Society of Ocean Engineers (KSOE), except a case that editorial board provides special admission of submission.

## Publication type

Article types include scholarly monographs (original research articles), technical articles (technical reports and data), and review articles. The paper should have not been submitted to other academic journal. When part or whole of a manuscript was already published to conference papers, research reports, and dissertations, then the corresponding author should note it clearly in the manuscript.

## Copyright

After published to JOET, the copyright of manuscripts should belong to KSOE. A transfer of copyright (publishing agreement) form can be found in submission website (<http://www.joet.org>).

## Manuscript submission

Manuscript should be submitted through the on-line submission website (<http://www.joet.org>). The date that manuscript was received through on-line website is the official date of receipt. Other correspondences can be sent by an email to the Editor in Chief or secretariat. The manuscript must be accompanied by a signed statement that it has been neither published nor currently submitted for publication elsewhere. The manuscript should be written in English or Korean. Ensure that online submission are in a standard word processing format. Corresponding author must write the manuscript using the JOET template provided in Hangul or MS Word format. Ensure that graphics are high-resolution.

Be sure all necessary files have been uploaded/ attached.

## Authors' checklist

Please refer to "Authors' Checklist" for details.

## Article structure

Manuscript must be edited in the following order: (1) Title, (2) Authors' names and affiliations, (3) Keywords, (4) Abstract, (5) Nomenclature (optional), (6) Introduction, (7) Main body (analyses, tests, results, and discussions), (8) Conclusions, (9) Conflict of interest (optional), (10) Funding (optional), (11) Acknowledgements (optional), (12) References, (13) Appendices (optional), (14) Author's ORCID.

## Abstract

A concise and factual abstract is required. The abstract should state briefly the background, purpose and methods of the research, the principal results and conclusions. An abstract should be written in around 300 words. References are not cited in abstract whenever possible. Also, non-standard or uncommon abbreviations should be avoided, but if essential they must be defined at their first mention in the abstract itself.

## Keywords

Immediately after the abstract, provide a maximum of 5 or 6 keywords.

## Unit

Use the international system units(SI). If other units are mentioned, please give their equivalent in SI.

## Equations

All mathematical equations should be clearly printed/typed using well accepted explanation. Superscripts and subscripts should be typed clearly above or below the base line. Equation numbers should be given in Arabic numerals enclosed in parentheses on the right-hand margin.

## Tables

Tables should be numbered consecutively with Arabic numerals. Each table should be fully titled. All tables should be referred to in the texts.

## Figures

Figures should be numbered consecutively with Arabic numerals. Each figure should be fully titled. All figures should be referred to in the texts. All the illustrations should be of high quality meeting with the publishing requirement with legible symbols and legends.

## Conflict of interest

It should be disclosed here according to the statement in the Research and publication ethics regardless of existence of conflict of interest. If the authors have nothing to disclose, please state: "No potential

conflict of interest relevant to this article was reported.”

### Funding

Funding to the research should be provided here. Providing a FundRef ID is recommended including the name of the funding agency, country and if available, the number of the grant provided by the funding agency. If the funding agency does not have a FundRef ID, please ask that agency to contact the FundRef registry (e-mail: fundref.registry@crossref.org). Additional detailed policy of FundRef description is available from <http://www.crossref.org/fundref/>. Example of a funding description is as follows: The study is supported by the Inha University research fund (FundRef ID: 10.13039/501100002632), and the Korea Health Personnel Licensing Examination Institute research fund (FundRef ID: 10.13039/501100003647).

### Acknowledgments

Any persons that contributed to the study or the manuscript, but not meeting the requirements of an authorship could be placed here. For mentioning any persons or any organizations in this section, there should be a written permission from them.

### References in text

References in texts follow the APA style. Authors can also see how references appear in manuscript text through the ‘Template’.

### Reference list

Reference list follows the APA style. Authors can see how references should be given in reference section through the ‘Template’.

### Appendices

The appendix is an optional section that can contain details and data supplemental to the main text. If there is more than an appendix, they should be identified as A, B, C, etc. Formulae and equations in appendices should be given separate numbering: Eq. (A1), Eq. (A2), etc.; in a subsequent appendix, Eq. (B1) and so on. Similarly for tables and figures: Table A1; Fig. A1, etc.

### ORCID (Open Researcher and Contributor ID)

All authors are recommended to provide an ORCID. To obtain an ORCID, authors should register in the ORCID web site: <http://orcid.org>. Registration is free to every researcher in the world. Example of ORCID description is as follows:

Joonmo Chung: <https://orcid.org/0000-0003-1407-9031>

### Peer review and publication process

The peer review process can be broadly summarized into three groups: author process, review process, and publishing process for accepted submissions. General scheme is presented in Figure 1.

#### Check-in process for review

If the manuscript does not fit the aims and scope of the Journal or does not adhere to the Instructions to Authors, it may be rejected immediately after receipt and without a review. Before reviewing, all submitted manuscripts are inspected by Similarity Check powered by iThenticate (<https://www.crossref.org/services/similarity-check/>), a plagiarism-screening tool. If a too high degree of similarity score is found, the Editorial Board will do a more profound content screening.

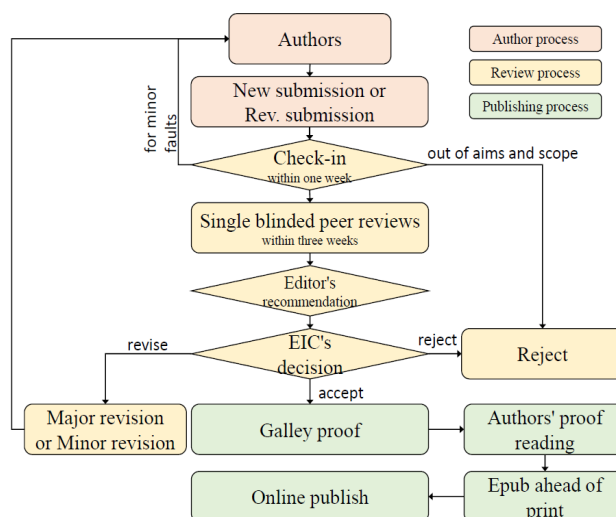


Figure 1 Flow chart of the peer review and publication process of JOET

The criterion for similarity rate for further screening is usually 15%; however, rather than the similarity rate, the Editorial Board focuses on cases where specific sentences or phrases are similar. The settings for Similarity Check screening are as follows: It excludes quotes, bibliography, small matches of 6 words, small sources of 1%, and the Methods section.

#### Number of reviewers

Reviewers will be selected from the list of reviewers. Manuscripts are then peer reviewed by at least 2 experts in the corresponding field, usually by 2.

**Peer review process and the author response to the reviewer comments**  
JOET adopts single blind review, which means that the authors do not know the identity of the reviews. All papers, including those invited by the Editor, are subject to peer review.

The review period is 4 weeks. Usually the first decision is made within a week after completion of the review. The Editorial Board's decision after the review will be one of followings: Accept, Minor revision, Major revision, or Rejection. The Editorial Board may request the authors to revise the manuscript according to the reviewers' comments. If there are any requests for revision of the manuscript by the reviewers, the authors should do their best to revise the manuscript. If the reviewer's opinion is not acceptable or is believed to misinterpret the data, the author should reasonably indicate that. After revising the manuscript, the author should upload the revised files with a separate response sheet to each item of the reviewer's commentary. The author's revisions should be completed within 3 months after the request. If it is not received by the due date, the Editorial Board will notify the author. To extend the revision period beyond 3 months, the author should negotiate that with the Editorial Board. The manuscript review process can be provided for up two rounds. If the authors wish further review, the Editorial Board may consider it. The Editorial Board will make a final decision on the approval of the submitted manuscript for publication and can request any further corrections, revisions, and deletions of the article text if necessary. Statistical editing is also performed if the data requires professional statistical review by a statistician.

### *Processing after acceptance*

If the manuscript is finally accepted, the galley proof will be sent to the corresponding author after professional manuscript editing and English proofreading. Proofreading should be performed for any misspellings or errors by the authors. Proofreading manuscript for publication is provided to the corresponding author, and the corresponding author must review the proofreading manuscript. Corresponding authors are responsible for the content of the proofreading manuscript and any errors. After final proofreading, the manuscript may appear at the journal homepage as an article in press with a unique DOI number for rapid communication. All published articles will be replaced by the replacement XML file and a final PDF.

### *Feedback after publication*

If the authors or readers find any errors, or contents that should be revised, it can be requested from the Editorial Board. The Editorial Board may consider erratum, corrigendum or a retraction. If there are any revisions to the article, there will be a CrossMark description to announce the final draft. If there is a reader's opinion on the published article with the form of Letter to the editor, it will be forwarded to the authors. The authors can reply to the reader's letter. Letter to the editor and the author's reply may be also published.

### *How the journal handle complaints and appeals*

The policy of JOET is primarily aimed at protecting the authors, reviewers, editors, and the publisher of the journal. If not described below, the process of handling complaints and appeals follows the guidelines of the Committee of Publication Ethics available from: <https://publicationethics.org/appeals>

#### *- Who complains or makes an appeal?*

Submitters, authors, reviewers, and readers may register complaints and appeals in a variety of cases as follows: falsification, fabrication, plagiarism, duplicate publication, authorship dispute, conflict of interest, ethical treatment of animals, informed consent, bias or unfair/inappropriate competitive acts, copyright, stolen data, defamation, and legal problem. If any individuals or institutions want to inform the cases, they can send a letter via the contact page on

our website: <https://www.joet.org/about/contact.php>. For the complaints or appeals, concrete data with answers to all factual questions (who, when, where, what, how, why) should be provided.

#### *- Who is responsible to resolve and handle complaints and appeals?*

The Editorial Board or Editorial Office is responsible for them. A legal consultant or ethics editor may be able to help with the decision making.

#### *- What may be the consequence of remedy?*

It depends on the type or degree of misconduct. The consequence of resolution will follow the guidelines of the Committee of Publication Ethics (COPE).

### **Article processing charge**

#### *Payment due*

Article processing charge (APC) covers the range of publishing services JOET provides. This includes provision of online tools for editors and authors, article production and hosting, and customer services. Upon editorial acceptance of an article for the regular review service and upon submission of an article for the fast review service, the corresponding author will be notified that payment is due.

#### *APC*

The APC up to 6 pages is ₩200,000 (or \$200) and ₩550,000 (or \$550) for the for the regular and fast review services, respectively. An extra APC of \$50 per page is charged for papers longer than 6 pages. No taxes are included in this charge. For the fast review service, an advance fee of ₩250,000 (\$250) should be paid on submission.

#### *Payment methods*

*Credit card payment* can be made online using a secure payment form as soon as the manuscript has been editorially accepted. We will we send a receipt by email once payment has been processed. Please note that payment by credit card carries a surcharge of 10% of the total APC.

*Invoice payment* is due within 7 days of the manuscript receiving editorial acceptance. Receipts are available on request.



Original Research Article, Technical Article, Review Article, etc

## Title of Article

Firstname Lastname<sup>1</sup>, Firstname Lastname<sup>2</sup> and Firstname Lastname<sup>3</sup>

<sup>1</sup>Professor, Department of OO, OO School, OO University, Busan, Korea

<sup>2</sup>Graduate Student, Department of OO, OO University, Seoul, Korea

<sup>3</sup>Senior Researcher, Department of OO, OO Engineering, Corp., Seoul, Korea

**KEY WORDS:** Lumped mass line model, Explicit method, Steel lazy wave riser (provide a maximum of 5 or 6 keywords.)

**ABSTRACT:** A concise and factual abstract is required. The abstract should state briefly the background, purpose and methods of the research, the principal results and conclusions. An abstract should be written in around 300 words. References are not cited in abstract whenever possible. Also, non-standard or uncommon abbreviations should be avoided, but if essential they must be defined at their first mention in the abstract itself.

### Nomenclature (Optional)

$ITOC$	Increment of total operating cost (\$/yr)
$LHV$	Lower heating value (kJ/kg)
$P_w$	Power (kW)
$T$	Temperature (K)
$V$	Volume (m <sup>3</sup> )
$\rho$	Density (kg/m <sup>3</sup> )

## 1. Introduction

The introduction should briefly place the study in a broad context and highlight why it is important. It should define the purpose of the work and its significance. The current state of the research field should be reviewed carefully and key publications cited. Please highlight controversial and diverging hypotheses when necessary. Finally, briefly mention the main aim of the work and highlight the principal conclusions. As far as possible, please keep the introduction comprehensible to scientists outside your particular field of research.

## 2. General Information for Authors

### 2.1 Research and Publication Ethics

Authorship should be limited to those who have made a significant contribution to the conception, design, execution, or interpretation of the reported study. All those who have made significant contributions should be listed as co-authors. Where there are others who have participated in certain substantive aspects of the research project, they should be acknowledged or listed as contributors.

The corresponding author should ensure that all appropriate co-authors and no inappropriate co-authors are included on the paper, and that all co-authors have seen and approved the final version of the paper and have agreed to its submission for publication.

Details on publication ethics are found in the journal's website (<http://joet.org/authors/ethics.php>). For the policies on research and publication

Received 00 February 2100, revised 00 October 2100, accepted 00 October 2100

Corresponding author Firstname Lastname: +82-51-759-0656, e-mail@e-mail.com

It is a recommended paper from the proceedings of 2019 spring symposium of the Korea Marine Robot Technology (KMRTS).

© 2100, The Korean Society of Ocean Engineers

This is an open access article distributed under the terms of the creative commons attribution non-commercial license (<http://creativecommons.org/licenses/by-nc/4.0>) which permits unrestricted non-commercial use, distribution, and reproduction in any medium, provided the original work is properly cited.

ethics not stated in the Instructions, Guidelines on Good Publication (<http://publicationethics.org/>) can be applied.

### 2.2 Requirement for Membership

One of the authors who submits a paper or papers should be member of The Korea Society of Ocean Engineers (KSOE), except a case that editorial board provides special admission of submission.

### 2.3 Publication Type

Article types include scholarly monographs (original research articles), technical articles (technical reports and data), and review articles. The paper should have not been submitted to other academic journal. When part or whole of a manuscript was already published to conference papers, research reports, and dissertations, then the corresponding author should note it clearly in the manuscript.

Example: It is noted that this paper is revised edition based on proceedings of KAOST 2100 in Jeju.

### 2.4 Copyright

After published to JOET, the copyright of manuscripts should belong to KSOE. A transfer of copyright (publishing agreement) form can be found in submission website (<http://www.joet.org>).

### 2.5 Manuscript Submission

Manuscript should be submitted through the on-line submission website (<http://www.joet.org>). The date that manuscript was received through on-line website is the official date of receipt. Other correspondences can be sent by an email to the Editor in Chief or secretariat. The manuscript must be accompanied by a signed statement that it has been neither published nor currently submitted for publication elsewhere. The manuscript should be written in English or Korean. Ensure that online submission are in a standard word processing format. Corresponding author must write the manuscript using the JOET template provided in Hangul or MS Word format. Ensure that graphics are high-resolution. Be sure all necessary files have been uploaded/ attached.

#### 2.5.1 Author's checklist

Author's checklist and Transfer of copyright can be found in submission homepage (<http://www.joet.org>).

## 3. Manuscript

Manuscript must be edited in the following order: (1) Title, (2) Authors' names and affiliations, (3) Keywords, (4) Abstract, (5) Nomenclature (optional), (6) Introduction, (7) Main body (analyses, tests, results, and discussions), (8) Conclusions, (9) Conflict of interest (optional), (10) Funding (optional), (11) Acknowledgements (optional), (12) References, (13) Appendices (optional), (14) Author's ORCID.

### 3.1 Unit

Use the international system units(SI). If other units are mentioned, please give their equivalent in SI.

### 3.2 Equations

All mathematical equations should be clearly printed/typed using well accepted explanation. Superscripts and subscripts should be typed clearly above or below the base line. Equation numbers should be given in Arabic numerals enclosed in parentheses on the right-hand margin. The parameters used in equation must be defined. They should be cited in the text as, for example, Eq. (1), or Eqs. (1)–(3).

$$G_{GEV}(x; \mu, \sigma, \xi) = \begin{cases} \exp[-(1 + \xi(x - \mu)/\sigma)^{-1/\xi}] & \xi \neq 0 \\ \exp[-\exp(-(x - \mu)/\sigma)] & \xi = 0 \end{cases} \quad (1)$$

in which  $\mu$ ,  $\sigma$ , and  $\xi$  represent the location ("Shift" in figures), scale, and shape parameters, respectively.

### 3.3 Tables

Tables should be numbered consecutively with Arabic numerals. Each table should be typed on a separate sheet of paper and be fully titled. All tables should be referred to in the texts.

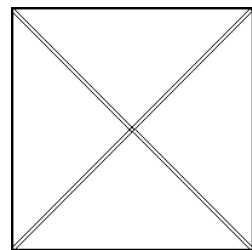
**Table 1** Tables should be placed in the main text near to the first time they are cited

Item	Buoyancy riser
Segment length <sup>1)</sup> (m)	370
Outer diameter (m)	1.137
Inner diameter (m)	0.406
Dry weight (kg/m)	697
Bending rigidity (N·m <sup>2</sup> )	1.66E8
Axial stiffness (N)	7.098E9
Inner flow density (kg·m <sup>3</sup> )	881
Seabed stiffness (N/m/m <sup>2</sup> )	6,000

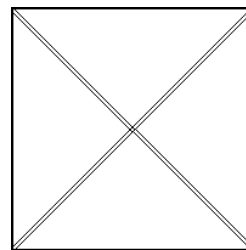
<sup>1)</sup>Tables may have a footer.

### 3.4 Figures

Figures should be numbered consecutively with Arabic numerals. Each figure should be fully titled. All the illustrations should be of high quality meeting with the publishing requirement with legible symbols and legends. All figures should be referred to in the texts. They should be referred to in the text as, for example, Fig. 1, or Figs. 1–3.



(a) Description of what is contained in the first panel



(b) Description of what is contained in the second panel

**Fig. 1** Schemes follow the same formatting. If there are multiple panels, they should be listed as: (a) Description of what is contained in the first panel; (b) Description of what is contained in the second panel. Figures should be placed in the main text near to the first time they are cited

### 3.5 How to Describe the References in Main Texts

All references should be listed at the end of the manuscripts, arranged in order of Alphabet. References in texts follow the American Psychological Association (APA) style. The exemplary form of listed references is as follows:

Single author: (Kim, 1998) or Kim (1998)

Two authors: (Kim and Lee, 2000) or Kim and Lee (2000)

Three or more authors: (Kim et al., 1997) or Kim et al. (1997)

Two or more papers: (Lee, 1995a; Lee, 1995b; Ryu et al., 1998)

Year unknown: (Kim, n.d.) or Kim (n.d.)

## 4. Results

This section may be divided by subheadings. It should provide a concise and precise description of the experimental results, their interpretation as well as the experimental conclusions that can be drawn. Tables and figures are recommended to present the results more rapidly and easily. Do not duplicate the content of a table or a figure with in the Results section. Briefly describe the core results related to the conclusion in the text when data are provided in tables or in figures. Supplementary results can be placed in the Appendix.

## 5. Discussion

Authors should discuss the results and how they can be interpreted in perspective of previous studies and of the working hypotheses. The findings and their implications should be discussed in the broadest context possible. Future research directions may also be highlighted

## 6. Conclusions

This section can be added to the manuscript.

### Conflict of Interest (Optional)

It should be disclosed here according to the statement in the Research and publication ethics regardless of existence of conflict of interest. If the authors have nothing to disclose, please state: “No potential conflict of interest relevant to this article was reported.”

### Funding (Optional)

Please add: “This research was funded by Name of Funder, grant number XXX” and “The OOO was funded by XXX”. Check carefully that the details given are accurate and use the standard spelling of funding agency names at <https://search.crossref.org/funding>

### Acknowledgments (Optional)

In this section you can acknowledge any support given which is not covered by the author contribution or funding sections. This may include administrative and technical support, or donations in kind (e.g., materials used for experiments). For mentioning any persons or any organizations in this section, there should be a written permission from them.

## References

- Journal name should not be abbreviated.
- A private report with limited access or download availability can not be a reference.
- Include the digital object identifier DOI or URL for all references where available.
- Reference list follows the American Psychological Association (APA) style.

#### Referring to journal publications:

Author, A.A., Author, B.B., & Author, C.C. (Year). Title of Article. Journal Title, vol(no), pp-pp. <https://doi.org/xx.xxxx/xxxxxx>

Author, A.A., Author, B.B., Author, C.C. (accepted; in press). Title of Article. Title of Periodical. Retrieved from <http://xx.xxx/x.pdf>

Lee, T.K., Kim, T.W., Rim, C.W., & Kim, S.C. (2013). A Study on Calculation of Local Ice Pressures for ARAON Based on Data Measured at Arctic Sea. Journal of Ocean Engineering and Technology, 27(5), 88–92. <https://doi.org/10.5574/KSOE.2013.27.5.088>

Lee, T.K., Kim, T.W., Rim, C.W., & Kim, S.C. (accepted; in press). A Study on Calculation of Local Ice Pressures for ARAON Based on Data Measured at Arctic Sea. Journal of Ocean Engineering and Technology, Retrieved from <http://xxx.xxx/xxx.pdf>

#### Referring to conference proceedings:

Author, A.A., Author, B.B., & Author, C.C. (Year). Title of Article. Proceeding Title, City, Country, pp-pp. <https://doi.org/xx.xxxx>

Aoki, S., Liu, H., & Sawaragi, T. (1994). Wave Transformation and Wave Forces on Submerged Vertical Membrane. Proceedings of International Symposium Waves - Physical and Numerical Modeling, Vancouver, Canada, 1287–1296.

Tsukamoto, C.L., Lee, W., Yuh, J., Choi, S.K., & Lorentz, J. (1997). Comparison Study on Advanced Thruster Control of Underwater Robots. Proceedings of International Conference on Robotics and Automation, 1845–1850. <https://doi.org/110.1109/ROBOT.1997.619056>

#### Referring to books:

Author, A.A. (Year). Title of Book (xx ed.). Location: Publisher.

Strunk, W., & White, E.B. (2000). The Elements of Style (4<sup>th</sup> ed.). New York, USA: Longman.

Schlichting, H. (1968). Boundary Layer Theory (6<sup>th</sup> ed.). New York, USA: McGraw-Hill.

#### Referring to theses or dissertations:

Author, A.A. (Year). Title of Doctoral Dissertation or Master’s thesis (Doctoral Dissertation or Master’s thesis). Name of Institution, City, Country.

Giovanni, I. (1998). Modelling and Identification of Underwater Robotic Systems (Ph.D. Thesis). University of Genova, Genova, Italy.

Referring to technical reports, rules, or guidelines:

Author, A.A. (Year). Title of report (Reprot No. xxx), Location: Publisher.

Likhomanov, V. (2010). Full-Scale Ice Trials of the Korean Research Icebreaker ARAON. Daejeon, Korea: Arctic and Antarctic Research Institute (AARI).

ABS. (2011). Guide for Ice Loads Monitoring Systems. Houston, USA: American Bureau of Shipping.

Lloyd's Register. (2011). FDA ICE Fatigue Induced by Ice Loading, ShipRight Design and construction - Fatigue Design Assesment. London, United Kingdom: Lloyd's Register.

Larson, M., & Kraus, N.C. (1989). SBEACH: Numerical Model for Simulating Storm-Induced Beach Change - Report 1 Empirical Foundation and Model Development (Technicla Report CERC-89-9). Coastal Engineering research center Vicksburg Ms.

Referring to patents:

Righsholder, A.A. (Year). Title of Patent. Patent number, Patent office with country.

Dawoo Shipbulding & Maringe Engineering (DSME). (2013). Distance Length Standardization Method for Preventing Interference at the time of Uploading Cell Guide of Container Ship. Unexamined Patent Publication 1020130044635, Korean Interllectual Property Office.

Referring to websites:

Righsholder, A.A. (Year). Title of webpage. Retrieved Month Year from <http://xxxx>

International Association of Classification Societies (IACS). (2010a). Common Structural Rules for Bulk Carriers. Retrieved July 2010 from <http://www.iacs-data.org.uk>

US Congressional Hearing. (2009). Strategic Importance of the Arctic in Us Policy. Retrieved June 2019 from <https://fas.org/irp/arctic.pdf>

Dawoo Shipbulding & Maringe Engineering (DSME). (2013). Distance Length Standardization Method for Preventing Interference at the time of Uploading Cell Guide of Container Ship. Retrieved June 2019 from <https://patentimages.storage./pdfs/792.pdf>

Referring to software:

Righsholder, A.A. (Year). Title of Software. Downloaded Month Year from <http://xxxx>

Standard

Organization. (Year). Title of the standard in italics [Translated title – if applicable] (Standard No.). Retrieved from <https://...>

International Organization for Standardization. (2005). Industrial sewing machines: Safety requirements for sewing machines, units and systems (ISO Standard No. 10821). Retrieved from <http://www.standard.no/no/Nettbutikk/produktkatalogen/Produktpresentasjon/?ProductID=113554>

Translation

Author, A. A. (Year of publication). Title of work: Capital letter also for subtitle (T. Translator, Trans.). Location: Publisher. (Original work published YEAR). DOI

Ura, T., & Takakawa, S. (2015). All about Submersibles (W.S. Kim, D.S. Kim, Y.H. Choi, C.H. Park, J.S. Park, P.M. Lee, H.S. Jung, Trans.). Korea: CIR. (Original Work Published in 1994, Japan: Seizan-Shoten Publishing)

in text: (Ura and Takakawa, 1994/2015)

Referring to some exceptional cases:

- when authors are missing, institution can replace authors

National Oceanic and Atmospheric Administration (NOAA). (2015). Deep-ocean Assessment and Reporting of Tsunamis (DART). Retrieved December 2019 from <https://nctr.pmel.noaa.gov/Dart/>

- when dates or years are missing, it is replaced with "n.d."

National Oceanic and Atmospheric Administration (NOAA). (n.d.). Deep-ocean Assessment and Reporting of Tsunamis (DART).

- when more then seven authors, first 6 authors ... last author.

Yeu, T., Choi, H.T., Lee, Y., Chae, J., Lee, Y., Kim, S.S., ... Lee, T.H. (2019). Development of Robot Platform for Autonomous Underwater Intervention. Journal of Ocean Engineering and Technology, 33(2), 168-177. <https://doi.org/10.26748/KSOE>. 2019.021

## Appendix (Optional)

The appendix is an optional section that can contain details and data supplemental to the main text. For example, explanations of experimental details that would disrupt the flow of the main text, but nonetheless remain crucial to understanding and reproducing the research shown; figures of replicates for experiments of which representative data is shown in the main text can be added here if brief, or as Supplementary data. Mathematical proofs of results not central to the paper can be added as an appendix.

All appendix sections must be cited in the main text. In the appendixes, Figures, Tables, etc. should be labeled starting with 'A', e.g., Fig. A1, Fig. A2, etc.

Examples:

<https://doi.org/10.26748/KSOE.2019.022>

<https://doi.org/10.26748/KSOE.2018.4.32.2.095>

## Author ORCIDs

All authors are recommended to provide an ORCID. To obtain an ORCID, authors should register in the ORCID web site: <http://orcid.org>. Registration is free to every researcher in the world. Example of ORCID description is as follows:

Author name	ORCID
So, Hee	0000-0000-000-00X
Park, Hye-Il	0000-0000-000-00X
Yoo, All	0000-0000-000-00X
Jung, Jewelry	0000-0000-000-00X

# Authors' Checklist

The following list will be useful during the final checking of a manuscript prior to sending it to the journal for review. Please submit this checklist to the KSOE when you submit your article.

## < Checklist for manuscript preparation >

- I checked my manuscript has been 'spell-checked' and 'grammar-checked'.
- One author has been designated as the corresponding author with contact details such as
  - E-mail address
  - Phone numbers
- I checked abstract 1) stated briefly the purpose of the research, the principal results and major conclusions, 2) was written in around 300 words, and 3) did not contain references (but if essential, then cite the author(s) and year(s)).
- I provided 5 or 6 keywords.
- I checked color figures were clearly marked as being intended for color reproduction on the Web and in print, or to be reproduced in color on the Web and in black-and-white in print.
- I checked all table and figure numbered consecutively in accordance with their appearance in the text.
- I checked abbreviations were defined at their first mention there and used with consistency throughout the article.
- I checked all references mentioned in the Reference list were cited in the text, and vice versa according to the APA style.
- I checked I used the international system units (SI) or SI-equivalent engineering units.

## < Authorship checklist >

JOET considers individuals who meet all of the following criteria to be authors:

- Made a significant intellectual contribution to the theoretical development, system or experimental design, prototype development, and/or the analysis and interpretation of data associated with the work contained in the article.
- Contributed to drafting the article or reviewing and/or revising it for intellectual content.
- Approved the final version of the article as accepted for publication, including references.

## < Checklist for publication ethics >

- I checked the work described has not been published previously (except in the form of an abstract or as a part of a published lecture or academic thesis).
- I checked when the work described has been published previously in other proceedings without copyright, it has clearly noted in the text.
- I checked permission has been obtained for use of copyrighted material from other sources including the Web.
- I have processed Plagiarism Prevention Check through reliable web sites such as [www.kci.go.kr](http://www.kci.go.kr), <http://www.ithenticate.com/>, or <https://www.copykiller.org/> for my submission.
- I agree that final decision for my final manuscript can be changed according to results of Plagiarism Prevention Check by JOET administrator.
- I checked one author at least is member of the Korean Society of Ocean Engineers.
- I agreed all policies related to 'Research and Publication Ethics'
- I agreed to transfer copyright to the publisher as part of a journal publishing agreement and this article will not be published elsewhere including electronically in the same form, in English or in any other language, without the written consent of the copyright-holder.
- I made a payment for reviewing of the manuscript, and I will make a payment for publication on acceptance of the article.
- I have read and agree to the terms of Authors' Checklist.

Title of article :

Date of submission : DD/MM/YYYY

Corresponding author :

signature

Email address :

※ E-mail this with your signature to [ksoehj@ksoe.or.kr](mailto:ksoehj@ksoe.or.kr)

# Publishing Agreement

## ARTICLE DETAILS

Title of article :  
Corresponding author :  
E-mail address :  
DOI : <https://doi.org/10.26748/KSOE.2XXX.XXX>

## YOUR STATUS

I am one author signing on behalf of all co-authors of the manuscript.

## ASSIGNMENT OF COPYRIGHT

I hereby assign to the Korean Society of Ocean Engineers, the copyright in the manuscript identified above and any tables, illustrations or other material submitted for publication as part of the manuscript (the "Article"). This assignment of rights means that I have granted to Korean Society of Ocean Engineers the exclusive right to publish and reproduce the Article, or any part of the Article, in print, electronic and all other media (whether now known or later developed), in any form, in all languages, throughout the world, for the full term of copyright, and the right to license others to do the same, effective when the Article is accepted for publication. This includes the right to enforce the rights granted hereunder against third parties.

## SCHOLARLY COMMUNICATION RIGHTS

I understand that no rights in patents, trademarks or other intellectual property rights are transferred to the Journal owner. As the author of the Article, I understand that I shall have: (i) the same rights to reuse the Article as those allowed to third party users of the Article under the CC-BY-NC License, as well as (ii) the right to use the Article in a subsequent compilation of my works or to extend the Article to book length form, to include the Article in a thesis or

dissertation, or otherwise to use or re-use portions or excerpts in other works, for both commercial and non-commercial purposes. Except for such uses, I understand that the assignment of copyright to the Journal owner gives the Journal owner the exclusive right to make or sub-license commercial use.

## USER RIGHTS

The publisher will apply the Creative Commons Attribution-Noncommercial Works 4.0 International License (CC-BY-NC) to the Article where it publishes the Article in the journal on its online platforms on an Open Access basis.

The CC-BY-NC license allows users to copy and distribute the Article, provided this is not done for commercial purposes and further does not permit distribution of the Article if it is changed or edited in any way, and provided the user gives appropriate credit (with a link to the formal publication through the relevant DOI), provides a link to the license, and that the licensor is not represented as endorsing the use made of the work. The full details of the license are available at <http://creativecommons.org/licenses/by-nc/4.0/legalcode>.

## REVERSION OF RIGHTS

Articles may sometimes be accepted for publication but later rejected in the publication process, even in some cases after public posting in "Articles in Press" form, in which case all rights will revert to the author.

**I have read and agree to the terms of the Journal Publishing Agreement.**

Corresponding author:

name

signature

※ E-mail this with your signature to [ksoehj@ksoe.or.kr](mailto:ksoehj@ksoe.or.kr) (Papers will not be published unless this form is signed and returned)

# Research and Publication Ethics

Journal of Ocean Engineering and Technology (JOET) adheres to the guidelines published by professional organizations, including Committee on Publication Ethics (COPE; <https://publicationethics.org/>)

## 1. Authorship

*JOET considers individuals who meet all of the following criteria to be authors:*

- 1) Made a significant intellectual contribution to the theoretical development, system or experimental design, prototype development, and/or the analysis and interpretation of data associated with the work contained in the article.
- 2) Contributed to drafting the article or reviewing and/or revising it for intellectual content.
- 3) Approved the final version of the article as accepted for publication, including references.

Contributors who do not meet all of the above criteria may be included in the Acknowledgment section of the article. Omitting an author who contributed to your article or including a person who did not fulfill all of the above requirements is considered a breach of publishing ethics.

**Correction of authorship after publication:** JOET does not correct authorship after publication unless a mistake has been made by the editorial staff.

## 2. Originality and Duplicate Publication

All submitted manuscripts should be original and should not be in consideration by other scientific journals for publication. Any part of the accepted manuscript should not be duplicated in any other scientific journal without permission of the Editorial Board, although the figures and tables can be used freely if the original source is verified according to the Creative Commons Attribution License (CC BY-NC). It is mandatory for all authors to resolve any copyright issues when citing a figure or table from other journal that is not open access.

## 3. Conflict-of-Interest Statement

Conflict of interest exists when an author or the author's institution, reviewer, or editor has financial or personal relationships that inappropriately influence or bias his or her actions. Such relationships are also known as dual commitments, competing interests, or competing loyalties. These relationships vary from being negligible to having a great potential for influencing judgment. Not all relationships represent true conflict of interest. On the other hand, the potential for conflict of interest can exist regardless of whether an individual believes that the relationship affects his or her scientific judgment. Financial relationships such as employment, consultancies, stock ownership, honoraria, and paid expert testimony are the most easily identifiable conflicts of interest and the most likely to undermine the credibility of the journal, the authors, or of the science itself. Conflicts can occur for other reasons as well, such as personal relationships, academic competition, and intellectual passion. If there are any conflicts of interest, authors should disclose them in the manuscript. The conflicts of interest may occur during the research process as well; however, it is important to provide disclosure. If there is a disclosure, editors, reviewers, and reader can approach the manuscript after understanding the situation and the background of the completed research.

## 4. Management Procedures for the Research and Publication Misconduct

When JOET faces suspected cases of research and publication misconduct such as a redundant (duplicate) publication, plagiarism, fabricated data, changes in authorship, undisclosed conflicts of interest, an ethical problem discovered with the submitted manuscript, a reviewer who has appropriated an author's idea or data, complaints against editors, and other issues, the resolving process will follow the flowchart provided by the Committee on Publication Ethics (<http://publicationethics.org/resources/flowcharts>). The Editorial Board of JOET will discuss the suspected cases and reach a decision. JOET will not hesitate to publish

errata, corrigenda, clarifications, retractions, and apologies when needed.

## 5. Editorial Responsibilities

The Editorial Board will continuously work to monitor and safeguard publication ethics: guidelines for retracting articles; maintenance of the integrity of the academic record; preclusion of business needs from compromising intellectual and ethical standards; publishing corrections, clarifications, retractions, and apologies when needed; and excluding plagiarism and fraudulent data. The editors maintain the following responsibilities: responsibility and authority to reject and accept articles; avoiding any conflict of interest with respect to articles they reject or accept; promoting publication of corrections or retractions when errors are found; and preservation of the anonymity of reviewers.

## 6. Hazards and human or animal subjects

If the work involves chemicals, procedures or equipment that have any unusual hazards inherent in their use, the author must clearly identify these in the manuscript. If the work involves the use of animal or human subjects, the author should ensure that the manuscript contains a statement that all procedures were performed in compliance with relevant laws and institutional guidelines and that the appropriate institutional committee(s) has approved them. Authors should include a statement in the manuscript that informed consent was obtained for experimentation with human subjects. The privacy rights of human subjects must always be observed.

Ensure correct use of the terms sex (when reporting biological factors) and gender (identity, psychosocial or cultural factors), and, unless inappropriate, report the sex and/or gender of study participants, the sex of animals or cells, and describe the methods used to determine sex and gender. If the study was done involving an exclusive population, for example in only one sex, authors should justify why, except in obvious cases. Authors should define how they determined race or ethnicity and justify their relevance.

## 7. Secondary publication

It is possible to republish manuscripts if the manuscripts satisfy the conditions of secondary publication. These are:

- The authors have received approval from the Editorial Board of both journals (the editor concerned with the secondary publication must have access to the primary version).
- The priority for the primary publication is respected by a publication interval negotiated by editors of both journals and the authors.
- The paper for secondary publication is intended for a different group of readers
- The secondary version faithfully reflects the data and interpretations of the primary version.
- The secondary version informs readers, peers, and documenting agencies that the paper has been published in whole or in part elsewhere, for example, with a note that might read, "This article is based on a study first reported in the [journal title, with full reference]"
- The title of the secondary publication should indicate that it is a secondary publication (complete or abridged republication or translation) of a primary publication.

## 8. Complaints and Appeals

The process of handling complaints and appeals follows the guidelines of the COPE available from: <https://publicationethics.org/appeals>

## 9. Post-publication discussions and corrections

The post-publication discussion is available through letter to editor. If any readers have a concern on any articles published, they can submit letter to editor on the articles. If there found any errors or mistakes in the article, it can be corrected through errata, corrigenda, or retraction.



The Korean Society of Ocean Engineers